

CHEMIA

**STUDIA
UNIVERSITATIS BABEȘ-BOLYAI
CHEMIA**

1/2015

EDITORIAL BOARD OF STUDIA UNIVERSITATIS BABEȘ-BOLYAI CHEMIA

ONORARY EDITOR:

IONEL HAIDUC - Member of the Romanian Academy

EDITOR-IN-CHIEF:

LUMINIȚA SILAGHI-DUMITRESCU

EXECUTIVE EDITOR:

CASTELIA CRISTEA

EXECUTIVE CO-EDITOR:

RADU SILAGHI-DUMITRESCU

EDITORIAL BOARD:

PAUL ȘERBAN AGACHI, Babeș-Bolyai University, Cluj-Napoca, Romania

LIVAIN BREAU, UQAM University of Quebec, Montreal, Canada

HANS JOACHIM BREUNIG, Institute of Inorganic and Physical Chemistry,
University of Bremen, Bremen, Germany

MIRCEA DIUDEA, Babes-Bolyai University, Cluj-Napoca, Romania

JEAN ESCUDIE, HFA, Paul Sabatier University, Toulouse, France

ION GROSU, Babeș-Bolyai University, Cluj-Napoca, Romania

EVAMARIE HEY-HAWKINS, University of Leipzig, Leipzig, Germany

FLORIN DAN IRIMIE, Babeș-Bolyai University, Cluj-Napoca, Romania

FERENC KILAR, University of Pecs, Pecs, Hungary

BRUCE KING, University of Georgia, Athens, Georgia, USA

ANTONIO LAGUNA, Department of Inorganic Chemistry, ICMA, University of
Zaragoza, Zaragoza, Spain

JURGEN LIEBSCHER, Humboldt University, Berlin, Germany

KIERAN MOLLOY, University of Bath, Bath, UK

IONEL CĂTĂLIN POPESCU, Babeș-Bolyai University, Cluj-Napoca, Romania

CRISTIAN SILVESTRU, Babeș-Bolyai University, Cluj-Napoca, Romania

<http://chem.ubbcluj.ro/~studiachemia/>; studiachemia@chem.ubbcluj.ro

http://www.studia.ubbcluj.ro/serii/chemia/index_en.html

YEAR
MONTH
ISSUE

Volume 60 (LX) 2015
MARCH
1

S T U D I A
UNIVERSITATIS BABEȘ-BOLYAI
CHEMIA

1

STUDIA UBB EDITORIAL OFFICE: B.P. Hasdeu no. 51, 400371 Cluj-Napoca, Romania,
Phone + 40 264 405352

CUPRINS – CONTENT – SOMMAIRE – INHALT

MIHAI TODICA, RAZVAN STEFAN, CORNEL VIOREL POP, IONEL PAPUC,
OANA STAN, LOREDANA ELENA OLAR, UV-VIS and Fluorescence
Investigation of Some Poly(acrylic) Gels 7

MIHAI TODICA, CORNEL VIOREL POP, RAZVAN STEFAN, MIHAELA
NAGY, SORINA GARABAGIU, Spectroscopic Investigation of Some
Poly (Acrylic Acid) Gels with Embedded Gold Nanoparticles 19

IOANA BREZESTEAN, NICOLAE HAR, ALINA TANTĂU, MARIA GOREA,
MONICA M. VENTER, SIMONA CÎNTĂ PÎNZARU, Analytical Study
of Gallstones in Patients from Transylvania, Romania 29

NICOLAE CIOICA, RADU FECHETE, RAMONA CHELCEA, CONSTANTIN
COTA, MIHAI TODICA, CORNEL V. POP, ONUC COZAR, Water
Absorption and Degradation of Packages Based on Native Corn
Starch with Plasticizers 45

RAMONA I. CHELCEA, REMUS S. ȘIPOS, RADU FECHETE, DUMITRIȚA
MOLDOVAN, IOANA ȘUȘ, ZOLTAN PÁVAI AND DAN E. DEMCO,
One-Dimensional Laplace Spectroscopy Used for the Assessment
of Pore-Size Distribution on the Ovariectomized Rats Femur57

MARIA TOMA, DANIEL MARCONI, CLAUDIU LUNG, OANA PONTA, AUREL POP, Structural, Morphological and Optical Properties of RE-doped AZO Thin Films (RE=Nd, Gd, Er) Grown by RF Magnetron Sputtering	71
PAULA ILDIKÓ RITI, ADRIANA VULPOI, VIORICA SIMON, Magnesium Influence on Bioactivity of Silicate Glasses Prepared by Different Sol-Gel Routes	81
MARCEL BENEĂ, VASILE DIACONU, GHEORGHE DUMITROAIA, Preliminary Data on Bronze Age Pottery from Săvești (Neamț County, Romania).....	89
ANDREEA BRAȘOVAN, RAMONA FLAVIA CÂMPEAN, NELI KINGA OLAH, CLAUDIU MORGOVAN, CARMEN POPESCU, PAUL ATYIM, Physico-Chemical Characterization of Spring and Salt Lakes from Someseni Tureni (Cluj County)	99
MARIA-ALEXANDRA HOAGHIA, CECILIA ROMAN, ERIKA ANDREA LEVEI, DUMITRU RISTOIU, Footprint and Direct Impact of Anthropogenic Activities on Groundwaters from Medias Area.....	109
CRISTINA COMAN, LOREDANA FLORINA LEOPOLD, OLIVIA-DUMITRIȚA RUGINĂ, ZORIȚA DIACONEASA, POMPEI FLORIN BOLFĂ, NICOLAE LEOPOLD, MARIA TOFANĂ, CARMEN SOCACIU, Protein-Capped Gold Nanoparticles Obtained by a Green Synthesis Method	119
MARIA MUREȘAN, DANIELA BENEDEC, LAURIAN VLASE, RADU OPREAN, ANCA TOIU, ILIOARA ONIGA, Screening of Polyphenolic Compounds, Antioxidant and Antimicrobial Properties of Tanacetum Vulgare from Transylvania.....	127
BIANCA MOLDOVAN, ROZALIA MINTĂU, LUMINIȚA DAVID, Thermal Stability of Anthocyanins from Common Dogwood (<i>Cornus Sanguinea</i> L.) Fruits	139
ADINA MICLĂUȘ, Freeze-Drying Kinetics for Different Types of Food Products	147
VASILE MIRCEA CRISTEA, Model Predictive Control of the Temperature in Drying Food Products	157
TEODORA E. HARSA, ALEXANDRA M. HARSA, MIRCEA V. DIUDEA, QSAR Study on (1-Methylpiperidin-4-Yl) Propanoate Derivatives by Similarity Cluster Prediction.....	165
EMESE SIPOS, ZOLTÁN – ISTVÁN SZABÓ, LILLA LŐRINCZI, ADRIANA CIURBA, Rheological Behavior and Microbiological Studies of Carbopol® Hydrogels	177

GRIGORE COCIAN, CĂTĂLIN POPA, Measurement Method for Determining the Residual Flux Deposits in a Heat Exchanger from a Controlled Atmosphere Brazing Line	187
RALUCA POP, MIRCEA DIUDEA, MIHAI MEDELEANU, MIHAIELA ANDONI, Theoretical Evaluation of the Aromatic Character of Aza-Phospha-Coronenes.....	195
AGLAIA RALUCA DEAC, LIVIU COSMIN COTEȚ, GRAZIELLA LIANA TURDEAN, LIANA MARIA MURESAN, Determination of Cd(II) Using Square Wave Anodic Stripping Voltammetry at a Carbon Paste Electrode Containing Bi-doped Carbon Xerogel.....	203
SEPIDEH SADAT MADANI, KARIM ZARE, MAHMOOD GHORANNEVISS, MAJID MONAJJEMI, Comparative Study on Cobalt and Nickel NPS for MWCNT Growth by TCVD System	213
MONICA IOANA TOȘA, BALÁZS KOMJÁTI, JÁNOS MADARÁSZ, PÁL KOLONITS, LÁSZLÓ POPPE, JÓZSEF NAGY, Stable Hydrate of a β -Lactamcarbaldehyde	229
DIANA-LARISA VLĂDOIU, VASILE OSTAFE, ADRIANA ISVORAN, Computational Analysis of the Structural Properties of Alpha - and Beta – Galactosidases	239
JOVANA ŠUĆUR, ALEKSANDRA POPOVIĆ, MILOŠ PETROVIĆ, GORAN ANAČKOV, DJORDJE MALENCIĆ, DEJAN PRVULOVIĆ, Allelopathic Effects and Insecticidal Activity of <i>Salvia Sclarea</i> L.	253
COSTEL SÂRBU, RODICA DOMNICA NAȘCU-BRICIU, Modelling and Prediction of Lipophilicity for Natural Compounds with Strong Biological Activity	265

Studia Universitatis Babes-Bolyai Chemia has been selected for coverage in Thomson Reuters products and custom information services. Beginning with V. 53 (1) 2008, this publication is indexed and abstracted in the following:

- Science Citation Index Expanded (also known as SciSearch®)
- Chemistry Citation Index®
- Journal Citation Reports/Science Edition

UV-VIS AND FLUORESCENCE INVESTIGATION OF SOME POLY(ACRYLIC) GELS

**MIHAI TODICA^{a*}, RAZVAN STEFAN^b, CORNEL VIOREL POP^a,
IONEL PAPUC^b, OANA STAN^a and LOREDANA ELENA OLAR^b**

ABSTRACT. Poly(acrylic) gels, (PAA), with polymeric concentrations 0.5, 1 and 1.5%, in aqueous state and neutralized with triethanolamine, (TEA), were investigated by UV-VIS and fluorescence methods. Such gels are suitable to obtain biocompatible matrices for some medical drugs. The aqueous gel with 1% PAA concentration shows an important absorption at 214 nm. At 1.5% PAA concentration the absorption increases and the peak shifts slowly to 212 nm. The absorption increases after neutralization and the maximum of absorbance shifts to 200 nm. Excitation of aqueous gels at 250, 270 and 290 nm is followed by two important fluorescence transition centered at 320 and 405 nm. The position of the fluorescence peaks is influenced by the polymeric concentration and by the neutralization. The UV-VIS and fluorescence investigations indicate some conformational changes determined by the neutralization.

Keywords: *poly(acrylic) gels; UV-VIS and fluorescence; neutralized gels*

INTRODUCTION

The development of intelligent medical pharmaceuticals requests the use of biocompatible matrices able to ensure a controlled delivery rate of the active substance, [1]. Some polymers, like the Poly(acrylic), (PAA), are suitable for this purpose. This polymer has a good stability and it is well accepted by the majority of living tissues. However the polymeric matrix obtained directly by polymerization has an acid character that is undesired for medical application. To prevent any repulsion reaction from the tissues this polymer is neutralized with triethanolamine, (TEA). Often this polymer it is used

^a "Babes-Bolyai", University, Faculty of Physics, 1 Kogalniceanu str, RO-40047 Cluj-Napoca, Romania. * Corresponding author: mihai.todica@phys.ubbcluj.ro

^b USAMV, Departments: I Preclinic and III Paraclinic, Cluj-Napoca, Romania

for the preparation of medical gels for skin disease treatment or skin care. Good mechanical properties are required in these situations. The polymeric matrix must be enough flexible to allow the organic motions of the body, must ensure good adherence to the skin, and must be removed simple after the complete delivery of the drug. Some of such properties are enhanced after neutralization, due to the cross linking effect induced by the TEA. Other benefic effect of neutralization is the increase of the viscoelastic properties of polymeric matrix, [2]. During the therapy these gels are frequently exposed voluntarily or involuntarily to UV or sun radiation. Under the action of these radiations modification of the local conformation of the polymeric matrix can occurs. In these situations it is important to know the response of such matrices, (the absorbance and the effect of neutralization), to the UV-VIS radiations. Moreover, it is possible to initiate the delivery of the active substance, or the excitation of some luminophors included in the drug by irradiation of the system with a specific radiation. In this case the investigation of the fluorescence properties of the polymeric matrix is suitable. In our work we investigated these aspects for some aqueous PAA gels, before and after neutralization with TEA. Such studies represent a first step towards the preparation of polymeric matrix with controlled release of the active substance.

RESULTS AND DISCUSSION

The absorption of the UV-VIS radiation is determined mainly by the transition of the electrons from a full bonding or non-bonding orbital into an empty anti-bonding orbital, [4, 5]. The spectral domain of absorption depends on the molecular particularities of the samples. In the pure PAA the most important absorption is observed around 207 nm, and it is determined mainly by the $\pi \rightarrow \pi^*$ transition of the carbonyl groups, [6]. In ours systems we expect to observe this transition with some modifications, due to the presence of water and TEA. In order to disclose the contribution of each component to the total absorbance, we analyzed the components separately and then in combination each to other. The pure PAA shows a maximum of absorption at 212 nm, with the amplitude 1.9 a.u, after that the absorbance decreases progressively in the domain 250-700 nm. For pure TEA the absorbance reach its maximum at 200 nm, with the amplitude 3.86 a.u, and then the absorbance decreases almost sharp until 250 nm, and remains almost constant in the domain 250-700 nm, (Fig. 1). The absorption spectra of the gels have almost the same shape as the spectrum of the pure polymer. An important peak is observed at 212-214 nm then the absorbance decreases progressively in the domain 250-700 nm, like in the case of pure

PAA. However some differences appear between the pure components and the gels. For instance the absorbance of the gels is less intense than the absorbance of pure PAA, but increases with the concentration of the polymer. The amplitude of the absorption peak of pure PAA is 1.9 a.u. (Fig. 1), the amplitude of 1% gel is 0.29 a.u. and the amplitude 1.5% gel 0.53 a.u. (Fig. 2). Note that the measurements were done in the same conditions in order to perform quantitative analyze. So we can conclude that the absorbance of the gels increases with the concentration of the polymer, with asymptotic tendency to reach the absorbance of pure polymer. Other modification concerns the position of the absorption peak. At 1.5% PAA concentration the absorption peak appears at 212 nm, as in the case of pure PAA, but at 1% PAA concentration the absorption peak shifts slowly to 214 nm, (Fig. 2).

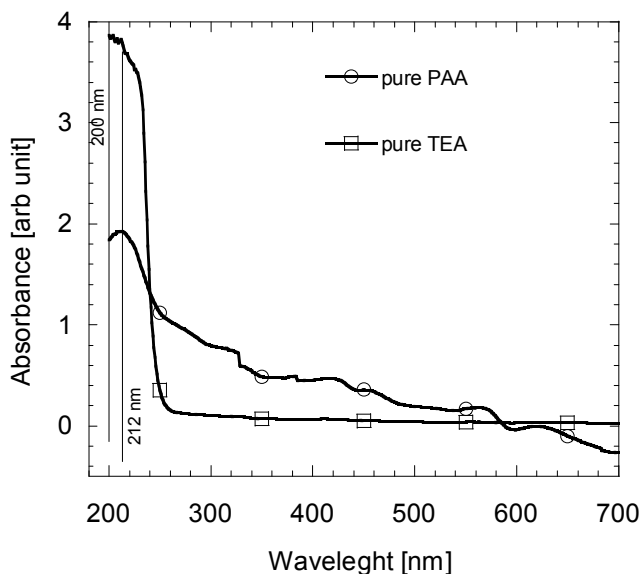


Figure 1. The UV-VIS absorption spectra of pure PAA and TEA

These differences are caused by the difference in water content of these systems. The samples with great polymeric concentration are characterized by high absorbance, and the peak is observed at 212 nm, whereas at great water concentration the peak shifts towards 214 nm and its amplitude diminish. As first conclusion we note the dependence of the amplitude and position of the absorption peak of the gels in function of the

polymer concentration, [7]. More important changes of the amplitude and position of the absorption peak appear after neutralization. At a given concentration of the polymer, i.e. 1%, the absorbance of the neutralized sample is greater than the absorbance of the aqueous gel, (0.56 for neutralized sample and 0.29 a.u. for aqueous gel). This increase is determined by the presence of neutralizer in the system

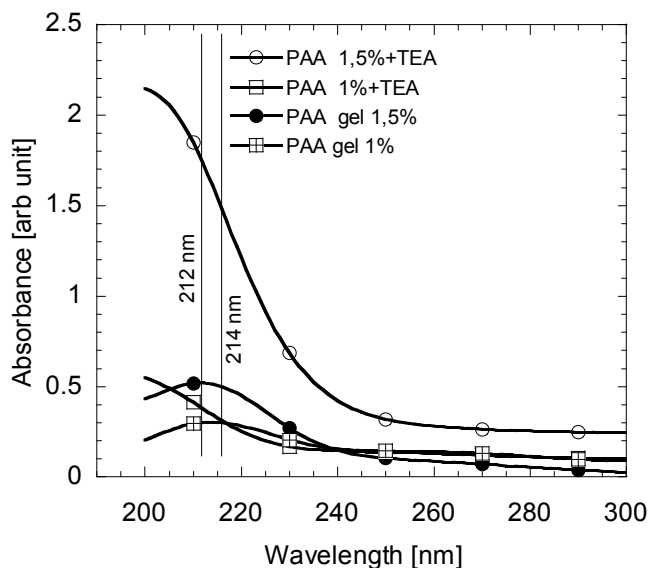


Figure 2. The UV-VIS absorption spectra of PAA gels with concentrations 1% and 1.5% in aqueous and neutralized state

As shown previously the neutralizer has absorption greater than the polymer. When the concentration of polymer, (respectively the TEA), increases, (i.e. 1.5% PAA), the absorbance increases at 2.16 a.u. with the tendency to reach the absorbance of pure TEA, (3.86 a.u.). In this sample the quantity of TEA is greater than in the sample 1%, because the ration PAA/TEA is all the times 1/1.5 constant. Other modification is the shift of the position of the absorption peak from 212 nm towards 200 nm, (Fig. 2). This shift is determined by the presence of TEA, for which the absorption peak appears at 200 nm. As conclusion, after neutralization the absorbance of the gels increases due to the presence of neutralizer, [8].

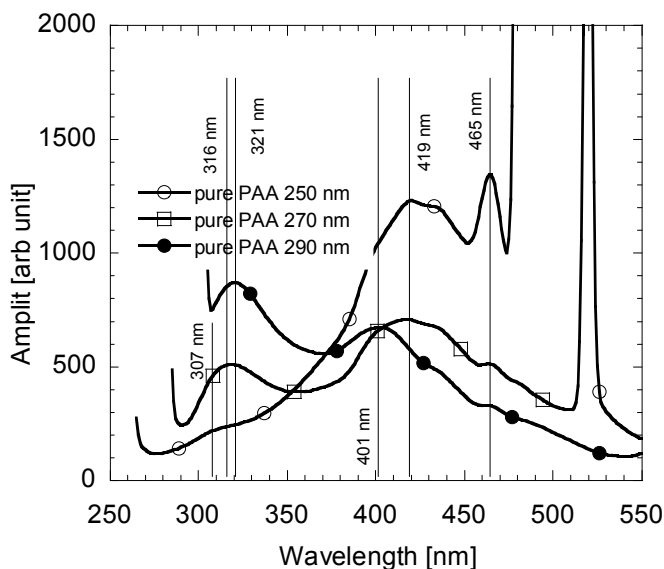


Figure 3. The fluorescence spectra of pure PAA at different excitation wavelengths

In the fluorescence experiments the electrons are excited from their initial state to a high energy level by irradiation with a source of light with well defined wavelength. The return to the initial state can be realized directly between the two energy levels by emission of one photon with the same energy that those of the exciting radiation, or by intermediate state. In this last case the transitions are accompanied by the emission of two photons with energy smaller than those of the exciting photon. These transitions are identified in the fluorescence spectra by the apparition of two emission peaks situated at wavelengths higher than the wavelength of the exciting photon, [9]. Although the excitation is made all the time at the same wavelength, the position of the intermediate state is not all the time the same, that results in the broadening of the spectrum. When the excitation frequency changes, the mechanism of fluorescence emission remains the same, but the position of the energy levels excited changes as well as the position of the peaks in the fluorescence spectrum. Analyze of these changes gives information about the structure of the atoms involved in the excitation process, [10, 11].

We analyzed first the pure components. The spectrum of pure PAA excited at 250 nm shows two clear peaks, a sharp one with high amplitude at 465 nm, and a large one at 419 nm with smaller amplitude. A weak shoulder can be seen at 307 nm, (Fig. 3). That means three transitions with different probabilities of apparition, the most probable corresponding to the lowest energy, (465 nm). At 270 nm excitation the first two peaks remains at the same wavelength but their amplitudes are smaller compared with the peaks observed at 250 nm excitation. In addition the rapport of amplitudes of these peaks is changed compared with the similar situation observed at 250 nm excitation. The first one became smaller and appears rather as a shoulder, whereas the second one has greater amplitude. A third peak appears at 316 nm. It represents the shoulder observed previously at 307 nm, but now it is well defined and shifts towards higher wavelengths. At 290 nm excitation the peak at 465 nm diminish again but remain at the same wavelength, the second peaks shifts to 401 nm and its amplitude diminish very few. The third peak increases substantially and shifts to 321 nm, (Fig. 3). That means a change of

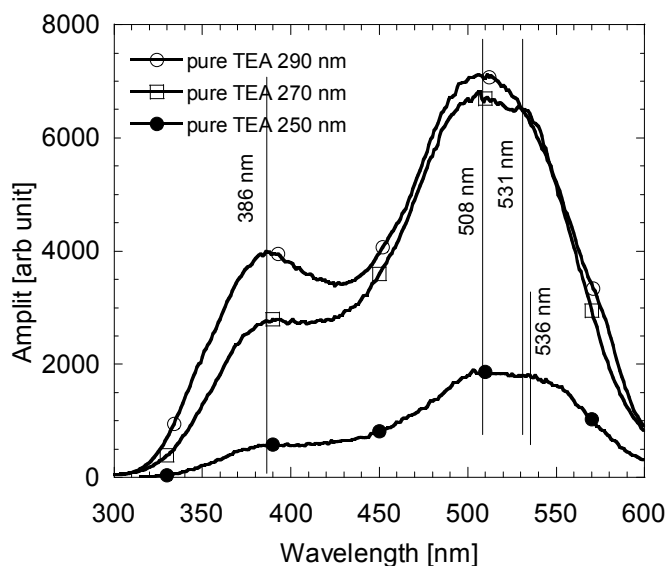


Figure 4. The fluorescence spectra of pure TEA at 250, 270 and 290 nm excitation wavelengths

the position of intermediate energy levels, as well as a change of the probabilities of these transitions. Now the transitions at high energy, (316 and 321 nm), become favorites.

The spectrum of pure TEA excited at 290 nm show two clear peaks with different amplitudes, a small one at 386 nm and a higher one at 508 nm. The high amplitude at 508 nm shows that the fluorescence transitions at low energy are favorites. At 270 nm excitation the spectrum has almost the same shape as at 290 nm, with the difference that the amplitude of the peak at 386 nm diminish slowly, and the peak at 508 nm reaches one shoulder at 531 nm. At 250 nm excitation the amplitude of the peak 386 nm diminish again and the second peak became broad with two shoulders at 508 and 536 nm, (Fig. 4). The presence of the peaks at 386 and 508 nm in all spectra indicates two fluorescence transitions that are less influenced by the energy of the excitation photons. The apparition of the 531 nm shoulder at 270 nm excitation, which become more evident and shifts slowly to 536 nm at 250 nm excitation, indicates a third fluorescence transition which is more probable at higher energy excitation.

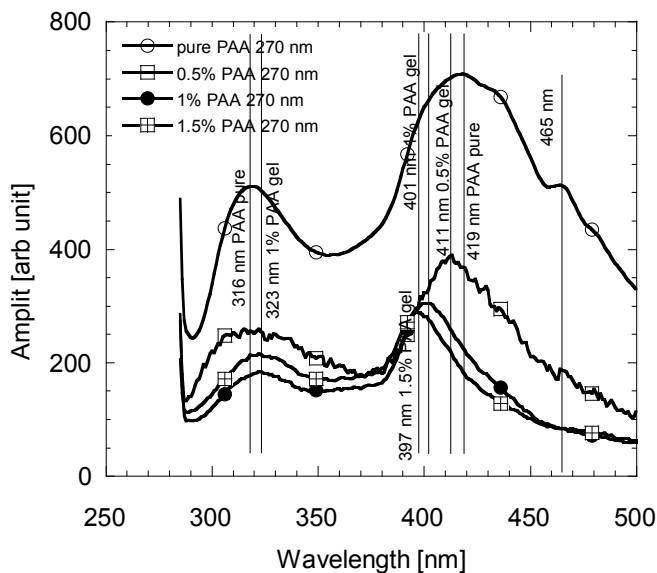


Figure 5. The fluorescence spectra of pure PAA and aqueous gels with concentrations 0.5, 1 and 1.5% excited at 270 nm

The fluorescence spectra of aqueous gels, before neutralizations, are almost similar to those of the pure polymer. We analyzed only the excitation at 270 nm, being the situation which provides the most useful details for discussion. All the samples contain two clear peaks as the pure polymer, a small peak around 316 nm and a higher one around 419 nm, but their amplitudes and positions depend on the polymeric concentration, (Fig. 5). At 0.5% polymeric concentration the first peak appears at 316 nm like in the

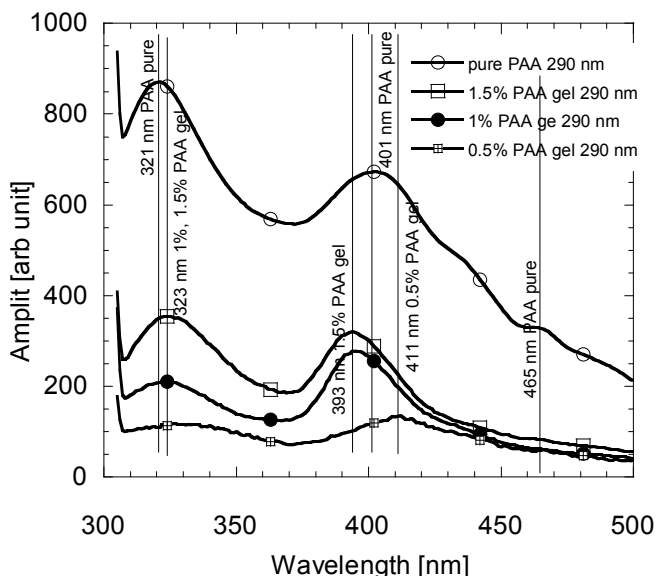


Figure 6. The fluorescence spectra of pure PAA and aqueous gels with concentrations 0.5, 1 and 1.5% excited at 290 nm

case of pure PAA, but its amplitude is much smaller than those of the pure polymer. This behavior can be explained taking into account the small quantity of polymer in this gel. The second peak appears at 411 nm, instead 419 nm as for pure PAA. When the polymeric concentration increases, (i.e. 1.5%), the first peak shifts slowly to 323 nm and the second one shifts towards 397 nm. The ratio of the amplitudes of these peaks remains almost the same for all the concentrations, and shows that the fluorescence transition at low energy, (419-397), is more probable. At 290 nm excitation, the shape of the spectra is not dramatically changed compared with the shape of spectra

recorded at 270 nm excitation. The spectra contain two major peaks around 320 and 410 nm. The first peak appears at 323 nm for samples 1% and 1.5% and shifts towards 330 nm and decreases substantially in amplitude for concentration 0.5%. The second one appears at 393 nm for samples 1% and 1.5% and shifts towards 411 nm for concentration 0.5%, (Fig. 6). We can observe that there are not dramatically changes compared with the situation observed at 270 nm excitation.

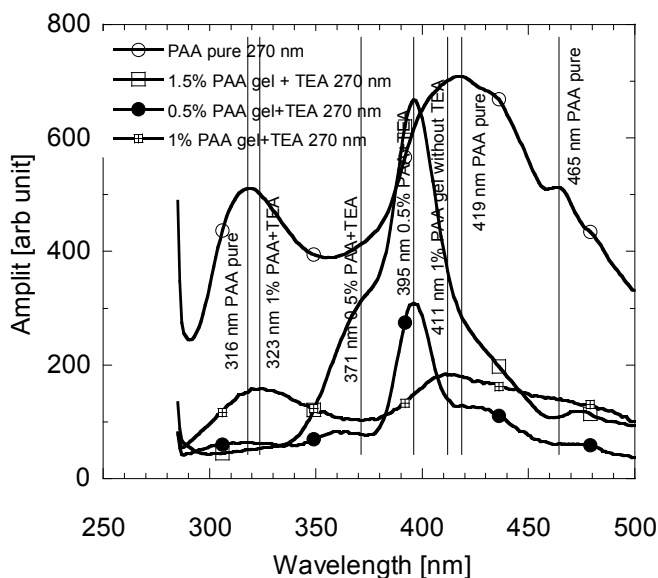


Figure 7. The fluorescence spectra of pure PAA and of neutralized gels with the polymeric concentration 0.5, 1 and 1.5%.

After neutralization the fluorescence spectra of samples show some differences compared with the un neutralized samples. At 270 nm excitation, for the sample with 1.5% polymeric concentration, we can observe a shoulder at 371 nm and a peak at 395 nm, (Fig. 7). The same sample without TEA shows peaks at 323 and 397 nm, (Fig. 6). The pure TEA show peaks at 386 nm. Practically the peak at 397 nm is assigned to the polymer and it is less influenced by the neutralization. The shoulder at 371 nm can be regarded as the peak of TEA, shifted from 386 to 371 nm. At 1% polymeric concentration the spectrum shows two peaks at 323 nm and 411 nm, (Fig. 7). The same sample, before neutralization, shows peaks at 323 and 401 nm, (Fig. 6).

We can observe that only the second peak was influenced by neutralization. At 0.5% concentration we can observe a well defined peak at 395 nm, (Fig. 7). In the un neutralized sample this peak appears at 411 nm, (Fig. 6). We can observe also two shoulders at 360 and 428 nm, which can be regarded as superposition of the peaks of pure TEA and PAA, (TEA at 386 and 508 nm, and PAA at 316 and 465 nm).

CONCLUSIONS

The UV-VIS spectra of the PAA and pure TEA contain maxima of absorption at 212 nm respectively at 200 nm. The absorbance of aqueous gels, before neutralization, increases with the concentration of the polymer and the peaks of absorption shift slowly towards higher wavelengths when the water concentration increases. The absorbance of the neutralized sample is greater than the absorbance of the aqueous gel and shift from 212 nm to 200 nm. The fluorescence spectra of pure PAA and pure PAA excited at different wavelengths contain peaks with amplitudes and positions depending on the frequency of excitation. This behavior is correlated with the modification of the intermediate atomic levels involved in the fluorescence emission, and with the modification of the transition probability from these levels. The spectra of gels, before neutralization, are almost similar to those of pure PAA, indicating low effect of water into the structure of the polymer. The neutralization reaction induces some modification of the electronic molecular structure, effect correlated with the modification of the position of the fluorescence peaks in the domain 395-415 nm.

EXPERIMENTAL SECTION

The PAA is a polymer with great affinity towards the water. The gel can be obtained by mixing the powder polymer, in solid state, with water. We use PAA with molecular mass 104400 g/mol which was mixed with distilled water, at room temperature, during 4 hours, until a homogeneous gel is obtained. The concentrations of the polymer in the solutions were 0.5%, 1% and 1.5% g/g. At higher concentration of polymer it is not possible to obtain homogeneous gels, [3]. The aqueous gels were neutralized with TEA in the proportion 1.5/1 g/g TEA/PAA. At this ratio base/polymer the PH of gel is about 6.5-7. The UV-VIS investigation was done with Jasco V-670 system with scan speed 200 nm/min, UV-VIS bandwidth 2 nm, and NIR bandwidth 8 nm. The fluorescence investigation was done with Jasco SP6100 system.

REFERENCES

- [1]. M.K. Chun, C.S. Cho, and H.K. Choi, *Journal of Applied Polymer Science*, **2001**, 79, 1525.
- [2]. C. Tiu, J. Guo and P.H.T. Uhlherr, *Journal of Industrial Engineering and Chemistry* **2006**, 12, 5, 653.
- [3]. M. Todica, C.V. Pop, Luciana Udrescu, Traian Stefan, *Chimese Physical Letters*, **2011**, 28, 12, 128201-1
- [4]. B. Stuart, "Polymer Analysis", John Wiley and Sons, Chichester, **2002**, chapter 5.
- [5]. M. Rubinstein, and R. Colby, "Polymer Physics", Oxford University Press, Oxford, **2002**, chapter 5.
- [6]. M. Todica, T. Stefan, S. Simon, I. Balasz, L. Daraban, *Turkish Journal Of Physics*, **2014**, 38, 2, 261.
- [7]. M. Todica, L. Udrescu, "Metode experimentale in fizica polimerilor", Presa Universitara Clujeana, **2013**, chapter 4.
- [8]. M. Navaneethana, K.D. Nishab, S. Ponnusamya, C. Muthamizhchelvana, *Materials Chemistry and Physics*, **2009**, 117, 443.
- [9]. Joseph R. Lakowicz, "Principles of Fluorescence Spectroscopy", Springer, **2006**, chapter 3.
- [10]. S. Garabagiu, C. Pestean, R. Stefan, *Journal of Luminescence*, **2013**, 143, 271.
- [11]. M. Baia, S. Astilean, T. Iliescu, "Raman and SERS Investigations of Pharmaceuticals", Springer-Verlag Berlin, Heidelberg, **2008**.

SPECTROSCOPIC INVESTIGATION OF SOME POLY (ACRYLIC ACID) GELS WITH EMBEDDED GOLD NANOPARTICLES

MIHAI TODICA^{a*}, CORNEL VIOREL POP^a, RAZVAN STEFAN^b,
MIHAELA NAGY^a and SORINA GARABAGIU^c

ABSTRACT. Some physical properties of poly (acrylic acid) gels with embedded gold nanoparticles, (PAA-GNP), as prepared and after neutralization with triethanolamine, (TEA), were investigated by UV-VIS and fluorescence methods. The UV-VIS spectra of the PAA-GNP gels contain the characteristics absorption peaks of both PAA and GNP pure components, with modified intensities and positions. Excitation at 250 nm of pure PAA and pure GNP are followed by characteristic fluorescence transitions. The peaks of pure components appear in the fluorescence spectrum of the PAA-GNP gels with some modifications compared with the pure state. Some modifications of the UV-VIS and fluorescence spectra were observed after neutralization with TEA. The particularities of these spectra indicate some changes of the conformation of the polymeric matrices after the introduction of GNP and after neutralization.

Keywords: *poly (acrylic acid), gold nanoparticles, UV-VIS and fluorescence.*

INTRODUCTION

In the last decades the development of intelligent pharmaceutical has known a high interest due to the advantages offered by these systems compared to the traditional pharmaceutical products. These systems offer the possibility to transport the active substance only in the desired region of the living bodies, the possibility to release the drug with controlled rate, and the possibility to initiate the delivery at desired time [1, 2]. Usually such

^a *Universitatea Babeş-Bolyai, Facultatea de Fizică, Str. M. Kogălniceanu, Nr. 1, RO-400084 Cluj-Napoca, Romania. * Corresponding author: mihai.todica@phys.ubbcluj.ro*

^b *USAMV, Departamentul Preclinic I si Paraclinic III, Cluj-Napoca, Romania*

^c *Institutul National de Cercetare si Dezvoltare a Tehnologiilor Izotopice si Moleculare, Cluj-Napoca, Romania*

pharmaceuticals consist of two main parts, the host matrix and the medical drug or an inorganic compound with therapeutic effect. Many polymers were tested as host matrix, the poly (vinyl alcohol) (PVA), poly (ethylene oxide) (PEO), and most recently the poly (acrylic acid) (PAA). Inorganic compounds as TiO_2 or graphite were introduced in these matrices in order to obtain polymeric gels and membranes with enhanced absorption in the UV domain [3, 4]. The well known pharmaceutical, the clotrimazole, was introduced into PAA matrix to obtain gels with possible use in the treatment of skin diseases, [5]. Particularly attention is focused actually on the gold nanoparticles (GNP) which can attach on their surface different compounds with antimicrobial effect. The advantages of such systems are the good compatibility with the living tissues, the great chemical stability and the possibility to initiate the pharmaceutical effect, (the delivery of the active substance, fluorescence emission, or local heating), by external excitation of the system with a well defined radiation [6]. Usually IR or UV-VIS radiation is used for this purpose. But the irradiation of the polymeric matrix could have undesired effects on the structure and local conformation of the chains, with negative consequences on the mechanical properties and physical stability of the system. On the other side, the answer of GNP to external excitation depends on their shape and size and the connections established with the host matrix. The efficiency of the excitation of GNP depends on the absorption properties of the system.

The irradiation in the UV-VIS domain produces excitation of the electrons from a full bonding or non-bonding orbital into an empty anti-bonding orbital [7-9]. The incident photon is absorbed if its energy corresponds to the difference between the electronic levels involved in the transition. The absorption is proportional with the concentration of the absorber, [10]. In the PAA the most important absorption is determined mainly by the $\pi \rightarrow \pi^*$ transition of the carbonyl groups and it is observed around 207 nm, [11]. The absorption is modified after introduction of GNP and after neutralization. The investigation of the UV-VIS absorption of these systems deals with our work.

The UV excitation of PAA-GNP system can be followed by characteristic fluorescence emission. The absorption of the incident photon produces the excitation of the electron from the electronic fundamental level to an excited vibrational level of the next electronic level. The excited electron recovers its initial state by two mechanisms, non radiative transition between the vibrational levels of the excited electronic state and then radiative transition between the electronic levels. A part of the energy of the incident photon is lost by transfer to other vibrational modes of the molecule or by thermal conversion during the vibrational transitions, [12, 13]. From this reason the photon emitted

by fluorescence has small energy compared with the absorbed one. The fluorescence spectrum contains emission lines situated at higher wavelength than that of the excitation photon. Modification of the energetic levels of the molecule determined by chemical bonds established with other neighbors leads to modification of the fluorescence spectrum. This is a way to investigate the possible interaction between the GNP and PAA matrix, and represents other objective of our work.

We performed preliminary studies on the PAA gels with embedded GNP by UV-VIS and fluorescence methods. PAA is a hydrophilic polymer well accepted by the living tissues, but its acid character could have some times undesired effects on the living tissues. In addition, in aqueous gel, without any reinforcement of its local organization, this polymer is characterized by low mechanical resistance and low viscosity. Improvement of these properties can be obtained by neutralization with triethanolamine (TEA). Moreover, the neutralization eliminates the acid character of the gel and enhances its compatibility with the living tissues. For these reasons, a part of our study is dedicated to the investigation of neutralized PAA gels. Our goal is the obtainment of polymeric gels containing GNPs with enhanced absorption properties in the UV domain and specific fluorescence emission.

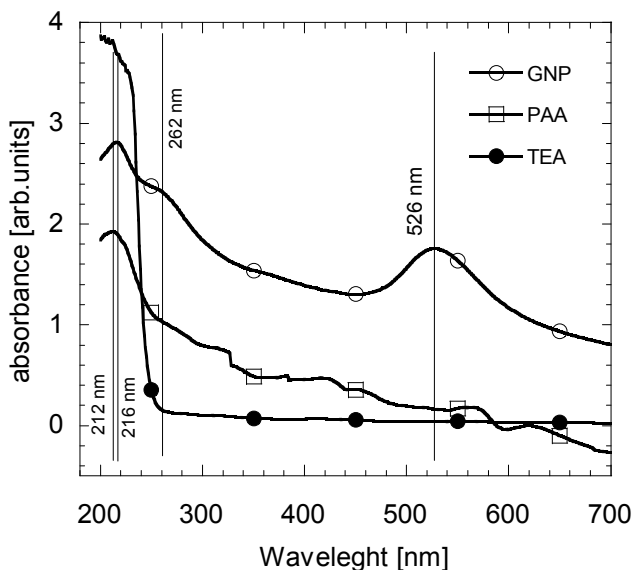


Figure 1. The UV-VIS absorption spectra of pure PAA, TEA and GNP

RESULTS AND DISCUSSION

In order to disclose the possible interactions between the polymer and GNP, the components were analyzed separately and then in combination in the gel. The pure PAA shows a maximum UV-VIS absorption at 212 nm, with the amplitude of 1.9 a.u., after that the absorbance decreases progressively in the domain 250-700 nm. The pure TEA has a maximum at 200 nm, with the amplitude of 3.86 a.u, and then the absorbance decreases sharply until 250 nm, and remains almost constant in the domain 250-700 nm (Figure 1). The spectra of pure GNP show an absorption peak at 216 nm with the amplitude of 3.8 a.u. and another one at 526 nm with the amplitude of 1.75 a.u. (Figure 1). The second peak is determined by the plasmonic resonance of the gold nanoparticles. A shoulder can be seen at 262 nm.

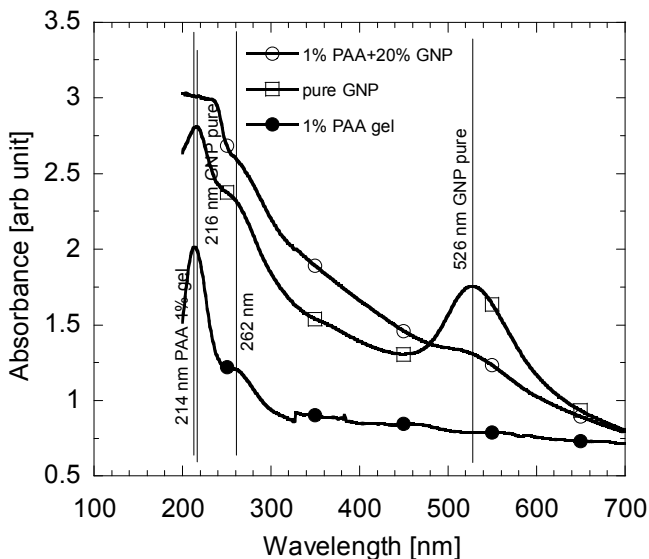


Figure 2. The UV-VIS absorption spectra of pure GNP, 1% PAA gel and 1% PAA gel with GNP

The spectrum of the aqueous gels, without GNP and TEA, contains the characteristic elements of pure PAA, but some differences appear. At 1% wt. PAA concentration the absorption peak of PAA gel without GNP shifts slowly from 212 to 214 nm (Figure 2).

This effect is determined by the perturbation of the hydrogen bonds established between the PAA monomers in the presence of water. This behavior was analyzed in previous paper [14]. The spectra of PAA gel with embedded GNP contain the characteristic peaks of both the components, pure PAA and pure GNP. We can see an intense peak in the domain 212-216 nm, a small one at 526 nm and a shoulder at 262 nm. However some differences appear between the pure components and the gels. The peak at 526 nm of GNP at has much small amplitude in the gel compared with the pure GNP. This decrease of the intensity is explained by the screening effect determined by the attachment of the polymeric chains to the surface of gold nanoparticles. A great fraction of GNPs are almost entirely covered by a thin layer of polymer. The incident radiation cannot penetrate the polymeric layer attached to the surface of the gold nanoparticles, (or penetrates it very few), and the GNPs cannot be excited by the radiation. The absorption of the radiation is determined mainly by the polymer. For this reason the absorption peak of the polymer at 212-216 nm can be clearly seen in the spectrum. Although this mechanism is dominant, some GNPs are not covered, or are partially covered by the polymeric layer, giving a small contribution to the spectrum, fact that explain the existence of the small peak at 526 nm and the shoulder at 262 nm.

After neutralization with TEA the absorption properties of samples change. First we analyzed the samples without GNP. For these gels the absorbance of the neutralized sample is greater than the absorbance of the aqueous gel, (almost two times greater for the neutralized sample) (Figure 3). This increase of the absorbance is determined by the presence of neutralizer in the system, which has absorption greater than the polymer. Other modification is the shift of the position of the absorption peak from 214 nm towards 200 nm (Figure 3). This shift is determined by the presence of TEA, for which the absorption peak appears at 200 nm. We can affirm that the neutralization enhances the absorbance of the gels [15]. For the samples with GNP, after neutralization, we can observe the attenuation of the shoulder at 526 nm. The shoulder at 262 nm almost disappears. That means that almost all the GNPs are covered by a thin layer of polymer and the incident radiation cannot excite these nanoparticles. The peak 212-216 nm becomes narrow and shifts towards 212 nm (Figure 3).

This shift is determined by the presence of the neutralizer in the samples. The UV-VIS investigations were completed by fluorescence measurements. We analyzed first the pure components. The spectrum of pure PAA excited at 250 nm shows two clear peaks, a sharp one with high amplitude at 465 nm, and a large one at 419 nm with smaller amplitude.

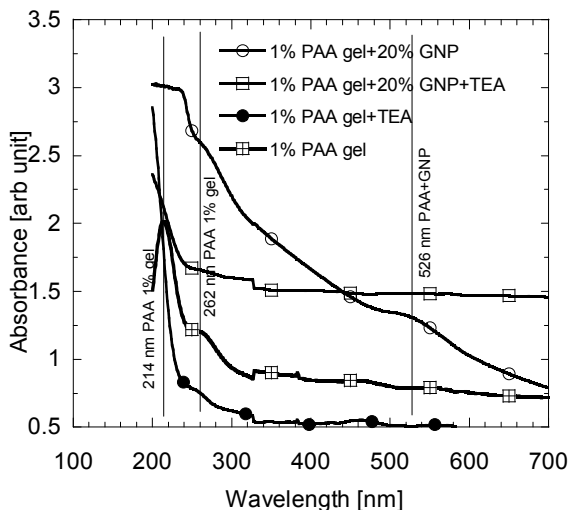


Figure 3. The UV-VIS spectra of PAA aqueous gel and PAA-GNP gel, before and after neutralization

A weak shoulder can be seen at 307 nm (Figure 4). These peaks are associated with three electronic transitions with different probabilities of apparition, the most probable corresponding to the lowest energy, (465 nm). The pure TEA shows a peak at 386 nm and the GNP shows a peak at 407 nm (Figure 4).

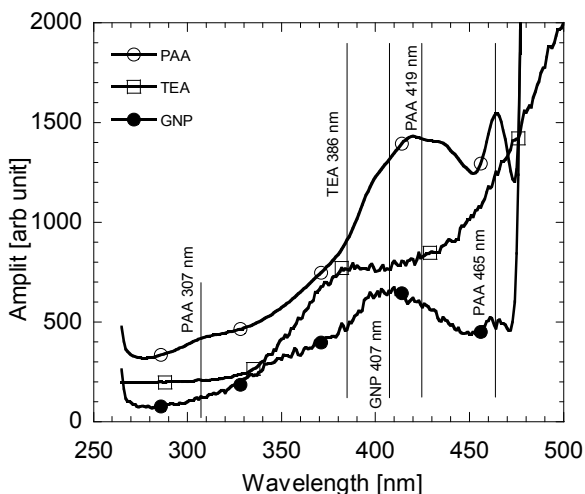


Figure 4. The fluorescence spectra of pure PAA, TEA and GNP excited at 250 nm

The spectrum of the 1% wt. PAA gel, without GNP, is almost similar to the spectrum of pure PAA, but some differences of the amplitude and position of the peaks can be seen. The first peak appears at 465 nm as in the case of pure PAA, but it has small amplitude. The second one appears at 412 nm, (instead 419 nm as for pure PAA), and its amplitude is greater than those of the first peak. The shoulder at 307 nm of pure PAA is now shifted at 321 nm (Figure 5). The gel excited at 250 nm shows three fluorescence transitions, as the pure PAA, but the most probable transition is situated at 412 nm, instead 465 nm for pure PAA. After the incorporation of GNP in the structure of the gel, we can observe the broadening between 400 and 420 nm of the peak initially centered at 419 in pure PAA and 412 nm in 1% wt. PAA gel. We can attribute this effect to the presence of GNPs, which gives its peak at 407 nm. The shift of the peak in the gel is determined by the superposition of the peaks of pure PAA and pure GNP. The peak at 465 nm remains at the same wavelength and

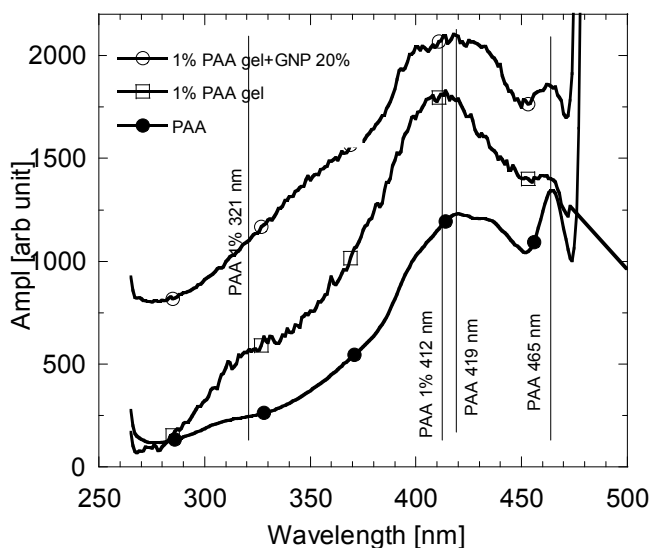


Figure 5. The fluorescence spectra of pure PAA, 1% PAA gel and 1% PAA-GNP gel, excited at 250 nm

the shoulder at 321 nm disappears. After neutralization no great differences appear. The peaks at 465 nm and 412 nm can be seen again without shift or important modification of the shape (Figure 6). However the amplitude of the peak 465 nm is greater for the neutralized sample. A small and broad shoulder

can be seen at 331 nm. This one can be associated to the shoulder at 321 nm observed in the spectrum of the gel without GNP. In the neutralization reaction new chemical bonds appear between the PAA monomers and TEA molecules. The electronic structure of these systems is modified, fact that give rise to modifications of the fluorescence spectra. These modifications are in concordance with the UV-VIS observations. The GNP do not react with TEA, fact that explains the relatively small modification of the fluorescence peaks assigned to these particles. On the other hand, the neutralization is followed by modification of the local conformation of the polymer, changes that can be seen by other experimental methods, including IR, Raman and viscosity measurements. Complete characterization of the effect of neutralization can be achieved by correlation of the data collected by different experimental techniques as indicated above.

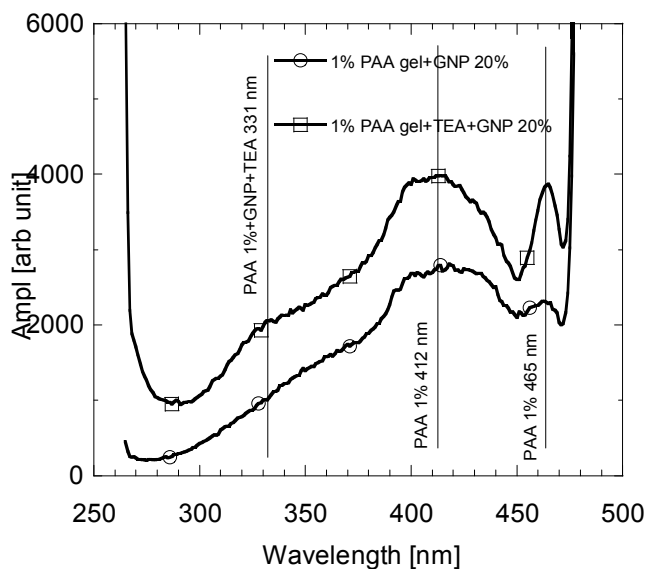


Figure 6. Comparison between the fluorescence spectra of the 1% PAA gels-GNP, before and after neutralization with TEA, excited at 250 nm

CONCLUSIONS

The introduction of GNP into the matrices of aqueous PAA gel, before neutralization, has as consequence the apparition of new absorption peaks in the UV-VIS spectra. After neutralization with TEA the UV-VIS absorption of PAA aqueous gels increases. This tendency is more pronounced in the

samples with GNP. This behavior is determined by the modification of local polymeric conformation after hydration of the polymer and after neutralization. The modification of some chemical bonds by neutralization is followed by the some modification of the electronic states of the molecules. This mechanism is confirmed by the modification of the fluorescence spectra before and after neutralization.

EXPERIMENTAL SECTION

The aqueous PAA was obtained by mixing the powder polymer, (molecular mass 104400 g/mol), with distilled water at room temperature until a homogeneous composition is obtained. The concentration of the polymer in the solutions was 1% wt. The aqueous gels were neutralized with TEA in the proportion 1.5/1 g/g TEA/PAA. At this ratio base/polymer the PH of gel is about 6.5-7.

The gold nanoparticles were prepared on basis of standard methods presented in literature, [16, 17]. We used 100 ml aqueous solution of 1 mM tetrachloroauric acid which was brought to its boiling point. Then we added 6 ml sodium citrate (1%) and the mixture was stirred at constant temperature for 15 minutes. After that the solution was left to cool down to room temperature. Sodium citrate is responsible for the reduction of Au ions from solution, with the formation of spherical nanoparticles [18]. Then the GNPs were introduced in the gel and the system was stirred 4 hours until a homogeneous dispersion of GNPs was obtained. The samples contain 1% wt polymer and 20% wt GNP. After that the composition was neutralized with TEA following the same procedure used for the neutralization of the gels without TEA. All the precursors, PAA, TEA, tetrachloroauric acid and sodium citrate were purchased from Aldrich and used without further purification.

The UV-VIS spectra were recorded with a Jasco V-670 system with scan speed 200 nm/min, UV-VIS bandwidth 2 nm, and NIR bandwidth 8 nm. The fluorescence investigation was done with Jasco SP6100 system.

REFERENCES

- [1]. A.S. Hoffman, *Adv. Drug Del. Rev.* **2002**, 43, 3.
- [2]. P. Sriamornsak, R.A. Kennedy, *Int. J. Pharm.* **2006**, 323, 78.
- [3]. M. Todica, E. Dinte, C.V. Pop, C. Farcau, S. Astilean, *Journal of Optoelectronics and Advanced Materials*, **2008**, 10, 823.

- [4].M. Todica, Luciana Udrescu, G. Damian, S. Astilean, *Journal of Molecular Structure*, **2013**, 1044, 328.
- [5].C.V. Pop, T. Stefan, S. Astilean, M. Todica, *Studia Universitatis Babes-Bolyai, Chemia*, **2011**, LVI, 3, 35
- [6].Sorina Garabagiu, C. Pestean, R. Stefan, *Journal of Luminescence*, **2013**, 143, 271.
- [7].J.P. Cohen Addad, "Physical Properties of Polymeric Gels", John Wiley and Sons, Chichester, **1996**, chapter 5.
- [8].Barbara Stuart, "Polymer Analysis", John Wiley and Sons, Chichester, **2002**, chapter 2.
- [9].R.J. Young, P.A. Lowell, "Introduction to Polymers", Chapman and Hall, London, **1991**, chapter 2.
- [10]. M. Todica, Luciana Udrescu, "Metode experimentale in fizica polimerilor", Presa Universitara Clujeana, **2013**, chapter 4.
- [11]. [M. Todica, Traian Stefan, S. Simon, I. Balasz, L. Daraban, *Turkish Journal of Physics*, **2014**, 38, 261.
- [12]. A.F. Danet, "Analiza instrumentala", Editura Universitatii din Bucuresti, **2011**, chapter 1.
- [13]. J.R. Lakowicz, "Principles of Fluorescence Spectroscopy", Springer, Berlin, **2006**, chapter 2.
- [14]. M. Todica, R. Stefan, C.V. Pop, I. Papuc, Oana Stan, Loredana Elena Olar, accepted to *Studia Universitatis Babes-Bolyai, Chemia*, **2014**.
- [15]. M. Navaneethana, K.D. Nishab, S. Ponnusamy, C. Muthamizhchelvana, *Materials Chemistry and Physics*, **2009**, 117, 443.
- [16]. Yin Ding, Jian Gao, Xiaoyu Yang, Jian He, Zhengyang Zhou, Yong Huc, *Advanced Powder Technology*, **2014**, 25, 244.
- [17]. M. Moreno, Rebeca Hernández, D. López, *European Polymer Journal*, **2010**, 46, 2099.
- [18]. G. Mihailescu, L. Olenic, Sorina Garabagiu, G. Blanita, E. F. Cosma, A.S. Biris, *Journal of Nanoscience and Nanotechnology*, **2010**, 10, 2527.

ANALYTICAL STUDY OF GALLSTONES IN PATIENTS FROM TRANSYLVANIA, ROMANIA

IOANA BREZESTEAN^a, NICOLAE HAR^b, ALINA TANTĂU^c, MARIA
GOREA^d, MONICA M. VENTER^d, SIMONA CÎNTĂ PÎNZARU^{a*}

ABSTRACT. Here we report the vibrational spectroscopy characterization on human gallstones from patients in Transylvania, Romania. A number of 93 gallstones resulted after surgical intervention were preliminary classified in 6 groups after provenance, shape and color aspect and investigated using optical microscopy and FT-(micro)-Raman spectroscopy in conjunction with the FT-IR. Optical microscopy of the gallstones cross sections revealed concentric layers growing depositions alternating with axial crystalline agglomerated biomaterial. Two distinct type of crystallinity on one hand and different spatial crystals distribution, on the other hand were optically observed. The studied specimens randomly showed very narrow amorphous zones. The microstructure, chemical composition, the nucleation and growing mechanism of gallstones were correlated with the vibrational spectroscopy data. Vibrational assignment allowed identifying cholesterol in all the samples. Other weak bands attributable to bilirubinate salts were randomly observed with different extent in all the groups. Brown, yellowish-brown and yellow gallstones showed higher content of bilirubinate as revealed by the relative intensity ratio of the bilirubinate band at 1620 cm^{-1} versus cholesterol band at 1464 cm^{-1} with values between 0.57 and 0.875. FT-vibrational techniques accurately provided the proof of the cholesterol specificity in the choletitiasis prevalence in the area and allowed getting additional insight into their growing mechanism.

Keywords: Human gallstones, Transylvania, FT-Raman spectroscopy, FT-IR, cholesterol

^a Babes-Bolyai University, Faculty of Physics, Biomolecular Physic Department, Kogalniceanu 1, RO-400084, Cluj-Napoca, Romania. * Corresponding author: simona.cinta@phys.ubbcluj.ro

^b Babes-Bolyai University, Biology and Geology Faculty, Department of Mineralogy, Kogalniceanu 1, RO-400084, Romania

^c 4-th Medical Clinic 16-18-20 Republicii Street 400015, Cluj-Napoca, Romania and "Iuliu Hatieganu" University of Medicine and Pharmacy, Cluj-Napoca, Victor Babes 8, RO-400012, Romania

^d Babes-Bolyai University, Faculty of Chemistry and Chemical Engineering, 11 Arany János, RO-400028, Cluj-Napoca, Romania

INTRODUCTION

Gallstone or choletitiasis appearance in the gall bladder is one of the most common gastroenterology disease and constitutes a major health problem worldwide requiring the highest budget in the gastroenterology treatment. Gallstones are clumps of solid biomaterial that are formed in the gall bladder or in the choledoch duct as a result of bile concentration associated with metabolic syndrome and gastric disease. The main function of the gall bladder is to concentrate bile by the absorption of water and sodium. Traditionally, gallstones were classified as cholesterol stones, pigment stones, or mixed stones (a combination of cholesterol and pigment stones) based on their composition, which can only be determined reliably after their removal. Cholesterol stones are composed primarily of cholesterol. Pigment stones are composed of bilirubinate and other substances such as calcium, which are found in the bile. The occurrence of gallstone disease is 2-3 times more common in women than in men [1].

Gallstones and their medical consequences represent a relevant cost factor in Western countries healthcare systems. The incidence of gallstones is 15% in America, 5.9~21.9% in Europe, 4~15% in Asia and 3~11% in China [2, 3]. According to Sachiorafas et al [2] about 10-20% of inhabitants in the most western countries developed gallstones while the percentage of asymptomatic patients being 50-70% at the diagnosis moment. In Germany, 10.5–24.5% of the female and 4.9–13.1% of the male population are estimated to carry gallstones, and about 170,000 cholecystectomies are performed annually [2-5]. A very recent exhaustive study [3] showed that the gallbladder stones were classified into 8 types and more than ten subtypes, including cholesterol stones, pigment stones, calcium carbonate stones, phosphate stones, calcium stearate stones, protein stones, cystine stones and mixed stones. Current research suggests that different types of gallstones have different pathogenesis [6–9]. Research on the systematic classification of gallbladder stones may help to reveal the formation mechanism of different types of gallstones.

Major types of stones observed in patients are a) white b) black and c) brown stones. This classification based on the color, was proposed at the NIH workshop [11]. Earlier FT-IR and FT-Raman studies suggested an additional category called mixed stones having different proportions of cholesterol and bilirubin [10]. Black and brown color stones contain bilirubin in large amounts in addition to small quantities of cholesterol. The pigmented stones can be further

sub-categorized on the basis of minor variations in chemical composition, such as the presence of calcium carbonate. Three main lipids found in the bile are bile acids, cholesterol and phospholipids [12]. According to the current opinion in the field, gallstones formation is a complex bioprocess where the physical, metabolic, genetic and geographical factors compete to the formation of the precipitated agglomeration of insoluble biomaterial in the gallbladder and even in the choledoch duct [13,14].

In recent years there has been an increasing trend in the number of reported cases. The formation of gallstones *in vivo* takes years and it is quite difficult to monitor such events from nucleation to the consolidation and final diagnostic [15]. Gallstone formation is therefore very poorly understood. Surprisingly, in the last few decades there has been significant rise in gallstone disease among children [15-18]. Removal of the gallbladder by surgical methods is the only solution available to the gallstone disease today and therefore, the disease has a strong impact [19-21]. Earlier reports [19] suggested that biochemical features of a human 42-kDa biliary glycoprotein shows concentration-dependent cholesterol crystallization-promoting activity. Other results showed that the insoluble materials of gallstones are mainly composed of bilirubinate salts and proteins [22].

Since the risk factors of the choletitiasis disease may vary from one region to another, being influenced by the dietary habits, genetic factors, medical history of the patient, race, geographical zone, as well as by other diseases, the literature reports revealed various analytical data on chemical composition of gallstones [3, 6, 10, 20, 22]. To the best of our knowledge, in Romania, such studies were absent, although the risk of gallstones becoming symptomatic was evaluated for medical purpose [23].

Vibrational spectroscopy techniques could provide valuable information on the nature and chemical composition of the gallstones, thus, the specific factors competing in the gallstones formation could be properly managed for prevention. Although the gastroenterology clinics report their own research results on the statistical aspects or surgical removal success [23, 24], the nature of the surgical resulted biomaterial is unknown. On the other hand, the mechanism of gallstone formation and consequently their control and growing inhibition is poorly understood. It should be noted that in spite of the recent pharmaceutical development, a proper formulation for dissolving and eliminating the gallstones is absent. The aim of this work was to explore the capability of the vibrational spectroscopy techniques for assessing the nature and the growing mechanism of the gallstones collected from patients in Transylvania, Romania.

RESULTS AND DISCUSSION

Fourier Transform (FT)-Raman and FT-IR were used as the main analytical techniques for the determination of human gallstone structural composition. These techniques could provide rapid, qualitative and quantitative information about their structure. The gallstones biomaterial taken under study is illustrated in the Fig. 1 and the physical properties of the stones and their origin are described in the Table 1.

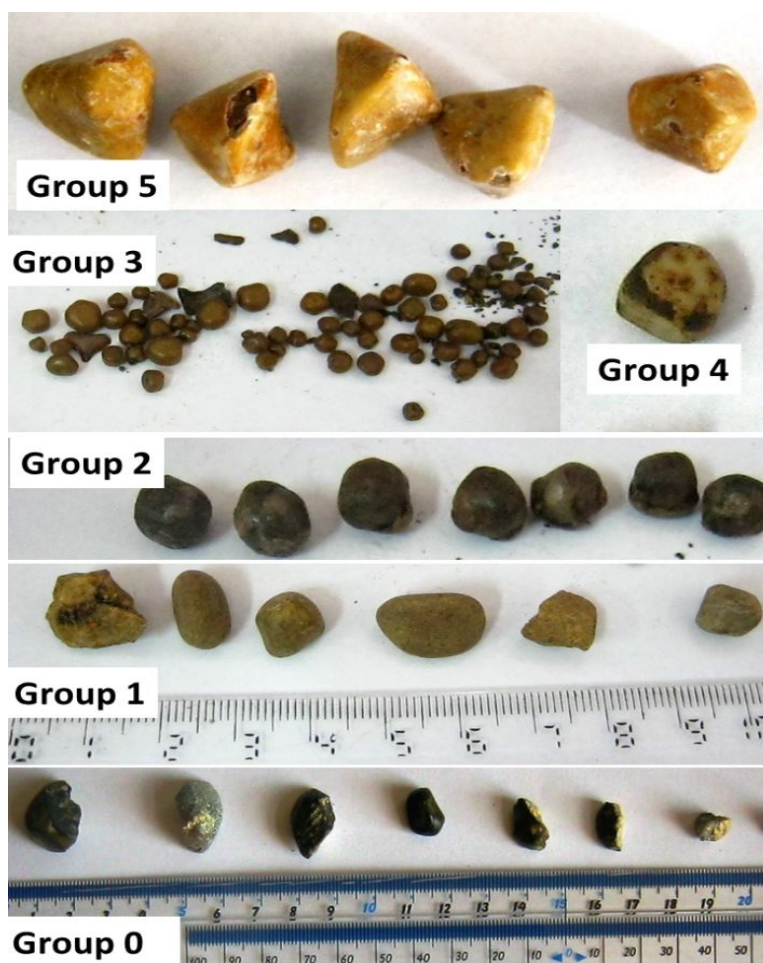


Figure 1. Gallstones from patients in Transylvania, Romania, taken under study.

Table 1. Sample groups classification according to their physical properties and origin.

Group	Provenience	Color	Physical Appearance/Size	Observed specific gravity
0	9 samples of a group of 55 pieces resulted from a surgery intervention in 3-rd Medical Clinics Cluj-Napoca from one patient (woman)	Grey-black	Lustrous grey colored particles up between 0.2-2cm diameter; some layering apparent on fragmentation; brown granules apparent	Low
1	6 samples from a group Of 12 pieces resulted from a surgery intervention in 3-rd Medical Clinic Cluj-Napoca from a male patient	Yellowish brown	Stone size ranging between 0.5-1.5 cm present abrasive and harsh structure	Low
2	7 samples resulted from a surgery intervention in 3-rd Medical Clinic Cluj-Napoca from male patients	Black	Stone size ranging between 1-1.5 cm, present abrasive surface	Low
3	65 samples resulted from surgery interventions in 4-th Medical Clinic Cluj-Napoca from many patients (male and female)	Brown	Stone size ranging between 0.2-1 cm present polish surface	Low
4	1 sample resulted from a laparoscopic intervention in 3-rd Medical Clinic Cluj-Napoca	Yellow-brown	Stone size ranging 1.4 cm present abrasive surface and some layering apparent on fragmentation; brown granules apparent	Low
5	4 samples resulted from a surgery intervention in Clinical Hospital Blaj, Alba County, Transylvania	Yellowish White	Stone size ranging between 1.5-2 cm present highly polished surface from all of the samples	Low

FT-Raman spectroscopy of gallstones

Raman spectroscopy is currently a widely used method based on inelastic scattering of the light on materials. It is an advanced technique

that allows to acquire rich information about the chemical composition by measuring vibrational frequencies of the chemical bonds of the investigated structure with high spatial resolution within a unique non-destructive manner. FT-Raman technique prevails over the dispersive Raman techniques in the case of materials with high fluorescence such as gallstones, because of its incorporated NIR laser for excitation which could significantly diminished the fluorescence of the colored materials and for the capability to provide the whole spectral range at once.

Representative raw FT-Raman spectra collected from different sample groups numbered from 0 to 5 are showed in the Fig. 2. For each sample group the spectra were acquired from the external side (crust), internal layers observed in the gallstone cross section and nucleation center.

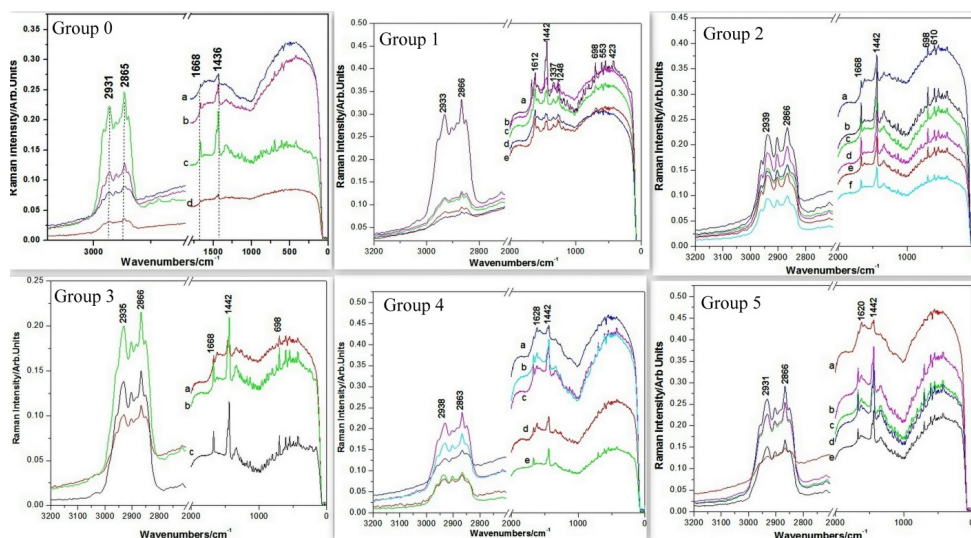


Figure 2. Representative raw FT-Raman spectra collected from various parts of the gallstones from the six groups. Group 0: (a) external part, (b) edges, (c) yellow pigment, (d) middle section; Group 1: (a) external part, (b) edges, (c) yellowish brown pigment, (d) middle, (e) nuclear center; Group 2: (a) external part, (b, c) external part brown, (d) pigment part inside of the gallstone, (e) middle, (f) nucleation center; Group 3: (a) external part, (b) edges, (c) white part inside of the gallstone; Group 4 (a) external part, (b) edges, (c) yellow pigment, (d) middle, (e) nuclear center; Group 5: 4 (a) external part, (b) edges, (c) yellowish white pigment, (d) middle, (e) nucleation center. Excitation: 1064 nm, 350 mW.

The core of one sample from the Group 1 was isolated and kept in ethanol for 24 hours. The treatment allowed recording high quality FT-Raman spectrum with substantially decreased background as shown in the Fig. 3. Ethanol extraction highlighted the bile pigments responsible for high intensity Raman background even for the NIR laser line excitation. FT-Raman spectrum of pure cholesterol (99%, Sigma-Aldrich) is shown for comparison. The gallstone core clearly revealed all the bands attributable to cholesterol and additionally a weak, broaden band at 1620 cm^{-1} .

Table 2. FT-Raman vibrational data (cm^{-1}) of gallstones and their proposed assignment.

Group 0	Group1	Group2	Group3	Group4	Group5	Literature values / cm^{-1} [3, 22, 26]	Assignment	Molecular species
Raman bands/ cm^{-1}								
2931	2938	2933	2939	2935	2931	2964s,2935s, 2904s	$\nu_{\text{as}}(\text{CH}_2, \text{CH}_3)$	Cholesterol
2865	2863	2866	2866	2866	2866	2886s,2850s, 2807s	$\nu_{\text{s}}(\text{CH}_2, \text{CH}_3)$	
1668	1668	1668	1668	1668	-	1671m	$\nu(\text{C}=\text{C}, \text{C}=\text{O})$	
-	1620	1620	1612	-	1620	1618s	$\nu(\text{C}=\text{C}, \text{C}=\text{O}),$ $\delta(\text{N-H})$	Bilirubinate salts
1436	1442	1442	1442	1442	1442	1461m,1438m	$\delta(\text{CH}_2, \text{CH}_3)$	Cholesterol
-	-	1337	-	-	-	1341m	$\delta(\text{CH}_2, \text{CH}_3),$ ring stretching	
-	-	1248	-	-	-		$\nu(\text{C-C})$	
-	-	698	698	698	-		Bending modes	Cholesterol
-	-	-	610	-	-			
-	-	553	-	-	-			
-	-	423	-	-	-			

Abbreviations: ν - stretching, δ -bending.

In the raw FT-Raman spectra of all the samples (Fig. 2), the cholesterol bands were clearly identified, without other sample treatment. This fact confirms that the dominant species is cholesterol in all the analyzed samples, allowing to conclude that the FT-Raman technique showed effectiveness in rapid chemical composition assessment of such complex bioprobes. The main

bands observed are summarized in the Table 2 together with the proposed assignments.

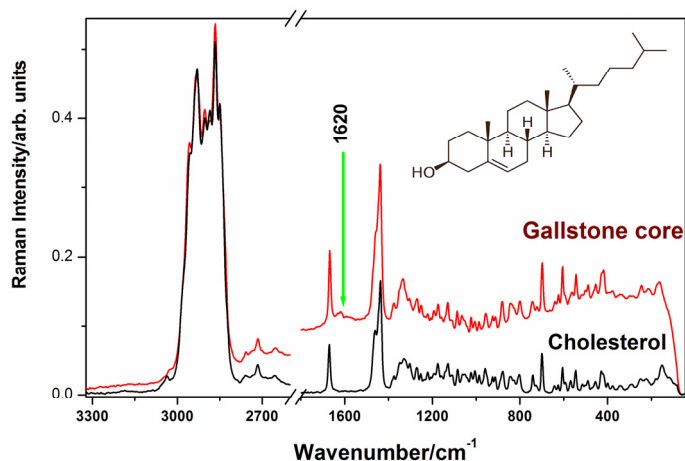


Figure 3. FT-Raman signal collected from cholesterol powder (99%, Sigma-Aldrich), compared to that of the gallstone core belonging to the Group 0. The molecular structure of cholesterol is inserted. Excitation: 1064 nm, 350 mW.

As shown by the Figure 2 the summarized display of the FT-Raman spectral feature of gallstones collection revealed some change in the relative intensity of the bands on passing from exterior through the inner layers to the gallstone center. Each sample was measured on the exterior side and in the interior layers of the cross section. Each group of samples showed similar spectral feature both on the exterior side and in the interior layers. The cross sections of several samples were carefully investigated using FT-micro-Raman spectroscopy in order to extract as much information as possible with high spatial resolution. Although the micro-Raman signal is almost 10 times weaker because of the excitation energy loss along the optical fiber to the Raman microscope and back, the cross sections revealed similar bands attributable to the cholesterol. The difference between adjacent inner layers of gallstones was mainly based on the different background intensity, the dark layers exhibiting the highest background in detriment of signal to noise ratio. Therefore, the micro-Raman spectra were considered not relevant for additional information and are not given here. Since most of the spectra collected from each group were similar, a selection of Raman data collected from the external, internal, edges, nucleation center and different pigmented areas (yellow pigment, yellowish white, yellowish green, brown) from the cross

sections are summarized in the Figure 2 and Table 2. The observed Raman bands at 2931, 2865, 1668, 1436-1442, 1336, 1271, 699, 604, 544, 417, 247 cm^{-1} and crystalline lattice vibration at 162 cm^{-1} were unambiguously assigned to cholesterol, but other bands characteristic of bilirubinate salts that were not overlapped by those of cholesterol, in the 1612-1620 cm^{-1} range were clearly observed with weak to medium intensity in all the sample groups. The complete vibrational characterization of the bilirubin was earlier reported [27]. The theoretically predicted 1567 cm^{-1} backbone stretching mode [27] has a corresponding band in the Raman spectra of acidic forms of bilirubin derivatives. This band was observed at 1564 cm^{-1} with weak intensity on the overall background in all the present sample groups Raman spectra (Figs. 3, 4) while cholesterol spectrum revealed no band on that position. Another specific band free of cholesterol overlap was observed at 1620 cm^{-1} . We also noticed the highest intensity fluorescence background in the spectra collected from the dark edge of the samples (black or brown).

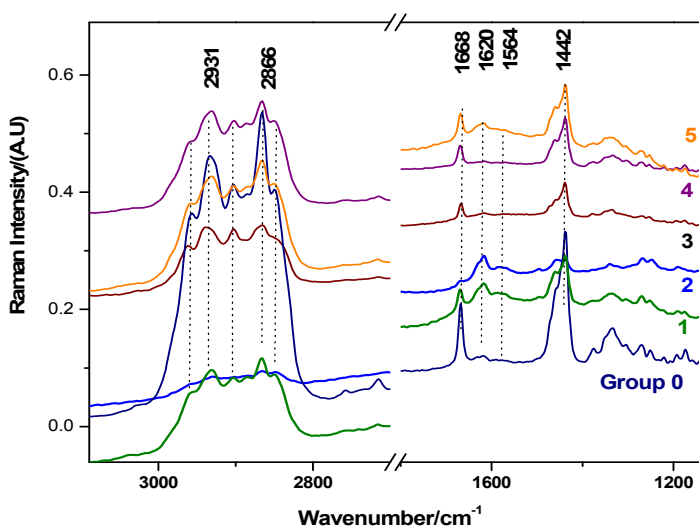


Figure 4. Comparison of the representative FT-Raman spectra of the five gallstone groups. Spectra were collected from the lighter exterior area of the largest sample from each group. The clear differences are displayed in the 1668-1620 cm^{-1} range, where the balance between cholesterol and bilirubinate salts contribution respectively, is highlighted. In the high wavenumber range, the cholesterol bands are dominant in all the groups. Excitation: 1064 nm, 350 mW. Offset was applied for clarity and due to the fluorescence background extent the high wavenumber range displays changes in spectral ordering.

The highlighted Raman spectral differences between the five groups are shown in the Fig. 4, where the Raman spectra were collected from the lighter area on the external side of the largest sample from each group. Analysis of the FT-Raman results showed that the Group 1, 2 and 5 of brown, yellowish brown and yellow gallstones exhibit visible Raman contribution from both cholesterol and bilirubinate salts with relative intensity extent and could be classified as mixed gallstones, whereas the rest of samples were likely to be cholesterol dominant, although the bilirubinate pigments responsible for the dark color were present but with lower extent.

FT-IR analysis of gallstones

ATR-FT-IR spectra from the nucleation center, exterior surface and inner layers of each gallstone groups have been recorded in the 4000-650 cm^{-1} range. A selection of representative absorbance spectra collected from each gallstones group is displayed in the Fig. 5 for both the exterior side (upper) and the core (lower).

The FT-IR spectral feature showed much similarity, a direct evidence of the differences between groups being reflected in the relative intensity of the weak bands of bilirubinate contribution. The subtle change in the relative intensity of the absorbance bands in the 1600-1700 cm^{-1} range can be considered relevant for identification of the bilirubinate salts in the gallstones since cholesterol does not exhibit IR bands in this range [22].

Cholesterol exhibits IR bands at 2933, 2865, 1466, 1365 and 1057 cm^{-1} [21]. The calcium bilirubinate shows characteristic very strong IR bands at 1620, 1696, 1663 and strong to medium intensity band at 1572, and 1250 cm^{-1} which were assigned to (C=C, C=N, C=O) stretching vibration of lactam, (C-O) stretching of COOH; (C-O, C-N, C-C) stretching, asymmetric stretching $\nu_{\text{as}}(\text{COOH})$, and (C-O) stretching or C-N stretching coupled with NH deformation $\nu(\text{C-N})$, $\delta(\text{NH})$, respectively [3, 22, 25]. Assigning the IR spectra collected from the gallstones (Fig. 5) the cholesterol bands were dominant in all the recorded spectra, indicating the main compound both in the exterior layers and the gallstones core. The vibrational FT-IR data are summarized in the Table 3 with the proposed assignment. Calculating the relative intensity ratio of the bilirubinate band at 1620 cm^{-1} versus cholesterol band at 1464 cm^{-1} , the values range between 0.57 and 0.875, with the highest values distributed on specimens from group 1, 2 and 5, suggesting the higher bilirubinate content in the samples from these groups. These findings are in agreement with the Raman results, allowing to conclude that all the studied gallstones were cholesterol-based biomaterials with different extent of bilirubinate content. Although the color can be related to the pigment content,

the presence of other cations from the physiological salts can contribute to the color change, as previously reported for copper bilirubinate gallstones of black color [28]. Complementary methods like energy-dispersive X-ray spectroscopy could bring additional insight into this issue.

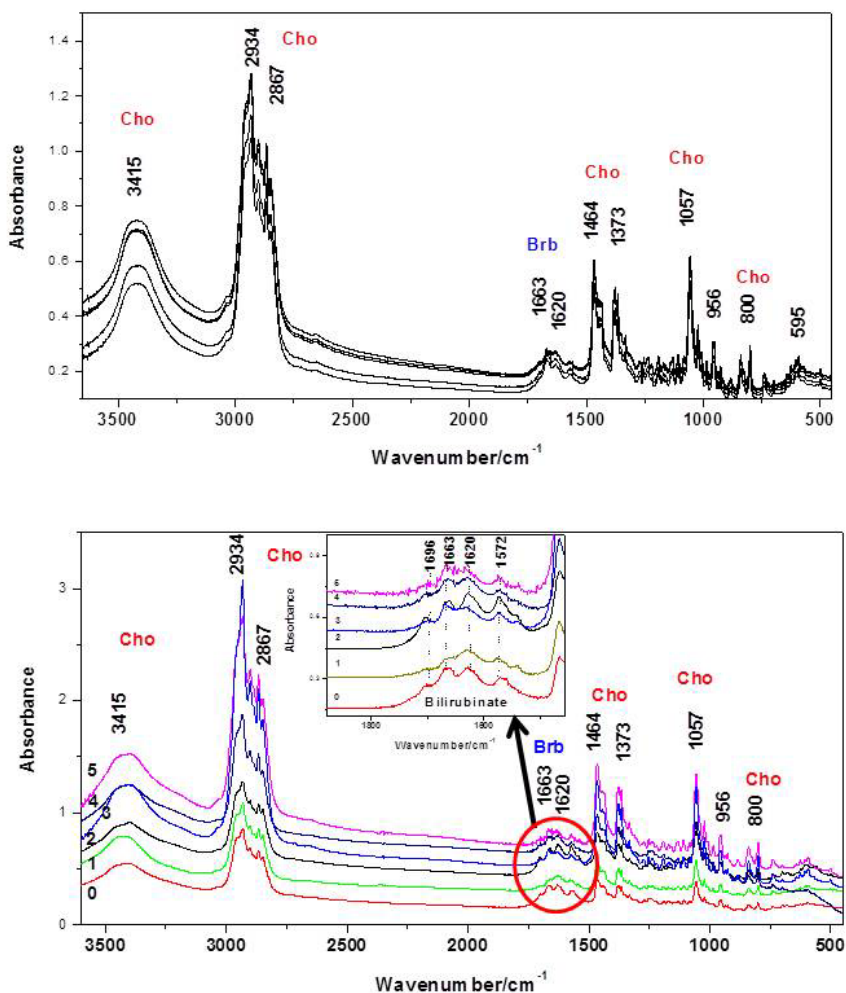


Figure 5. Representative ATR-FT-IR spectra collected from the exterior (upper) and gallstone core area (lower) from each of the five groups from 0 to 5. Insertion: Spectral range from 1800-1600 cm^{-1} where the bilirubinate (Brb) contributions are distinctly shown is highlighted. Cholesterol (Cho) does not exhibit IR bands in this range [22]. Central area (gallstone core) showed clear differences concerning bilirubinate content, highest rates being observed in group 1 followed by 2.

Table 3. FT-IR vibrational data (cm^{-1}) of gallstones and their proposed assignment.

FT-IR bands/ cm^{-1}	Assignments	Literature values [3, 22,25]
Bands due to Cholesterol		
3405	OH stretching	3401
2936	CH asymmetric stretching of CH_3	2725
2902	CH symmetric stretching of CH_3	2860
2868	CH symmetric stretching of CH_2	2860
1465	CH bending of CH_2	1460
1375	CH bending of CH_3	1380
1056	C-C stretching	1050
Bands due to Bilirubin		
1663	OC=O stretching	1670
1630	C=O carbonyl stretching	1626
1573	C=C stretching	1575
1251	C-O-C stretching	1244
1019	C-H in plane bending	1021
957	C-C ring stretching	923
877	C-H out of plane bending	879
838	C-H out of plane bending	832

The vibrational FT-Raman complemented by the FT-IR data suggested a clear nucleation process followed by the additional growing layers of crystalized cholesterol. No distinctive layers of bilirubinate were found in any of the studied samples. The gallstone formation starts when the amorphous cholesterol is organized as small balls which later crystallized and forms the core of gallstone. The core represents the crystallization support/center for the next layers of cholesterol resulting polished stones surfaces when agglomeration occurs in limited biological space.

This study also demonstrated that the chemical composition cannot be strictly related to the color classification criteria. FT-Vibrational techniques accurately provided the proof of the cholesterol specificity in the choletitiasis prevalence in patients from Transylvania, although the pure cholesterol gallstones were not observed.

CONCLUSIONS

This study presents the first analytical study of the gallstones composition and structure from patients in Transylvania, Romania. Although the cholesterol was the main compound found in all the studied samples and according to the current classifications criteria the gallstones would be cholesterol-type, however, cholesterol-bilirubinate mixed stones were considered dominant in Transylvania, based on the Raman and IR spectroscopy data. Cholesterol-bilirubinate stones found in Romanian patients appeared brownish yellow, amber, grey, yellowish brown or black-brownish and were spherical or polyhedron in shape. They were of different sizes, soft, and the surfaces were smooth and glossy or rough. Raman spectra of gallstones exhibit huge fluorescence background for all the visible laser lines, even the NIR line at 1064 nm, which could be removed by the ethanol extraction procedure. The resulted material resembled well the crystalline cholesterol spectra.

The formation, layer-by layer growing mechanism and crystallization mode was described based on vibrational spectroscopy data.

Analytical studies involving complementary techniques, such as X-ray diffraction and thermal analyses are in due course in order to assess the crystalline properties and possible inorganic phases that were not visible through the vibrational techniques. Such complementary approach will certainly contribute to understand cholelithiasis pathogenesis and hence stones growing inhibition and prevention.

EXPERIMENTAL SECTION

Instrumentation

ATR-FT-IR- spectra were recorded using an FT-IR (Bruker) Equinox 55 spectrometer with an ATR Miracle module with ZnSe crystal. FT-Raman and FT-micro Raman spectra were recorded using the integrated FRA 106S Raman module coupled with the Equinox 55 Bruker spectrometer. A fiber optic coupled Ramanscope II Raman microscope with an Olympus 10x objective was used to acquire micro-Raman spectra. A Nd:YAG laser operating at 1064 nm, with an output power of 350 mW, was used for excitation. The number of scans co-added was differed from one sample to another, depending on the fluorescence background extent of each case. Detection was accomplished with a Ge detector operating at liquid nitrogen temperature.

An attenuated total reflectance module with ZnSe crystal for sample contact was used to record absorbance spectra in the 4000-650 cm^{-1} range. The largest samples from each group were cross-sectioned for achieving an optimal crystal contact. The spectral resolution was 4 cm^{-1} .

Materials

Gallstones biomaterial were obtained from volunteer patients that underwent surgery intervention in medical clinics from Cluj-Napoca, Romania. The biomaterial was preliminary classified into 6 groups, numbered from 0 to 5 (Fig. 1), as follows: Group 0: 9 gray samples were selected from a total of 55 pieces of gray color ranging from 2 cm to 1 mm diameter, from a single patient (woman, 60 years old); Group 1 consisted of 6 yellowish-brown samples from a total of 12 pieces ranging from 1.7 cm to 0.5 cm in diameter from a male patient; Group 2 comprised 7 black-brownish samples of about 1 cm diameter; Group 3 comprised 65 brown samples ranging from 0.5 cm to 1 mm diameter from 4 different patients, Group 4 consisted of 1 laparoscopy broken sample of yellowish brown color; and Group 5 comprised the largest 5 yellow samples resulted from a surgery intervention suffered by a woman (45) in the Clinical Municipal Hospital Blaj, Alba County in Transylvania. Before analysis, gallstone samples were cleaned with ethanol and placed in different sterile opaque containers.

Cholesterol powder ($\geq 99\%$) was acquired from Sigma-Aldrich and stored at -20°C up to the measurement time.

ACKNOWLEDGMENTS

I. Brezestean would like to thank the financial support from the Babes-Bolyai University for the 2013-2014 scientific performance scholarship.

REFERENCES

- [1]. A.J. Harding, Gallstones: Causes and Treatments. William Heinemann Medical Books, London, **1964**.
- [2]. G.H. Sakorafas, D. Milingos, G. Peros, *Digestive Diseases and Science*, **2007**, 52 (5), 1313

- [3]. T. Qiao, R-H. Ma, X. Luo, L. Yang, Z. Luo, et al. *PLoS ONE*, **2013**, 8(10), e74887. doi:10.1371/journal.pone.0074887.
- [4]. Z. Zhang, *World Chinese J. Digestol.* **2008**, 16 (11), 1200.
- [5]. L.Y. Chen, Q.H. Qiao, S.C. Zhang, Y.H. Chen, G.Q. Chao, et al. *World Journal of Gastroenterology*, **2012**, 18 (31), 4215.
- [6]. T. Maki, *Annals of Surgery*, **1966**, 164 (1), 90.
- [7]. G. Elek, A. Rockenbauer, *Klinische Wochenschrift* **1982**, 60 (1), 33.
- [8]. J. Ahlberg, T. Curstedt, K. Einarsson, J. Sjoval, *Journal of Lipid Research*, **1981**, 22 (3) 404.
- [9]. K. Einarsson, K. Nilsell, B. Leijd, B. Angelin, *New England Journal of Medicine*, **1985**, 313 (5), 277.
- [10]. C. Paluszkiwicz, W.M. Kwiatek, M. Galka, D. Sobieraj, D. Wentrup-Byrne, *Cellular and Molecular Biologu* **1998**, 44, 65.
- [11]. B.W. Trotman, R.D. Soloway, **1982**, 2:879.
- [12]. J.J. Roslyn, M.J. Zinner, *Principles of Surgery* **1994**, 1376-1399.
- [13]. M. Donovan, *Gastroenterology Clinics of North America* **1999**, 28 (1), 75.
- [14]. C.W. Ko, S.P. Lee, *Gastroenterology Clinics of North America* (**1999**) 28, 1, 99.
- [15]. J.G. Wu, G.R. Shen, Y.Y. Gao, X.S. Chou, K.L. Zhang, J.H. Lin, S.G. Zhu, *Chinese Scientific Bulletin* **1979**, 24 (22), 1054.
- [16]. G.D. Offner, D.H. Gong, N.H. Aldhal, *Gastroenterology*, **1994**, 106, 755.
- [17]. K. Chijiwa, A. Koga, T. Yamasaki, K. Shimada, H. Noshiro, F. Nakayama, *Biochimica Biophysica Acta*, **1991**, 1086, 44.
- [18]. P.R.C. Harvey, G.A. Upadhy, S.M. Strasberg, *Journal of Biological Chemistry* **1991**, 266, 13996.
- [19]. M. Abei, H. Nuutinen, P. Kawczak, J. Schwarzendrube, S.P. Pillay, R.T. Holzbach, *Gastroenterology*, **1994**, 106, 231.
- [20]. B. F. Smith, *Jouranal of Lipid Research* **1987**, 28, 1088.
- [21]. H. Hrbasova, R. Vondruskova, M. Spundova, Z. Marecek, G. Entlicher, *International Journal of Biochemistry and Cellular Biology* **2000**, 32 (6), 609.
- [22]. G. Liu, Da Xing, Haimin Yang, Jie Wu, *J. Mol. Struct.* **2002**, 616, 187.
- [23]. M. Acalovschi, D. Blendea, C. Feier, A.I Letia, N. Ratiu, D.L Dumitrascu and A. Veres, *American Journal of Gastroenterology* **2003**, 98, 1856.
- [24]. M. Tantau, V. Mercea, D. Crisan, A. Tantau,, G. Mester, S. Vesa, Z. Sparchez, *Journal of Gastrointestinal Liver Diseases*, **2013**, 22, 2, 141.
- [25]. J.R. Ferraro, J.G. Wu, R.D. Soloway, W.H. Li, Y.Z. Xu, D.F.Xu, G.R. Shen, *Applied Spectroscopy* **1996**, 50, 7922.
- [26]. S. Kothai, K. Gayathri, V. Kannappan, P.T. Perumal, K. Manimegalai, *International Journal of Chemical Technological Research*, **2009**, 1, 3, 430.
- [27]. B. Yang, R.C. Taylor, M.D. Morri, X.-Z. Wang J.-Guang WV, B.-Z. Yu and G.-X. Xv, *Spectrochimica Acta A*, **1993**, 49, 12., 1735.
- [28]. W.-H. Li, G.-R. Shen, R. D. Soloway, Z.-L. Yang, X.-B. Tong, E. Wu, D.-F. Xu, J.G. Wu, and G.X. Xu, *Biospectroscopy*, **1995**, 1, 149.

WATER ABSORPTION AND DEGRADATION OF PACKAGES BASED ON NATIVE CORN STARCH WITH PLASTICIZERS

NICOLAE CIOICA^{a,*}, RADU FECHETE^b, RAMONA CHELCEA^b,
CONSTANTIN COTA^a, MIHAI TODICA^c, CORNEL V. POP^c,
ONUC COZAR^{a,c}

ABSTRACT. The starch in native forms or chemically modified is found as the main component of biodegradable packaging materials. Regarding this the water can produce a fast degradation, of the order of days, of such materials. Four types of packaging materials, one witness and three with different starch, glycerol and water ratios were subjected to natural degradation after absorption of distilled water. The degradation process was monitored by various NMR relaxometry methods based on the measurement of CPMG (Carr-Purcell-Meiboom-Gill) decays with a T_1 filter to exclude the signal from free water. The analysis of NMR signal decays was performed using a Laplace inversion algorithm and the dynamic components were identified from the T_2 transverse relaxation times distributions. We found that the best package with 68/17/15 ratios between starch/glycerol/water is extremely degraded after just one day forming a colloid substance. After that in time we observe a quasi-solid precipitation at the bottom of NMR tube. The reduction of dynamics is observed also in the T_2 -distributions measured for 5 days. The most resistant package (78/19.5/2.5) was that with a large content of starch but which was also reaching the swallow limit in five days and start to be decomposed.

Keywords: starch, plasticizers, extrusion, degradation, NMR relaxation

^a National Institute of Research Development for Machines and Installations Designed to Agriculture and Food Industry Bucuresti – Cluj-Napoca Branch, 59, Al. Vaida-Voievod Str., RO-400458, Romania. * Corresponding author: inmacj@rdsmail.ro

^b Technical University of Cluj-Napoca, Department of Physics and Chemistry, 25 G. Baritiu Str., RO-400027, Cluj-Napoca, Romania

^c Babes-Bolyai University, Faculty of Physics, 1 Kogalniceanu Str., RO-400028 Cluj-Napoca, Romania

INTRODUCTION

Biodegradable polymers represent a promising solution to the environmental problem of plastic waste disposal [1]. Among the candidates polymers, the starch presents interest for the products which require rapid degradation [2,3]. The target of recent investigations in the field of bioplastics is to obtain commercial packaging material produced from pure starch, a natural polymer, and to exclude synthetic polymers from the formulation [4]. Native starches are non-plastic due to the intra- and intermolecular hydrogen bonds between the hydroxyl groups in starch molecules, which represent their crystallinity. Native starch exists in a semi-crystalline granule and is comprised of two major polysaccharides: amylose and amylopectin. Amylose consists of α -(1-4)- linked D-glucose and amylopectin that has the same backbone as amylose but with myriad α -(1-6)-linked branch points [5,6].

To obtain loose fill packaging, thermal and mechanical processing should disrupt semi-crystalline starch granules using extrusion, a conventional technology used in synthetic plastic manufacture. Because the melting temperature of pure starch is substantially higher than its decomposition temperature, it is necessary to use plasticizers. According to the literature glycerol is most commonly used plasticizer [7]. If the total thermal and mechanical energy provided to the starch is insufficient, the product will show unmelted starch granules of clear crystallographic structure. Similarly, the proportion of plasticizer and its chemical nature, influence strongly the physical properties of the processed starch by controlling its destructureation and depolymerisation and by affecting the final properties of the material. An insufficient amount of plasticizer may result in an incomplete destruction of the crystallographic structure of starch [8,9].

Abiotic hydrolysis is the most important reaction for initiating the environmental degradation of biopolymers [10]. Polymer hydrolytic degradation, as abiotic disintegration, may be defined as the scission of chemical bonds in the polymer backbone by the attack of water to form oligomers and finally monomers. In the first step, water contacts the water-labile bond, by either direct access to the polymer surface or by imbibition into the polymer matrix followed by bond hydrolysis. The hydrophilic and hydrophobic nature of polymeric materials influences their degradation rate, and the susceptibility to hydrolysis follows this order: (1) hydrophilic with hydrolysable bonds, (2) hydrophobic with hydrolysable bonds, (3) hydrophilic with no hydrolysable bonds, and (4) hydrophobic with no hydrolysable bonds [11]. All biodegradable polymers contain hydrolysable bonds, such as glycosides, esters, orthoesters, anhydrides, carbonates, amides, urethanes, ureas, etc. [12]. Polymers with strong covalent bonds in the backbone (like C-C) and with no hydrolysable groups require longer times to degrade [13].

The hydrophilic nature of starch plays an important role in initiating biodegradation process [14]. The degradation of starch-based packaging includes the disintegration into their monomers. Therefore unstable and hydrolysable linkages are required, where chemical, biological or photochemical reactions can take place [15].

A number of non-destructive techniques can be used to obtain information about the degradation mechanism of biopolymer. These include: Fourier transform infrared spectroscopy (FTIR), differential scanning calorimetry (DSC), nuclear magnetic resonance spectroscopy (NMR), X-ray photoelectron spectroscopy (XPS), X-ray Diffraction (XRD), contact angle measurements and water uptake [10]. For the structures within starch and starch-based products, both ^1H and ^{13}C high resolution NMR spectroscopy can be used to identify and quantify branch points and end groups [16,17]. Although reducing ends of starch molecules can be determined chemically and non-reducing ends can be determined by the difference in reducing power before and after debranching, ^1H NMR is the method of choice for quantifying the degree of branching based on the ratio of intensities observed for anomeric proton signals for (1-6)- and (1-4)-linked residues [16, 18].

This paper presents the results of water absorption and ^1H NMR investigations obtained for four types of packaging materials, one witness and three with different starch, glycerol and water ratios subjected to natural degradation after absorption of distilled water.

RESULTS AND DISCUSSION

Fig.1. presents the normalized mass of the swallowed water absorbed during five days by three packages based on native corn starch with different formula presented in Table 1. The experiment was performed for four packages, if we consider also the control specimen, but one of our products, which present the formula with the lowest starch content or lowest starch/water ratio (4.53 – sample 3), was degraded after one day. The hardest sample, with lowest water content (sample 1 with 78/19/2.5 starch/glycerol/water ratio) absorbed the lowest quantity of water (~ 50 % from sample's mass in day 5) with a smallest velocity. If the water content of formulas increases, then the quantity of absorbed water after 5 days increases to ~ 66 %. Moreover the absorption velocity is much higher, and as one can observe from Fig. 1 in 1 day the sample 2 (72/18/10) absorbed already water of ~ 60 % from sample mass. If the water content in the production formula of package increases as for the sample 3, which is the best package, the sample loses its integrity and becomes a colloid. The control package, which as we will see below is similar with package 3, absorbs a large quantity of distilled water ~ 1586 % from

sample mass. The swallowed water must be accommodated between amylose and/or amylopectin polymer chain segments modifying their dynamics. One can observe that the percentage of more mobile components associated with lateral branches is reduced and becomes more mobile while the additional

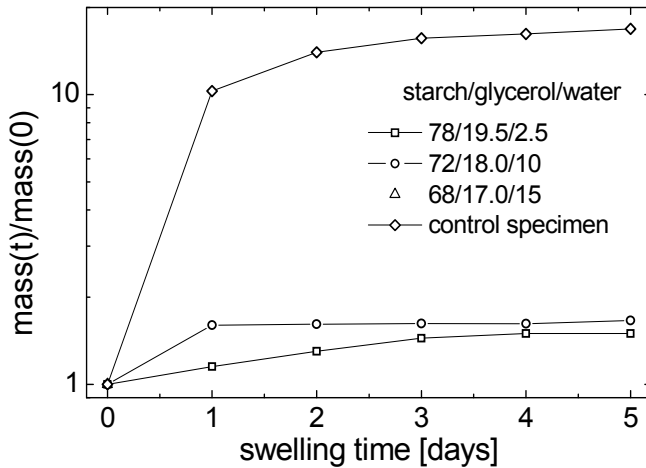


Figure 1. The normalized mass uptake during five days by three packages samples with 4:1 starch: glycerol constant ratio compared with a control specimen. The package with starch/glycerol/water 68/17/15 was degraded after 1 day. The lines are drawn to guide the eyes. The errors are under 5% error limits.

water content leads to a largest immobilization of amylopectin polymer chain segments in the core packed branches [19]. Therefore such changes can be well monitored by NMR relaxometry.

Fig. 2 presents the decays of the CPMG echoes trains for package sample 1 (78/19.5/2.5) and 3 (68/17/15). The curves recorded at 1 – 5 days are compared with the CPMG decays curves recorded for dry sample (contain only the water introduced in the manufacturing process). As expected, in both cases, the CPMG curve measured for the dry samples decay much faster than for the sample packages with water. Large differences between samples can be observed for the CPMG curves recorded during the monitoring of degradation process. While the sample 1 (with a low water content in the production formula – see Table 1) maintains its integrity and starting with day 2 present a reduced decay of CPMG curve indicating that the components (among them the amylose and amylopectin polymer chain segments) becomes more mobile, the sample 3 present a different behavior. First of all, the CPMG

decay decays much slower (in 4 s compared with ~ 320 ms for sample 1) since the measurement was performed not for the package sample per se but for the colloidal solution resulted from the degradation of package in water. In the same time, the dissolution process of the (best) package in water continues for \sim three days (see the CPMG echoes represented with triangle with top down in Fig. 2b which decays the slowest) then a precipitation process can be intuited from the increased decay of the CPMG curves corresponding to days 4 (diamond) and five (stars).

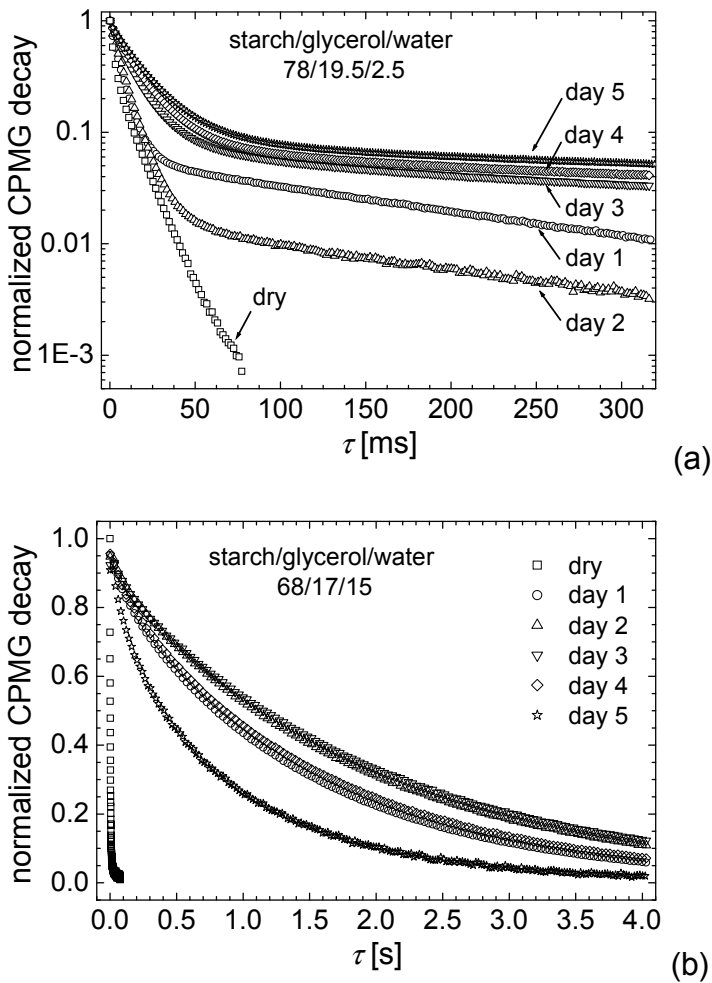


Figure 2. Compared CPMG decays during 5 days and dry samples for mixtures of starch/glycerol/water: 78/19.5/2.5 (a) and 68/17/15 (b).

A much better interpretation of the CPMG curves can be obtained if we will analyze the normalized T_2 relaxation times distributions obtained by Laplace inversion of the measured curves. Such normalized T_2 -distributions are presented in Figs. 3 and 4 separately first for samples 1 and 2 which could maintain their structural integrity during the five days of water absorption and then for samples 3 and 4 which were measured as colloid.

In Fig. 3a the normalized T_2 -distributions recorded for sample 1 with the largest starch/water ratio (small water content in the initial formula) show the most dramatically changes in the dynamics of components.

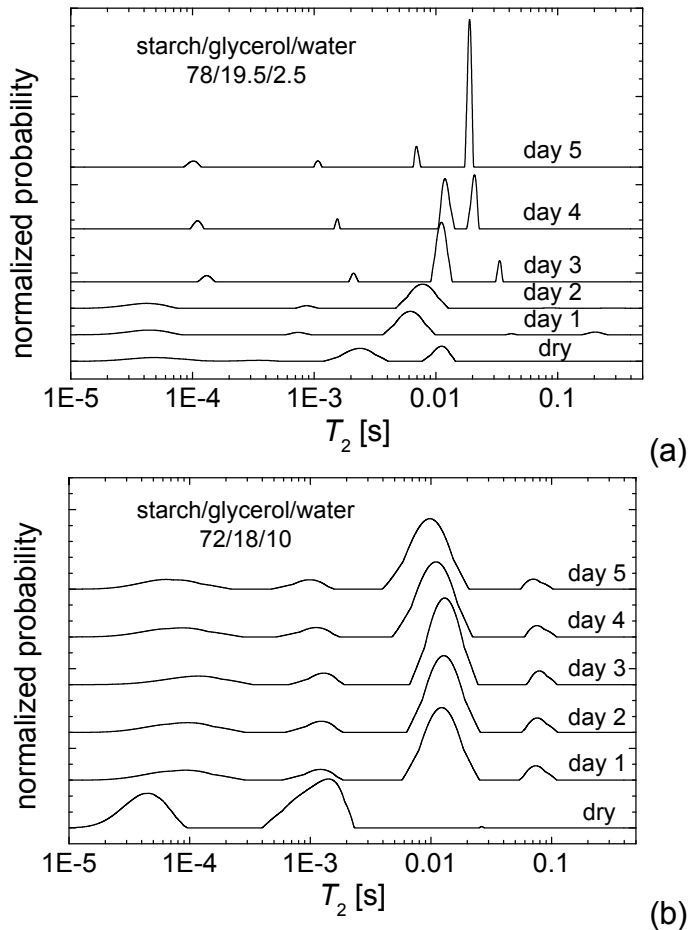
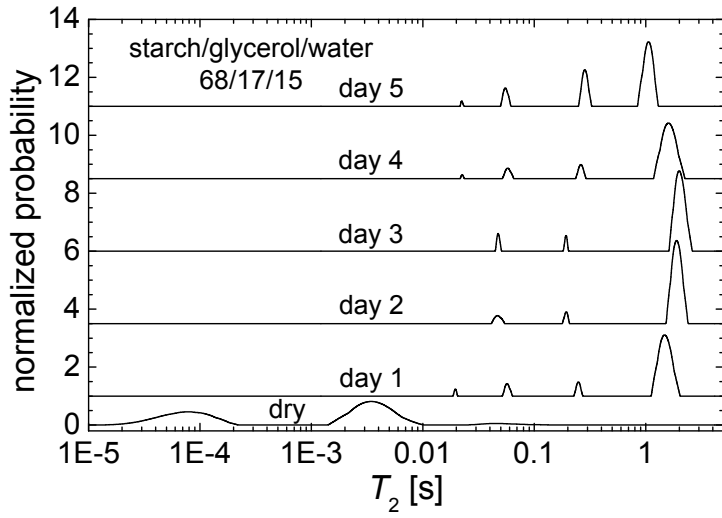


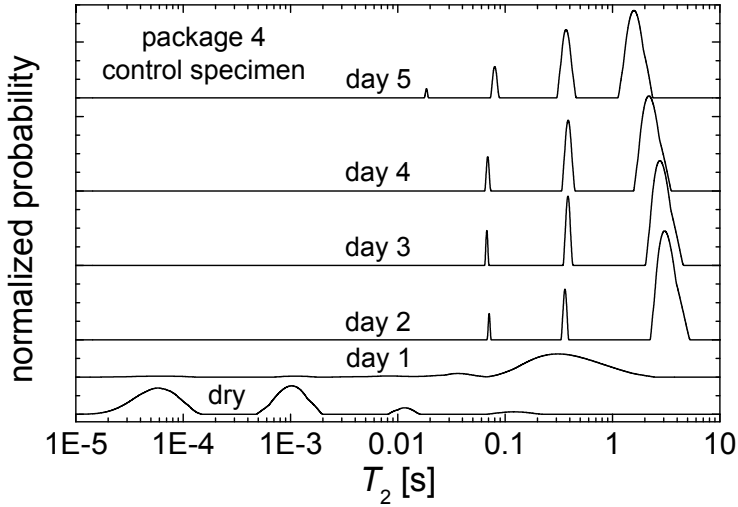
Figure 3. The normalized T_2 relaxation times distributions of packages samples with starch/glycerol/water: 78/19.5/2.5 (a) and 72/18/10 (b) for 5 days water absorption compared with dry samples.

For the dry sample the majority of ^1H reservoirs are characterized by T_2 values of ~ 2.5 ms and ~ 11 ms which can be considered as semi-mobile, and a small ^1H reservoirs is characterized by T_2 values of ~ 50 μs located into a rigid region (probably in the junctions of lateral branches with the amylopectin polymer backbone). One day of water absorption lead to the conservation of the rigid component but a collapse of the peaks located at T_2 values of the order of milliseconds to a unique peak located at T_2 values of ~ 6.3 ms. In the same time two new peaks appears at largest T_2 values (~ 41.3 ms and ~ 210 ms) indicating a largest mobility associated with the ^1H from these reservoirs. After another day (2) of water swallowing maintains the new composition observed in day 1 with a slight increase of mobility observed form the shift of T_2 values to largest numbers. A dramatically changes can be observed starting with day 3. First of all, one can observe that the peaks in the normalized T_2 -distributions becomes more narrow indicating a reduced distribution compared dray sample or with not so degraded sample (first two days). While first three peaks ($T_2 \sim 0.13$ ms, ~ 2 ms and ~ 10.9 ms) are shifted to larger T_2 values compared with the values measured in day 2, the most mobile peak ($T_2 \sim 33.6$ ms) contain a larger ^1H reservoir but is moved to smaller T_2 value. In the next two days of water absorption, with the exception of the main peak (which present the largest area under the peak) which is moving slowly towards a larger T_2 value the rest of peaks are moving to smaller T_2 value. This is an indication that the excess of water lead also to a stiffening of some components (more mobile but also more rigid) of this package formula. Among all samples, sample 2 (72/18/10) once swallow the initial amount of water become more stable in time (see Fig. 3b). The dry sample is characterized by two relative rigid components. These are observed also for degraded sample but into a much smaller percentage. The largest ^1H reservoirs are found at T_2 values ~ 11 ms and ~ 75 ms. For this package one can observe also a slight increase of the T_2 values up to the day 3 then a slight decay of the T_2 values in days 4 and 5. The same conclusion, of some component stiffening after day 3 as in the case of the previous sample can be underlined.

Despite of the different condition of measurement (the state of sample in colloidal solution) a similar behavior can be observed in the case of the sample 3 of which normalized T_2 -distributions are presented in Fig. 4a. For the dry sample the T_2 -distributions is characterized by T_2 values smaller than 10 ms. In one day, the sample 3, of which formula contain the largest amount of water (the starch/glycerol ratio being the same in all formulas), is degraded to a colloidal stage characterized by T_2 values larger than 10 ms. Three of four distinct dynamic components are observed in this case. In the same time one can observe a degradation which continues in the first 3 days but starting with day 4 a precipitation was visual observed and is validated by the decrease of the main peak (more mobile – with the largest T_2) T_2 values towards lower values, then with a reduced mobility.



(a)



(b)

Figure 4. The normalized T_2 relaxation times distributions of packages samples with starch/glycerol/water: 68/17/15 (a) and a control specimen (b) for 5 days water absorption compared with dry samples.

The degradation behavior of the control specimen is similar with the behavior of the sample 3, the best package formula, with some minor differences. The control specimen reaches the largest degradation effects not in one day as in the case of sample 3 but in two days. From this point (day two) the control specimen starts to precipitate, as easily observed by visual inspection, but also denoted, as in the case of sample 3, by the decrease of the main peak T_2 values towards lower values starting from $T_2 \sim 3$ s to ~ 1.5 s.

CONCLUSIONS

A series of formulas were tested in order to obtain packages based on native corn starch with plasticizers with a reduced time of degradation while swallowed in water and are compared with the performances of a control sample. The swallowing capabilities were estimated from inflation (water uptake) and the degradation a process was monitored from the analysis of normalized T_2 -relaxation times distributions measured during five days of observations. We observe that with the decrease of the starch/initial-water ratio the samples becomes more and more soluble in water and for a certain formula (starch/glycerol/water: 68/17/15) the tested sample is degraded under in less that one day. Nevertheless, in all cases a degradation process continues slowly in time but starting with day 3 part of each package start to precipitate. This behavior is observed also in the case of the control specimen with slightly different timing.

EXPERIMENTAL SECTION

The normal corn starch used in this study was obtained from SC Amylon Sibiu, Romania, having water content on wet basis (wt.b) of 10.76 %, a density of 0.561 g/cm^3 . The amylose content was 21%. The glycerol used in formulas was purchased from SC Nordic Invest SRL Cluj Napoca and had a concentration of 99.5% and a density of 1.262 g/cm^3 . The water used was from the water supply system. Table1 shows the ratio of the components in the used formulas.

Table 1. The content and ratio of starch-glycerol-water components in the used formulas

Sample	Starch [%]	Glycerol [%]	Water [%]	Starch/ Glycerol	Starch/ Water
1	78	19.5	2.5	4	31.2
2	72	18	10	4	7.2
3	68	17	15	4	4.53
4	control specimen with unknown values				

The packages samples were cut to fit into a 10 mm diameter NMR tube and 1 cm³ of distilled water was added. For samples 1 and 2 each day the excess water was removed and the water uptake was measured using an AGN 200 C analytical balance with a precision of 0.0001 mg. For samples 1 and 2 one cm³ of distilled water was added after NMR measurements. Sample 3 and 4 being largely degraded after 1 and 2 days, respectively, were measured by NMR relaxometry in the state of colloid. The mass uptake for sample 4 was measured for another part that the part used in the NM measurements.

The ¹H NMR relaxation measurements was performed using the Bruker Minispec spectrometer with the 10 mm probe-head. The Larmor frequency was 19.688 MHz and the temperature was set to 35 °C. For the T_2 spin-spin relaxation times measurements the pulse length was 10.1 μs and 4000 CPMG echoes were recorded with 256 scans and a recycle delay of 0.5 sec which acts as a T_1 filter to reduce the contribution of the free water. In order to find the T_2 spin-spin relaxation times distributions, the CPMG decays curves were analyzed using the UPIN algorithm, which perform a Laplace inversion of the measured data [20].

A corotating intermeshing twin-screw extruder ZK 25 (Collin, Germany) was used to conduct the extrusions. The screw has a diameter of 25 mm and a length to diameter ratio of 30:1. A die plate with one orifice of 3 mm was used. The starch was fed into the extruder hopper with a twin-screw volumetric feeder (Model DSV 020D, Definitive Inovation, Italy). The plasticizers were added into the working area through a pipe connection located at 170 mm from axis of the supply hopper with a peristaltic pump (Model SP 311/12, VELP, Italy). The screw speed was 150 rpm and the barrel temperatures (from the feeding port to the die section) 30, 50, 80, 100 and 120 °C, respectively. Finally, the extruding product was collected and cooled to room temperature.

ACKNOWLEDGMENTS

This work was supported by CNCSIS –UEFISCDI, project number PN II – IDEI code 284/2011 and 307/2011.

REFERENCES

- [1]. D.S. Rosa, C.L. Carvalho, F.Gaboardi, M.L. Rezende, M.I.B. Tavares, M.S.M. Petro, M.R. Calil, *Polymer Testing* , **2008**, 27, 827.
- [2]. N. Canigueral, F. Vilaseca, J.A. Mendez, J.P. Lopez, L. Barbera, J. Puig, *Chemical Engineering Science*, **2009**, 64, 2651.

- [3]. G.M. Glenn, S.H. Imam, W.J. Orts, *Materials Research Society Bulletin*, **2011**, 36, 696.
- [4]. M. Mitrus, L. Moscicki, *Chemical Engineering Research And Design*, 2014, 9, 2778.
- [5]. M.R. Almeida, R.S. Alves, L.B.L. R. Nascimbem, R. Stephani, R.J. Poppi, L.F.C. de Oliveira, *Analytical and Bioanalytical Chemistry*, **2010**, 397, 2693.
- [6]. A. Buléon, P. Colonna, V. Planchot, S. Ball, *International Journal of Biological Macromolecules*, **1998**, 23, 85.
- [7]. H. Liu, F. Xie, L. Yu, L. Chen, L. Li, *Progress in Polymer Science*, **2009**, 34, 1348.
- [8]. R.C.R. Souza, C.T. Andrade, *Advances in Polymer Technology*, **2002**, 21, 17.
- [9]. J.J. G. Van Soest, N. Knooren, *Journal of Applied Polymer Science*, **1997**, 64, 1411.
- [10]. A.A. Shah, F. Hasan, A. Hameed, S. Ahmed, *Biotechnology Advances*, **2008**, 26, 246.
- [11]. D.F. Williams and S.P. Zhong, *International Biodeterioration & Biodegradation*, **1994**, 34, 95.
- [12]. A. Göpferich, *Biomaterials*, **1996**, 17, 103.
- [13]. V. Hasirci, K. Lewandrowski, J.D. Gresser, D.L. Wise, D.J. Trantolo, *Journal of Biotechnology*, **2001**, 86, 135.
- [14]. L. Slade, H. Levine, *Carbohydrate Polymers*, **1993**, 21, 105.
- [15]. M. Wollerdorfer, H. Bader, *Industrial Crops and Products*, **1998**, 8, 105.
- [16]. M.J. Gidley, S.M. Bociek, *Journal of the American Chemical Society*, **1985**, 107, 7040.
- [17]. O. Cozar, N. Cioica, C. Filip, C. Cota, X. Filip, *Studia Universitatis Babeş-Bolyai Chemia*, **2013**, 58, 275.
- [18]. Z.H. Ao, S. Simsek, G.Y. Zhang, M. Venkatachalam, B.L. Reuhs, B.R. Hamaker, *Journal of Agricultural and Food Chemistry*, **2007**, 55, 4540.
- [19]. N. Cioica, R. Fechete, C. Cota, E.M. Nagy, L. David, O. Cozar, *Journal of Molecular Structure*, **2013**, 1044, 128.
- [20]. G.C. Borgia, R.J.S. Brown, P. Fantazzinit, *Journal of Magnetic Resonance*, **1998**, 132, 65.

ONE-DIMENSIONAL LAPLACE SPECTROSCOPY USED FOR THE ASSESSMENT OF PORE-SIZE DISTRIBUTION ON THE OVARIECTOMIZED RATS FEMUR

RAMONA I. CHELCEA^{a*}, REMUS S. ȘIPOS^b,
RADU FECHETE^a, DUMITRIȚA MOLDOVAN^a, IOANA ȘUȘ^c,
ZOLTAN PÁVAI^b and DAN E. DEMCO^a

ABSTRACT. The ^1H 1D NMR T_2 distribution method was implemented for the measurement of the *proximal part of the femoris* of a series of ovariectomized and non-ovariectomized Wistar albino rats. The rats were sacrificed at 2, 4, 6 and 8 weeks after ovariectomy and the *proximal part of femoris* was harvested. The CPMG echoes train decays measured for the dried bone were analysed by Laplace inversion and an average of T_2 distributions was considered for all rats' groups. The 1D normalized T_2 distributions present four peaks which were associated with protons in four major environments. The first one corresponds to the protons from bound water to collagenous matrix. The second one was correlated with fluids in osteocyte lacunae and canaliculi channels, while the third one was correlated with fluids in secondary pores like Haversian and transverse Volkmann canals. Finally the last one corresponds to soft matter like bone marrow and to the fluids in primary pores like trabecular bone cavities. The femoral bone of ovariectomized and non-ovariectomized rats was treated as a quasi-porous media and from the T_2 distributions the pores-size distributions were estimated function of observation time or evolution after ovariectomy. The results show that mainly the large cavities of *proximal part of femoris*, with the diameter in the range from 0.05 mm to 2 mm, are affected by osteoporosis for the ovariectomized rats.

Keywords: NMR relaxation, Laplace spectroscopy, T_2 distributions of dried bone, ovariectomized Wistar rats, osteoporosis.

^a Technical University of Cluj-Napoca, Department of Physics and Chemistry, 25 G. Baritiu Str., RO-400027, Cluj-Napoca, Romania

^b Department of Morphological Sciences University of Medicine and Pharmacy, 540139, Tg-Mures, Romania

^c University of Medicine and Pharmacy, 540139, Tg-Mures, Romania

* Corresponding author: Ramona.Chelcea@phys.utcluj.ro

INTRODUCTION

Osteoporosis is characterized as a reduction in bone mass and a damage of compact and cancellous bone architecture, resulting a bone thinning with the effect on increased cortical porosity, bone fragility and fracture risk [1]. In any bone, the cross section shows dense areas without cavities corresponding to compact bone and areas with numerous interconnecting cavities corresponding to cancellous bone. Whereas the compact bone is dense, the cancellous bone presents a structure of interconnected trabecular plates and bars surrounding marrow-filled cavities [2]. For an osteoporotic bone, these cavities become larger and trabecular bone is disrupted. At the same time, the cancellous bone becomes thinner and its porosity increases. One can consider the bone as a composite material consisting of a collagenous matrix which is mineralized with non-stoichiometric bioapatite (1.5 molar ratio of Ca/P in amorphous calcium phosphate phase), a highly disordered structure with many point deficiencies and carbonate substitutions [3]. In addition, it contains water, part of which is bound to collagen while a larger fraction occupies the spaces of the Haversian and lacuno-canalicular system [4]. In fact, it is considered that the cortical bone consist in app. 65 % mineral, app. 10 % organic matrix and app. 25 % water [5]. The bone is a heterogeneous, hierarchical porous structure with cavities which are the largest pores, followed by the vascular, lacunar-canalicular and collagen-apatite porosities [6].

Bones, additional to internal organ protection and locomotion, are a source of key regulatory inorganic ions like calcium, magnesium and phosphate. Recent biochemical studies show that various factor which control the formation and growth of bioapatite crystals can alter the bone mineralization processes can lead to diseases like osteoporosis [3]. At micrometer to millimeter scale (tissue scale) the bone consist of cells that control the initial production of mineralized tissues as: i) the osteoblast cell that are responsible with the mineralization of the extracellular triple-helical collagen matrix and orchestrate the coupling of bone formation and bone remodeling. The osteoblast cells are responsible with production of bone marrow consisting of proteins and polysaccharides. Under the influence of various hormonal factors and local cytokines, osteoblasts release mediators which mediates the activity of osteoclasts; ii) the osteocytes, which are a different type of osteoblast embedded in mineral, communicating with each other by interconnected canaliculae; and iii) the osteoclast multinucleated resorbing cells which can send bio-chemical messages everywhere along the tissues. In response to these signals, the bounded osteoclast to bone surface release enzymes and acid which remove minerals and organic matrix from bone [3]. Then the osteoblast and osteoclast cells are mainly responsible with the bone formation and resorption and dysfunctionality in the regulation of calcium, magnesium and phosphate level can lead to diseases like osteoporosis. Thus, for example the bisphosphonates decrease bone resorption by altering the osteoclast functions [7]. Therefore, the maintenance of ion levels is one of the major non-mechanical functions of the bone [3].

There are many similarities between human and rat bone, therefore for preclinical studies, rats models are frequently used in osteoporosis studies. In order to obtain the equivalent of postmenopausal osteoporosis in women, an estrogen deficiency can be induced by means of surgical ovariectomy [8].

The bone morphological changes can be assessed using several approaches: standard histological techniques, immunohistochemistry, confocal microscopy, micro-CT [9], scanning (SEM) and transmission (TEM) electron microscopy [10], and more recently, by cryo-porometry and thermo-porometry [11]. The osteoporosis studies are widely found in the medical literature but the number of studies with the subject the bone osteoporosis, by NMR in general or by NMR relaxometry in particular, is small. In this sense, Fantazzini *et al.* used the ^1H transverse and longitudinal relaxation times distribution to study the L1 to L6 rat lumbar vertebrae [12].

Laplace spectroscopy or the T_2 distributions becomes in the last decade a standard method in the study of porous materials [13]. The study of various materials extends the Laplace algorithms from exponential [14] to non-exponential [15] kernels. Moreover 2D Laplace analyses allow the identification and qualitative study of molecular exchange processes [16] and from here the pore interconnectivity.

The aim of this paper is to show that the dried femoral bone treated as a quasi-porous media can be used to assess the effects of osteoporosis. The NMR relaxometry measurement combined with Laplace analysis is used to obtain the Laplace spectra characteristic to the ovariectomized (OVX) and non-ovariectomized (NOVX) witness (W) rats. Finally, from the averaged T_2 distributions we estimate the pores-size distributions function of evolution after ovariectomy for the studied series of rats. Since many of the literature results [17] show that the large cavities of *proximal part of femoris* are mainly affected by osteoporosis for the ovariectomized rats we keep for the study only the *proximal part of femoris*.

RESULTS AND DISCUSSION

Figure 1 presents the comparison between the normalized CPMG decays of *proximal part of femoris* measured for a non-ovariectomized rat (labeled with 10) and an ovariectomized rat (labeled with 11). The sacrifice of rats was performed after 8 weeks from ovariectomy, in the case of OVX rats or after the same period of observation for the NOVX rats. At the beginning ($\tau < 50$ ms) the two curves seems to overlap, which means that the ^1H pools with the shortest relaxation time T_2 have the same origin. According to ref. [18] the T_2 values under millisecond (measured for a human cortical bone) correspond to bound water (primary to collagen) while the T_2 values larger that 1 ms (up to 1 s) correspond to pore water and lipids (bone marrow). We believe that also in rats' *proximal part of femoris* the shortest T_2 can be associated with ^1H belonging to bound water.

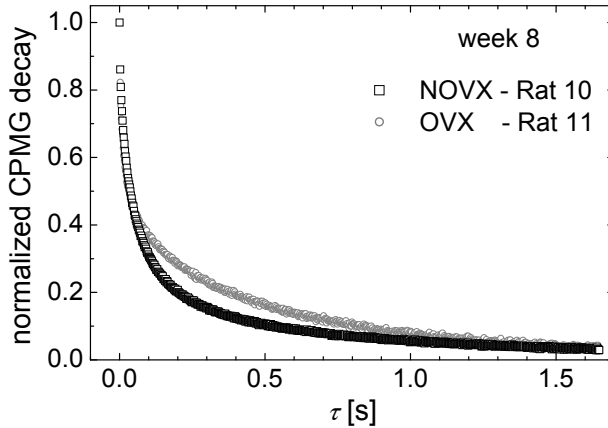


Figure 1. The normalized CPMG decays of *proximal part of femoris* for non-ovariectomized and ovariectomized rats 10 and 11, respectively; measured after 8 weeks from ovariectomy.

After a time of $\tau > 50$ ms the decay of CPMG curves corresponding to the ovariectomized and non-ovariectomized rats presents different behavior. The curves measured for the OVX rat decay much slowly, indicating that exist another ^1H pool characterized by a larger T_2 value. This result is in accord with the idea that for the ovariectomized rats the cavities are larger, and from here a larger value for the T_2 . From this type of measurement one cannot identify with enough degree of certitude the number of ^1H pools or protons in different environments having various T_2 values. The problem can be easily solved by considering the Laplace analysis of the CPMG decays curves.

The peak assignment in the resulted T_2 -distributions can be made if we treat the bone tissue as a porous media [19]. The variations in the local surface-to-volume ratio can lead to distributions of relaxation times, sometimes over decades. In trabecular bone it is easy to see differences in dimensions of intertrabecular spaces in samples but for that, the bone has to be defatted and saturated with water [19], which is our case.

Figure 2 presents the averaged of the normalized T_2 distributions obtained for the witness non-ovariectomized rats belonging to the groups which were sacrifices after two and eight weeks of observation. In order to avoid the variation of T_2 distributions inside of the same group of study, due to the diversity of the genetic material of rats or due to a variation in the rats' activity etc, the analysis was performed on the averaged curves and not on the particular normalized T_2 distributions. In all cases we observe a number of four peaks. One of this peaks, with the T_2 values under millisecond [18] is well resolved, but since correspond to bound water to collagenous matrix is not of interest in

the study of osteoporosis. Then we observe a group of three peaks which are not so resolved. From small to large T_2 values these peaks can be associated with: i) fluids in osteocyte lacunae and canaliculi channels ($T_2 \sim 10 - 20$ ms); ii) with fluids in secondary pores like Haversian and transverse Volkmann canals ($T_2 \sim 40 - 90$ ms) and iii) with fluids in primary pores like trabecular bone cavities ($T_2 > 200$ ms).

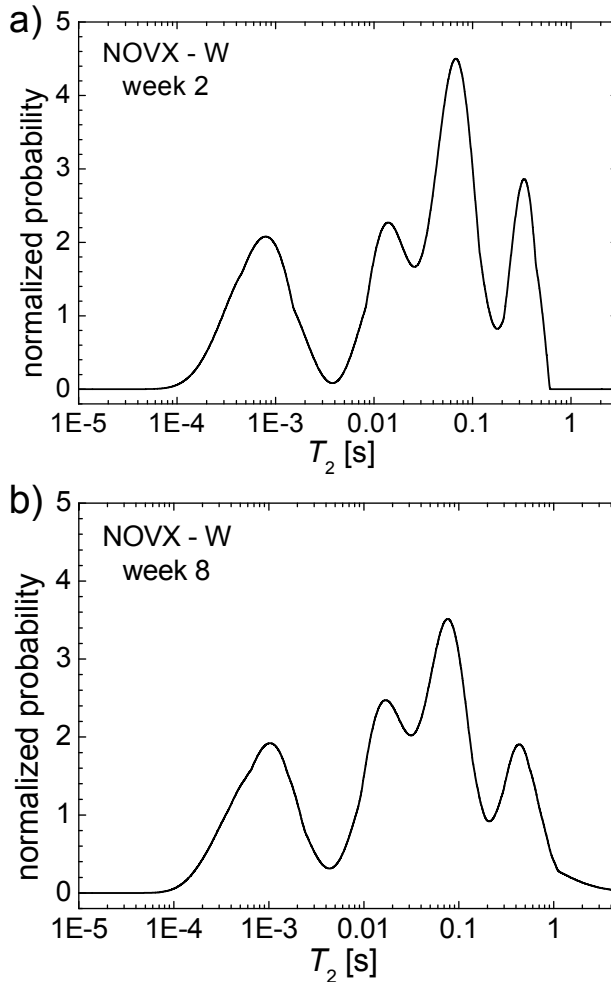


Figure 2. The average normalized T_2 distributions of non-ovariectomized (NOVX) witness (W) rats measured at a) 2 weeks and b) 8 weeks of observation.

The general shape of the averaged normalized T_2 distributions of NOVX-W measured at two weeks of observation (Fig. 2a) is similar with the corresponding T_2 -distribution obtained for the rats' sacrificed at eight weeks (Fig. 2b). This result is not surprising since the rats are witness (not treated with medicine) and are non-ovariectomized. Nevertheless, we observe a slight change in the relative height of the three peaks of interest (corresponding to the ^1H from pores pools or with $T_2 > 10$ ms) between week 2 and 8, indicating a certain dynamical changes in the *proximal part of femoris* pores structure. Moreover, we observe a net decrease of all peaks intensities in the average normalized T_2 distributions measured at 8 weeks compared with the similar curve measured at 2 weeks. This leads to an evident increase of the peaks widths. The larger width in the T_2 distributions obtained at 8 weeks, which can be confirmed also by a visual inspection of curve (see Fig. 2b) where the T_2 values are extended towards much larger values than 600 ms (as in the case of T_2 distributions obtained at 2 weeks – See Fig. 2a) is an indices of increased inhomogeneity correlated with an increase of pores sizes in rats' femoral bone, as they become older.

The averaged normalized T_2 distributions obtained for the rat groups sacrificed at two weeks after ovariectomy (see Fig. 3a) is similar with the corresponding distributions obtained for the non-ovariectomized rats, in particular those sacrificed after eight weeks of observation (see Fig 2b). Nevertheless, the further evolution of the bone structure for the OVX rats, due to the ovariectomy induced osteoporosis can be observed in the measured averaged normalized T_2 distributions. Figure 3b presents such a distribution for the OVX rats from the group sacrificed at eight weeks after ovariectomy. Compared with the T_2 distributions recorded for the first group (Fig. 3a) one can observe: i) a relative conservation of the peak corresponding to bound water ($T_2 < 3$ ms); ii) a significant decrease of the area under the medium pores, associated with protons from the fluids located in Haversian and transverse Volkmann canals; iii) a corresponding increase of the area under the small and large pores. From osteoporosis point of view we are more interested about the time evolution of large pores, i.e. the trabecular bone cavities. Then, the ovariectomy induces osteoporosis can be clearly observed from the evolution in time of the average normalized T_2 distributions (in particular the characteristics of the peak located at large T_2 values) measured for the OVX rats after ovariectomy. Moreover, one can take a step forward and analyse, quasi-quantitatively (into an approximation limit), the dimension of large pores. For that, we have to remember that, if the bone is de-fatted and saturated with water, then the bone tissue can be treated as a porous media [19]. In this case the variations in the local surface-to-volume ratio lead to local changes of the relaxation times according to the relation [20],

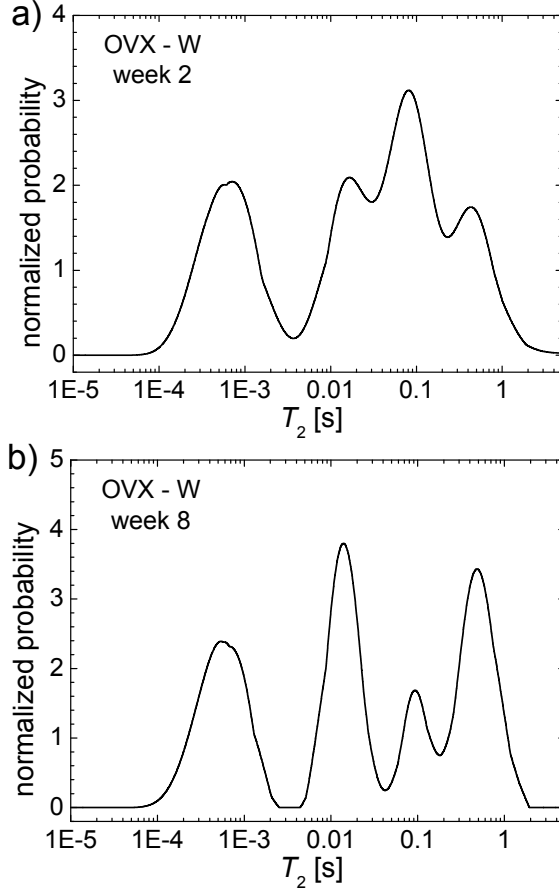


Figure 3. The average normalized T_2 distributions of ovariectomized (OVX) witness (W) rats measured at a) 2 weeks and b) 8 weeks of observation.

$$\frac{1}{T_2^{\text{measured}}} = \frac{1}{T_2^{\text{free water}}} + \rho \left(\frac{S}{V} \right)_{\text{pore}}, \quad (1)$$

where T_2^{measured} is the measured transverse relaxation time, $T_2^{\text{free water}} \cong 3$ s is the transverse relaxation time of the bulk water, ρ is the surface relaxation and S and V are the surface and volume of a particular pore [20]. If one can consider that the trabecular cavities, i.e. the large pores, can be considered, with a good approximation, as spherical, then the surface $S = 4\pi r^2$ and the volume $V = 4\pi r^3/3$ where r is the pore radius.

Introducing the previous relations and values, in the approximation of the spherical pores the average diameter of a pore can be estimated from the measured transverse relaxation time T_2^{measured} as,

$$\bar{d}_{\text{pore}} = \frac{18 \cdot \rho \cdot T_2^{\text{measured}}}{3 - T_2^{\text{measured}}} \quad (2)$$

In equation (2) we observe that in order to calculate the average pore diameter \bar{d}_{pore} usually we have to know also the surface relaxation ρ . Here we consider a different approach. First we estimate the surface relaxation ρ considering some histological images measured previously [21] and then with the estimated value of ρ we use the eq. (2) for all the average normalized T_2 distributions to calculate the distribution of pores diameters.

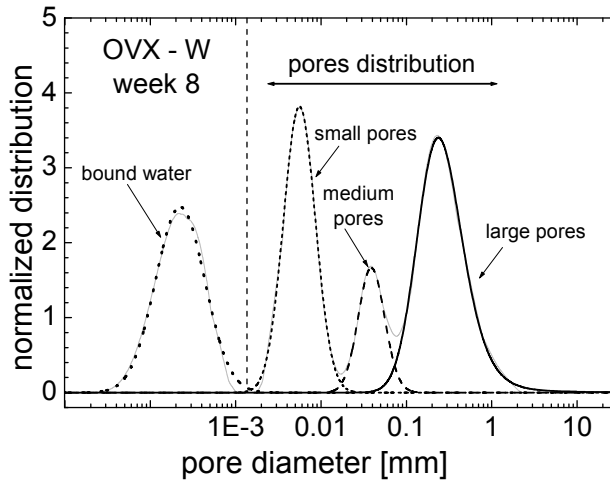


Figure 4. The distribution of pores diameters obtained from average T_2 distributions (Fig. 3b) using Eq. (2) for the witness ovariectomized rats groups sacrificed at 8 weeks from ovariectomy.

An example of such distribution is presented in Fig. 4. There the average normalized T_2 distributions measured for the OVX-W group sacrificed at 8 weeks after ovariectomy, and presented in Fig. 3b, was converted using eq. (2) into a pore diameter distribution (presented with light gray in Fig. 4).

The distributions of all three types of pores can be found using the decomposition of overall *pore diameter distribution*. The result is presented also in Fig. 4 where we have: i) with dots the distribution of bound water; ii) the

distribution of pores diameters for small pores (short dots line), medium pores (dot line) and large pores (continuous line). We have to underline that the conversion based on the eq. (2) has sense only for pores and not for the peak corresponding to the bound water. Then in this case the diameter of pores estimated for the *proximal part of femoris* of our study group of albino Wistar rats with osteoporosis induced by ovariectomy sacrificed at eight weeks after surgical procedure are found in the range from 1 μm to ~ 2 mm. We observe also that the diameters of majority of the large pores (trabecular cavities) are with one order of magnitude smaller, and then the highest probability is to find trabecular cavities with a diameter of ~ 0.24 mm.

From all parameters that characterize the average normalized T_2 distributions (peaks: high, width, maximum and integral area) for all small, medium and large pores, we found that $T_{2,\text{max}}^{\text{measured}}$, which is the transverse relaxation time value which give the maximum probability to find large pores (cavities) in proximal part of rats' femurs, is the most suitable to describe the evolution of witness rats subjected or not to ovariectomy. In this sense the $T_{2,\text{max}}^{\text{measured}}$ values are presented in Fig. 5a function of observation time for the witness (non-treated with medicine) non-ovariectomized (NOVX-W) and ovariectomized (OVX-W) rats. Applying the previously described procedure, the time evolution of the averaged trabecular cavities dimensions for the OVX-W and NOVX-W rats are compared in Fig. 5b. For both groups, we observe an increase of the trabecular cavities diameters with time for NOVX-W from ~ 0.15 mm at two weeks to ~ 0.21 mm at eight weeks and for OVX-W from ~ 0.21 mm at two weeks to ~ 0.24 mm at eight weeks. The increase of trabecular cavities for the witness non-ovariectomized rats can be explained by the fact that at 16 months (the age of rats at the begging of experiment) the rats are not fully developed (are not adults). Then, the increase of trabecular cavities for the witness ovariectomized rats is a combination of natural growth with the induced osteoporosis. In fact, in all but youngest bone we found a phase characterized by a high disorder, a high degree of carbonate substitution, substantial OH deficiency, and presence of lattice vacancies. A large amount of bioapatite atoms are on the surface of the crystal providing a large specific sorption area of ions, proteins and drugs [3]. The bone is considered a dynamics tissue which, depending on the animal diet, health and physical exercises, can progress from poorly crystalline apatite with high HPO_4^{2-} content and low level of crystallinity to a mineral with relative high crystallinity, low acid phosphate content, an increased degree of organization and more carbonate substitutions [22-24]. Despite the statistical diversity, the osteoporosis effect can be the best observed from the fact that, at all observation times, the average diameter of trabecular cavities are larger for the ovariectomized rats than for the non-ovariectomized rats (see Fig. 5b).

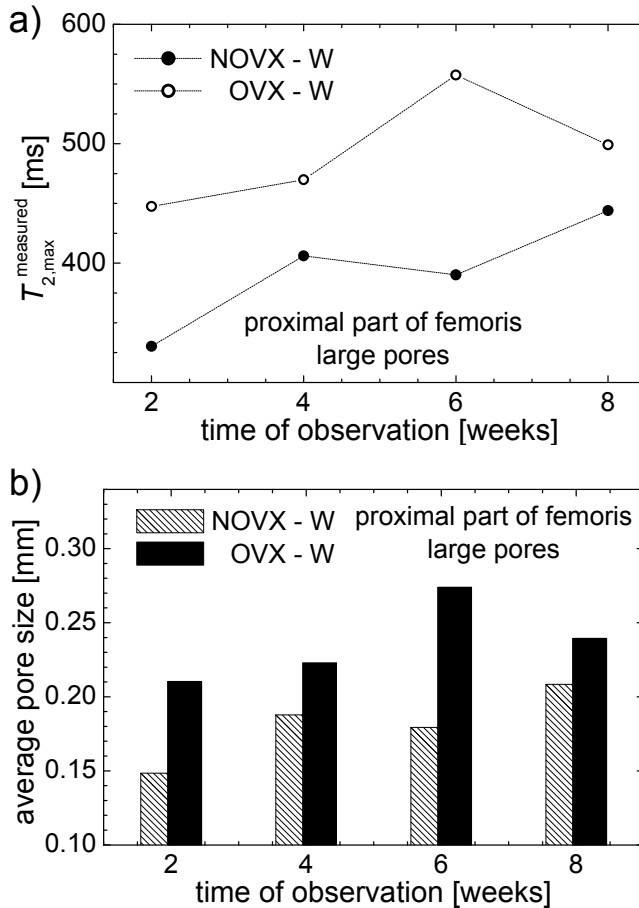


Figure 5. a) The T_2 values corresponding to large pores of *proximal part of femoris* of non-ovariectomized (NOVX) and ovariectomized (OVX) rats function of observation time and b) the average values of large pores obtained from Fig. a) using Eq. (2).

CONCLUSIONS

The ovariectomy induced osteoporosis of albino Wistar rats' femurs was studied by NMR relaxometry combined with Laplace spectroscopy. For that we use a dried and filled with water *proximal part of femoris*, proved to be the femur part (compared with diaphysis or distal epiphysis) more sensitive to the changes in the bone structure affected by osteoporosis, as a porous media. From Laplace spectrum or the average normalized T_2 distributions we estimates, in the spherical

pores approximation, the distribution of pores dimensions specific to albino Wistar rats' femurs *proximal part of femoris*. We found that the overall distribution of pores sizes lies in the range from 1 μm to several millimeters. Then we evaluate the evolution in time of these pores on a period of eight weeks of observation for ovariectomized and non-ovariectomized rats and we found that the osteoporosis is clearly observed for the large pores i.e. the trabecular cavities. The same conclusion is obtained from NMR measurements of *proximal part of femoris*, diaphysis and distal epiphysis with bone marrow and from histological images of the same lot of rats (unpublished results). Therefore valuable results can be obtained by *in vivo* measurement of MRI localized combined with relaxation NMR experiments.

EXPERIMENTAL SECTION

A number of 24 Albino Wistar adult female rats were used for this study. At the beginning of the observation the age of rats was 16 months which is 47 years old in women human correspondent [25, 26], and the average weight was 300 grams. Half of them have been ovariectomized (label OVX) while half remained non-ovariectomized (label NOVX). The ovariectomy surgical protocol applied on the rats was previously described in ref. [21]. The animals were divided into 8 groups of 3 rats each. After the ovariectomy at 2, 4, 6, and 8 weeks of observation, the animals from each group were sacrificed with an overdose of ketamine and xiline (8-10 mg/kg). From each rat the right femoral bone was harvested and was then cut in three parts. The first section was made under the trochanter (see Fig. 6–up) and the second one above the intercondylar fossa, resulting three parts: i) *proximal part of femoris*, which contain the femoral head, femoral neck and proximal diaphysis (see Fig. 6–down); ii) diaphysis and iii) distal epiphysis. In order to remove the bone marrow, the femoral bone was kept in air a period of two months. Then the dried bone was kept in formalin another two months before NMR measurements. In correspondence with ovariectomy induced osteoporosis many other investigation were performed: i) the extended lot of animals contains 72 Albino Wistar rats, 24 remains untreated, 24 being treated with statins and 24 were treated with fibrates; ii) during the life time of animals the left femur was fractured and after rats sacrifice this femur was harvested for optical inspection of fracture and histopatological examinations. The healing process was statistically evaluated by a score received by each treated or untreated, ovariectomized or non-ovariectomized animal; iii) the rats diaphysis microstructure was observed by histological images; iv) extended NMR investigations of *proximal part of femoris*, diaphysis and distal epiphysis with bone marrow were performed and the effect of statin and fibrate drugs in the osteoporosis

reversibility was estimated (unpublished results). All the animal investigation has been approved by the Ethics Committee of the University of Medicine and Pharmacy of Targu Mures, Romania with the number 29/26.06.2012.

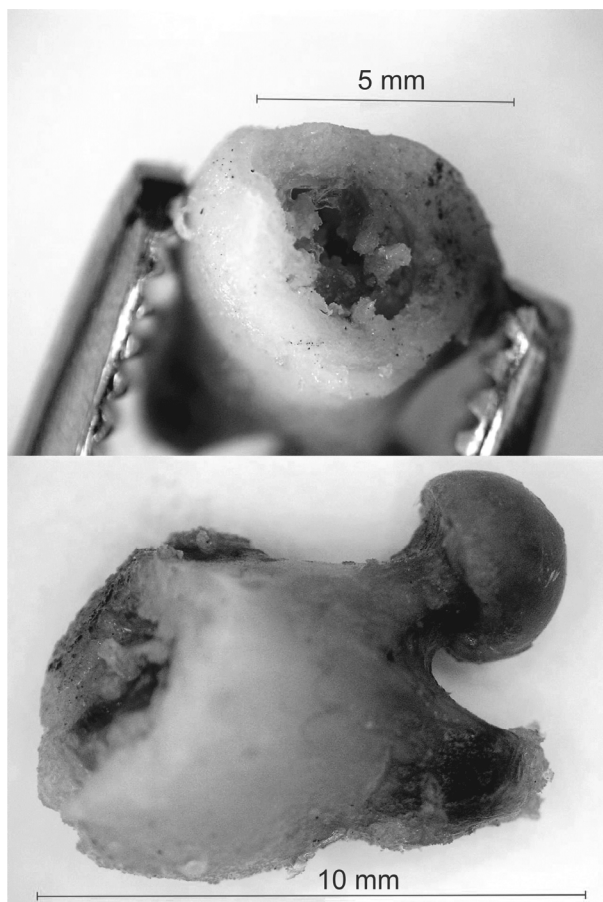


Figure 6. Optical images of an albino Wistar rats' *proximal part of femoris* a) section under the trochanter and b) whole part.

The ^1H NMR relaxation measurements was performed using the Bruker Minispec spectrometer with the 10 mm probe-head. The Larmor frequency was 19.688 MHz and the temperature was maintained constant at 35 °C. For the T_2 spin-spin relaxation times measurements the pulse length was 12.5 μs and 4000 CPMG echoes with an echo time of 0.4 ms were recorded. A recycle delay of 5 s and 128 scans and ensures a good sample magnetization a good

signal to noise ratio. In order to find the T_2 spin-spin relaxation times distributions, the CPMG curves were analyzed using the UPIN algorithm, which perform a Laplace inversion of the measured data [27].

ACKNOWLEDGMENTS

This work was supported by CNCSIS –UEFISCDI, project number PN II – IDEI code 307/2011.

REFERENCES

- [1]. W. Koopman, M. Moreland, in: “Arthritis and allied conditions: a textbook of rheumatology” 15th edition, Lipincott Williams & Wilkins, Philadelphia, **2004**, 3:78-96.
- [2]. Brandi M.L., *Rheumatology*, **2009**, 48, iv3.
- [3]. A.L. Boskey, *Elements*, **2007**, 3, 387.
- [4]. H.H. Ong, S.L. Wehrli, and F.W. Wehrli, *Journal of Bone and Mineral Research*, **2012**, 27, 2573.
- [5]. T. Sukenari, M. Horii, K. Ikoma, M. Kido, S. Hayashi, Y. Hara, T. Yamasaki, K.I. Matsuda, M. Kawata, T. Kubo, *Journal of Magnetic Resonance Imaging*, **2014**, doi: 10.1002/jmri.24765.
- [6]. L. Cardoso, S.P. Fritton, G. Gailani, M. Benalla, S.C. Cowin, *Journal of Biomechanics*, **2013**, 46, 253.
- [7]. S. Bohic, C. Rey, A. Legrand, H. Sfihi, R. Rohanzadeh, C. Martel, A. Barbier and G. Daculsi, *Bone*, **2000**, 26, 341.
- [8]. W.S.S. Jee, W. Yao, *Journal of Musculoskeletal and Neuronal Interactions*, **2001**, 1, 193.
- [9]. J.E.M. Brouwers, B. van Rietbergen, R. Huiskes, K. Ito, *Osteoporosis International*, **2009**, 20, 1823.
- [10]. D. Sharma, C. Ciani, P.A. Ramirez Marin, J.D. Levy, S.B. Doty, S.P. Fritton, *Bone*, **2012**, 51, 488.
- [11]. M. Jablonski, V.M. Gun'ko, A.P. Golovan, R. Leboda, J. Skubiszewska-Zieba, R. Pluta, V.V. Turov, *Journal of Colloid and Interface Science*, **2013**, 392, 446.
- [12]. P. Fantazzini, C. Garavaglia, M. Palombarini, R.J.S. Brown, G. Giavaresi, R. Giardino, *Magnetic Resonance Imaging*, **2004**, 22, 689.
- [13]. Y.Q. Song, L. Venkataramanan, M.D. Hürlimann, M. Flaum, P. Frulla, and C. Straley, *Journal of Magnetic Resonance*, **2002**, 154, 261.
- [14]. D. Moldovan, M. Pop, R. Fechet, A. Baudouine, M. Todica, *Studia UBB Chemia*, **2011**, 3, 103.

- [15]. D. Moldovan, R. Fechete, D.E. Demco, E. Culea, B. Blümich, V. Herrmann, M. Heinz, *Journal of Magnetic Resonance*, **2011**, *208*, 156.
- [16]. R. Fechete, D. Moldovan, D.E. Demco, B. Blümich, *Diffusion Fundamentals*, **2009**, *10*, 14.1.
- [17]. Y. Uyar, Y.. Baytur, U. Inceboz, B.C. Demir, G. Gumuser, K. Ozbilgin, *Maturitas*, **2009**, *63*, 261.
- [18]. R.A. Horch, D.F. Gochberg, J.S. Nyman, M.D. Does, *PLoS ONE*, **2011**, *6*, e16359 1.
- [19]. P. Fantazzini, R.J.S. Brown, G.C. Borgia, *Journal of Magnetic Resonance*, **2003**, *21*, 227.
- [20]. George R. Coates, Lizhi Xiao, and Manfred G. Prammer, "NMR Logging Principles and Applications", Halliburton Energy Services Publication H02308, Houston, USA, **1999**.
- [21]. R.S. Sipos, Z. Pap, A.S. Szalai, I. Sus, A.V. Gabor, Z. Pavaí, K. Branzaniuc, *Acta Medica Marisiensis*, **2010**, *56*, 479.
- [22]. C.A. Morris, *Journal of Biomedical Optics*, **2000**, *5*, 259.
- [23]. A.L. Boskey, *Current Osteoporosis Reports*, **2006**, *4*, 71.
- [24]. K. Verdelis, L. Lukashova, J.T. Wright, R. Mendelsohn, M.G.E. Peterson, S. Doty, A.L. Boskey, *Bone*, **2007**, *40*, 1399.
- [25]. N.A. Andreollo, E.F. Santos, M.R. Araújo, L.R. Lopes, *ABCD. Arquivos Brasileiros de Cirurgia Digestiva*, **2012**, *25*, 49.
- [26]. P. Sengupta, *Biomedicine International*, **2011**, *2*, 81.
- [27]. G.C. Borgia, R.J.S. Brown, P. Fantazzini, *Journal of Magnetic Resonance*, **1998**, *132*, 65.

STRUCTURAL, MORPHOLOGICAL AND OPTICAL PROPERTIES OF RE-DOPED AZO THIN FILMS (RE=Nd, Gd, Er) GROWN BY RF MAGNETRON SPUTTERING

MARIA TOMA^a, DANIEL MARCONI^{a,b,*}, CLAUDIU LUNG^a,
OANA PONTA^c, AUREL POP^a

ABSTRACT. In this paper we describe the influence of substrate-target distance of AlZnO films doped with rare earth (RE= Nd, Gd, Er) ions, on structural, morphological and optical properties. The transparent conductive RE doped AZO thin films were fabricated by radio frequency (RF) magnetron sputtering using a power of 100 W and the deposition pressure of 2.1×10^{-2} mbar. The deposition was performed on glass substrates heated at 150°C and with a time deposition of 90 minutes. Therefore, we obtained AZO thin films doped with RE ions. The influence of substrate-target distance for each rare earth ions on the structure of thin films was analyzed by X-ray diffraction (XRD). Scanning electron microscopy (SEM) shows the uniformity of the surface which consists of well-defined spherical crystallites. The decreasing of target-substrate distance leads to an increase in grain size. However, there is a slight change in the size and topography of films by doping with different 4f elements. The energy dispersive X-ray spectroscopic analysis (EDX) results show presence of an oxygen deficiency (oxygen stoichiometry lower than 50 wt.%). The optical transmittance through the films was measured in the wavelength range 375–1000 nm. The refractive index, transparency and thickness of obtained films were determined.

Keywords: RE doped AZO thin films, XRD, SEM, EDX, optical transmission.

^a Babes-Bolyai University, Physics Faculty, M. Kogalniceanu No. 1, 400084, Cluj-Napoca, Romania

^b Department of Molecular and Biomolecular Physics, National Institute for Research and Development of Isotopic and Molecular Technologies, Donat 67-103, 400293 Cluj-Napoca, Romania. * Corresponding author: daniel.marconi@phys.ubbcluj.ro

^c Institute for Interdisciplinary Research in Bio-Nano-Sciences, Str. Treboniu Laurean, Nr. 42, Cluj-Napoca, Romania

INTRODUCTION

As an II-VI semiconductor material, zinc oxide (ZnO) with band gap energy (3.37 eV at room temperature), similar to TiO₂, has attracted considerable attention due to its unique properties, such as high electron mobility and conductivity, high transmittance in visible and IR region of the spectrum. Therefore, transparent conductive oxide (TCO) thin films are considered promising materials for light emitting materials [1, 2], transistors [3], gas sensors [4], magnetic semiconductors [5, 6] and photocatalysts [7]. Also, ZnO doped with aluminium, (AZO), have some new domains of application, in the electromagnetic spectrum as terahertz spectroscopy and imaging are becoming potential tools for characterizing various materials including semiconductor, high-temperature, superconductor and biomaterial specimens [8-11], nanowires [12, 13] and coatings for energy-efficient windows or organic solar cells [14, 15].

In this work, we prepared AZO thin films doped with rare earth (RE=Nd, Gd, Er) ions, due to its wide applications such as solar cells [15, 16], flexible organic light-emitting diodes [17-19], spintronic devices [20] data storage, radiation detection and even biomedical applications [21, 22]. These thin films were synthesized in RF magnetron sputtering, at different distances between substrate and target and they were analysed using XRD measurements for structural properties, SEM and EDX for surface and stoichiometry properties. Optical measurements were studied using PARAV program for calculating the transmittance spectra and refractive index [23]. The results shows that the thickness of thin films depends on the distance between the target-substrate and also, the nature of the dopant components (Nd, Gd, Er), according with other studies [24].

RESULTS AND DISCUSSION

Structural properties

Figure 1 shows the diffraction patterns of the obtained films. As seen in these figures, all the films are polycrystalline with hexagonal wurtzite type structure.

According to the literature [25, 26], it was observed that the location of 4f elements atoms in analyzed thin films was not possible due to the large difference between the atomic radii of the elements (Zn, Al, Er, Gd, Nd), resulting in distortion and displacement of the peaks in the X-ray diffractogram. Also with increasing target-substrate distance a (100) preferential orientation in was observed for Gd and Nd dopants. However, doping affects the growth of crystallites, damaging the structure, which for AZO films is more evident than in the case of doping with Er.

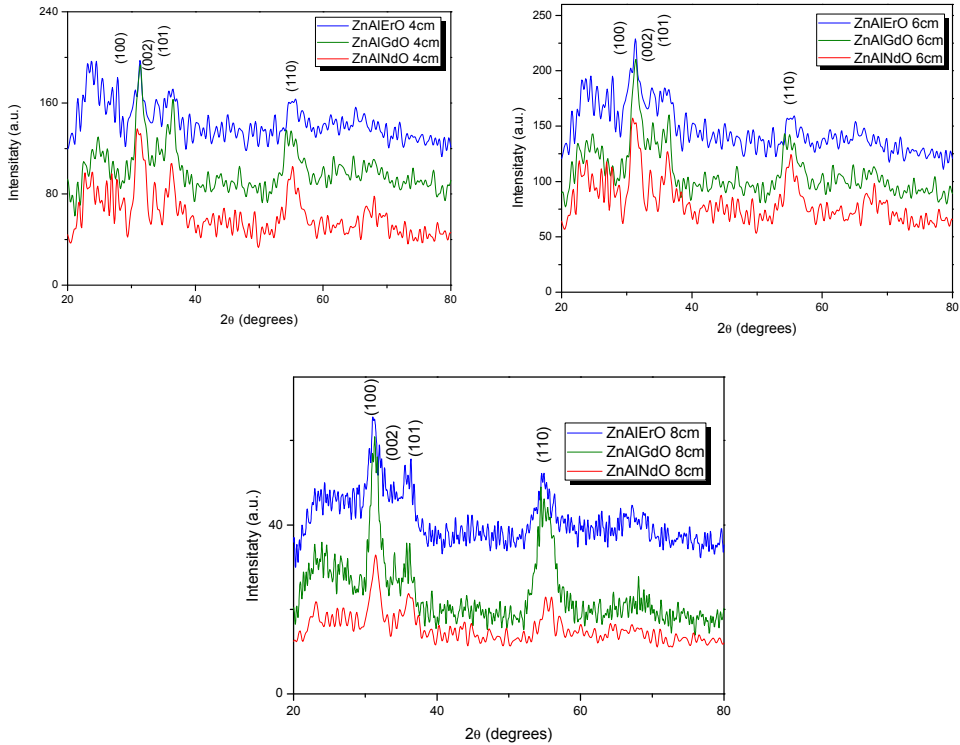


Figure 1. X-ray diffraction spectra of AZO-Er, AZO-Gd and AZO-Nd with three different target-substrate distances.

All diffraction peaks are consistent with previously reported data for ZnO, suggesting that most of the rare earth ions might have been incorporated in the Zn^{2+} sites of the ZnO lattice. This can be understood considering the larger ionic radii of Er^{3+} (0.89 Å), Gd^{3+} (0.938) and Nd^{3+} (0.983) in comparison to that of Zn^{2+} (0.74 Å), which makes the replacement more and more difficult, thus distorting the ZnO lattice. [27, 28].

Morphological properties

SEM images show that the surface of all thin films is smooth, uniform and consists of spherical grains. With the decrease of the distance between target-substrate, we observed an increase in grain size that is well emphasized for the thin films doped with Gd (Figure 3) and Nd (Figure 4). However, addition of rare earth ions varies the structure in general and a kind of disorder

is noticed in the images in accordance with the literature [29]. Also, the images of AZO thin films doped with Er (Figure 2) point out a more homogeneous distribution of the grains in size, keeping the same deposition conditions [30].

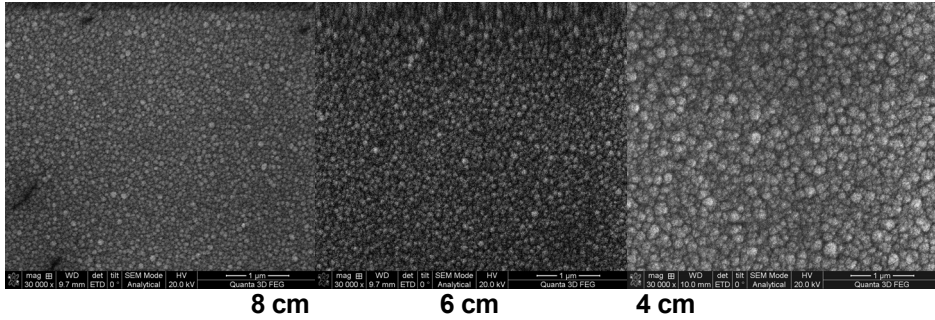


Figure 2. SEM image of AZO-Er thin films

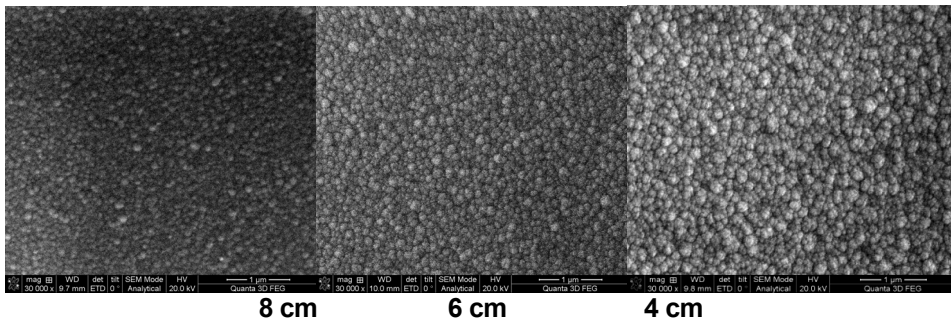


Figure 3. SEM image of AZO-Gd thin films

In Figure 5 we present the EDX spectra for Er, Gd, Nd doped AZO thin films. Therefore, with the increase of distance between target-substrate (small thickness of the films), we received signals for the components of the glass substrate.

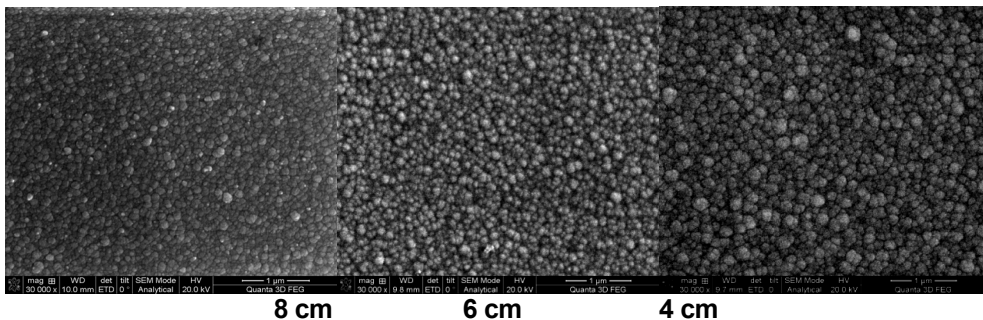


Figure 4. SEM image of AZO-Nd thin films

STRUCTURAL, MORPHOLOGICAL AND OPTICAL PROPERTIES OF RE-DOPED AZO THIN FILMS

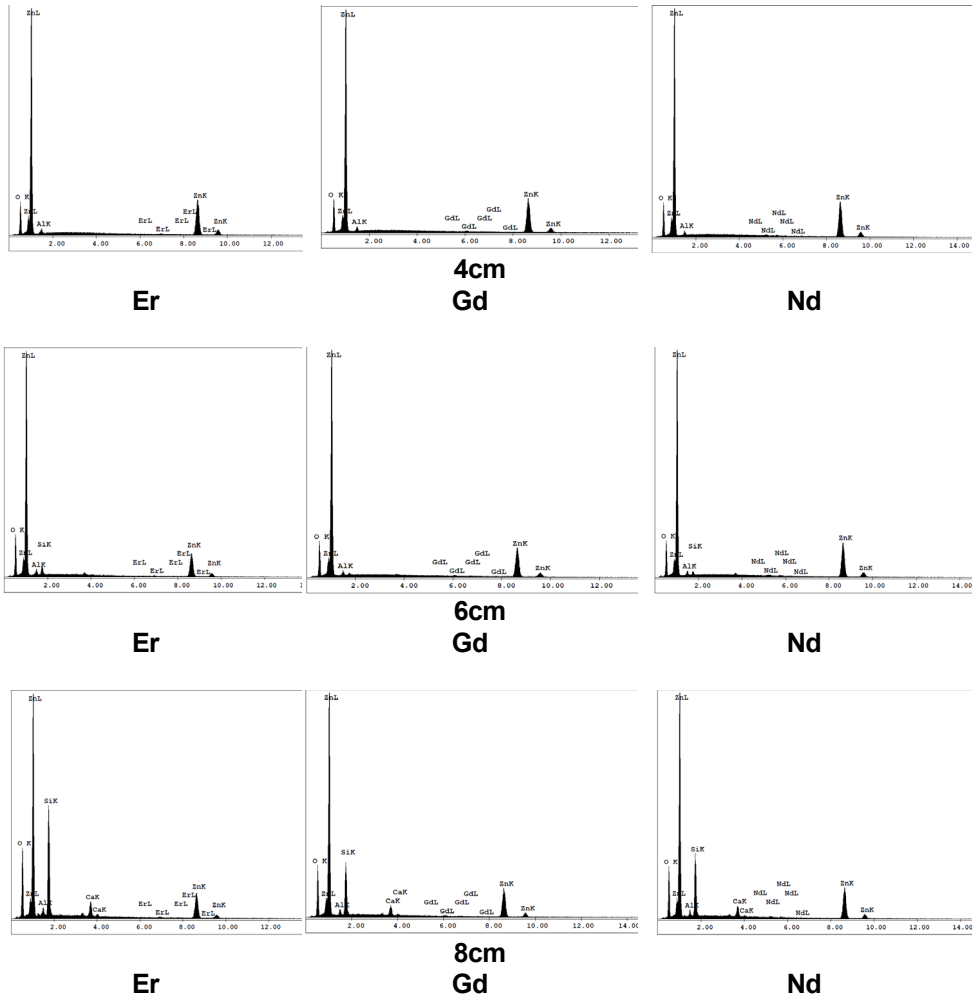


Figure 5. EDX spectra of the studied films

Energy dispersive X-ray (EDX) analysis and elemental mapping images displayed the existence of rare earth ions in the structure of AZO thin films. The percentage of rare earth ions is better observed for thicker films that were obtained for the smallest distance between target-substrate (4 cm) is presented in Table 1. EDX measurements highlight a lack of oxygen, 50% lower than that for Zn, for a constant gas flow in the chamber [25].

Table 1. Elemental weights (wt.%) of Zn, O and dopant elements in the thin films.

Sample	Distance (cm)	Dopant wt.%	Oxygen wt.%	Zinc wt%
AZO-Er	4	1.63	13.32	82.37
	6	2.80	20.79	68.19
	8	2.31	24.43	42.72
AZO-Gd	4	2.32	14.28	80.74
	6	2.03	16.39	78.82
	8	1.85	20.06	56.72
AZO-Nd	4	1.45	14.08	81.95
	6	1.63	14.74	79.37
	8	1.46	19.04	57.11

Optical properties

In Figures 6, Figure 7 and Figure 8 are presented the transmittance spectra and the refractive index of AZO-RE doped thin films. It is shown that the transmittance spectra decreases with the increase of the distance between target-substrate highlighting that the transmittance is influenced of the film thickness and also, the nature of the doping component, in accordance with the literature [31-33]. Furthermore, the refractive index shows a decrease with the increase of wavelength spectra.

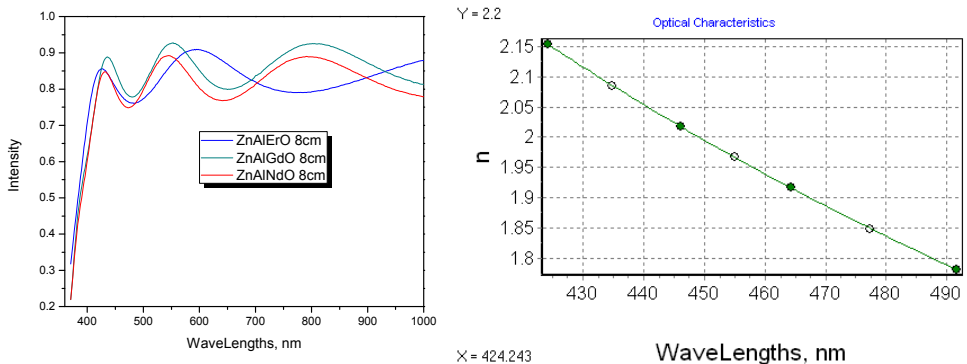


Figure 6. Spectroscopic measurements of the AZO-RE thin films deposited at a distance of 8 cm and refractive index chart

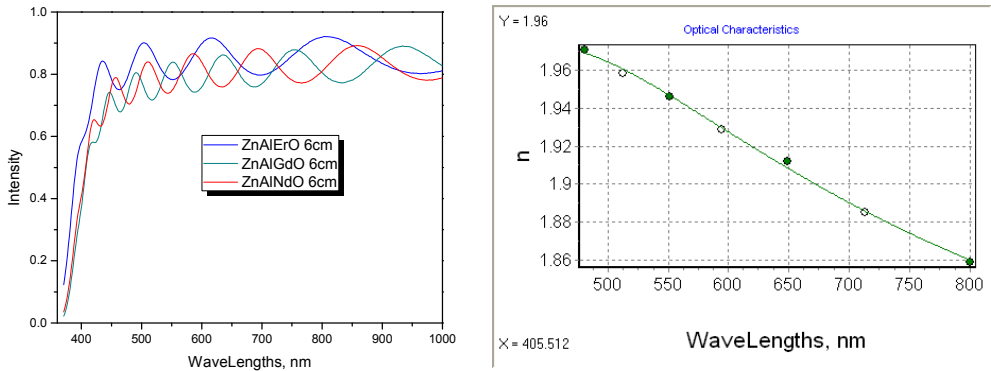


Figure 7. Spectroscopic measurements of the AZO-RE thin films deposited at a distance of 6 cm and refractive index chart

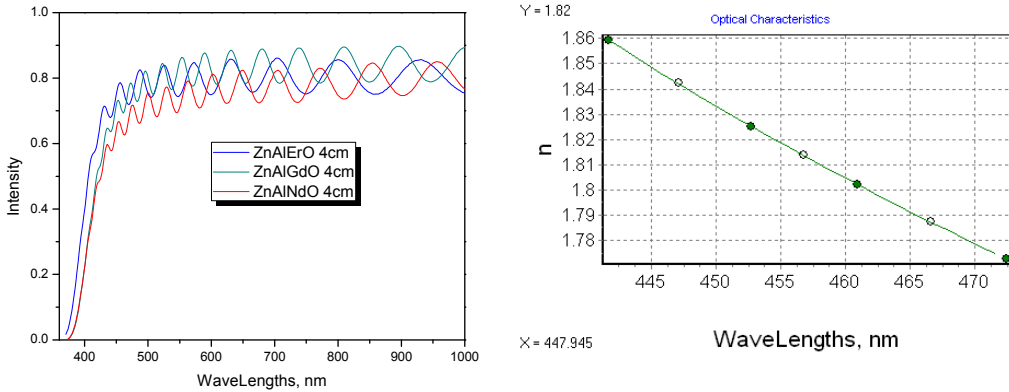


Figure 8. Spectroscopic measurements of the AZO-RE thin films deposited at a distance of 4 cm and refractive index chart

Table 2 shows the thickness dependence of AZO-RE films deposited at different distances.

Table 2. The thickness of the AZO films doped with Er, Gd, Nd deposited at different distances

d (cm)	h (nm) Er	h (nm) Gd	h (nm) Nd
8	346	485	496
6	668	833	811
4	1600	2286	2529

It is found that the film thickness for the same target-substrate distance is influenced by the nature of the dopant (the highest values are obtained for Nd and lowest for Er). The film thickness increases dramatically with decreasing of the target-substrate distance. By decreasing the distance from 8 cm to 4 cm, the film thickness increases approximately 4.6 times in case of the films with Er and Gd and 5.1 times for Nd doped films.

CONCLUSIONS

High quality transparent Er, Gd and Nd doped AlZnO thin films were grown using the RF sputtering technique on glass substrate starting from polycrystalline targets and characterized by XRD, SEM and EDX techniques. The effect of 4f elements and target-substrate distance on structural and morphological properties was studied.

XRD measurements show that all the deposited films are polycrystalline in nature. The increase of target-substrate distance has a (100) preferential orientation, observed for Gd and Nd doped AlZnO thin films. The 4f doping affects the growth of crystallites, damaging the structure, which for AlZnO films is more evident than for Er doping.

The SEM images of the thin films showed the uniformity of the surface which consists of well-defined spherical grains. With decreasing of target-substrate distance the grain size increases.

The EDX analysis results show that the oxygen stoichiometry is lower than 50 wt.% and the stoichiometry of the amount of Zn is more than 50 wt.%. These results highlight the presence of an oxygen deficiency.

Optical measurements highlight a slight decrease of the transmittance spectra (about: 83%) with the decrease of the target-substrate distance, because the increase of film thickness. Also, the refractive index decreases with the increase of wavelength from 400 nm to 1000 nm.

EXPERIMENTAL SECTION

Ceramic preparation

We prepared three ceramic targets obtained by solid state reaction method, using mechanically mixed powders of 97 wt. % of ZnO (99.99% purity), 2 wt. % of Al₂O₃ (99.97%), 1 wt.% of Gd₂O₃ (99.9%), Er₂O₃ (99.9%), Nd₂O₃ (99.9%). They were mechanical processed, pressed at a pressure of 490 MPa and annealed at a temperature of 930 °C for 90 minutes.

Deposition process

The RE-doped AZO thin films were fabricated by RF magnetron sputtering using a power of 100 W. The deposition was performed on glass substrates heated at a constant temperature of 150 °C, the deposition pressure was maintained at 2.1×10^{-2} mbar. The films were deposited in an oxygen–argon atmosphere with the ratio Ar:O₂=10:6 sccm. By modifying the distance between target and substrate for 4 cm, 6 cm and 8 cm and the type of dopant (Nd, Gd, Er), we obtained nine different thin films. The films' thickness was measured with a piezoelectric sensor.

Measurements

To emphasize structural properties we analyzed the surface of the thin films using Bruker Advance D8 XRD diffractometer in Bragg-Bretano ($\theta - 2\theta$) configuration with an CuK α anode ($\lambda_{\text{CuK}\alpha} = 0.154$ nm). XRD patterns were obtained with a step size of 0.1 and an integration time of 5 s/step.

The microstructure and stoichiometry of the thin films deposited under different distances between substrate and target were evaluated using SEM and EDX. For this type of measurements we used a FEI Quanta 3D FEG 200/600 with double electron beam in vacuum module with EDT (Everhart Thornley Detector) from ICEI Cluj Napoca.

Optical measurements of the AZO-doped thin films were performed using a J.A. Woollam M2000V ellipsometer in transmission mode in the range of wavelengths between 375-1000 nm from INCDTIM Cluj Napoca. To highlight the optical properties of the thin films we used the PARAV program.

REFERENCES

- [1].Y.R. Ryu, J.A. Lubguban, T.S. Lee, H.W. White, T.S. Jeong, C.J. Youn, B.J. Kim, *Applied Physics Letters* **2007**, *90*, 131115.
- [2].X.M. Teng, H.T. Fan, S.S. Pan, C. Ye, G.H. Li, *Journal of Applied Physics* **2006**, *100*, 053507.
- [3].Z.-X. Xu, V.A.L. Roy, P. Stallinga, M. Muccini, S. Toffanin, H.-F. Xiang, C.-M. Che, *Applied Physics Letters* **2007**, *90*, 223509.
- [4].T. Gao, T.H. Wang, *Applied Physics A* **2005**, *80*, 1451.
- [5].T. Heng, S. Lau, S. Yu, H. Yang, K. Teng, J. Chen, *Journal of Physics of Condensed Matter* **2007**, *19*, 356214.
- [6].J. Zhang, X. Li, J. Shi, Y. Lu, D. Sellmyer, *Journal of Physics of Condensed Matter* **2007**, *19*, 036210.
- [7].A. Bokare, M. Pai, A. A. Athawale, *Solar Energy* **2013**, *91*, 111.

- [8]. D. Girbovan, M. A. Bodea, D. Marconi, J. D. Pedaring, A. Pop, *Studia UBB Chemia*, **2011**, LVI(3), 213.
- [9]. D. Marconi, C. Lung, Maria Toma, A. V. Pop, *Studia UBB Physica*, **2013**, 58(2), 15.
- [10]. W.-E. Lai, Y.-H. Zhu, H.-W. Zhang, Q.-Y. Wen, *Optical Materials* **2013**, 35, 1218–1221.
- [11]. P.V. Korake, R.S. Dhabbe, A.N. Kadam, Y.B. Gaikwad, K.M. Garadkar, *Journal of Photochemistry and Photobiology B: Biology* **2014**, 130, 11.
- [12]. R. Amiruddin, M.C. Santhosh Kumar, *Ceramics International* **2014**, 40, 11283.
- [13]. R.G. Gordon, “Criteria for Choosing Transparent Conductors”, *MRS Bulletin* **2000**, 25, 52.
- [14]. N. Wolf, T. Stubhan, J. Manara, V. Dyakonov, C.J. Brabec, *Thin Solid Films* **2014**, 564, 213.
- [15]. J.C. Wang, W.T. Weng, M.Y. Tsai, M.K. Lee, S.F. Horng, T.P. Perng, C.C. Kei, C.C. Yu, H.F. Meng, *Journal of Materials Chemistry* **2010**, 20, 862.
- [16]. B. Liu, S. Qiu, R. Hu, Y. Liao, N. Chen, G. Du, *Applied Surface Science* **2012**, 259, 705.
- [17]. P.-H. Lei, C.-M. Hsu, Y.-S. Fan, *Organic Electronics* **2013**, 14, 236.
- [18]. K.-T. Hung, H.-T. Wu, S.-W. Fu, H.-J. Chen, C.-Y. Hsiao, C.-F. Shih, *Organic Electronics* **2013**, 14, 182.
- [19]. W. Lin, R. Ma, W. Shao, B. Liu, *Applied Surface Science* **2007**, 253, 5179.
- [20]. H. Shi, P. Zhang, S.-S. Li, J.-B. Xia, rXiv:1005.1115v1 [cond-mat.mtrl-sci], 7 May **2010**.
- [21]. X. Ma, Z. Wang, *Materials Science in Semiconductor Processing* **2012**, 15, 227.
- [22]. D.Y. Lee, J.-T. Kim, J.-H. Park, Y.-H. Kim, I.-K. Lee, M.-H. Lee, B.-Y. Kim, *Current Applied Physics* **2013**, 13, 1301.
- [23]. D. Girbovan, D. Marconi, R. Redac, A.V. Pop, *Optoelectronics And Advanced Materials* **2012**, 6(9-10), 859.
- [24]. F. Wang, M.Z. Wu, Y.Y. Wang, Y.M. Yu, X.M. Wu, L.J. Zhuge, *Vacuum* **2013**, 89, 127.
- [25]. A. Neren Ökte, *Applied Catalysis A: General* **2014**, 475, 27.
- [26]. S. Ilican, Y. Caglar, M. Caglar, B. Demirci, *Journal Of Optoelectronics And Advanced Materials* **2008**, 10, 2592.
- [27]. C. Dewei, L. Sean, *New Journal of Glass and Ceramics* **2012**, 2, 13.
- [28]. R. Zamiri, A.F. Lemos, A. Reblo, H. A. .Ahanger, J.M.F. Ferreira, *Ceramics International* **2014**, 40, 523.
- [29]. Q. Hua, W. Ligang, L. Ruijin, Y. Wenfeng, *Optik* **2014**, 125(15), 3902.
- [30]. Y. Chen, X.L. Xu, *Physica B* **2011**, 406, 3121.
- [31]. S. Flickyngerova, K. Shtereva, V. Stenova, D. Hasko, I. Novotny, V. Tvarozek, P. Sutta, E. Vavrinsky, *Applied Surface Science* **2008**, 254, 3643–3647.
- [32]. D.-S. Kim, J.-H. Park, S.-J. Lee, K.-J. Ahn, M.-S. Lee, M.-H. Ham, W. Lee, J.-M. Myoung, *Materials Science in Semiconductor Processing* **2013**, 16, 997.
- [33]. S. Flickyngerova, K. Shtereva, V. Stenova, D. Hasko, I. Novotny, V. Tvarozek, P. Sutta, E. Vavrinsky, *Applied Surface Science* **2008**, 254, 3643.

MAGNESIUM INFLUENCE ON BIOACTIVITY OF SILICATE GLASSES PREPARED BY DIFFERENT SOL-GEL ROUTES

PAULA ILDIKÓ RITI^a, ADRIANA VULPOI^a, VIORICA SIMON^{a*}

ABSTRACT. Xerogels of SiO₂, SiO₂-CaO, SiO₂-MgO and SiO₂-CaO-MgO compositions were prepared following the acid catalysed and quick alkali mediated sol-gel routes. The samples were characterized by X-ray diffraction, scanning electron microscopy and elemental composition energy-dispersive X-ray spectroscopy both before and after 8 days immersion in simulated body fluid. The results indicate that the calcite formation is favoured on calcium containing samples with up to 15 mol % MgO prepared by quick sol-gel route. Above this concentration magnesium inhibits the calcite formation and implicitly the expected bioactivity.

Keywords: *sol-gel, magnesium, bioactivity*

INTRODUCTION

The sol-gel synthesis method is a low temperature preparation technique largely applied to obtain bioactive glasses [1-4]. Si-Ca-based bioactive glasses are investigated for more than four decades, and the first results were reported by Hench and co-workers [1]. The acid and quick set sol-gel techniques provide accessible way to obtain bioactive glasses [3] which can be used for bone repair or regeneration [5]. The sol-gel route is a synthesis technique based on inorganic polymerisation reactions of metal alkoxide and metal salt precursors [6, 7]. The “quick-set” process was developed [8] to obtain rapid gelation by the pH adjustment of the acid sols with dilute ammonium hydroxide that reduces at room temperature the gelation time from several days to a few minutes.

^a Babes-Bolyai University, Faculty of Physics and Institute for Interdisciplinary Research on Bio-Nano-Sciences, 1 M. Kogalniceanu str., RO-400084, Cluj-Napoca, Romania.

* Corresponding author: viosimon@phys.ubbcluj.ro

Bioactivity is a property of the materials to form a bond with a living tissue [4] and this ability is related to the development of an apatite layer when these materials are immersed in physiological solutions [4,9].

Magnesium is an important element for the human body, and magnesium ions play a significant role in the qualitative changes of bone matrix [10, 11]. Nevertheless further investigations concerning the magnesium ions effect on the bioactivity properties are needed.

In the present study are reported the results related to the bioactivity tested *in vitro*, in simulated body fluid, for six compositions prepared following the acid catalysed and quick alkali mediated sol-gel routes. The main objective was to investigate the magnesium influence on the bioactivity of the synthesized samples.

RESULTS AND DISCUSSION

The structural properties of the xerogel samples (Table 1) were analysed by X-ray diffraction (XRD). The XRD patterns are presented in Figure 1. Before incubation in simulated body fluid (SBF) at 37°C, both acid catalysed (A) and quickly gelled (Q) samples show a predominant amorphous structure denoted in the 2θ range by a broad peak recorded between 15-35°. As can be observed from diffractograms, during SBF immersion calcium carbonate crystals in form of calcite (PDF # 60-7239) were developed on the surface of some samples. Crystalline calcium carbonate can adopt several structures differing in the lattice parameters of the crystal. The atomic structure with the lowest lattice energy, and hence the most stable, is calcite. After 8 days soaking in SBF the results prove that the growth of calcite crystals was not yet achieved on pure SiO₂ samples and on the samples with the highest amount of magnesium, i. e. 20 mol % MgO, whether they were prepared by acid or quick gelation route. At the same time one remarks that up to 15 mol % MgO the addition of magnesium to calcium containing silicate samples brings forward their bioactivity. The self-assembling of calcite occurs among the first stages of bioactivity of glass-ceramics [12]. Concurrently, the presence of carbonates on samples surface would further promote the crystallization of the carbonated hydroxyapatite. Hydroxyapatite has a similar crystal structure and close lattice match to calcite. This structural compatibility is expected to favor nucleation of hydroxyapatite and permit the formation of a coherent, possibly epitaxial, layer of hydroxyapatite on the surface of calcite [13].

For investigation of morphological properties scanning electron microscopy (SEM) images were taken before and after immersion in SBF (Figures 2 and 3). The morphologies depend on the chemical composition and the preparation route of the samples. The glasses prepared by Q route appear more porous in comparison with the samples of similar composition prepared by A route. After SBF immersion clear changes are observed on the samples

surface. The quickly gelled samples present higher bioactivity. Magnesium together with calcium enhances the samples bioactivity but only whether MgO content does not exceed 15 mol % MgO concentration. Higher magnesium content inhibits the calcite formation.

In Figures 2 and 3 are also presented the compositions determined from energy dispersive X-ray spectroscopy (EDS) measurements before and after immersion in SBF. The EDS results support the bioactivity of the matrices.

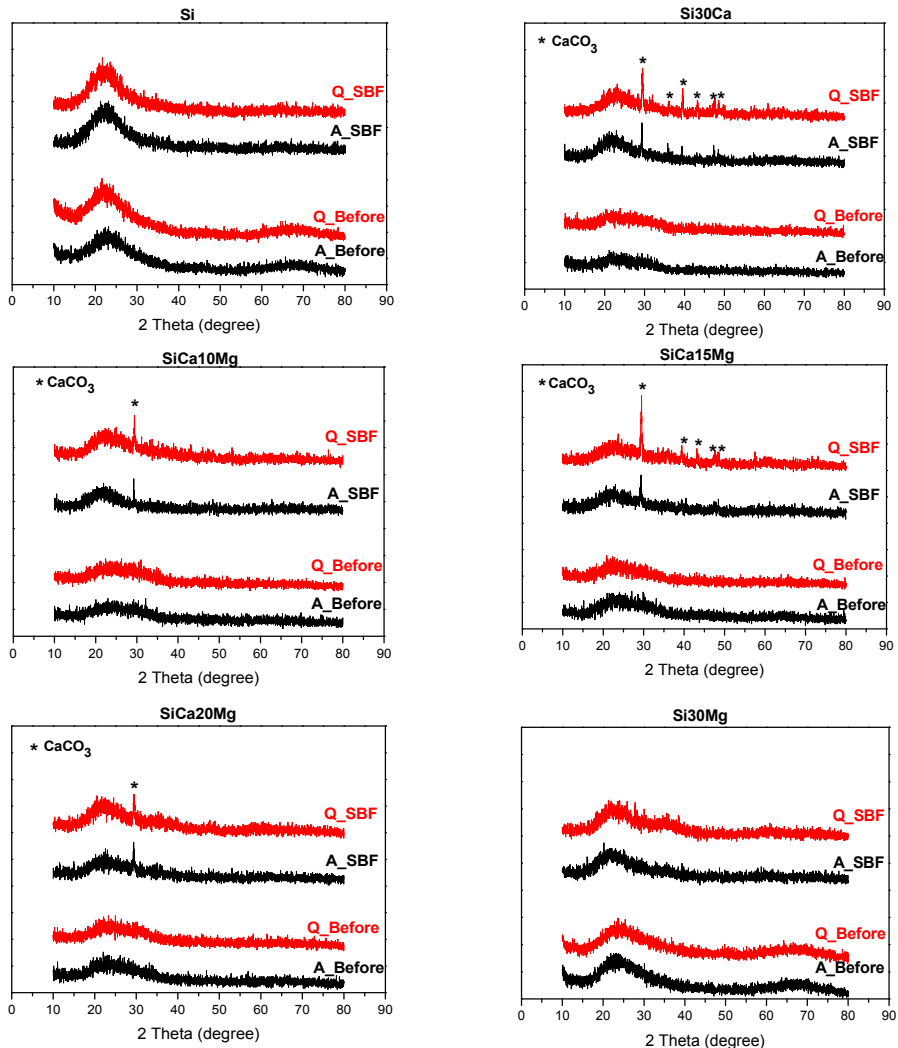


Figure 1. X-ray diffractograms recorded before and after 8 days SBF immersion of the investigated samples

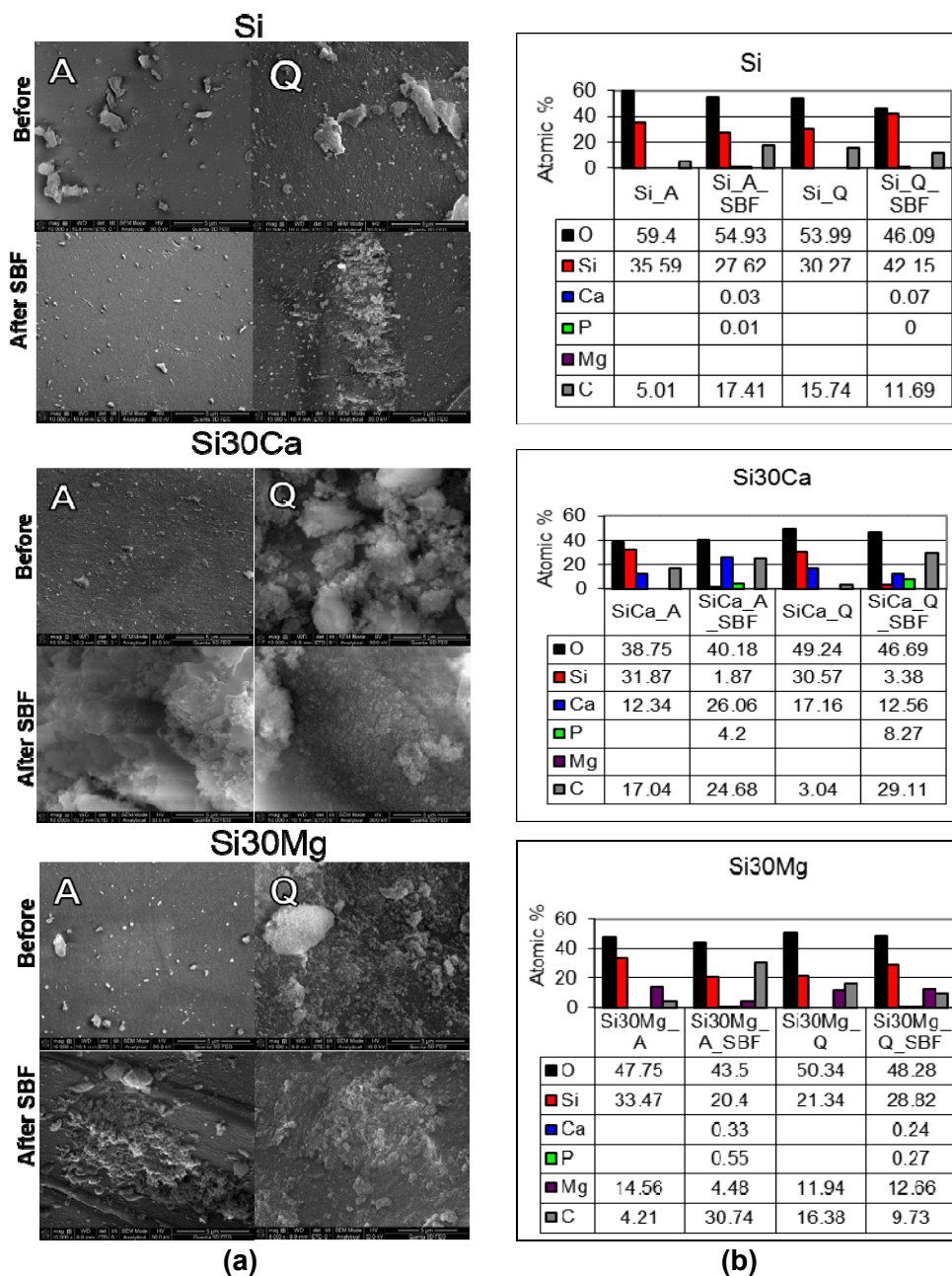


Figure 2. SEM images (a) and EDS results (b) for acid catalysed (A) and quickly gelled (Q) Si, Si₃₀Ca and Si₃₀Mg samples before and after immersion in SBF. Scale bars correspond to 5 μm.

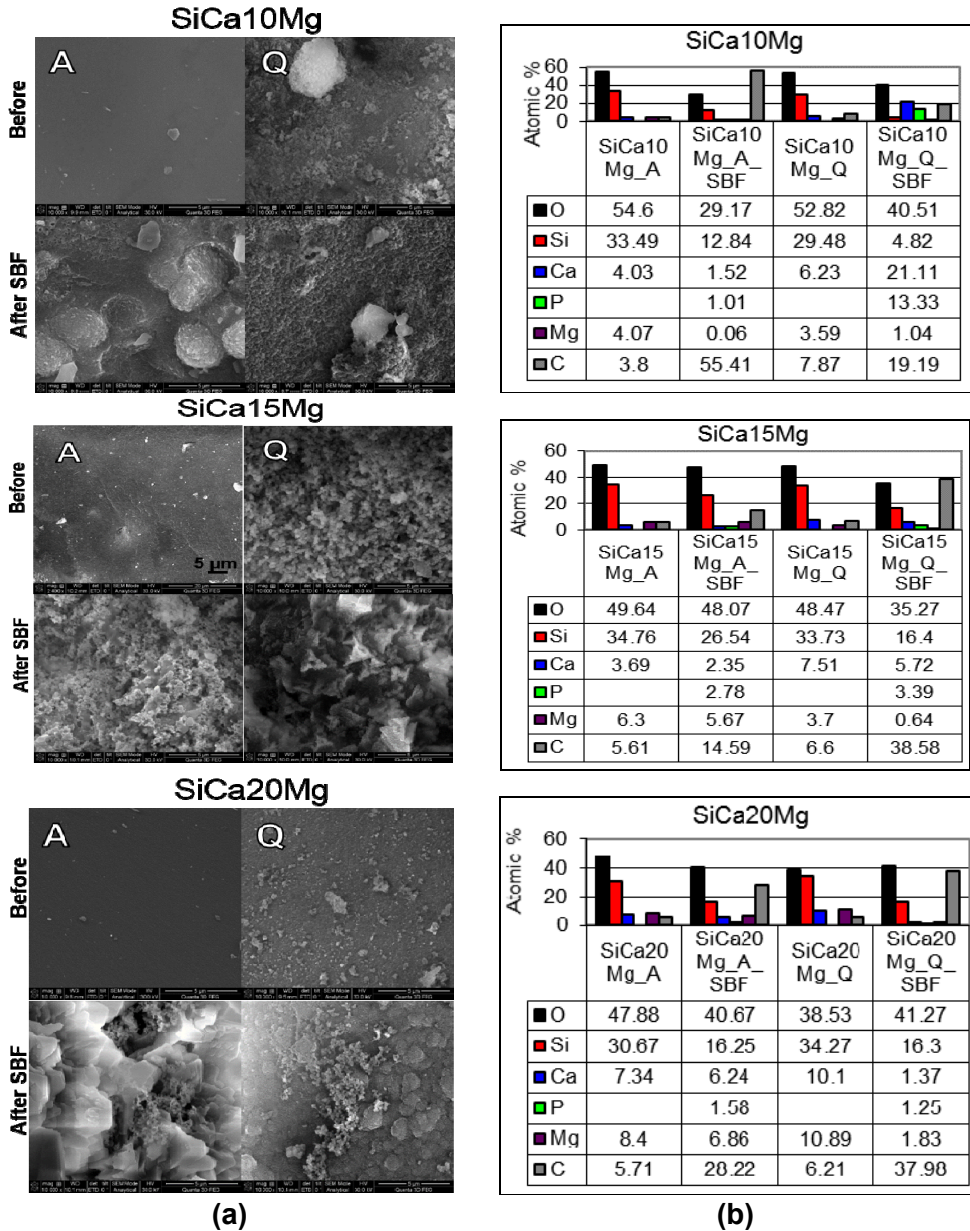


Figure 3. SEM images (a) and EDS results (b) for acid catalysed (A) and quickly gelled (Q) SiCa10Mg, SiCa15Mg and SiCa20Mg samples before and after immersion in SBF. Scale bars correspond to 5 µm.

Excepting the pure SiO₂ quickly gelled sample, phosphorus is detected on all other samples after immersion in SBF. For Si₃₀Ca, SiCa₁₀Mg and SiCa₁₅Mg compositions phosphorus content on the samples quickly gelled by addition of ammonium hydroxide is higher than for the samples which were only acid catalysed. Generally, the magnesium content decreased after immersion in SBF and suggests a release of magnesium ions in simulated body fluid. Carbon presence on all samples before immersion in SBF is primary due to the ubiquitous carbon contamination. After immersion in SBF the carbon content considerably increased, excepting Si_Q and Si₃₀Mg_Q samples, in good agreement with the occurrence of calcite crystallites evidenced by XRD analysis. The values of Ca/P ratio for SiCa₁₀Mg_Q (1.58) and SiCa₁₅Mg_Q (1.69) are close to that of hydroxyapatite (1.67) and denote the enhanced bioactivity potential of these samples, expecting the further nucleation of hydroxyapatite on the surface covered with calcite after 8 days immersion in SBF.

CONCLUSIONS

Pure silica and silicate xerogels with different contents of CaO and MgO acting as glass network modifiers were prepared via acid and quick gelation sol-gel method. The samples treated at 600°C for 6 hours have a predominant amorphous character. After 8 days incubation in simulated body fluid the XRD analysis evidenced the development of calcium carbonate calcite phase on all calcium containing samples. Calcite formation denotes a first stage preceding the nucleation of hydroxyapatite related to samples bioactivity. Scanning electron microscopy and energy dispersive X-ray spectroscopy (EDS) data support the XRD results. In the case of quickly gelled samples the bioactivity indicia are better than for the samples obtained following the one step acid catalysed route. Magnesium inhibits the calcite formation whether MgO content exceeds 15 mol % but up to this concentration the addition of magnesium to calcium containing silicate samples appears to promote their bioactivity.

EXPERIMENTAL SECTION

SiO₂, SiO₂-CaO, SiO₂-CaO-MgO and SiO₂-MgO samples were prepared via sol-gel method following (i) the acid catalysed route (noted A), and (ii) the quick alkali mediated route (noted Q). The compositions of the prepared samples are given in Table 1.

Table 1. The samples symbol related to composition and preparation way.

Symbol	Composition (mol %)
Si_A / Si_Q	100 SiO ₂
Si30Ca_A / Si30Ca_Q	70SiO ₂ ·30CaO
SiCa10Mg_A / SiCa10Mg_Q	70SiO ₂ ·20CaO·10MgO
SiCa15Mg_A / SiCa15Mg_Q	70SiO ₂ ·15CaO·15 MgO
SiCa20Mg_A / SiCa20Mg_Q	70SiO ₂ ·10CaO·20 MgO
Si30Mg_A / Si30Mg_Q	70SiO ₂ ·30 MgO

The reagents used for glass synthesis were tetraethoxysilan SiC₈H₂₀O₄ (TEOS) supplied by Merck– precursor for SiO₂, Ca (NO₃)₂·4 (H₂O) supplied by Lar-Ner, and Mg (NO₃)₂·6 (H₂O) supplied by Penta. For preparation of pure SiO₂ samples TEOS, ethanol, distilled water and nitric acid were continuously stirred (pH ~ 2) and the mixture was allowed to react for 30 minutes under continuous stirring for the acid hydrolysis of TEOS. Then a half of the solution was left for gelation (Si_A), and in the other half 2 mL 1 M ammonia was added drop wise (pH ~ 8) under continuous stirring for quick gelation (Si_Q). For the multicomponent samples the precursors of CaO and MgO, i. e. Ca (NO₃)₂·4 (H₂O) and Mg (NO₃)₂·6 (H₂O), were dissolved in distilled water, and added to the 2 pH TEOS solution under continuous stirring. The samples Si30Ca_A, Si30Ca_Q, SiCa10Mg_A, SiCa10Mg_Q, SiCa15Mg_A, SiCa15Mg_Q, SiCa20Mg_A, SiCa20Mg_Q, Si30Mg_A, Si30Mg_Q were obtained following the same procedure as for pure SiO₂. In case of multicomponent samples obtained by quick gelation 4 ml 1 M ammonia for Si30Ca_Q and Si30Mg_Q, 7.5 ml 1 M ammonia for SiCa10Mg_Q, 11 ml 1 M ammonia for SiCa15Mg_Q, and 12 ml 1 M ammonia for SiCa20Mg_Q was added. The samples prepared by A route had different gelation times: 2 days Si_A, 5 days Si30Ca_A, 5 days SiCa10Mg_A, 4 days SiCa15Mg_A, 6 days SiCa20Mg_A, and 10 days for Si30Mg_A. The gelled samples were dried for 24 hours at 110°C. The dried gels were calcinated at 600°C for 6 hours.

The structural properties of 600°C treated samples were analysed with a Shimadzu XRD-6000 diffractometer, using Cu Ka radiation ($\lambda = 1.5418 \text{ \AA}$), with Ni-filter with a speed of 2°/ min, in the 10–80° range (2 θ). Scanning electron microscopy (SEM) images were taken with a FEI Quanta 3D FEG dual beam microscope for morphological properties investigation. Before SEM imaging the samples were covered with a 5nm gold layer in a Q150R ES rotary pumped sputter coater in argon atmosphere. Chemical analysis of local area was carried out by energy dispersive X-ray spectroscopy (EDS) measurements performed on the same microscope.

In vitro investigation of the calcinated samples was performed in simulated body fluid (SBF) prepared according to Kokubo's protocol [14]. 40 mg of sample were immersed in 10 ml SBF at 37°C and kept under static conditions for 8 days. The SBF was renewed in the fourth day. After SBF immersion the samples were filtered on filter paper and washed three times with bidistilled water and after that dried at 37 °C in air for 24 hours.

ACKNOWLEDGMENTS

P.I. Riti wishes to thank for the financial support provided by The Sectoral Operational Programme Human Resources Development - POSDRU/159/1. 5/S/132400. A. Vulpoi acknowledge's financial support provided by Babes-Bolyai University, project number GTC_34037/201.

REFERENCES

- [1]. L.L. Hench, R.J. Splinter, W.C. Allen, T.K. Greenlee, *Journal of Biomedical Materials Research*, **1971**, 5, 117.
- [2]. W. Xia, J. Chang, *Materials letters*, **2007**, 61, 3251.
- [3]. M.I. El-Gohary, K.M. Tohamy, M.M. El-Okr, A.F. Ali, I.E. Soliman, *Nature and Science*, **2013**, 11, 26.
- [4]. P. Sepulveda, J.R. Jones, L.L. Hench, *Journal of Biomedical Materials Research*, **2002**, 61, 301.
- [5]. A. Balamurugan, G. Sockalingum, J. Michel, J. Faure, V. Banchet, L. Wortham, S. Bouthorsa, D. Laurent-Maquina, G. Balossier, *Materials Letters*, **2006**, 60, 3752.
- [6]. B. Topuz, M. Ciftcioglu, *Journal of Membrane Science*, **2010**, 350.
- [7]. W.M. Jones, D.B. Fischbach, *Journal of Non-Crystalline Solids*, **1988**, 101, 123.
- [8]. C. Wu, J. Chang, J. Wang, S. Ni, W. Zhai, *Biomaterials*, **2005**, 26, 2925.
- [9]. J. Ma, C.Z. Chen, D.G. Wang, X.G. Meng, J.Z. Shi, *Journal of Sol-Gel Science and Technology*, **2010**, 54, 69.
- [10]. S. Hesaraki, M. Safari, M.A. Shokrgozar, *Journal of Materials Science: Materials in Medicine*, **2009**, 20, 2011.
- [11]. P.I. Riti, A. Vulpoi, O. Ponta, V. Simon, *Ceramics International*, **2014**, 40, 14741.
- [12]. C. Berbecaru, H.V. Alexandru, G.E. Stan, D.A. Marcov, I. Pasuk, A. Ianculescu, *Materials Science and Engineering B*, **2010**, 169, 101.
- [13]. S. Naidu, G.W. Scherer, *Journal of Colloid and Interface Science*, **2014**, 435, 128.
- [14]. H. Takadama, T. Kokubo, "Bioceramics and Their Clinical Applications", Woodhead Publishing, Cambridge, **2008**, pp. 165–182.

PRELIMINARY DATA ON BRONZE AGE POTTERY FROM SĂVEȘTI (NEAMȚ COUNTY, ROMANIA)

MARCEL BENE^{a*}, VASILE DIACONU^b,
GHEORGHE DUMITROAIA^c

ABSTRACT. The paper presents the results of the mineralogical and physical analyses carried out on 20 potsherds from Săvești (Neamț county, Romania) belonging to Noua Culture. The goal of this investigation was to provide information on the type of temper materials, the way that the vessels were shaped, the temperature and firing conditions. Generally, the colour is homogenous, grey to black indicating reducing atmosphere. Exceptions are three samples with a “sandwich”-type structure and one sample with a yellowish-brown colour that suggest an oxidizing atmosphere during firing. The matrix is relatively uniform, with clasts of various sizes (up to 3-4 mm). Macroscopically, quartz grains, micas, and ceramoclast were identified. Based on microscopic grain size, two types of ceramics can be separated: semifine (lutitic-siltic-arenitic), and coarse (lutitic-arenitic-siltic). Based on the ratio between crystalline vs. amorphous phases, microcrystalline-amorphous and amorphous-microcrystalline to amorphous fabrics were described. The presence in some samples of elongated primary pores and the preferential orientation of micas lead to a flow texture. As non-plastic materials (temper), crystalloclasts (quartz, micas, iron oxi-hydroxides, feldspars, epidote, zircon, rarely carbonates), lithoclasts (quartzite, micaschist, gneiss), and ceramoclasts were identified. The X-Ray diffraction analyses confirm the microscopic observations. Some physical characteristics were also measured: the water adsorption values range between 7.17 % and 14.44 %. According to the macroscopic, microscopic and compaction features we estimate the firing temperature of the studied potsherds to be between 850-900°C.

Key words: *archaeometry, Bronze Age pottery, mineralogical and physical analyses, Noua Culture, Romania.*

^a Babeș-Bolyai University, Faculty of Biology and Geology, Department of Geology, 1, Kogălniceanu St., RO-400084 Cluj-Napoca, Romania

^b Museum of History and Ethnography Târgu Neamț / Neamț County Museum Complex, 37 Ștefan cel Mare St., 615200 Târgu Neamț, Romania

^c Neamț County Museum Complex, 10 Mihai Eminescu St., 610029 Piatra Neamț, Romania.

* Corresponding author: marcel.benea@ubbcluj.ro

INTRODUCTION

The study of ancient ceramics is a necessary element for understanding prehistoric technology. This especially when it comes to investigating shaping of ceramic vessels, dimensional parameters, mineralogical composition, intensity and conditions of the firing process [1, 2, 3, 4].

The present study is of special significance, giving the fact that currently there are only a few mineralogical analyses on Bronze Age pottery from sites in the East Carpathians. Recently, several studies have been published on this topic, but they only focus on pottery lots from the Middle Bronze Age, namely the Komarov and Costișă cultures [5, 6, 7].

The site of Săvești (Răucești commune, Neamț county) is located on the right bank of Moldova River in a contact area between the Subcarpathians and the Suceava Plateau. In 1986, Gheorghe Dumitroaia undertook an archaeological survey of a Late Bronze Age settlement (Noua culture) located in the north-west part of the village, in the so-called "Izvoare" spot). A surface of approximately 150 square meters was investigated; the research revealed traces of a surface dwelling, hearths and stone agglomerations. The archaeological material is mainly represented by pottery, animal osteological remains and stone artifacts [8, 9].

We should emphasize that the site area is well known for the high density of the Noua culture settlements. This can be partly due to the existence in the region of numerous salt sources (namely saltwater springs) [10,11]. Twenty potsherds identified in the Săvești settlement were analysed for their mineralogy and physical properties. They resulted from different types of vessels, most of them having medium and small sizes. In terms of shapes, jars, cups and bowls dominate. There is a close connection between the pottery types and the quality of the utilized clay. From this point of view, we can separate two categories of ceramics: coarse ware and fine pottery. For example, the jars and bowls are made of coarse/rough, inhomogeneous clay mixed with crushed shards, micro gravel and even crushed quartzite. Alternatively, the cups are made of more homogeneous clay, fact that allowed the potter to manufacture vessels with thin walls. In some cases, the surface of the ceramic vessels is rough and fine cracks are present, while in others the surface was covered with slip. Among the analyzed pieces, only two fragments were decorated.

The color of the potsherds is generally even with slight differences between the exterior and the interior vessels walls. The colors range from reddish to black, suggesting both reducing and oxidizing firing conditions.

In order to identify certain structural parameters, we have chosen to study potsherds that belong to all areas: top, middle and base.

The LBA populations (15th–12th centuries BC) and especially the communities of the Noua culture distinguish themselves through a certain mobility determined by their economical behavior based on animal husbandry [12]. In this context, our study aims to clarify whether the ceramic production had a local character or on the contrary, clay and some of the degreasers were brought from the surrounding areas. Also, defining the quality of the paste correlated to the shape of the vessels could provide some clues concerning the pottery's functionality.

RESULTS AND DISCUSSION

Macroscopical studies

As a rule, the ceramic fragments show homogenous colour with grey to black shades that suggest reducing firing conditions. Only the outer walls show brownish to brown-reddish thin rims (< 1 mm-thick). Exceptions from this trend are samples 2, 12 and 19 showing a sandwich-type structure and sample 8 respectively, showing a light brown-yellowish color – all these samples point to oxidizing firing conditions.

In most of the samples, the matrix is relatively homogenous, with scattered clasts; exceptions are samples 17, 18 and 19. The grain-size distribution in the matrix ranges from semi-fine to coarse. The clasts show various sizes (e.g., in samples 13, 16, 19 reaching up to 3-4 mm).

Macroscopically we could identify quartz grains, mica lamellae and fragments of ceramoclasts.

Porosity is relatively constant, being represented by both primary pores that are usually elongated and parallel to the ceramic surfaces, and irregular secondary pores. The pore sizes range from 0.5 x 1.0 to 1.5 x 3.0 mm.

Polarized light microscopy

In order to identify the mineral components of the matrix and the flux, the fabric of the ceramic shards and the thermal transformations we have studied the samples by optical microscopy under transmitted light. The grain-size measurements led to defining two ceramic types: semifine (lutitic-siltic-arenitic type) and coarse (lutitic-arenitic-siltic) ceramics (these terms apply as follows: lutite < 0.004 mm, silt = 0.004-0.063 mm; arenite = 0.063-2 mm) [13, 14, 15]. Based on the ratio between crystalline vs. amorphous phases in the matrix, two fabric types can be defined: microcrystalline-amorphous and amorphous-microcrystalline to amorphous (Figs.1, 2).

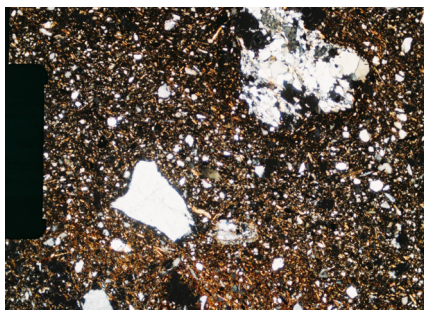


Fig.1 Sample 2 – Semifine ceramics with microcrystalline - amorphous matrix; quartz, micas, quartzite and micaschist clasts; N+, scale bar = 0.5 mm

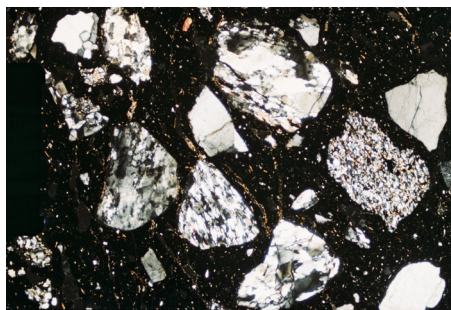


Fig.2 Sample 18 – Coarse ceramics with amorphous to microcrystalline matrix; quartz, micas, quartzite, micaschist and gneiss clasts; N+, scale bar = 0.5 mm

The presence of elongated pores in the studied shards suggests that the ceramics was obtained by plastic shaping. In some of the samples, the preferential orientation of the mica lamellae and of the primary, elongated pores define a relatively obvious flow texture (Figs. 3, 4, 5, 6).

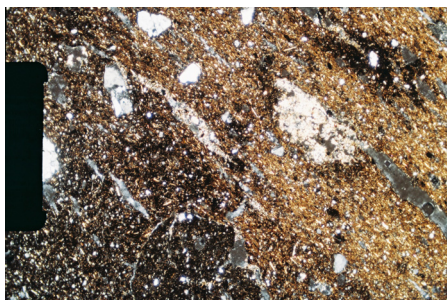


Fig.3 Sample 17 – Semifine ceramics with microcrystalline - amorphous matrix; elongated pores parallel to the surface; quartzite lithoclasts, quartz, calcite and micas crystalloclasts; N+, scale bar = 0.5 mm

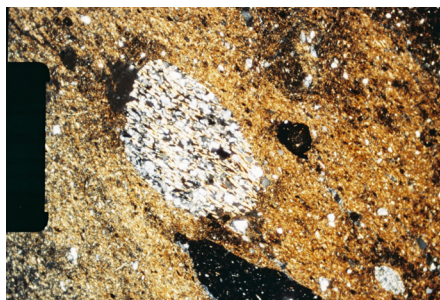


Fig.4 Sample 9 – Semifine ceramics with microcrystalline - amorphous matrix; micaschist lithoclasts, ceramoclasts, quartz and orientated micas; N+, scale bar = 0.5 mm

The crystalloclasts are represented by quartz (from subangular to rounded, with more or less pronounced fissures), micas (muscovite, and rare biotite), iron oxi-hydroxides (mainly hematite) aggregates and feldspars, plagioclases, epidote and zircon in subordinate amounts. The relative high birefringence of the micas (Figs. 5, 6) points to firing temperatures less than 850°- 900°C. Also, the specific features of the matrix and its low birefringence suggest that clay minerals are mainly represented by kaolinite/montmorillonite and subordinately by illite. Only a few samples (5, 10, and 17) contain carbonates.

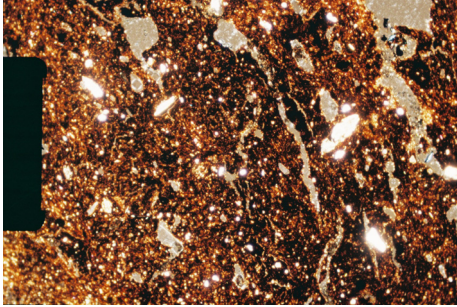


Fig. 5 Sample 15 – Semifine to coarse ceramics with microcrystalline - amorphous matrix; ceramoclasts, elongated pores / fissures, quartz and birefringent micas; N+, scale bar = 0.5 mm

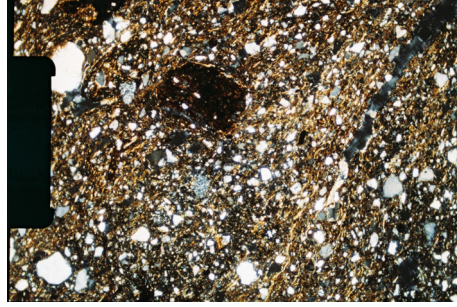


Fig. 6 Sample 5 – Semifine ceramics with microcrystalline to amorphous matrix; circular and elongated pores, ceramoclasts, quartzite lithoclasts, quartz, carbonates and micas; N+, scale bar = 0.5 mm

Lithoclasts are represented by quartzites, micaschists and gneisses (all metamorphic rocks) and their sizes normally range between 2 and 3 mm (maximum sizes in samples 12, 16, 18; Figs. 2, 7, 8). The plagioclase feldspars in these metamorphic lithoclasts are polysynthetically-twinned while the quartz grains show undulatory extinction and mosaic-type structure. The fact that some carbonate grains were not thermally-decomposed indicates low firing temperatures (<850°-900°C).

Ceramoclasts are present in all the studied samples in amounts of ~2 % and with sizes up to 2.5 mm.

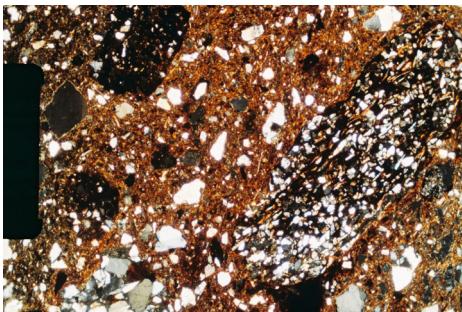


Fig. 7 Sample 12 – Semifine to coarse ceramics with microcrystalline - amorphous matrix; quartzite lithoclasts, ceramoclasts, quartz and micas; N+, scale bar = 0.5 mm

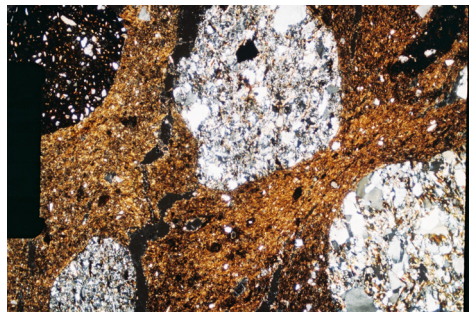


Fig. 8 Sample 16 – Semifine to coarse ceramics with microcrystalline - amorphous matrix; micaschist lithoclasts and ceramoclasts; N+, scale bar = 0.5 mm

X-Ray diffraction

The mineralogical composition obtained by means of X-Ray diffraction (XRD) is relatively simple: it confirms the microscopic observations (Figs. 9 and 10). Due to the ubiquitous presence of quartz and quartzite clasts that dominate the XRD patterns, the presence of the other minerals is hard to be evidenced. However, besides quartz the following minerals could be easily identified: feldspars (albite–anorthite), illite, and muscovite. Montmorillonite–chlorite interstratifications are present only in samples 2 and 8. Calcite peaks were best observed in samples 1, 2, 4, 5, 10 and 17. Iron oxo-hydroxides (hematite, goethite) peaks are partly covered by those of phyllosilicates (illite, muscovite).

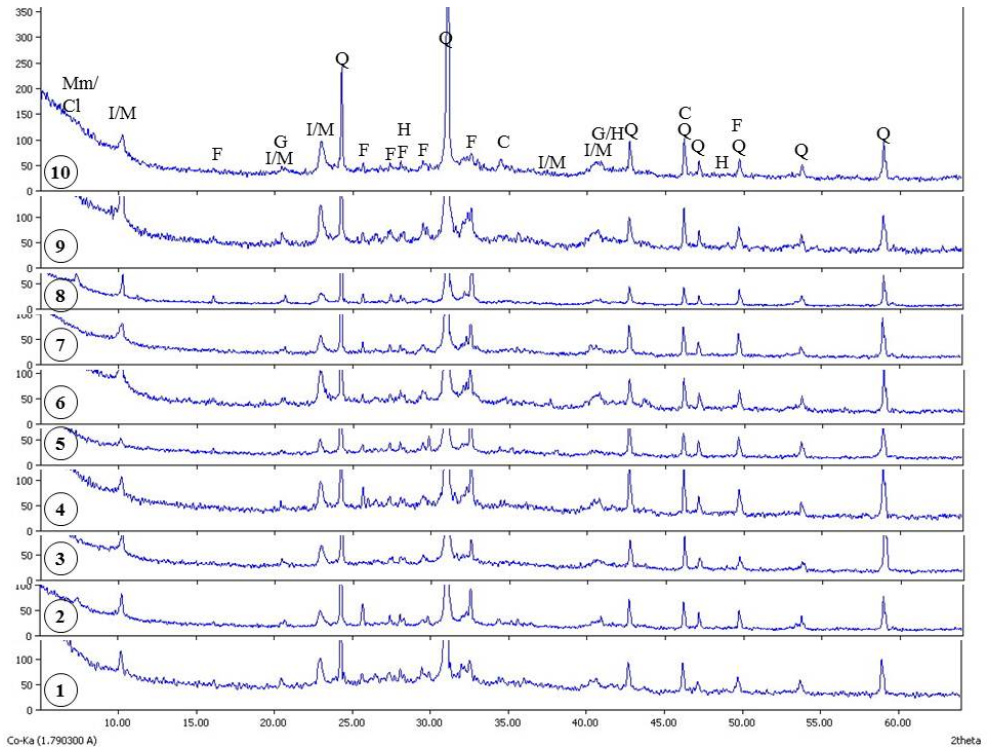


Figure 9. XRD patterns of the studied ceramic fragments; sample no. is indicated in the lower left corner; Q – quartz, F – feldspars (Ca–Na), I/M – illite/muscovite, C – calcite, Mm/Cl – montmorillonite/chlorite, H – hematite, G – goethite.

PRELIMINARY DATA ON BRONZE AGE POTTERY FROM SĂVEȘTI (NEAMȚ COUNTY, ROMANIA)

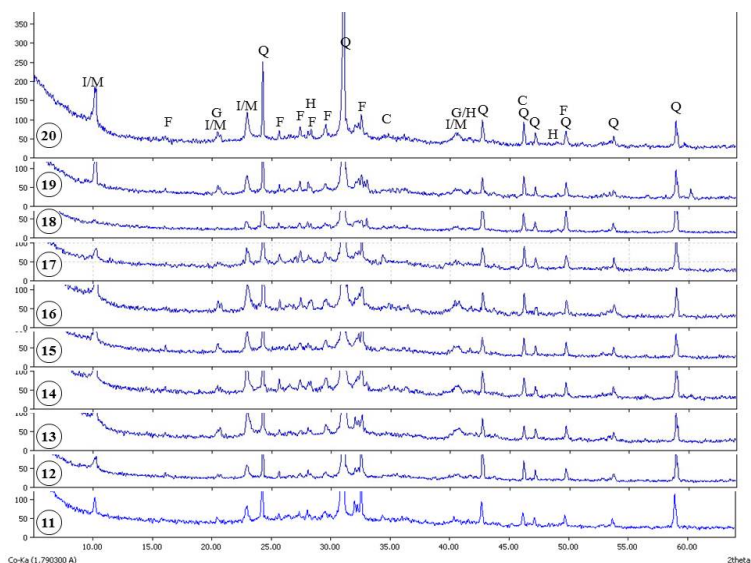


Figure 10. XRD patterns of the studied ceramic fragments; sample no. is indicated in the lower left corner; Q – quartz, F – feldspars (Ca-Na), I/M – illite/muscovite, C – calcite, H – hematite, G – goethite.

Physical characteristics

In order to observe the variability of the compaction degree in each ceramic fragment, three samples from each potsherd were analysed. The values of the physical characteristics are presented in Table 1, where water absorption ranges from 7.17 % to 14.44 %.

Table 1. Compactness characteristics of some of the studied ceramic samples

Sample no.	Apparent density [g/cm ³]	Water absorption [%]	Apparent porosity [%]
1	1.89	10.46	19.82
3	1.87	10.84	20.32
4	1.86	12.00	22.41
5	1.93	11.76	22.74
6	2.00	7.17	14.37
7	1.97	9.47	18.72
8	1.96	10.28	20.15
10	1.99	7.46	14.85
11	1.83	9.79	17.95
15	1.84	12.35	22.73
17	1.93	9.99	19.30
20	1.81	14.44	26.18

For the rest of the analysed potsherds, the obtained water absorption values vary significantly. The variability of physical parameters even in the case of the same ceramic sherd can arise from several causes: (1) thickness of the ceramic body, (2) inhomogeneity of the material (the raw materials mixture), (3) variable temperatures of firing/unequable flames formed in different parts of the kiln, (4) the „sandwich” structure of the sherd revealing oxidizing/reducing atmosphere, (5) the fine fissures in quartz and quartzite clasts as a consequence of firing. These, together with the presence of fissures and pores resulted from processing, lead to variations of the physical parameters.

CONCLUSIONS

The grey- to black colours of most of the studied potsherds suggest reducing firing conditions for this type of pottery. The rare samples showing exceptionally brownish-yellowish hues (e.g., sample 8) point to oxidizing conditions, i.e. a better control during the firing. This latter case is suggested also by samples 2, 12 and 19 displaying a “sandwich”-type structure. The thin (often < 1 mm-thick) rim at the outer surface of the potsherds may be the result of both *in situ* weathering and a change in the firing regime.

The porosity features, marked by the presence of mainly elongated primary pores displayed parallel to the surface of the shard, and of irregular secondary pores indicate that this ceramics was obtained by plastic shaping. The ceramic shows a relatively high compaction degree, with the water absorption values ranging between 7.17 % and 14.44 %.

Based on the grain-size, two types of ceramics can be separated: semifine (lutitic-siltic-arenitic) and coarse (lutitic-arenitic-siltic) ceramics. The ratio between crystalline vs. amorphous phases defines the ceramic's fabric: microcrystalline-amorphous and amorphous-microcrystalline to amorphous. The typical features of the matrix and its low birefringence indicate that the main clay minerals are the kaolinite/montmorillonite interstratifications and subordinate illite.

The crystalloclasts are represented by quartz (from subangular to rounded, and with various degrees of fissuring), micas (often muscovite and rarely biotite), hematite aggregates and subordinately plagioclase feldspars, epidote and zircon. The lithoclasts consist of quartzites, micaschists and gneisses. Additionally, ceramoclasts were noticed in all the studied samples.

The corroborated macro- and microscopic results point to a firing temperature between 850°-900°C.

Concerning the source of the raw materials, we can only make assumptions based on our mineralogical-petrographical results and the information in the geological references [16, 17, 18, 19]. The sites where the potsherds were collected are located in the foredeep eastwards from the Eastern Carpathians border. Westwards, six tectonic napes build-up the Moldavides tectonic unit (from west to east): Teleajen, Macla, Audia, Tarcău, Vrancea and Peri-carpathian. They represent the East-Carpathian flysch unit represented by a succession of Cretaceous to Lower Miocene deposits. Among the sedimentary flysch formations it is worthy to mention the marls, clays, sands and various typed of quartzitic sandstones with lithic fragments (quartzites, micaschists, gneisses) (e.g., Tarcău sandstone, Kliwa sandstone). Thus, the non-plastic raw materials that could have been used as ceramic flux are omnipresent in the alluvia of the rivers (usually having their sources in the west of the region) that flow into the Moldova River (eastwards).

The presence of the quartz, feldspar and micas crystalloclasts and of the lithoclasts (mainly represented by quartzites) supports the hypothesis of local raw materials for the studied ceramics.

The grey to black colour of most of the potsherds pointing to reducing conditions during firing, as well as the relatively low and very diverse compaction values within the same sherd plead additionally for a local ceramic industry.

EXPERIMENTAL SECTION

The macroscopic investigation was performed by using a Nikon SMZ 645 binocular. The microscopic study was performed on thin sections ($< 25 \mu\text{m}$) in polarized light by using a Nikon Eclipse E200 microscope. The microphotographs were taken with a NIKON FDX-35 camera.

The XRD patterns were obtained with a Bruker D8 Advance (Bragg-Brentano geometry) diffractometer, with Co anticathode (Co-K_α , $\lambda_{\text{Co}} = 1.79026 \text{ \AA}$), 35kV, 40 mA, in the 5° – 65° 2θ interval, $\Delta 2\theta = 0.02^\circ$.

The physical characteristics (apparent density, water absorption, apparent porosity) were measured after water saturation, by boiling of the ceramic fragments. From every ceramic sample three fragments were collected for physical characterization.

ACKNOWLEDGEMENTS

The study was supported by PN-II-ID-PCE-2011-3-0881 project funds (UEFISCDI-CNCS/Romanian Ministry of Education). Many thanks are due to Reader Dr. Maria Gorea for the physical characteristics determination and to Dr. Dana Lüttge for the revision of the English version.

REFERENCES

- [1]. W. Noll, "Alte Keramiken und ihre Pigmente. Studien zu Material und Technologie", E. Schweitzerbart'sche Verlagsbuchhandlung, Stuttgart, **1991**, 334 p.
- [2]. M. Benea, M. Gorea, N. Har, *Rom. J. Materials*, **2007**, 37(3), 219-228.
- [3]. M. Gorea, R. Creț, F. Kristaly, *Studia Universitatis Babeș-Bolyai, Chemia*, **2011**, LVI (4), 97-106.
- [4]. M. Benea, M. Gorea, N. Har, *Studia Universitatis Babeș-Bolyai, Chemia*, **2013**, LVIII (4), 147-159.
- [5]. B.P. Niculică, V. Vasilache, D. Boghian, I. Sandu, An archaeometric study of several ceramic fragments from the Komariv (Komarow) settlement of Adâncata-Sub Pădure, Suceava County, in V. Cotiugă (ed.), Third Arheoinvest Congress. Interdisciplinary Research in Archaeology, June 6th–8th 2013, Iași, Romania, Programme and abstracts, Ed. Universității „Al. I. Cuza”, Iași, **2013**, 68-69.
- [6]. N. Bolohan, *Studia Antiqua et Archaeologica*, **2013a**, XIX, 199-239.
- [7]. N. Bolohan, On Clay and Pots in the Middle Bronze Age. A Case Study from Siliștea-Pe Cetățuie, Neamț County. In: B. Rezi, R. Németh, S. Berecki (eds.), "Bronze Age crafts and craftsman in the Carpathian Basin". Proceedings of the International Colloquium from Târgu Mureș, 5-7 October 2012, Ed. Mega, Târgu Mureș, **2013b**, 33-56.
- [8]. Gh. Dumitroaia, *Memoria Antiquitatis*, **1992a**, XVIII, 63-143.
- [9]. Gh. Dumitroaia, *Carpica*, **1992b**, XXIII, 119-141.
- [10]. V. Diaconu, *Cercetări istorice* (S.N.), **2011**, XXVII-XXIX (2008-2010), 45-66.
- [11]. O. Weller, R. Brigand, M. Alexianu, *Memoria Antiquitatis*, **2007**, XXIV, 121-190.
- [12]. A. C. Florescu, *Arheologia Moldovei*, **1964**, II-III, 143-216.
- [13]. C. Ionescu, L. Ghergari, *Cercetări arheologice*, **2006**, XIII, 451-460.
- [14]. C. Ionescu, L. Ghergari, O. Țentea, *Cercetări arheologice*, **2006**, XIII, 413-436.
- [15]. C. Ionescu, L. Ghergari, Caracteristici mineralogice și petrografice ale ceramicii romane din Napoca. In: V. Rusu-Bolindeț, "Ceramica romană de la Napoca. Contribuții la studiul ceramicii din Dacia romană," Bibliotheca Musei Napocensis, XXV, Editura Mega, Cluj-Napoca, **2007**, 434-462.
- [16]. D. Bădescu, "Tectono-stratigraphic evolution of the Eastern Carpathians during Mesozoic and Cenozoic", Ed. Economică, București, **2005**, 312 p. (in Romanian)
- [17]. V. Mutihac, M.I. Stratulat, R.M. Fechet, "Geologia României", Ed. Did. și Ped., București, **2007**, 249 p. (in Romanian)
- [18]. M. Săndulescu, *Rom. J. of Tectonics and Regional Geology*, **1994**, 2, 3–16.
- [19]. *** Geological Map of Romania, 1:200.000, Piatra Neamț Sheet, Geological Institute, Bucharest, **1968**.

PHYSICO-CHEMICAL CHARACTERIZATION OF SPRING AND SALT LAKES FROM SOMESENI TURENI (CLUJ COUNTY)

ANDREEA BRAȘOVAN^a, RAMONA FLAVIA CÂMPEAN^b,
NELI KINGA OLAH^{c,b}, CLAUDIU MORGOVAN^c,
CARMEN POPESCU^c, PAUL ATYIM^c

ABSTRACT. The study refers to the analysis of the chemical composition of water samples from Pata Rât salt lake and salty spring from Micești. The physical and mineralogical characteristics of water and sludge specific of Pata Rât lake are suitable to be used in alternative treatments for rheumatism, skin peeling treatments and skin SPA therapy. The difference in salt crystallization in homogeneous and heterogeneous conditions was evaluated by using a model of salt crystallization in homogeneous conditions. The optical mineralogical micro-photographs in polarized light of the water samples are providing information about heterogeneous crystallization of salt. The mineralogical composition of the water sample was determined by X-ray diffraction and the following minerals were determined: quartz, calcite, lepidolite and kaolinite. By colorimetry were determined the physico-chemical properties of salty water. It was determined also the pH and the conductivity.

Keywords: *salty natural water, pH, conductivity, microscopy, X ray diffraction.*

INTRODUCTION

The salt deposits from Transylvania are the purest in the world, they are made by massive blocks of sodium chloride, crystallized in simple cubic system in the form of halite [1]. They were formed by lowering the water level

^a Babeș-Bolyai University, 1, Kogălniceanu Street, 400084, Cluj-Napoca

^b SC PlantExtrakt SRL, 407059 Rădaia.

^c "Vasile Goldis" Western University of Arad, Faculty of Medicine, Pharmacy and Dental Medicine, 86 Rebreanu Street, Arad, Romania

* Correspondent authors: olahdr@aol.com, rramona_c@yahoo.com, claudiumorgovan@yahoo.com, carmen_popescu@yahoo.com

of the Paratethys Sea in the Badenian, from the Middle Miocene era [2]. The sediments cover the thick layer of salt, which sometimes permeate the earth's surface in the form of mushrooms, which were later exploited (mines), or in the form of salty springs due to water sources which dissolve the salt [4]. The most representatives deposits are located along the Sovata-Praid and Cojocna-Turda line [3]. The presence of salt deposits influences considerably the topography and the stability of the targeted areas. They reported significant ground movements due to rapid change of salt deposits conformation affecting the railway embankment Apahida-Câmpia Turzii, Cluj County [4].

In Micești area, to Deleni and Tureni, the deep waters dissolved the salt and permeated the limestone, bringing at the surface layer of salty springs, the place being actually called "Valea Mărtoare".

The sodium chloride is a salt soluble in water. So the presence of fresh water springs in the proximity of a massive salt underground will lead to its gradual dissolution and in the formation of salty springs, such as those at Micești. Considering that specifically Badenian formations which cover the salt deposits are from limestone rock mixed with sandy quartz conglomerate and with a soil layer of clay structure [5], the dissolution of the salt appears as a cavity, proportional to the volume that causes the crumbling of this friable formations. In such cases, salt lakes have varied diameters and depths, depending on the areas conformation and on the water's flow rate.

This paper presents the evaluation of the mineralogical and the chemical composition of two natural water sources: salty spring from Micești respectively the Pata Rât salt lake.

RESULTS AND DISCUSSION

After performing the physico-chemical determinations on salt water samples were obtained the results shown in Table 1.

Table 1. The chemical composition and some physical properties of water samples from Pata Rât salt lake and salty spring from Micești

The property	Pata Rât salt lake*			Salty spring from Micești*
	Surface	10 cm	20 cm	
pH	7,04	7,06	7,21	6,05
Conductivity mS/cm	225,5	221,1	217,4	236
Chlorine, mg/L	<LOD	<LOD	<LOD	<LOD
Nitrites, mg/L	<LOD	<LOD	<LOD	<LOD
Sulphates, mg/L	101,2	100,8	100,5	200
Nitrates, mg/L	<LOD	<LOD	<LOD	<LOD
Iron, mg/L	<LOD	<LOD	<LOD	<LOD

Chlorides , mg/L	601,7	600,4	600,1	300
Hardness, German degrees mg/L CaCO ₃	25,8	25,5	25,3	450
Ammonium, mg/L	<LOD	<LOD	<LOD	<LOD
Lead, µg/L	<LOD	<LOD	<LOD	<LOD

* All determined values are the mean of 3 determinations.

The presence of suspensions in water can significantly affect its properties. One of the most important physical property is the conductivity, which is very high because of the huge quantities of dissolved sodium chloride. On the surface it is around 225,5 mS/cm at Pata Rât and 235,9 mS/cm at Miceşti. Not at least, the pH is a very important for the water characterization.

The salty water contains dissolved salts, ions: hardness due by Ca and Mg carbonates, chlorine, chlorides, sulphates, nitrates, ammonium, iron and lead. The hardness is a summ of the dissolved salts in the water, particularly slowly soluble such as carbonates. In this way both the adjacent soil and mineral particles in direct contact with salty water can affect in some ways the water hardness.

The increased hardness value obtained in the sample from Miceşti, proves that it has a higher hardness than the salt water from the lake. This can be explained by the structure of the adjacent soil.

An important physico-chemical property for water is the residual chlorine. These waters are natural and untreated in processing stations of water, so it is normal to be free of residual chlorine.

The content of chloride is given mainly by the dissolved halite. The presence of other ions is given by the minerals found in rocks structures adjacent to salts deposits. The chlorides content of the water samples shows values between 300 and 600 mg/l, given by the very rich content of sodium chloride. The obtained values show that the brine was formed in depth in the salt deposit and its concentration is not affected by the presence or the absence of mineral particles from the soil surface.

The sulphates content of water samples investigated presents a variation of 100-200 mg/l for each sample.

The nitrites content, ammonium, iron and lead is below to the detection limit of the used tests kits. You can say that they are missing from the salted water from Pata Rât lake and salty spring from Miceşti. That is likely to confirm the special origin of salted water from the investigated area.

By comparing the physico-chemical parameters of the Mierlei lake at different depths, more precisely at 10, 20, 40, 80 cm, with those of Pata Rât lake and the salty spring of Miceşti, the values are almost the same but with small variations. The pH value varies between 8,14 and 7,26. The conductivity value varies between 33,9 and 215,8 mS/cm.[10]

In order to see the difference of salt crystallization in homogeneous and heterogeneous conditions, it was performed a model of salt crystallization in homogeneous conditions [3]. Based on the FCC cell unit, in Figure 1 are shown the most important directions and their corresponding crystallographic planes, that are able to help the ideal salt crystal growth.

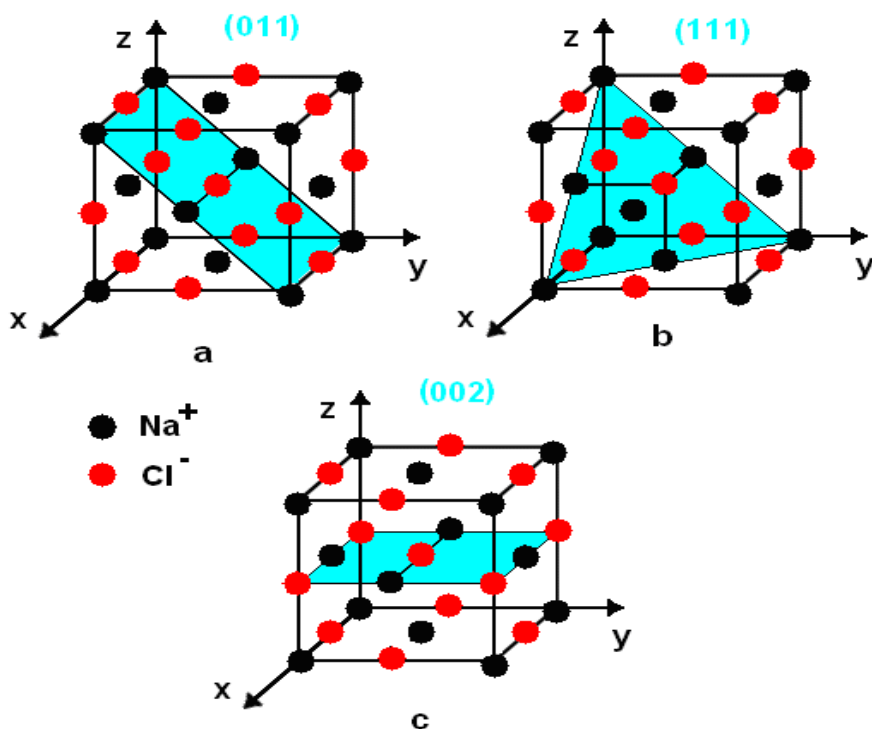


Figure 1. The evidence of crystallographic planes on the halite elementary cells. The crystallographic planes: a) $\{110\}$, b) $\{111\}$, and c) $\{200\}$.

The halite crystals have a complex cubic centered face (FCC) consisting of two cubic faces of Na⁺ and Cl⁻ ions overlaid, centering each the other face [6,3]. Considering the side of halite crystal FCC, here they are the following crystallographic planes, described by Miller indices [6]: $\{111\}$, $\{200\}$, $\{220\}$, $\{311\}$, $\{222\}$, $\{400\}$, $\{331\}$, $\{420\}$, și $\{422\}$ [2].

Figure 2 presents the microstructure of water sample taken from the surface of Pata Rât salt lake. It is observed the well-developed salt crystals after the crystallographic directions $\{110\}$ and $\{200\}$ accompanied by material particles of mineral origin [9].

The optical mineralogical micrography were not revealed significant differences for Pata Rât salt lake and the salty spring from Micești.

The mode of their crystallization is approaching ideal conditions, defects of packing of formed crystals not being visible. In polarized light, in Figure 4b, the salt crystals appear blue translucent on the dark background. Small, interesting inclusions are appearing, intercrystalline tabulated in blue light, which are not distinct on the observation in transmitted light. The situation was not observed in water samples taken in „static” conditions. This leads to the conclusion of the possible inclusion of calcium sulphate, which have been reported in the scientific literature as the accompanying of the Badenian salt [7]. The calcium sulphate can crystallize in two allotropics forms [6] of gypsum, forming filiform prismatic crystals, with shiny white appearance in polarized light with crossed nicols, and the anhydrite which form blue-violet tabular-lamellar crystals in polarized light with crossed nicols. Therefore, those observed in Figure 4b, could be traces of the anhydrite as inclusions, inside the halite crystals.

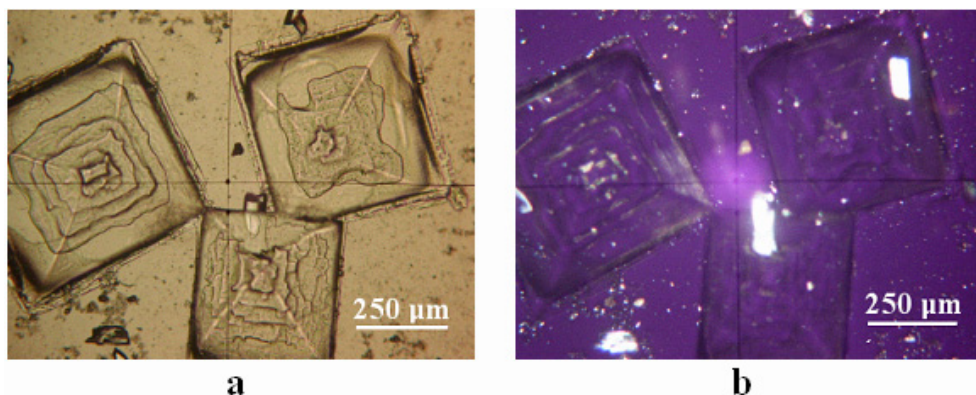


Figure 2. The optical mineralogical microphotographs:
a) in transmitted light and b) in polarized light with crossed nicols

The mineralogical composition of water samples were determined by X-ray diffraction. The resulting diffractograms are shown in Figure 3. It is observed very slender maximums and well developed for the halite, corresponding to planes {200} and {400}.

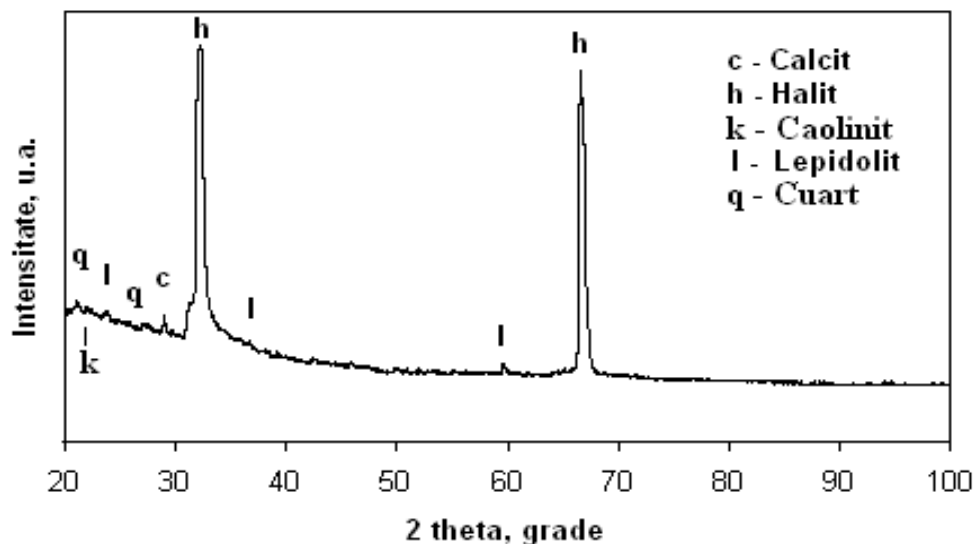


Figure 3. The salt water sample diffractogram.

The X-ray diffraction analysis of water samples have not revealed significant differences for the Pata Rât salt lake and salty spring from Micești.

The minerals found as solid particles, dispersed in water sample, present relatively small maximums in relation to the intensity of those for halite, fact in full compliance with microscopic observations. It was identified a certain maximum for quartz, calcite, lepidolite and kaolinite. These are suitable with those observed in the composition of adjacent lake soil and certifies their origin from the surface layers. The presence of these minerals dispersed in water sample did not interfere much with the halite crystal formation, demonstrated clearly in the microscopic observation.

At 10 cm depth, the density of mineral particles dispersed in unit volume increases, as shown in Figure 4a. It shows a salt crystal formed after direction {200} almost visible with the eye (about 1 mm) surrounded by mineral particles from aqueous suspension (calcite, quartz, very fine particles of lepidolite, kaolinite). That corresponds to a heterogeneous germination promoted by solid inclusions dispersed in the saline solution. In figure 4b can be observed no less than three intercrystallins inclusions of anhydrite and an anhydrite crystal formed at the halite crystal limit.

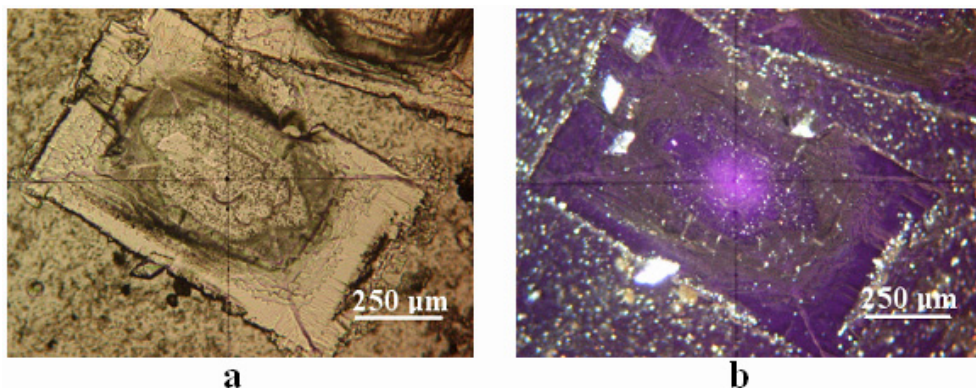


Figure 4. The optical mineralogical microphotographs for water sample from 10 cm depth: a) in transmitted light and b) in polarized light with crossed nicols

The X-ray diffraction analysis (Figure 5) shows well-developed maximums of halite corresponding to the crystallographic planes {200} and {400} for the water sample from 10 cm depth. The situation is somewhat similar with that of the surface sample, but the specific maximums of minerals dispersed from the sample, are considerably more intense, which confirms their high proliferation in unit volume of water sample. There were identified quartz, calcite, lepidolite and kaolinite [8].

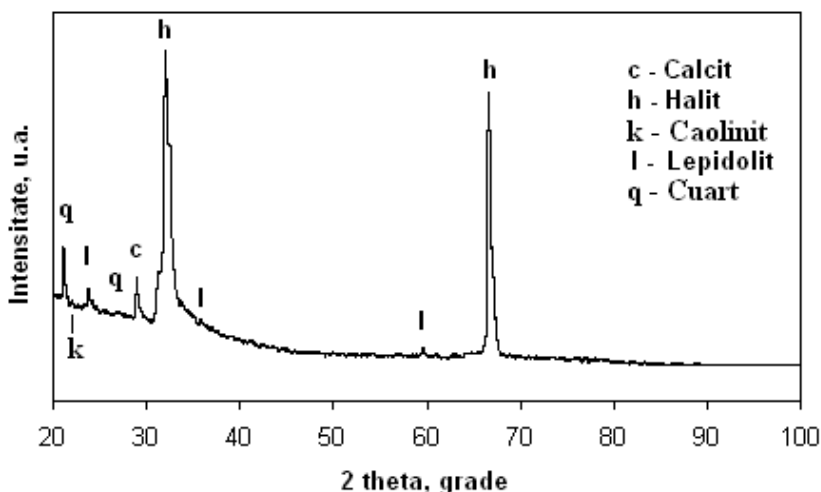


Figure 5. The sample diffractogram at 10 cm depth.

CONCLUSIONS

From the investigation results that the interrelationship soil-water-salt deposits demonstrates the formation of salt lakes in the Transylvanian Basin. The performed analysis shows a high solubility of sodium chloride in water, forming rapidly a saturated solution in contact with the underground salt. It is noted that the evaporation of water from such a natural brine, leads to the formation of microscopic crystals of halite. That in itself has a relative importance when it is separately evaluated, extremely useful mining method „Solvay”, where the salt is extracted by means of a saturated brine.

In the case of Pata Rât salt lake and the salty spring from Micești, it is revealed the close relationship between salt massive and the sediments above them, mediated by the presence of springs and deep water layers. The performed analysis revealed in these salty water sources, significant amounts of calcite embankment and mixed with large clay deposits and sandy-loamy deposits (kaolinite, lepidolite mixed with quartz and/or calcite sand).

Because of the lack of information regarding to these natural water sources from Cluj county region the results presented in this paper could have relevance for the future exploitation of these natural resources of very high purity waters. The physical-mineralogical characteristics of water samples and sludge samples adjacent to the Pata Rât salt lake, could be suitable for the use in alternative treatments of rheumatism, skin exfoliation treatments, SPA therapy for skin and beneficial for the osteoarticular system.

EXPERIMENTAL SECTION

In the current study there were collected 4 water samples, a sample from the salty spring from Micești and three samples from Pata Rât lake, from different depths (surface, 10 cm and 20 cm). The water samples were preserved at cold and the physico-chemical analysis were performed in the same day with the sampling.

The determination of the residual chlorine, chlorides, nitrites, nitrates, iron, lead, sulphates, ammonia, total hardness was performed by colorimetric methods using different reagents. The analyses were performed with Spectroquant ready to use reagents and the colorations were quantified with a Spectroquant photometer Nova60.

The nitrites in acidic solution react with sulfanilic acid to form a diazonium salt, which then reacts with N-(1-naphthyl) ethylenediamine dihydrochloride to form a red-violet azo dye, determined colorimetric.

The nitrates are reduced to nitrite ions that react in acidic solution with 2,6-dimethylphenol to form 4-nitro-2,6-dimethylphenol.

The lead in alkaline solution reacts with 4-(2'-pyridylazo)resorcinol to form a red complex.

The ammonium reacts with Neßler's reagent in order to form a yellow-brown compound.

The iron (III) ions are reduced to iron (II) ions that reacts with a triazine derivatives in order to form a red-violet complex.

The total hardness: in the presence of a green indicator the Ca^{2+} and Mg^{2+} ions react with Titriplex III in order to form a colorless, stable complex. The hardness ions that are present in excess relatively to Titriplex III react with the indicator in order to form a red complex.

The sulphates react with a red thorium-barium complex, releasing yellow thorium compound.

The chlorides react with silver ions, decolorizing the red-brown silver chromate.

The chlorine oxidizes the dipropyl-p-phenylenediamine to a red-violet dye.

The conductivity and pH were measured with HI 255 Combined Meter & EC/TDS/NaCl Hanna Instruments.

There were determined in the salty waters the mineralogical composition by X-ray diffraction and the salt crystallisation. For each water sample were prepared slides for microscopic investigation and X-ray diffraction analysis.

The X-ray diffraction analyses were performed using a DRON 3 diffractometer equipped with data acquisition module and Matmec V1.0 software. The mineral identification from the resulted X - ray diffraction patterns was done using MATCH 1.0 X – ray diffraction database powered by Crystal Impact Company.

The morphology outline was investigated by a dark field optical microscopy on a IOR 8 microscope. The quantitative measurement on the microphotographs was done using the Image J Processing soft.

The cross polarized light microphotographs were done on a mineralogical Laboval 2 Karl Zeiss Jena mineralogical microscope. The digital capture used for all microscopy investigation was done with a Samsung 8 MPx camera.

REFERENCES

- [1]. N. Har, O. Rusz, V. Codrea, O. Barbu, *Carpathian Journal of Earth and Environmental Sciences, Baia Mare*, **2010**, 5, 2, 127-135.
- [2]. M. Peryt, *Sedimentary Geology*, **2006**, 188–189, 379–396.

- [3]. I. Chicinaș, N. Jumate, V. Pop, „Fizica materialelor metode experimentale”, Presa Universitară Clujeană, Cluj Napoca, **2001**, 325.
- [4]. E. Constantinescu, L. Matei, „Mineralogie determinativă”, Ed. Universitatii din Bucuresti, Bucuresti, **1996**.
- [5]. Cs. Krézsek, (PhD thesis), Babeș-Bolyai University, Cluj-Napoca, Romania, **2005**, 166.
- [6]. G. Arghir, L.M. Gherghari, „Cristalografie Mineralogie. Îndrumător de lucrări de laborator”, Litografia IPC – N, **1989**, 371.
- [7]. E. Gergely, „Tureni, studiu monographic”, Ed. Casa Cărții de Știință, Cluj-Napoca, **2002**, 220.
- [8]. N. Cianga, D. Costea, „Journal: Aerul și Apa: Componente ale Mediului”, Cluj University Press, **2011**, 185-191.
- [9]. I. Petean, G. Arghir, R.F. Câmpean, M. Bărăian, Al. Gertrud Hosu Prack, *Acta Technica Napocensis Series: Matematica Aplicata si Mecanica*, **2011**, 54 (I), 193 – 200.
- [10]. S. Crognale, I. Máthé, V. Cardone, S.R. Stazi, B. Ráduly, *Geomicrobiology Journal*, **2013**, 30, 9.

FOOTPRINT AND DIRECT IMPACT OF ANTHROPOGENIC ACTIVITIES ON GROUNDWATERS FROM MEDIAS AREA

MARIA-ALEXANDRA HOAGHIA^{a,b,*}, CECILIA ROMAN^a,
ERIKA ANDREA LEVEL^a, DUMITRU RISTOIU^b

ABSTRACT. Groundwater represents an important and direct source of fresh water, vulnerable to contamination. Groundwater composition is easily influenced by anthropogenic activities. Lack of sewerage facilities impress direct footprint on groundwater composition. Nitrogen compounds (NO_2^- , NO_3^- , NH_4^+), SO_4^{2-} , K^+ , Cl^- , Mg^{2+} , Ca^{2+} , Na^+ , pH and total dissolved solids were analysed from seven well waters from Medias area. The results showed the seasonal variation of analysed parameters, the nitrogen compounds, K^+ and Ca^{2+} exceeding the maximum admissible concentration in the majority of samples. The Stiff and Piper diagrams confirmed that the studied waters are Ca-HCO_3 type and have the same sources.

Keywords: groundwater, anthropogenic activity, chemical composition, Piper diagram, Stiff diagram

INTRODUCTION

Groundwater constitutes the largest fresh water reservoir (97%), while surface waters represent the other 3% of the freshwater sources [1].

Groundwater is a natural and free resource directly used by the inhabitants from areas where water from wells is used as freshwater source. Worldwide, natural and anthropogenic activities may influence the groundwater composition, altering its quality [2-4]. Pressure on groundwater quality and quantity exists also in the EU. Footprint and direct impact of anthropogenic activities on the groundwater quality were determined all over the world [5-7]. Abundant use of pesticides, nitrogen fertilizers, land drainage and land sealing, population density, water abstraction for industrial purposes and for public supply are human interventions with negative effects on groundwater composition and quality [8-11]. In Romania, the main problems are related to contamination of groundwater, with nitrogen

^a INCDO INOE 2000, Research Institute for Analytical Instrumentation, 67 Donath, RO-400293 Cluj-Napoca, Romania

^b Babeş-Bolyai University, Faculty of Environmental Science and Engineering, 30 Fantanele, RO-400294 Cluj-Napoca, Romania

* Corresponding author: alexandra.hoaghia@icia.ro

compounds and organic substances both in rural and urban areas, due to the lack of sewerage facilities and poor agricultural practices [12]. Nitrogen compounds have two main sources: agricultural and non-agricultural. The population density is a variable non-agricultural source of nitrogen compounds in urban areas. Nitrogen compounds loadings are determined by septic systems, animal manure and fertilizers [13-14]. In the Romanian legislation, the threshold values for groundwater are specific for each groundwater body, considering their geological origin [15]. The footprint determination is significant for the establishment of the regional variations.

The aim of this study was to assess the groundwater footprint and direct impact of anthropogenic activities on groundwater as drinking water source (water wells) from Medias area, using samples collected from wells.

RESULTS AND DISCUSSION

The results show significant concentrations of chemical compounds in the studied well waters. High concentrations of nitrogen compounds (NO_2^- , NO_3^- , NH_4^+) and ions (SO_4^{2-} , Cl^- , K^+ , Mg^{2+} , Ca^{2+} , Na^+) and high values of pH and total dissolved solids (TDS) were measured in all samples. Nitrogen compounds, calcium and sulphate concentration exceed the maximum admissible concentrations (MACs) established by the Romanian legislation [16], regarding quality of drinking water (Table 1). Furthermore, potassium concentrations exceed MAC established by World Health Organization [17]. High K^+ and Ca^{2+} concentrations are part of the natural geological matrix.

Table 1. Average composition of the studied waters and maximum admissible concentrations, for drinking and groundwater

Well	pH	TDS	NO_2^-	NO_3^-	NH_4^+	SO_4^{2-}	Cl^-	Mg^{2+}	K^+	Ca^{2+}	Na^+	HCO_3^-
F1	8.5	438	3.2	39	1.4	145	80	27	26	194	136	281
F2	8.4	724	2.4	101	0.5	234	114	34	33	212	82	405
F3	8.3	719	3.4	135	0.7	289	104	28	36	284	83	483
F4	8.2	694	<0.05	260	0.6	239	45	23	34	308	87	519
F5	7.8	478	5.1	229	3.0	58	107	18	13	260	52	249
F6	8.4	551	1.8	160	0.4	197	87	15	13	346	55	433
F7	8.2	655	3.3	202	0.7	277	125	19	100	448	124	571
Maximum Admissible Concentration for drinking water*												
	8.5-9.5	-	0.5	50	0.5	250	250	-	-	200	200	-
Guideline values for drinking water**												
	-	-	3.0	50	-	-	-	200	20	-	-	-
Thresholds for groundwater***												
	-	-	0.5	-	0.8	250	250	-	-	-	-	-

* according to Law 311/2004 [16], ** according to WHO [17], *** according to Ministerial Order 621/2014 [15]

TDS varies during the year (November 2012 – May 2013). In the cold season (December 2012, January and February 2013), TDS levels were constant and high for samples F5 and F7 (415mg/l – 766mg/l), while in the rainy season (November 2012, March, April and May 2013) presents higher concentrations for the same samples (155mg/l – 865mg/l). Similarly, the chloride concentrations were the highest in the rainy season. The sample with the highest chloride concentration is F7 (43mg/l – 125mg/l) while sample F1 (9.3mg/l – 29mg/l) has the lowest values.

The Piper diagram (Figure 1) shows the dispersion of major cations and anions and classified the waters as Ca-HCO₃ type. All water samples are Ca-HCO₃ type. Stiff diagram represents the abundance of ions concentrations and variations between the water wells (Figure 2) and confirmed the fact that the major ions in the studied waters are Ca²⁺ and HCO₃⁻.

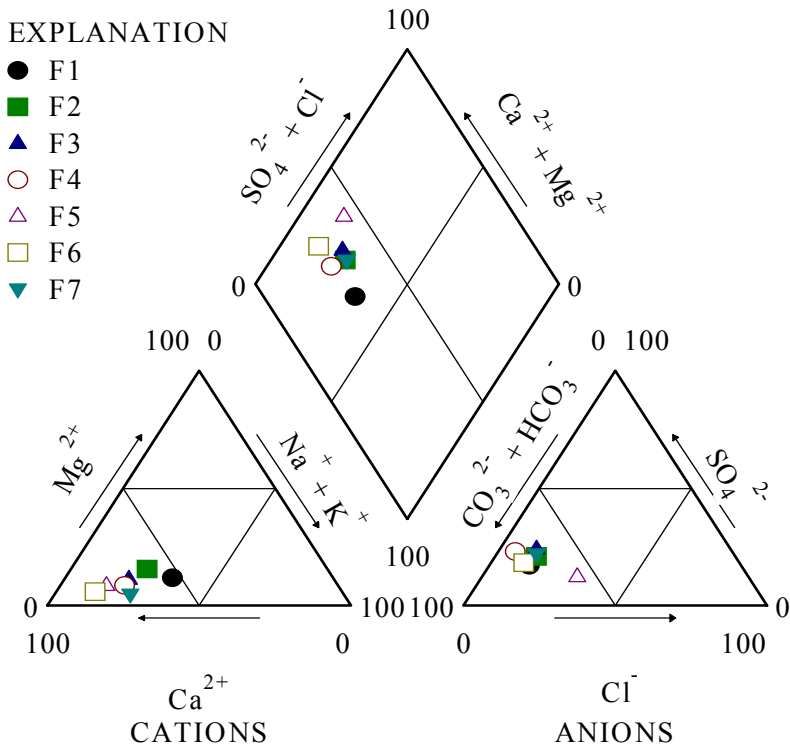


Figure 1. Representation of water types using Piper diagram

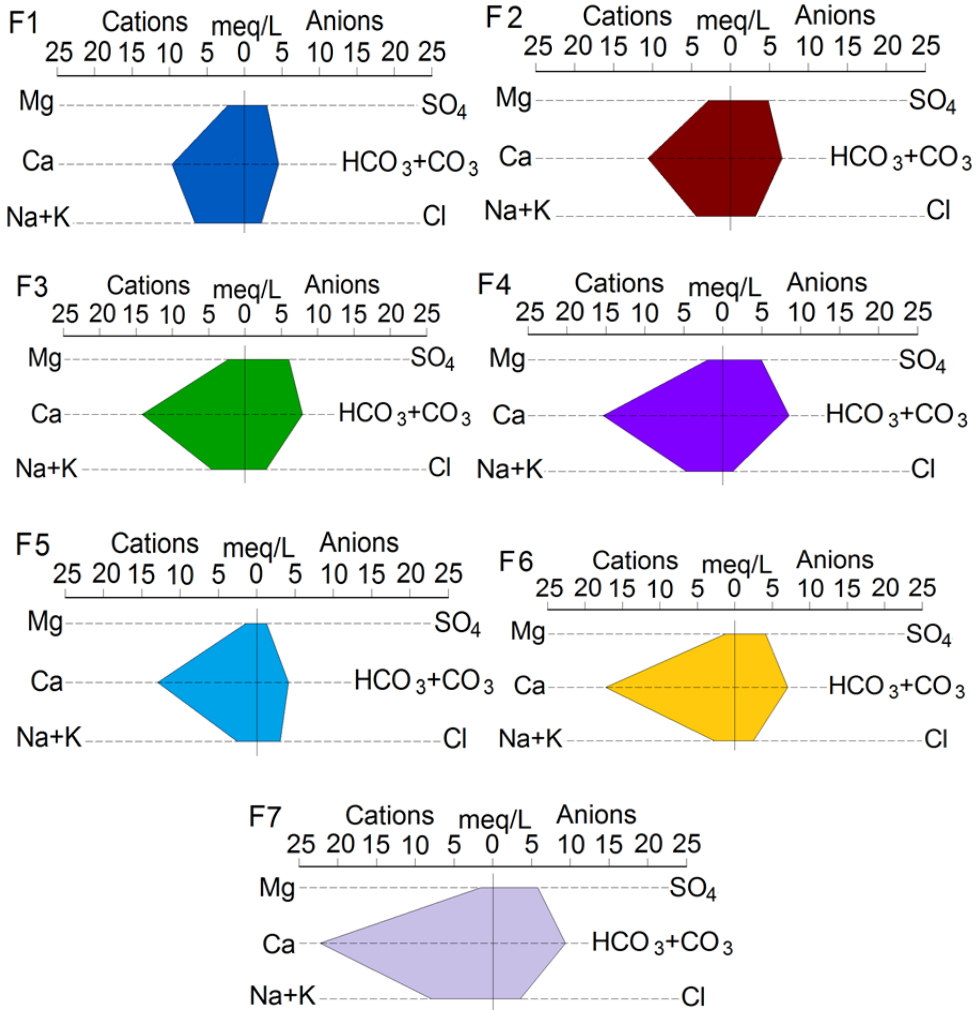


Figure 2. Stiff diagrams of average ions concentrations in wells waters (F1-F7)

Results show high concentrations for NO₂⁻, NO₃⁻ and NH₄⁺. In all samples except F1, the nitrate contents exceeded the MAC (50mg/l). The NO₃⁻ concentrations fluctuated during the year showing higher concentrations in the dry months than in the wetter period (Figure 3). The NO₂⁻ concentrations exceed six times the MAC (0.5mg/l) especially in the rainy period, as shown in Figure 4.

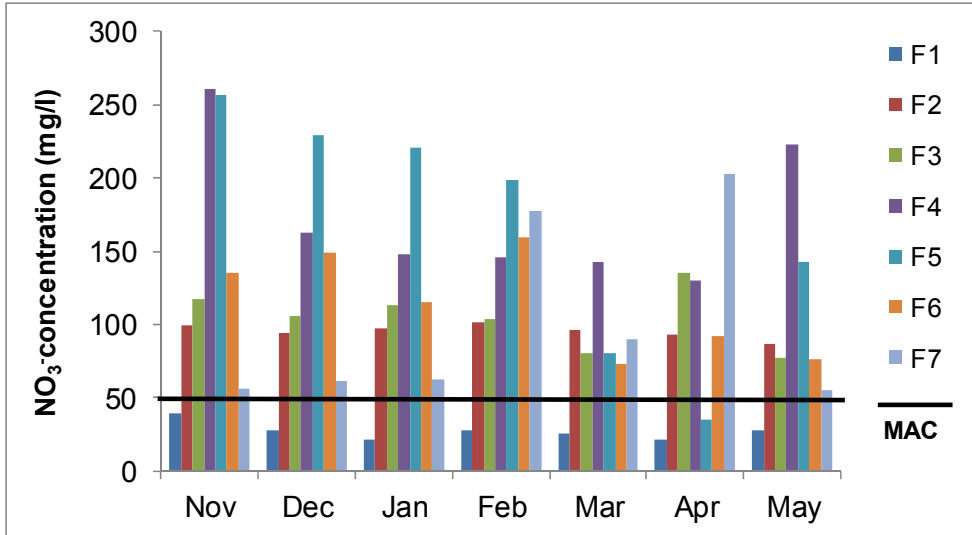


Figure 3. Monthly variation of NO₃⁻ concentration

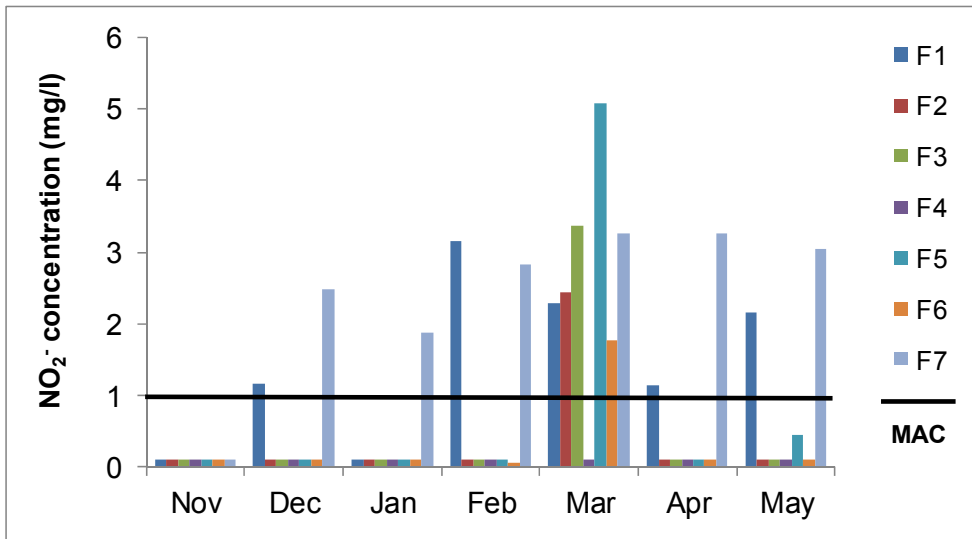


Figure 4. Monthly variation of NO₂⁻ concentration

Highest NO_3^- concentration is observed at sample F4 which is localized near (1m) to a former drain for household wastewater, manure water and rain water. Sample F4 has, also, 2 current toilets localized at 10m upstream. NO_2^- concentration exceeds MAC and reaches the highest concentration for sample F5 which has also the highest concentration for NH_4^+ exceeding MAC. The source of nitrogen compounds is an emptying pool situated at 3m distance, source that influence the pH of groundwater. Furthermore, F5 has the lowest value for pH. Sample F1 has the lowest NO_3^- concentration, but high concentrations for NO_2^- and NH_4^+ . A current toilet is localized at 1.5m upstream from the water well, which means a permanent and continuous supply with nitrogen compounds.

The direct influence of the presented contamination sources can be demonstrated by the parameters variation with the distances between wells and pollution sources. Generally, samples localized very close to the sources have higher concentrations of NO_2^- and NO_3^- compared to those situated at longer distances (Figure 5).

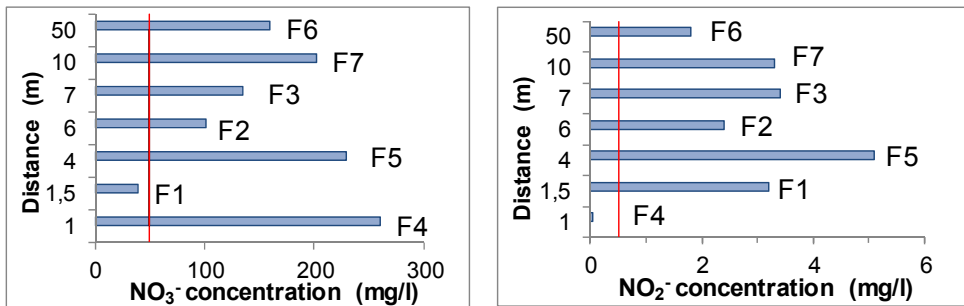


Figure 5. Relation of NO_3^- and NO_2^- concentrations in water with the distance between contamination source and well waters

All seven water wells are localized nearby anthropogenic sources, mostly sewerages. Thence, organic compounds are transferred from anthropogenic sources into the waters. It was observed a decrease of nitrogen compounds concentrations in rainy periods (stormwater dilutes the nitrogen compounds). The nitrogen compounds (NO_2^- , NO_3^- and NH_4^+) were identified in all samples, which imply the nitrogen transformations (nitrogen cycle: nitrification and denitrification).

CONCLUSIONS

Water wells from Medias area present high concentrations of nitrogen compounds (NO_2^- , NO_3^- , NH_4^+), that exceed the corresponding MACs [16-17]. Nitrogen compounds concentration varied during the sampling period (dry and rainy season). Sources for NO_2^- , NO_3^- , NH_4^+ are dry toilets, emptying pool, former stables, manure and straw stores localized at very short distances (5-10m) from water wells.

The SO_4^{2-} , K^+ and Ca^{2+} concentrations exceeded the MACs. Using Piper and Stiff diagrams, all water samples are Ca- HCO_3 type and have the same sources. The Na^+ , K^+ and Ca^{2+} sources are the natural geological matrix.

EXPERIMENTAL SECTION

Description of the study area

Transylvanian town, Medias has about of 44.000 inhabitants and is localized in the central part of the Sibiu County. In Medias area, Miocene and Pliocene sediment deposits are the main geological formations. Sediment deposits are represented by sands that interlaid with grey marls, soft limestone and andesite tuffs. Medium hills (450-600m) with horizontal fragmentation less pronounced and smooth cliffs surround the city that is crossed from West to East by Tarnava Mare River. Annual temperature mean is 8 °C and the mean annual rainfall is higher than 600mm [18].

Water-bearing has a depth of 1.2-10m, with flow rates ranging from 0.2-8m/s. High hill areas are characterized with 5-10m depth aquifers and meadow hill areas with 5m depth aquifers. Between 250-300m bedding depth water bed has been found, but only in the sediment areas [19].

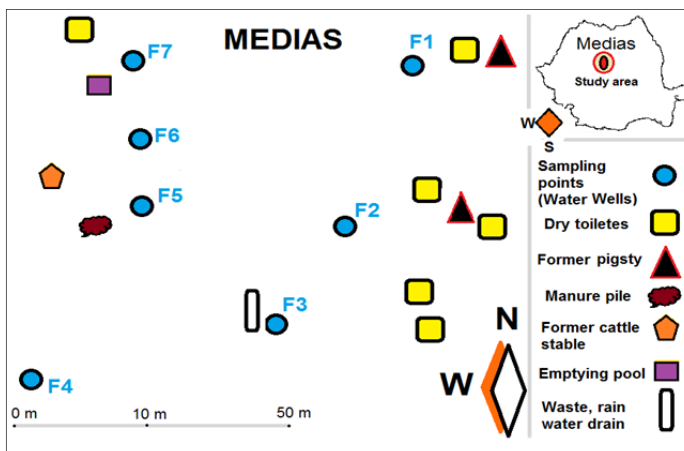


Figure 6. Sampling points and contamination sources

Seven private water wells from an old residential district inhabited by 13 % of the town's population, where the majority of the inhabitants lives in private houses and use well water as drinking water source were studied (Figure 6). Groundwater from Medias area is part of GWMU05 water body (Tarnava Mare river floodplain and terraces) with specific characteristics: industrial and agricultural pollution; groundwater is used in industrial, animal husbandry fields and for water supply [20].

Table 2. Characteristics for the studied water wells

Well	Distance from contamination sources (m)	Geographical coordinates	Age (years)	Depth (m)	Diameter (m)	Height above ground level (m)
F1	1.5m upstream from is a dry toilet and a former pigsty	46°8'56.34"N 24°22'10.64"E	25	5.0	1.25	0.00
F2	6m from an emptying pool	46°8'56.11"N 24°22'8.62"E	35	5.5	1.25	0.75
F3	6m downstream from a former cattle stable; 7m from a manure pile	46°8'55.35"N 24°22'8.32"E	38	5.0	1.25	1.00
F4	10m upstream from 2 dry toilets; 1m downstream from a former waste water drain	46°8'55.34"N 24°22'9.94"E	38	7.5	0.30	0.40
F5	4m from a dry toilet; 3m from an emptying pool	46°8'56.63"N 24°22'8.51"E	52	7.0	1.25	1.00
F6	50m downstream from a former cattle stable	46°8'54.34"N 24°22'8.28"E	48	4.5	0.40	0.00
F7	5 m upstream from a dry toilet; 10m upstream from a former pigsty and dry toilet	46°8'55.96"N 24°22'10.81"E	42	7.0	1.25	1.00

The studied water wells are at least 50 years old, with depths from 3 to 8m. People use the water from wells for house works, but also for drinking and cooking, although the wells location is nearby dry toilets, tank collectors, faces settlements and animal fenders (Table 2).

Sample collection

Since in the study area there are no other available access points to groundwater we chose as monitoring points the water wells used by locals as drinking water supply, as it reflects the footprint of the groundwater.

Samples were collected monthly between November 2012 and May 2013 (7 sampling campaigns) using hydrophore pump and bucket (for wells that had no hydrophore pump). Water samples were stored in 100ml polyethylene bottles (previously prewashed) and kept at 4 °C in a freezer. Before analysis samples were filtered using a plastic filter unit equipped with a 0.45µm cellulose acetate filter membrane.

Materials and methods

Instrumentation

A WTW 350 *i* Multiparameter was used for the physicochemical parameters (pH and TDS).

Ions (Cl^- , NO_2^- , NO_3^- , SO_4^{2-} , NH_4^+ , Mg^{2+} , Ca^{2+} , Na^+ , K^+) were analysed using ICS 1500 Dionex Ion Chromatography (IC) with suppressed conductivity detection. The instrument has two columns, one for anions determination and one for cations determination. The HCO_3^- content was determined by titration with HCl, against methyl orange indicator.

The abundance of ions in individual water samples, the nature of water wells and the relationships between water samples are presented with the help of two graphical approaches (Piper and Stiff diagrams) using the software GW Chart and AqQa 1.1.

ACKNOWLEDGMENT

This paper is a result of a doctoral research made possible by the financial support of the Sectorial Operational Program for Human Resources Development 2007-2013, co-financed by the European Social Fund, under the project POSDRU/159/1.5/S/133391 - “**Doctoral and postdoctoral excellence programs for training highly qualified human resources for research in the fields of Life Sciences, Environment and Earth**”.

REFERENCES

- [1]. P.H. Gleick, “*Water resources. In Encyclopedia of Climate and Weather, Edition by S. H. Schneider*”, Oxford University Press, New York, **1996**.
- [2]. B.G. Katz, *Encyclopedia of Caves*, **2012**, 2, 564-568.
- [3]. S. Chaudhuri, S. Ale, *Journal of Hydrology*, **2014**, 513, 376-390.
- [4]. A. Jurado, P. Gago-Ferrero, E. Vasquez-Sune, J. Carrera, E. Pujades, M.S. Diaz-Cruz, D. Barcelo, *Journal of Hazardous Materials*, **2014**, 271, 141-149.

- [5]. D. Pokhrel, B.S. Bhandari, T. Viraraghavan, *Environmental International*, **2009**, 35, 157-161.
- [6]. V.A. Nguyen, S. Bang, P.H. Viet, K.W. Kim, *Environmental International*, **2009**, 35, 466-472.
- [7]. P. Yogeshwar, B. Tezkan, M. Israil, M.E. Candansayar, *Journal of Applied Geophysics*, **2012**, 76, 127-135.
- [8]. K. Wick, C. Heumesser, E. Schmid, *Journal of Environmental Management*, **2012**, 111, 178-186.
- [9]. A.S. Nasr, M. Rezaei, M.D. Barmaki, *Geopersia*, **2013**, 3(1), 47-55.
- [10]. H. Gharibi, A.H. Mahvi, R. Nabizadeh, H. Arabalibeik, M. Yunesian, M.H. Sowlat, *Journal of Environmental Management*, **2012**, 112, 87-95.
- [11]. A. Jalgaonkar, *Carpathian Journal of Earth and Environmental Sciences*, **2008**, 1, 39-47.
- [12]. F. Salvagiotti, K.G. Cassman, J.E. Specht, D.T. Walters, A. Weiss, A. Dobermann, *Field Crops Research*, **2008**, 108(1), 1-13.
- [13]. B.T. Nolan, B.C. Ruddy, K.J. Hitt, D.R. Helsel, *Water Conditioning and Purification*, **1998**, 39(12), 76-79.
- [14]. D. Widory, W. Kloppmann, L. Chery, J. Bonnin, H. Rochdi, J.L. Guinamant, *Journal of Contaminant Hydrology*, **2004**, 72, 165-188.
- [15]. * * *, 621 Ministerial Order from 18th July **2014** regarding the approval of threshold values for groundwater from Romania. Official Gazette 2014, Part I, no. 535/18.07.2014 [In Romanian]
- [16]. * * *, 311 Law from 6th June **2004** that improves and complement 458 Law from 29 July **2002** regarding the quality of drinking water. Official Gazette 2004, Part I, no. 582/30.06.2004 [In Romanian].
- [17]. * * *, Guidelines for drinking water quality, Fourth edition, World Health Organization, **2011**. Online source:
http://www.who.int/water_sanitation_health/publications/2011/dwq_guidelines/en/.
- [18]. E.D. Horhoi, "Tarnava Mare channel environmental quality: a geoecological study (Calitatea mediului inconjurator in Culoarul Tarnavei Mari: studiu geoecologic)", Logos 1994 Press, Oradea, **2001**.
- [19]. C. Chira, A. Malacu, *Acta Palaeontologica Romaniaae*, **2008**, 6, 17-28.
- [20]. * * *, Environmental Minister of Romania (EMR), National Administration "Romanian Waters" Water Directorate Mures, "Basin Management Plan Hydrographic Mures" **2009**. Online source:
http://www.rowater.ro/damures/Planul%20de%20Management%20al%20Bazinului%20Hidrografic%20Mure/Planul%20de%20Management%20al%20Bazinului%20Hidrografic%20Mures%20-%202011/Plan%20Management%20BH%20Mures%20-%20vol.%20I_Final_Listare.pdf

PROTEIN-CAPPED GOLD NANOPARTICLES OBTAINED BY A GREEN SYNTHESIS METHOD

CRISTINA COMAN^a, LOREDANA FLORINA LEOPOLD^a,
OLIVIA-DUMITRIȚA RUGINĂ^a, ZORIȚA DIACONEASA^a,
POMPEI FLORIN BOLFĂ^b, NICOLAE LEOPOLD^c,
MARIA TOFANĂ^a, CARMEN SOCACIU^{a*}

ABSTRACT. A green synthesis protocol for the synthesis of colloidal gold nanoparticles is proposed. The synthesis involves the use of garlic (*Allium sativum*) extract as reducing agent. The reduction is carried out by slow addition of the *Allium sativum* extract to the chloroauric acid at boiling and gives spherically shaped nanoparticles, with 10-20 nm size distribution and mean diameters of 15 nm. The gold nanoparticles are characterized by UV-VIS spectroscopy, Fourier Transform Infrared Spectroscopy, Transmission Electron Microscopy, and Surface-Enhanced Raman Scattering. *In vitro* tests are also performed on human fetal lung fibroblast HFL-1 cells and the nanoparticles are found to be non cytotoxic for the cells in the concentration range used in our study. Confocal microscopy shows that the particles are localised in the cell cytoplasm.

Keywords: gold nanoparticles, FTIR, TEM, HFL-1 cells

INTRODUCTION

Gold nanoparticles (AuNPs) exhibit unique, size-dependent chemical, optical and electronic properties, which are different from the bulk gold. Their properties are closely related to the shape, size, degree of aggregation and surface functionalizing agents [1]. Nanoparticles are especially attractive for the presence of surface plasmon bands and for their large area to volume ratio

^a Faculty of Food Science and Technology, University of Agricultural Sciences and Veterinary Medicine, Mănăștur 3-5, 400372 Cluj-Napoca, Romania.

* Corresponding author: csocaciu@usamvcluj.ro

^b Faculty of Veterinary Medicine, University of Agricultural Sciences and Veterinary Medicine, Mănăștur 3-5, 400372 Cluj-Napoca, Romania

^c Faculty of Physics, Babeș-Bolyai University, Kogălniceanu 1, 400084 Cluj-Napoca, Romania

which allows loading of large amounts of bio-functionalizing agents onto their surface [2] especially important in biomedicine applications. Recently, there is more and more interest directed towards the green synthesis of AuNPs using plant or plant extracts [3-12], bacteria, fungi [13-15], yeasts [16], or eco-friendly reducing agents [17].

In this study we report the synthesis of stable gold nanoparticles with 15 nm diameter using *A. sativum* aqueous extract as a reducing agent for the chloroauric acid (HAuCl_4). The reduction process was studied by varying the amounts of *A. sativum* extract. The obtained nanoparticles were characterised by UV-VIS spectroscopy, Fourier Transform Infrared Spectroscopy (FTIR), Surface Enhanced Raman Scattering (SERS), and Transmission Electron Microscopy (TEM). *In vitro* experiments were also carried out on human fetal lung fibroblast (HFL-1) cells.

RESULTS AND DISCUSSION

The nanoparticle samples will be named according the amount of *A. sativum* extract used in the synthesis process.

The AuNPs formation is confirmed by UV-VIS spectroscopy (Figure 1). The UV-VIS shows absorption maxima at 543-544 nm. Basically at boiling, after the extract is added to the chloroauric acid, the solution changes from almost colourless to purple. The inset in Figure 1 shows the colours of the obtained AuNPs samples, while the UV-VIS spectra indicate that the prepared colloidal solutions absorb visible light at 543-544 nm (Table 1), which coincide with characteristic surface plasmon bands of AuNPs [1]. The presence of sharp, well defined surface plasmon bands indicates the presence of small particles with narrow size distribution. The wavelength of the surface plasmon resonance peak is independent on the amount of *A. Sativum* extract, only the absorption maxima show some dependence.

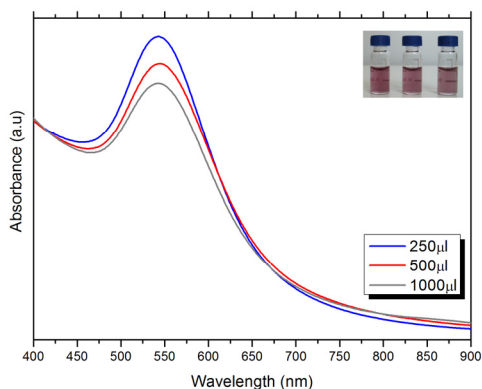


Figure 1. UV-VIS absorption spectra of the AuNP samples prepared by 'dropwise' addition of different amounts of *A. sativum* extract. The colours of the samples can also be observed in the inset.

Table 1. Surface plasmon resonance peak position for the different AuNPs preparations discussed above

Extract amount (μl)	250	500	1000
SPR peak wavelength	543	544	543

The presence of small particles with narrow size distribution is confirmed by TEM experiments. Figure 2 shows a typical TEM image for the 250μl sample, together with the size distribution of the AuNPs. The average size of the AuNPs was estimated using the ImageJ 1.46 software. The other samples, the 500 μl and 1000 μl respectively show very similar behaviour. The vast majority of nanoparticles are spherically shaped. Very few nanotriangles can be observed. The nanoparticles size varies between 10-20 nm, with mean diameters of 15 nm.

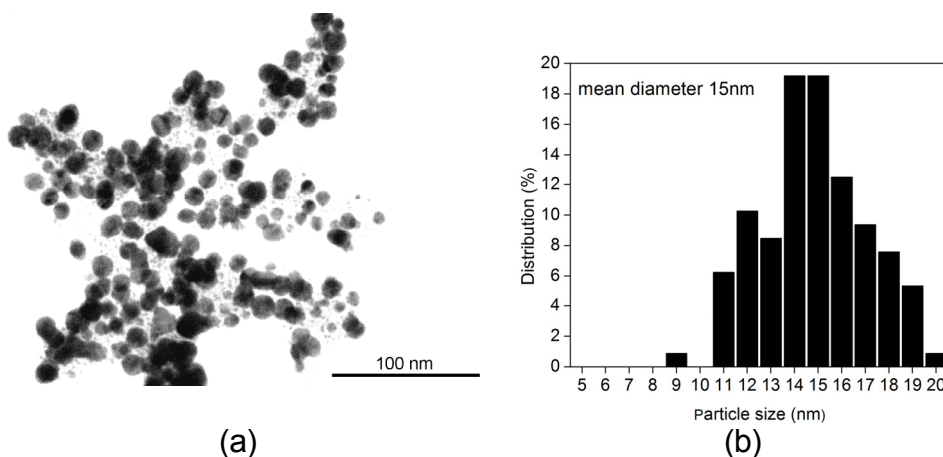


Figure 2. TEM images (a) and particle size distribution (b) the AuNP samples obtained by dropwise addition of 250 μl *A. sativum* extract to the HAuCl₄.

Further, FTIR studies were performed for the identification of the nature of the biomolecules involved in the reduction of the chloroauric acid and capping of the nanoparticles (Figure 3). Figure 3 shows the FTIR spectra of the *A. sativum* extract and of the AuNPs obtained by reduction of the chloroauric acid by the same extract. As can be seen, some IR bands (1524, 1651, 2928, 2958, and 3289 cm⁻¹) are common the *A. sativum* extract and the nanoparticles.

The peak at 1524 cm^{-1} corresponds to N-H bending vibrations and C-N stretching vibrations of the amide II band of proteins, while the peak at 1651 cm^{-1} corresponds to C=O stretching vibrations of the amide I band. The broad band at around 3289 cm^{-1} is another amide band of N-H stretching vibrations. These findings show that the AuNPs are capped by proteins in the *A. sativum*, implying thus that the extract, apart from being the reducing agent of the chloroauric acid, is also the capping agent of the nanoparticles.

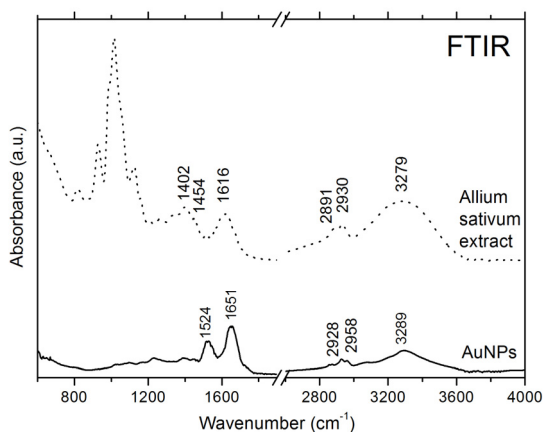


Figure 3. FTIR spectra of the *A. sativum* extract (upper spectrum) and of the AuNPs (bottom spectrum).

The stability of the AuNPs colloidal solutions was assessed by recording the evolution of their characteristic UV-VIS spectra in time (Figure 4). Their stability is not optimum and should be improved. This can be concluded from the slight change in the spectral appearance in time. The same is valid for the other samples obtained by dropwise addition.

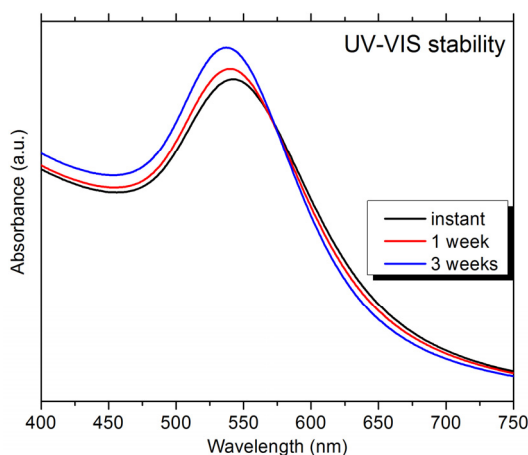


Figure 4. Time evolution of the UV-VIS spectra of the gold nanoparticle samples obtained by dropwise addition of $250\mu\text{l}$ of *A. sativum* aqueous extract to the HAuCl_4 .

Some preliminary *in vitro* studies on HFL-1 cells cultures were also carried out for testing the AuNPs cytotoxicity and to check if the nanoparticles are internalized inside the cells. We are able to prove the cellular internalization and localization of R123-labeled AuNPs by confocal microscopy (Figure 5). The red areas in the figure represent the cells nuclei, while the green areas are the R123-labeled AuNPs, which, as can be observed, are internalized in the cell cytoplasm.

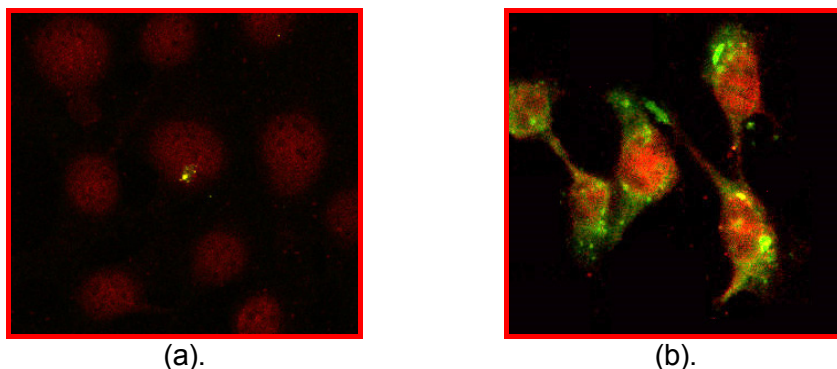


Figure 5. Fluorescence confocal microscopy images of (a) control sample and (b) HFL-1 cells incubated for 24 hours with the 250 μ l AuNPs sample labelled with R123. The red areas represent the cell nuclei stained in red with Draq5, while green fluorescence is given by the presence of the R123-AuNPs in the cell cytoplasm.

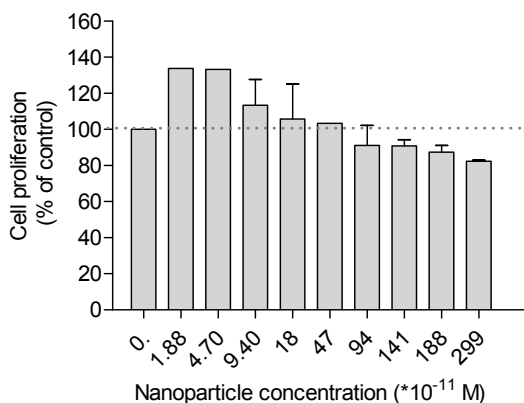


Figure 6. Effect of AuNPs on the proliferation of fetal lung fibroblast HFL-1 cells, treated with different concentrations of AuNPs for 24 h. Cell viability was assessed by the MTT assay. Data are expressed as mean \pm SEM ($n = 3$). No statistically significant differences compared with control were identified.

AuNPs did not have any significant anti-proliferation effect on fetal lung fibroblast HFL-1 cells after 24h as shown in Fig. 6. Low concentrations of AuNPs ($1.88 - 47 \times 10^{-11}$ M) stimulated cell proliferation in a dose dependent manner. AuNPs treatment administrated at the highest concentration of 299×10^{-11} M for 24 h decreased the HFL-1 cell proliferation with only 20 %.

The results of the study thus revealed that the nanoparticles developed here would be a suitable delivery system for *Allium sativum* extract in fibroblasts. The fact that the nanoparticles are not cytotoxic is an essential aspect when considering any potential applications of the nanoparticles in the biological field.

CONCLUSIONS

A green synthesis method gold nanoparticles was proposed. The method is based on the reduction of the chloroaurate ions by *A. sativum* extract, which acts both as reducing and capping agent. The obtained nanoparticles are spherical in shape, with 15 nm mean diameters. The nanoparticles show no toxicity towards HFL-1 cells, in the concentration range obtained in this study. As shown by confocal microscopy experiments, the AuNPs are internalized in the cell cytoplasm. The above mentioned aspects indicate potential of using the obtained particles in biomedical applications.

EXPERIMENTAL

Chemicals and materials

The chloroauric acid tetrahydrate ($\text{HAuCl}_4 \cdot 4\text{H}_2\text{O}$) was purchased from Merck. *A. sativum* cloves were obtained from a home grown source. Fetal bovine serum -Lonza, Ham's F12 Nutrient Mixture (Ham's F12), and Dulbecco's Modified Eagle Medium (DMEM) were purchased from Lonza Group Ltd. (Basel, Switzerland). Glutamine, penicillin, streptomycin, and amphotericin were purchased from Sigma. The rhodamine 123 (R123) was purchased from Sigma-Aldrich.

Gold nanoparticles synthesis

The *A. sativum* aqueous extract was obtained by boiling of 20 g of chopped garlic cloves from a home grown source with 150ml distilled water in a 250 ml Erlenmeyer flask. After boiling, the mixture was decanted; the supernatant was filtered and further used as reducing agent for the AuNPs. For the AuNPs synthesis, 25 ml of a 0.2 mM chloroauric acid solution was boiled and different amounts of *A. sativum* extract (250 μl , 500 μl , 1000 μl) were added "drop by drop" under stirring. A purple color formation was rapidly observed in all cases, indicating the formation of AuNPs.

Instrumentation and characterization methods

The UV-VIS spectra were recorded using a Perkin Elmer Lambda 25 UV-VIS spectrometer. The spectral resolution was 1 nm. The FTIR Attenuated Total Reflectance (FTIR-ATR) spectra were recorded on a Shimadzu IR-Prestige FTIR Spectrometer equipped with a diamond PIKE MIRacle single reflection plate unit. The spectra were taken with a resolution of 4 cm^{-1} and by co-adding 64 interferograms. The TEM images were obtained using a JEOL JEM1010 transmission electron microscope equipped with a MegaViewIII CCD camera. The microscope uses an accelerating voltage of 100 kV. The measurements were performed onto a copper grid. A drop of solution containing the nanoparticles was placed onto this copper grid and allowed to dry. Prior to TEM and FTIR experiments, the nanoparticles were centrifugated four times at 13,000 rpm for 15 min, followed by resuspension in distilled water to remove any unreacted compounds. The pellet obtained after the 4th centrifugation cycle was dried prior to measuring the FTIR spectra. This procedure was necessary for achieving good signal to noise ratio in the spectra.

MTT viability assay

For testing the nanoparticles cytotoxicity, MTT viability assays were carried out on the human fetal lung fibroblast (HFL-1) cell line. The HFL-1 cells were grown in a mixture of 1:1 v/v Ham's F12 and DMEM containing 4.5 g/L glucose, supplemented with 10% fetal bovine serum, 2 mM glutamine, 1% penicillin and streptomycin, 0.1% amphotericin. The cells were incubated in 5% CO₂ at 37° C, and 95% relative humidity. The cells were allowed to attach for 24 hours in 96-well plates. A number of 8000 HFL-1 cells were seeded in each plate. After 24 h, the cells were incubated overnight with eight different concentrations of AuNPs. Next day, the cell culture media was removed and MTT reagent in HBSS buffer (0.5 mg/ml) was added to each well. After 2 h of incubation the removal of MTT solution was carried out and the formazan crystals were dissolved in DMSO. The solubilized formazan formed in viable cells was measured at 550 nm and 630 nm (for sample and background, respectively) using the microplate reader HT BioTek Synergy (BioTek Instruments, USA). The results were expressed as percent survival relative to an untreated control.

Nanoparticles staining for cellular internalization

The nanoparticles cellular internalization was assessed by confocal microscopy. The fluorescence confocal microscopy was performed with a Zeiss LSM 710 confocal microscope, equipped with Zen software for image processing. The AuNPs were labeled with a fluorescent dye prior to experiments. Rhodamine 123 (R123) was used as fluorescent label. The R123-labeled nanoparticles were obtained by simultaneously adding the *A. sativum* extract and appropriate amounts of 1mM R123 to the chloroauric acid at boiling. Cell nuclei were stained using the cell permeable far-red

fluorescent DNA dye Draq5 (1, 5-bis{[2-(di-methylamino)ethyl]amino}-4, 8-dihydroxyanthracene-9, 10-dione). Cell staining was carried out using the non-fixed HFL-1 cells for 5 min, following three washing steps using phosphate buffer (pH 7.4).

ACKNOWLEDGEMENTS

This work was supported by a grant of the Romanian National Authority for Scientific Research, CNCSIS–UEFISCDI, project number PN-II-RU-TE-2011-3-0154. Lucian Barbu-Tudoran is acknowledged for technical help with the TEM experiments.

REFERENCES

- [1] M.C. Daniel and D. Astruc, *Chemical Reviews*, 2004, 104, 293.
- [2] N.T.K. Thanh and L.A.W. Green, *Nano Today*, 2010, 5, 213.
- [3] K.B. Narayanan and N. Sakthivel, *Advances in Colloid and Interface Science*, 2011, 169, 59.
- [4] S.S. Shankar, A. Ahmad, R. Pasricha and M. Sastry, *Journal of Materials Chemistry*, 2003, 13, 1822.
- [5] S.S. Shankar, A. Rai, A. Ahmad and M. Sastry, *Journal of Colloid and Interface Science*, 2004, 275, 496.
- [6] G.S. Ghodake, N.G. Deshpande, Y. P. Lee and E. S. Jin, *Colloids and Surfaces B: Biointerfaces*, 2010, 75, 584.
- [7] D. Philip, C. Unni, S.A. Aromal and V.K. Vidhu, *Spectrochimica Acta Part A: Molecular and Biomolecular Spectroscopy*, 2011, 78, 899.
- [8] S.L. Smitha, D. Philip and K.G. Gopchandran, *Spectrochimica Acta Part A: Molecular and Biomolecular Spectroscopy*, 2009, 74, 735.
- [9] S.P. Dubey, M. Lahtinen and M. Sillanpää, *Colloids and Surfaces A: Physicochemical and Engineering Aspects*, 2010, 364, 34.
- [10] K.P. Kumar, W. Paul and C.P. Sharma, *Process Biochemistry*, 2011, 46, 2007.
- [11] A.D. Dwivedi and K. Gopal, *Colloids and Surfaces A: Physicochemical and Engineering Aspects*, 2010, 369, 27.
- [12] M. Ahamed, M.A. Majeed Khan, M.K.J. Siddiqui, M.S. Alsalihi and S.A. Alrokayan, *Physica E: Low-dimensional Systems and Nanostructures*, 2011, 43, 1266.
- [13] K.B. Narayanan and N. Sakthivel, *Advances in Colloid and Interface Science*, 2010, 156, 1.
- [14] S. Gurunathan, K. Kalishwaralal, R. Vaidyanathan, D. Venkataraman, S.R.K. Pandian, J. Muniyandi, N. Hariharan and S. H. Eom, *Colloids and Surfaces B: Biointerfaces*, 2009, 74, 328.
- [15] L. Du, H. Jiang, X. Liu and E. Wang, *Electrochemistry Communications*, 2007, 9, 1165.
- [16] K.N. Thakkar, S.S. Mhatre and R.Y. Parikh, *Nanomedicine: Nanotechnology, Biology and Medicine*, 2010, 6, 257.
- [17] V.K. Sharma, R.A. Yngard and Y. Lin, *Advances in Colloid and Interface Science*, 2009, 145, 83.

SCREENING OF POLYPHENOLIC COMPOUNDS, ANTIOXIDANT AND ANTIMICROBIAL PROPERTIES OF *TANACETUM VULGARE* FROM TRANSYLVANIA

MARIA MUREȘAN^a, DANIELA BENEDEC^{a,*}, LAURIAN VLASE^a,
RADU OPREAN^a, ANCA TOIU^a, ILIOARA ONIGA^a

ABSTRACT. The purpose of this study was to investigate the phenolic compounds and to evaluate the antioxidant and antimicrobial properties of *Tanacetum vulgare* flowers from different areas of Transylvania (Romania). The identification and quantification of major phenolic compounds were performed by a LC-MS method. The total polyphenols, caffeic acid derivatives and flavonoids content was spectrophotometrically determined. The antioxidant activity was evaluated using the DPPH bleaching method. The antimicrobial tests were performed using the disk diffusion assay. The phenolic profile showed the presence of phenolic acid derivatives (gentisic, caffeic, chlorogenic, *p*-coumaric, and ferulic acids), flavonoid glycosides (hyperoside, isoquercitrin, rutin and quercitrin) and flavonoid aglycones (quercetin, patuletin, luteolin, kaempferol, apigenin). The extracts of *T. vulgare* from Sibiu contain higher amounts of total polyphenols, flavonoids and caffeic acid derivatives than the extracts of *T. vulgare* from Alba. Both ethanolic extracts showed good antioxidant activity and low inhibitory activity against Gram-positive bacteria. The displayed potent antioxidant activity of these extracts supports the ethnomedicinal uses for this species.

Keywords: *Tanacetum vulgare*, HPLC-MS, polyphenols, antioxidant, antimicrobial activities

INTRODUCTION

Tanacetum vulgare L. syn. *Chrysanthemum vulgare* (L.) Bernh., commonly known as tansy, is a species of the genus *Tanacetum* from *Asteraceae* family [1,2].

^a Iuliu Hatieganu University of Medicine and Pharmacy, Faculty of Pharmacy, 8, Victor Babes Street, 400012 Cluj-Napoca, Romania.

* Corresponding author: dbenedec@umfcluj.ro

The flora of Romania comprises around 12 species and a few subspecies and varieties of *Tanacetum* [2]. Some members of this genus are very important species for their medicinal value used over the years in all around the world. *T. vulgare* has a long history of medicinal use. In traditional medicine, tansy is used to heal wounds, fever, headache, gastrointestinal and liver diseases, rheumatic pain, and intestinal parasites, due to anthelmintic, carminative, antiseptic, antihypertensive, diuretic, anti-inflammatory and antispasmodic properties [1,3-6]. Previous studies on *T. vulgare* from France showed antioxidant and antiviral properties against the herpes simplex viruses HSV-1 and HSV-2 [7-8]. The crude alcoholic extract and the essential oil from *T. vulgare* possess vermifuge activities [9]. Phytochemical studies have shown that *T. vulgare* contain several biologically active metabolites, mainly sesquiterpene lactones, essential oil, phenolic compounds, polysaccharides [1,3,8,10-13]. Since no data on chemical composition of *T. vulgare* flowers from Romania was found in the literature, the aim of this study was to carry out a phytochemical analysis of this natural product, and to investigate the antioxidant and antimicrobial properties.

RESULTS AND DISCUSSION

Identification and quantification of phenolic compounds

Because of the complexity of the mixtures of polyphenolic compounds in the natural plant extracts, it is rather difficult to characterize every compound, but it is important to identify the major groups and the types of phenolic compounds [14]. In this work, the major types and their representative constituents of phenolic compounds in *T. vulgare* extracts were determined by HPLC analysis. In this regard, a liquid chromatographic method for the determination of nineteen phenolic compounds (eight phenolic acids, four quercetin glycosides, and seven flavonol and flavone aglycones) from natural products was used. The simultaneous analysis of different classes of polyphenols was performed by a single column pass, and the separation of all examined compounds was carried out in 35 min. The concentrations of identified polyphenolic compounds in the two samples of *T. vulgare* are presented in Table 1 and the HPLC chromatograms are shown in Figures 1-2. Quantitation was performed according to an external standard method [15-19].

Chlorogenic acid was identified in the two ethanolic extracts. *T. vulgare* from Sibiu was richer in chlorogenic acid ($4334.32 \pm 11.79 \mu\text{g/g}$), than the sample harvested from Alba ($3673.75 \pm 15.70 \mu\text{g/g}$) (Table 1). Caffeic acid and gentisic acid were identified in the extract of *T. vulgare* (Sibiu), but their concentration was too low to be quantified. Ferulic acid and *p*-coumaric acid

were found only in the sample from Alba (3.55 ± 0.32 and 4.41 ± 0.08 $\mu\text{g/g}$ respectively). The pattern of flavonoids indicates large quantitative differences between the two samples. Rutin and quercitrin were quantified in higher amounts in *T. vulgare* (Sibiu) versus *T. vulgare* (Alba). Thus, rutin was found in very large quantities in *T. vulgare* from Sibiu (350.15 ± 7.30 $\mu\text{g/g}$), whereas, in the sample from Alba, the content of rutin was below than 0.2 $\mu\text{g/g}$. The amount of quercitrin was 8.62 times higher in the sample from Sibiu, than the sample collected from Alba County (112.09 ± 2.91 $\mu\text{g/g}$, and 13.00 ± 0.04 $\mu\text{g/g}$, respectively). Hyperoside and isoquercitrin were identified and determined in small amounts in both samples (Table 1). Five flavonoid aglycones, i.e. quercetin, patuletin, luteolin, kaempferol and apigenin were found in the extracts of *T. vulgare*. Luteolin and quercetin were found in large quantities in both extracts (Table 1). Apigenin was quantified only in the sample from Sibiu, while kaempferol was identified only in the tansy of Alba (below limit of detection). Patuletin was also identified in the two extracts, but in too low concentration to be quantified. According to various literature sources, apigenin, acacetin, luteolin, cinaroside, eupatilin, cosmosiin, tilianin and jaceoside are the main flavonoids in tansy flowers [10-11].

Table 1. Polyphenolic compounds content in *T. vulgare* extracts ($\mu\text{g/g}$ plant)

Polyphenolic compounds	Rt \pm SD (min)	m/z	<i>T. vulgare</i> (Sibiu)	<i>T. vulgare</i> (Alba)
Gentisic acid	2.15 ± 0.07	179	<0.2	-
Caffeic acid	5.60 ± 0.04	179	<0.2	-
Chlorogenic acid	5.62 ± 0.05	353	4334.32 ± 11.79	3673.75 ± 15.70
<i>p</i> -Coumaric acid	8.70 ± 0.08	163	-	4.41 ± 0.08
Ferulic acid	12.20 ± 0.10	193	-	3.55 ± 0.32
Hyperoside	18.60 ± 0.12	463	17.51 ± 0.50	23.73 ± 0.37
Isoquercitrin	19.60 ± 0.10	463	14.29 ± 0.22	18.91 ± 0.10
Rutin	20.20 ± 0.15	609	350.15 ± 7.30	<0.2
Quercitrin	23.64 ± 0.13	447	112.09 ± 2.91	13.00 ± 0.04
Quercetin	26.80 ± 0.15	301	69.45 ± 2.86	56.24 ± 1.22
Patuletin	29.41 ± 0.12	331	<0.2	<0.2
Luteolin	29.10 ± 0.19	285	122.21 ± 2.91	165.77 ± 2.24
Kaempferol	32.48 ± 0.17	285	-	<0.2
Apigenin	33.10 ± 0.15	279	20.50 ± 1.60	-

Note: NF - not found, below limit of detection. Values are the mean \pm SD (n = 3).

Considering the 19 standard compounds used in this study, some other peaks were not identified. We analyzed the polyphenolic composition of the two ethanolic extracts of *T. vulgare* collected from different areas. The

simultaneous determination of wide range of polyphenolic compounds was performed using a rapid, highly accurate and sensitive HPLC method assisted by mass spectrometry detection [15-19]. The polyphenolic profile showed the presence of phenolic acid derivatives, four flavonoid glycosides and five flavonoid aglycones in *T. vulgare* flowers (Table 1, Fig. 1, 2). Additionally, the obtained results showed that these samples of *Tanacetum* could be considered as a *good* source of chlorogenic acid.

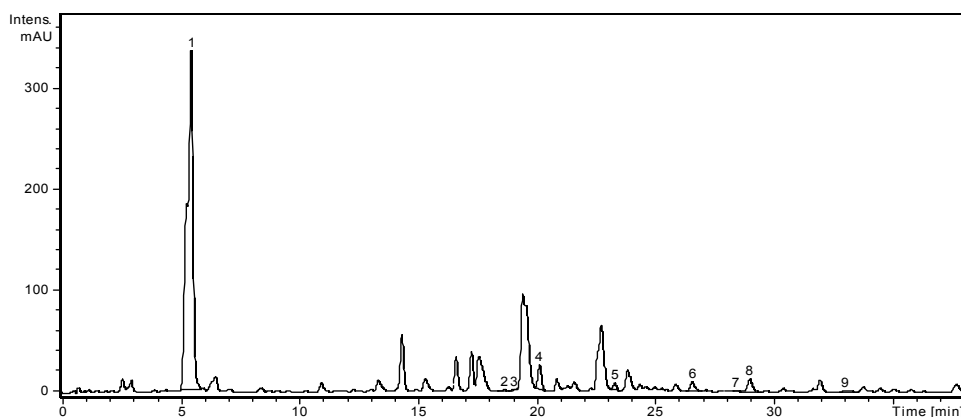


Figure 1. HPLC chromatogram of *T. vulgare* extract (Sibiu)

Notes: The identified compounds: 1, Chlorogenic acid; 2, Hyperoside; 3, Isoquercitrin; 4, Rutin; 5, Quercitrin; 6, Quercetin; 7, Patuletin; 8, Luteolin; 9, Apigenin

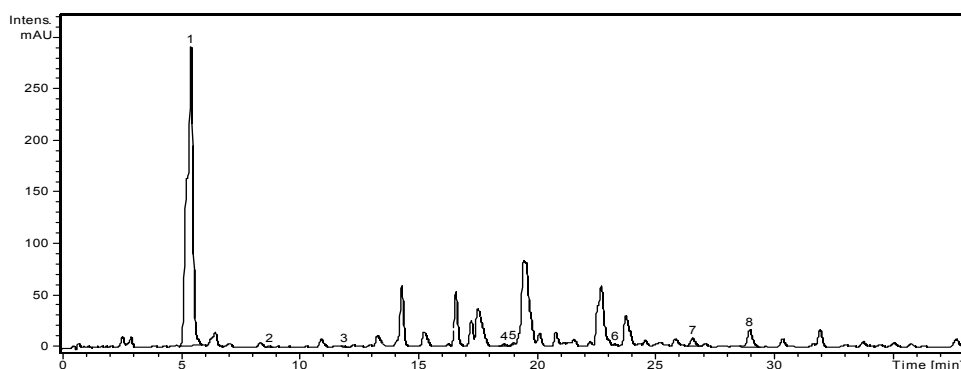


Figure 2. HPLC chromatogram of *T. vulgare* extract (Alba)

Notes: The identified compounds: 1, Chlorogenic acid; 2, p-Coumaric acid; 3, Ferulic acid; 4, Hyperoside; 5, Isoquercitrin; 6, Quercitrin; 7, Quercetin; 8, Luteolin

Estimation of polyphenol content and the antioxidant activity

The polyphenolic compounds, particularly flavonoids, have attracted a great deal of research on their broad distribution in medicinal plants, their physiological (including antioxidant) activities, and their health effects. While the flavonoid composition of many species from *Asteraceae* family was already determined, less is known about their phenolic acid derivatives and total polyphenolic content [8]. Due to their importance in plants and human health, it would be useful to know the concentration of the polyphenolic compounds which could indicate their potentials as therapeutic agents, but also for predicting and controlling the quality of medicinal herbs [16]. Thus, we determined the content of polyphenols in *T. vulgare* flowers from different areas of Romania. Also, we investigated the total antioxidant capacity, determined *in vitro* using the 2,2'-diphenyl-1-picrylhydrazyl free radical (DPPH) assay [17,20]. Table 2 gives comparative quantitative data on polyphenolic compounds levels in the two ethanolic extracts of *T. vulgare* from Sibiu and *T. vulgare* from Alba.

Concerning the content of total polyphenols, the highest amounts were determined in the extracts of *T. vulgare* collected from Sibiu (50.06 ± 3.42 mg/g) and *T. vulgare* from Alba (46.75 ± 3.37 mg/g) (Table 2). Also, the samples from Sibiu are richer in flavonoids and caffeic acid derivatives (10.35 ± 0.73 , and 11.82 ± 1.06 mg/g, respectively) than the samples from Alba (7.73 ± 0.27 , and 7.70 ± 0.22 mg/g, respectively). The ethanolic extracts obtained from Romanian species contain higher amounts of total polyphenols (between 46.75 and 50.06 mg/g) than the methanolic extract of the Polish species (between 24 and 39 mg/g), as previously published by Wegiera et al. [21]. The same Polish species had a lower concentration of flavonoids (0.71 mg/g) [21] than *T. vulgare* from Romania (between 7.73 and 10.35 mg/g).

The ethanolic extracts of *T. vulgare* harvested from Sibiu and Alba were investigated for the antioxidant activity. The antioxidant activity was assessed by the DPPH radical bleaching method. Trolox (0.025 mg/mL) and quercetin (10 µg/mL) were used as the positive controls (Table 2). The $IC_{50(DPPH)}$ values of the extracts increased in the following order: *T. vulgare* (Alba) > *T. vulgare* (Sibiu). The lower the IC_{50} value means the more powerful the antioxidant capacity. According to this method, *T. vulgare* from Sibiu, with $IC_{50} = 68.74 \pm 4.27$ µg/mL, showed a slightly higher radical scavenging activity than *T. vulgare* from Alba (70.67 ± 4.33 µg/mL), but lower than that of the standard quercetin (5.47 ± 0.16 µg/mL), or trolox (11.20 ± 0.20 µg/mL). The results were in agreement with the phenolic compounds values listed in Table 2. Therefore, it is likely that the phenolic constituents present in this species are responsible for the antioxidant and free radical scavenging activities. The literature data on the antioxidant activities of this species are difficult to compare because of the different used

methods. However, the related literature shows that this species has a good antioxidant activity [1,8,22]. Comparing the antioxidant activities of *T. vulgare* from Hadlow, U.K. and the same species from Romania, the ethanolic extracts of the Romanian species (68.74 - 70.67 $\mu\text{g/mL}$) exhibited a lower antioxidant activity than the methanol extract of the English species ($37 \pm 1.2 \mu\text{g/mL}$) [22]. The displayed potent antioxidant activity of *T. vulgare* extract could support the traditional medicinal uses of the plant as wound healing, to treat rheumatic pain and other inflammatory conditions [1].

Table 2. Total phenols and the results of DPPH method for *Tanacetum* extracts

Samples	TPC (mg GAE/g)	Flavonoids (mg RE/g)	Caffeic acid derivatives (mg CAE/g)	IC ₅₀ ($\mu\text{g/mL}$)
<i>T. vulgare</i> (Sibiu)	50.06 \pm 3.42	10.35 \pm 0.73	11.82 \pm 1.06	68.74 \pm 4.27
<i>T. vulgare</i> (Alba)	46.75 \pm 3.37	7.73 \pm 0.27	7.70 \pm 0.22	70.67 \pm 4.33
Quercetin	-	-	-	5.47 \pm 0.16
Trolox	-	-	-	11.20 \pm 0.20

Each value is the mean \pm SD of three independent measurements. GAE: Gallic acid equivalents; RE: rutin equivalents; CAE: caffeic acid equivalents

In vitro antimicrobial activity

Two ethanolic extracts of *T. vulgare* were investigated for their *in vitro* antimicrobial properties using a disk-diffusion method against a panel of microorganisms including *S. aureus*, *B. subtilis*, *E. coli*, *P. aeruginosa* and *C. albicans*. After incubation, all plates were examined for any zones of growth inhibition, and the diameter of these zones were measured in millimeters (Table 3) [20, 23].

Table 3. Results of the antimicrobial activity of *T. vulgare* extracts

Samples	Zone of inhibition (mm)				
	<i>S. aureus</i>	<i>B. subtilis</i>	<i>E. coli</i>	<i>P. aeruginosa</i>	<i>C. albicans</i>
<i>T. vulgare</i> (Sibiu)	11 \pm 1.00	10 \pm 0.00	6 \pm 1.00	6 \pm 0.00	6 \pm 0.00
<i>T. vulgare</i> (Alba)	12 \pm 1.00	11 \pm 1.00	7 \pm 1.00	6 \pm 0.00	6 \pm 0.00
Ciprofloxacin	30 \pm 3.00	23 \pm 1.00	36 \pm 4.00	20 \pm 1.00	-
Fluconazole	-	-	-	-	25 \pm 2.00

Notes: The values represent the average of three determinations \pm standard deviations.

Ciprofloxacin (25 $\mu\text{g/well}$) and Fluconazole (25 $\mu\text{g/well}$) were used as positive control.

The investigated extracts were less active against *S. aureus* and *B. subtilis* (inhibition diameter between 10 and 12 mm) and they did not show antibacterial activity against the tested Gram-negative bacterial strains: *E. coli* and *P. aeruginosa* (inhibition diameter < 10 mm) (Table 3). The samples were also inactive on *C. albicans* (inhibition diameter < 10 mm).

The results of the present investigation suggest that *T. vulgare* ethanolic extracts exhibited a low antibacterial activity against two Gram-positive bacterial strains (*S. aureus* and *B. subtilis*). No scientific data was available regarding the antibacterial action of *T. vulgare* flowers extracts. Antimicrobial activity has been reported only for essential oil isolated from *T. vulgare* [1].

CONCLUSIONS

We have determined the polyphenolic composition and the antioxidant activity for *Tanacetum vulgare* collected from different areals of Romania, for a better pharmacognostical characterisation of the indigenous species. The antioxidant activity evaluated using the DPPH bleaching method indicated that *T. vulgare* from Sibiu has important antioxidant effect, related with the total phenolic content. The phytochemical comparative study showed minor qualitative and quantitative differences between the studied samples. The antimicrobial tests underlined a low activity against the tested Gram-positive bacterial strains. Our results show that *T. vulgare* may be considered a potential source of polyphenols with antioxidant properties. Further *in vivo* studies concerning the pharmacologic properties of this medicinal plant is required in order to obtain natural pharmaceuticals with therapeutic efficacy.

EXPERIMENTAL SECTION

Plant material and extraction procedure

The flowers of *Tanacetum vulgare* L. were collected in July 2013 from different areas of Transylvania: Sibiu County (Voucher No. 24) and Alba County (Voucher No. 25), in the blossom period. Voucher specimens were deposited in the Herbarium of the Department of Pharmacognosy, Faculty of Pharmacy Cluj-Napoca, Romania. The natural product (flowers) was reduced to a proper degree of fineness. 10.0 g of the plant material was extracted with 100 mL of 70% ethanol (Merck, Darmstadt, Germany), for 30 minutes on a water bath, at 60 °C. The samples were then cooled down and centrifuged at 4.500 rpm for 15 min. and the supernatant was recovered [15-18].

HPLC–MS analysis

An Agilent 1100 HPLC Series system (Agilent, USA) was used equipped with a degasser, binary gradient pump, column thermostat, autosampler, and UV detector. The HPLC system was coupled with an Agilent 1100 mass spectrometer (LC/MSD Ion Trap VL). For the separation, a reverse-phase analytical column was employed (Zorbax SB-C18, 100 x 3.0 mm i.d., 3.5 μ m particle); the work temperature was 48°C. The detection of the compounds was performed on both UV and MS mode. The UV detector was set at 330 nm until 17.5 min, then at 370 nm. The MS system operated using an electrospray ion source in negative mode. The chromatographic data were processed using ChemStation and DataAnalysis software from Agilent, USA. The mobile phase was a binary gradient: methanol and acetic acid 0.1% (v/v). The elution started with a linear gradient, beginning with 5% methanol and ending at 42% methanol, for 35 minutes; then 42% methanol for the next 3 minutes. The flow rate was 1 mL/min and the injection volume was 5 μ L [15-19]. The MS signal was used only for qualitative analysis based on specific mass spectra of each polyphenol. The MS spectra obtained from a standard solution of polyphenols were integrated in a mass spectra library. Later, the MS traces/spectra of the analyzed samples were compared to spectra from library, which allows positive identification of compounds, based on spectral match. The UV trace was used for quantification of the identified compounds from MS detection. Using the chromatographic conditions described above, the polyphenols eluted in less than 35 minutes. Four polyphenols could not be quantified in current chromatographic conditions due overlapping (caftaric acid with gentisic acid and caffeic acid with chlorogenic acid). However, all four compounds can be selectively identified in MS detection (qualitative analysis) based on differences between their molecular mass and MS spectra. The detection limits were calculated as minimal concentration producing a reproducible peak with a signal-to-noise ratio greater than three. Quantitative determinations were performed using an external standard method. Calibration curves in the 0.5-50 mg/mL range with good linearity ($R^2 > 0.999$) for a five point plot were used to determine the concentration of polyphenols in plant samples [15-19]. The detection and quantification of polyphenols was performed in UV assisted by mass spectrometry detection. Due to peak overlapping, four polyphenol-carboxylic acids (caftaric, gentisic, caffeic, chlorogenic) were determined only based on MS spectra, whereas for the rest of the compounds the linearity of the calibration curves was very good ($R^2 > 0.998$), with detection limits in the range of 18 to 92 ng/mL. The detection limits were calculated as the minimal concentration yielding a reproducible peak with a signal-to-noise ratio greater than three. Quantitative determinations were performed using an external

standard method; retention times were determined with a standard deviation ranging from 0.04 to 0.19 min. For all compounds, the accuracy was between 94.1.3% and 105.3%. Accuracy was checked by spiking samples with a solution containing each standard compound in a 10 µg/mL concentration. In all analysed samples the compounds were identified by comparison of their retention times and recorded electrospray mass spectra with those of standards in the same chromatographic conditions.

Determination of polyphenolic compounds content

The total caffeic acid derivatives content was expressed as caffeic acid as previously described in the European Pharmacopoeia [24]. The extract (1 mL) was added to 2 mL 0.5 N HCl, 2 mL Arnow's reagent (10 g sodium nitrite and 10 g sodium molybdate made up to 100 mL with distilled water), 2 mL NaOH (at a concentration of 1 N) and 3 mL of distilled water. Each solution was compared with the same mixture without Arnow's reagent. The absorbance was spectrophotometrically determined at 525 nm. The percentage of phenolic acids, expressed as caffeic acid equivalent on dry weight, was calculated using an equation obtained from calibration curve of caffeic acid graph ($R^2= 0.994$) [16,24].

The total flavonoids content was determined and expressed as rutin, as previously described in the Romanian Pharmacopoeia [18]. Each extract (5 mL) was mixed with sodium acetate (5.0 mL, 100 g/L), aluminum chloride (3.0 mL, 25 g/L) and filled up to 25 mL with methanol in a calibrated flask. Each solution was compared with the same mixture without reagent. The absorbance was measured at 430 nm [18]. The total flavonoids concentrations were determined using an equation obtained from calibration curve of the rutin graph ($R^2 = 0.999$).

The total polyphenolic content (TPC) of the extracts was determined by spectrophotometric method using Folin-Ciocalteu reagent and gallic acid as standard to produce the calibration curve [17,24]. 2 mL of ethanolic extracts diluted 25 times were mixed with 1.0 mL of Folin-Ciocalteu reagent, 10.0 mL of distilled water and diluted to 25.0 mL with a 290 g/L solution of sodium carbonate. The samples were incubated in the dark for 30 min. The absorbance was measured at 760 nm and the total phenols were expressed as gallic acid equivalents/g of dry plant material (mg GAE/ g plant material) [17,24].

DPPH bleaching assay

A DPPH assay was employed to investigate the antioxidant activity of the ethanolic extracts of *T. vulgare*. The DPPH solution (0.25 mM) in methanol was prepared and 2.0 ml of this solution was added to 2.0 ml of extract solution (or standard) in ethanol at different concentrations (12.5-100 µg/mL). After 30

minutes of incubation at 40°C in a thermostatic bath, the decrease in the absorbance ($n = 3$) was measured at 517 nm. The percent DPPH scavenging ability was calculated as: $\text{DPPH scavenging ability} = (A_{\text{control}} - A_{\text{sample}}/A_{\text{control}}) \times 100$, where A_{control} is the absorbance of DPPH radical and methanol (containing all reagents except the sample) and A_{sample} is the absorbance of DPPH radical and sample extract. Afterwards, a curve of % DPPH scavenging capacity *versus* concentration was plotted and IC_{50} values were calculated. IC_{50} denotes the concentration of sample required to scavenge 50% of DPPH free radicals. Trolox and quercetin were used as positive control [16-17, 20,25-26].

Determination of antimicrobial activity

The disc-diffusion assay was used to determine the antimicrobial activity of the investigated ethanolic extracts of *T. vulgare* against a panel of microorganisms including gram-positive and gram-negative bacteria: *Staphylococcus aureus* (ATCC 25923), *Bacillus subtilis*, *Pseudomonas aeruginosa* (ATCC 27853) and *Escherichia coli* (ATCC 25922) and the fungus *Candida albicans* (ATCC10231)[23]. Each microorganism was suspended in Mueller Hinton (MH) broth and diluted approximately to $10E6$ colony forming unit (cfu)/mL. They were "flood-inoculated" onto the surface of MH agar and MH Dextrose Agar (MDA) and then dried. Six millimetres diameter wells were cut from the agar using a sterile cork-borer and 15 μL of each extract were delivered into the wells. The plates were incubated at 37°C and the diameters of the growth inhibition zones were measured after 18 h. Ciprofloxacin (25 $\mu\text{g/well}$) and Fluconazole (25 $\mu\text{g/well}$) were used as standard drugs. The controls were performed with only sterile broth and with only overnight culture and 10 μL of 70% ethanol [23]. All tests were performed in triplicate, and clear halos greater than 10 mm were considered as positive results.

Statistical analysis

All the samples were analysed in triplicate; the average and the relative SD were calculated using the Excel software package.

REFERENCES

- [1]. V. Kumar, D. Tyagi, *Journal of Pharmacognosy and Phytochemistry*, **2013**, 2, 159.
- [2]. V. Ciocarlan, "Illustrated Flora of Romania. Pteridophyta et Spermatophyta", Ceres Publishing House: Bucharest, Romania, **2009**.

- [3]. S. Rosselli, M. Bruno, F.M. Raimondo, V. Spadaro, M. Varol, A. T. Koparal, A. Maggio, *Molecules*, **2012**, *17*, 8186.
- [4]. L.T. Al-Barwary, *International Journal of Sciences: Basic and Applied Research*, **2013**, *11*, 84.
- [5]. S. Lahlou, A. Tahraoui, Z. Israili, B. Lyoussi, *Journal of Ethnopharmacology*, **2007**, *110*, 458.
- [6]. S. Lahlou, K.C. Tangi, B. Lyoussi, N. Morel, *Journal of Ethnopharmacology*, **2008**, *120*, 98.
- [7]. L.A. Alvarez, S. Habtemariam, M. Juan-Badaturuge, C. Jackson, F. Parra, *Phytotherapy Research*, **2011**, *25*, 296.
- [8]. D. Fraisse, C. Felgines, O. Texier, J.L. Lamaison, *Food Science and Nutrition*, **2011**, *2*, 181.
- [9]. L.S. Godinho, L.S. Aleixo de Carvalho, C.C. Barbosa de Castro, M.M. Dias, P. de Faria Pinto, A.E. Miller Crotti, P.L. Silva Pinto, J. de Moraes, A.A. Da Silva Filho, *The Scientific World Journal*, **2014**, *2014*, 1.
- [10]. C.A. Williams, J.B. Harborne, H. Geiger, J.R. Hoult, *Phytochemistry*, **1999**, *51*, 417.
- [11]. V.A. Kurkina, A.I. Khusainova, E.D. Daeva, V.I. Kadentse, *Chemistry of Natural Compounds*, **2011**, *47*, 284.
- [12]. Ya. Polle, R.G. Ovodova, A.S. Shashkov, Yu.S. Ovodov, *Carbohydrate Polymers*, **2002**, *49*, 337.
- [13]. O. Acha de la Cruz, J. Guerrero, R. Podea, I. Batiu, *Chemical Bulletin of „Politehnica” University of Timisoara*, **2008**, *53*, 10.
- [14]. M. Bichra, C. El-Modafar, A. El-Abbassi, H. Bouamama, F. Benkhalti, *Journal of Microbiology, Biotechnology and Food Sciences*, **2013**, *2*, 2320.
- [15]. C.S. Fodorea, L. Vlase, S.E. Leucuța, M. Tamas, *Chemistry of Natural Compounds*, **2005**, *41*, 400.
- [16]. R.I. Moldovan, R. Oprean, D. Benedec, D. Hanganu, M. Duma, I. Oniga, L. Vlase, *Digest Journal Nanomaterials and Biostructures*, **2014**, *9*, 559.
- [17]. D. Benedec, L. Vlase, I. Oniga, A.C. Mot, G. Damian, D. Hanganu, M. Duma, R. Silaghi-Dumitrescu, *Molecules*, **2013**, *18*, 8725.
- [18]. Romanian Pharmacopoeia Commission National Medicines Agency. Romanian Pharmacopoeia, Xth ed.; Medical Publishing House: Bucharest, Romania, **1993**.
- [19]. M.A. Anton, A.M. Pinteaa, D.O. Rugină, Z.M. Sconța, D. Hanganu, L. Vlase, D. Benedec, *Digest Journal Nanomaterials and Biostructures*, **2013**, *8*, 973.
- [20]. L. Vlase, D. Benedec, D. Hanganu, G. Damian, I. Csillag, B. Sevastre, A.C. Mot, R. Silaghi-Dumitrescu, I. Tilea, *Molecules*, **2014**, *19*, 5490.
- [21]. M. Wegiera, H.D. Smolarz, M.J. Druch, M. Korczak, K. Kopron, *Acta Poloniae Pharmaceutica. Drug Research*, **2012**, *69*, 263.
- [22]. M. Juan-Badaturuge, S. Habtemariam, C. Jackson, M.J. Thomas, *Natural Product Communications*, **2009**, *4*, 1561.
- [23]. D.S. Mi Reeves, L.O. White, “Principles of methods of assaying antibiotics. In *Pharmaceutical Microbiology*”, 3rd Edition, Blackwell Scientific Publication, **1983**.

- [24]. European Directorate for Quality Medicines, European Pharmacopoeia, 7th Edition, European Directorate for Quality Medicines, Strasbourg, **2010**.
- [25]. J.C. Espin, C. Soler-Rivas, H.J. Wichers, *Journal of Agricultural and Food Chemistry*, **2000**, *48*, 648.
- [26]. K. Slinkard, V.L. Singleton, *American Journal of Enology and Viticulture*, **1977**, *28*, 49.

THERMAL STABILITY OF ANTHOCYANINS FROM COMMON DOGWOOD (*CORNUS SANGUINEA* L.) FRUITS

BIANCA MOLDOVAN^a, ROZALIA MINTĂU, LUMINIȚA DAVID*

ABSTRACT. The Common dogwood (*Cornus sanguinea* L.) fruits are known for their high antioxidant activity, partially due to their anthocyanin content. The aim of this study is to examine the storage stability of anthocyanins from these fruits, at different temperatures (2°C, 22°C and 75°C). The results show that thermal degradation reaction of anthocyanins from Common dogwood fruits complies with first-order reaction kinetics. Degradation parameters, such as half-life $t_{1/2}$, reaction rate constant k and activation energy E_a values were determined. Anthocyanin extract stored at 2°C presented the highest stability with a degradation constant rate of $1.0 \cdot 10^{-3} \text{ h}^{-1}$. The calculated thermal degradation activation energy of the investigated fruits extract was $E_a = 40.35 \text{ kJ/mol}$.

Keywords: *Cornus sanguinea* L., anthocyanins, degradation kinetics

INTRODUCTION

The consumer acceptability and the appearance of food products are directly affected by their colour. Recent studies alert on the severe toxicity of synthetic dyes used in the food industry [1, 2]. Consequently, the food industry is now searching for natural food colorants as a safety alternative to the artificial ones. Plant sources are widely used to develop food additives that have both colouring and health beneficial properties. Anthocyanins, betacyanins, chlorophylls and carotenoids are the main groups of natural pigments. As red synthetic dyes are the most toxic and some of them, such as Amaranth Red and Ponceau GR, banned in the USA and Europe, finding new natural sources for red pigments significantly increased lately. Anthocyanins are the largest class of red water soluble natural colours that offer alternatives to synthetic toxic dyes.

^a Babeş-Bolyai University, Faculty of Chemistry and Chemical Engineering, 11 Arany Janos str., RO-400028, Cluj-Napoca, Romania, * Corresponding author muntean@chem.ubbcluj.ro

Anthocyanins are naturally occurring flavonoids which play an important role in the attractive colour (red, pink, orange, purple and blue) of fruits, flowers, leaves and vegetables. Studies have shown that they also possess a number of potential health benefits for humans, such as antioxidant, anticancer, anti-diabetic, anti-inflammatory and anti-obesity properties [3-5]. Many plants such as red grapes, red cabbage, Roselle calyx, blood orange are the main sources of anthocyanins for the food industry. All these plants present a high economical value, so looking for alternative anthocyanin sources is of great interest. Less consumed fruits, such as Black elderberry, European cranberrybush, Cornelian cherries gained lately attention for this purpose [6, 7].

Common dogwood (*Cornus sanguinea* L.) belongs to *Cornaceae* family, being native to most of Europe and Western Asia. The fruit is a black berry, containing a single seed, eaten especially by some mammals and birds [8]. Reported studies on *Cornus sanguinea* L. fruits and their properties are limited. Dogberries extracts are known to possess a high antioxidant activity, even higher than *Ginkgo biloba* extract [8]. Anthocyanins rich dogberries extract can be regarded as promising candidate for value-added ingredients for a variety of functional foods and nutraceuticals.

The colour of anthocyanins depends essentially on their different structural forms, strongly related to the pH value.

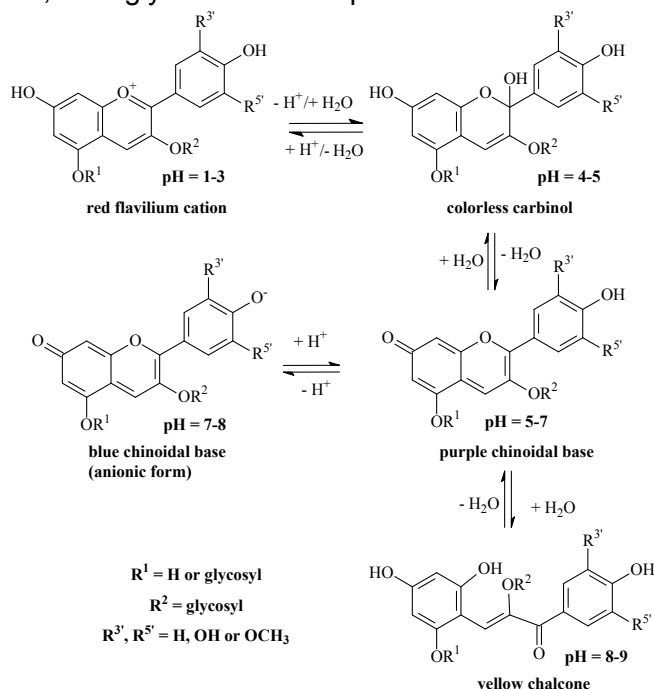


Figure 1. Chemical structures of anthocyanins as a function of pH

A mixture of equilibrium forms of anthocyanins: red flavylium cation, colourless carbinol, purple quinoidale base and yellow chalcone coexists (Figure 1) at pH values between 3 and 6 [9].

The use of anthocyanins as colorants in food systems is limited by their low stability. The degradation reaction of these red pigments results in appearance of undesirable colourless or brown compounds which affect the physicochemical properties of foods. The most important factor that affects the stability of anthocyanins is the temperature. Colour degradation can be observed when the temperature increases [10, 11].

Thus, investigation of anthocyanin degradation and measurement of their content at various intervals of storage is useful for the food industry.

However, to date, no information is available in the literature on the degradation kinetics of dogwood berries anthocyanins. Consequently the aim of this study was to evaluate the effect of temperature on the stability of these natural pigments and the accurate determination of the kinetic parameters for their degradation process in order to use *Cornus sanguinea* L. berries as source for natural red colorants.

RESULTS AND DISCUSSION

The total anthocyanin content of Common dogwood fruits extract was determined using the pH differential method developed by Giusti and Wrolstad [12]. This method measures differences in absorbance of the anthocyanin extracts at two different pH values – pH 1 and 4.5 - resulted as structural change of the red flavylium cation, the chemical form which predominates at pH = 1 in the colorless carbinol, the major structural form at pH = 4.5. This method allows an accurate determination of total monomeric anthocyanin content and is widely used for measuring this parameter in fruit extracts. The pigment content was calculated from the experimental data according equation (1) and expressed as cyanidine-3-glucoside (Cy-3-Glu) equivalents:

$$TA = \frac{A \cdot MW \cdot DF \cdot 1000}{\epsilon \cdot l} \quad (1)$$

where: TA = total anthocyanin content (mg/L)

A = absorbance, calculated as: (equation 2)

$$A = (A_{\text{pH } 1.0} - A_{\text{pH } 4.5})_{506 \text{ nm}} - (A_{\text{pH } 1.0} - A_{\text{pH } 4.5})_{700 \text{ nm}} \quad (2)$$

MW = molecular weight (g/mol)

DF = dilution factor

l = path length (cm)

ϵ = molar extinction coefficient (L/mol/cm)

1000 = conversion factor from gram to milligram.

The initial content of the total monomeric anthocyanins in the dogberries extract was 114.8 mg Cy-3-Glu equivalents / L.

The changes in the total anthocyanin content during storage of Common dogwood fruits extracts at different temperatures was investigated in order to establish the degradation reaction kinetic order as well as the kinetic parameters of this reaction. The graphical method was used to determine the order of reaction for the degradation of anthocyanins by action of temperature. The degradation process of anthocyanins was strongly influenced by temperature. The decreases of the anthocyanin content of the investigated extracts during storage at 2°C and 22°C were plotted as a function of time (Figure 2).

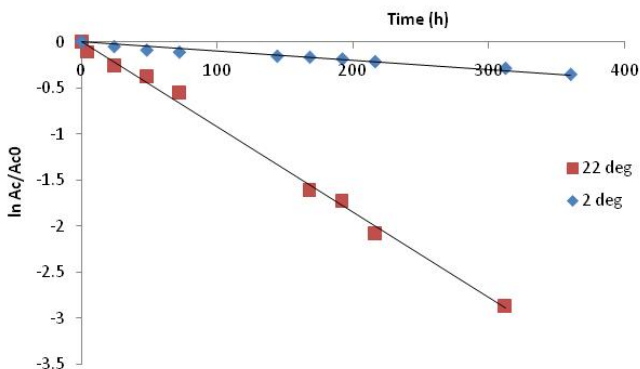


Figure 2. Influence of temperature on the degradation reaction of anthocyanins from Common dogwood fruits extract at 2°C and 22°C

The high linear correlation coefficients R^2 (Table 1) clearly indicate that the degradation of dogberries anthocyanins from aqueous extract stored at low temperatures followed first order reaction kinetics.

Table 1. Kinetic parameters of the degradation process of anthocyanins from dogberries extract at different temperatures

Temp. (°C)	k (h ⁻¹)	t _{1/2} (h)	R ²
2	0.001	693	0.9467
22	0.0093	74.52	0.9956
75	0.0504	13.75	0.9903

This kinetic model was reported by other researchers [13-16]. The monomeric anthocyanin content decreased 80% when the extract was stored at room temperature (22°C), while storage at refrigerator (2°C) resulted in cca. 15% loss of the anthocyanins in one week. Increasing the storage temperature from 2°C to 22°C caused a 9.3 fold increase of the reaction rate constant, from $k_{2^{\circ}\text{C}} = 1 \cdot 10^{-3} \text{ h}^{-1}$ to $k_{22^{\circ}\text{C}} = 9.3 \cdot 10^{-3} \text{ h}^{-1}$ (Table 1).

As expected, the anthocyanins degradation process was greater when the extract was exposed to elevated temperatures (75°C). Figure 3 presents the linear regression of the anthocyanin content from the extract stored at the above mentioned temperature. The half-life value of the degradation reaction determined from the experimental data was 13.75 h, the process being 50 fold faster than at 2°C. The decrease of anthocyanins content over time fitted a first order kinetics with a good regression coefficient.

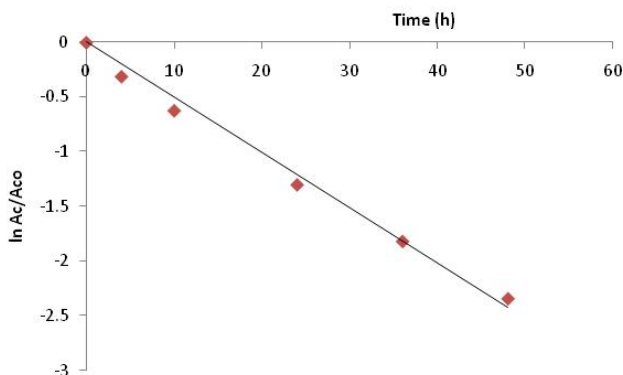


Figure 3. Influence of temperature on the degradation reaction of anthocyanins from Common dogwood fruits extract at 75°C

The temperature dependence of the degradation process was described by the Arrhenius equation (3):

$$k = K_0 e^{-E_a/RT} \quad (3)$$

where: k = rate constant (h^{-1})

K_0 = frequency factor (h^{-1})

E_a = activation energy (kJ/mol)

R = universal gas constant (8.314 J/mol/K)

T = absolute temperature (K)

Plotting $\ln k$ as a function of $1/T$ (Figure 4) the Arrhenius activation energy E_a was calculated. The activation energy for the dogberries anthocyanins degradation $E_a = 40.35$ kJ/mol was comparable to the values found in the literature. Other researchers reported similar values for the degradation process of plums anthocyanins ($E_a = 37.48$ kJ/mol) [17] but also higher values were found for anthocyanins from other sources, e.g. 65.32 kJ/mol for grape pomace [18] and 58.55 kJ/mol for Cornelian cherries pigments [7], proving that the natural colorants from *Cornus sanguinea* L. fruits are less susceptible to degradation by exposure to elevated temperatures.

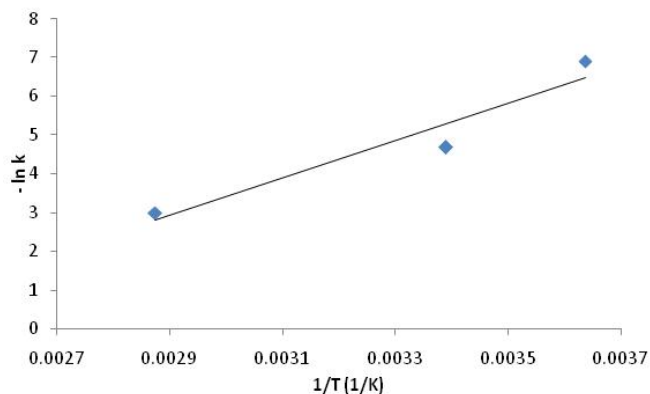


Figure 4. The Arrhenius plots for degradation of anthocyanins in dogberries extracts

All these results clearly indicate that low storage temperatures are required to minimize the loss of anthocyanins from Common dogwood fruits.

CONCLUSIONS

The results from the present research provide accurate information regarding the kinetic parameters of the degradation process of anthocyanins from *Cornus sanguinea* L. fruits. The reaction kinetics of this process fitted to a first-order model in all the investigated conditions. Increasing temperature resulted in higher degradation rate constants values which ranged from $1 \cdot 10^{-3} \text{ h}^{-1}$ to $50.4 \cdot 10^{-3} \text{ h}^{-1}$. The determined E_a value for the investigated process suggests that the anthocyanins from dogberries are rather stable, fact that indicates that these berries can be used as an important alternative source of natural red colorants for the food industry.

EXPERIMENTAL SECTION

Chemicals and reagents

All chemicals and reagents were purchased from Merck (Darmstadt, Germany), were of analytical grade and were used without further purification. A TYPDP1500 Water distiller (Techosklo LTD, Držkov, Czech Republic) was used to obtain the distilled water.

Plant material

Samples of Common dogwood fruits (dogberries) were harvested in September 2014 from Cluj-Napoca, Romania. Fruits were packed in polyethylene bags and kept frozen at -18°C .

Extract preparation

The frozen dogberries were crushed in a mortar. Sixty g of fruit puree were transferred to an Erlenmeyer flask and 250 mL of distilled water were added. After stirring for 1 h at room temperature, the mixture was filtered under vacuum. The filtrate was quantitatively transferred to a 250 mL volumetric flask and made up to the mark with distilled water.

Determination of anthocyanin content

The crude fruit extract was mixed with the corresponding buffer solution (potassium chloride buffer, $\text{pH} = 1.0$ or sodium acetate buffer, $\text{pH} = 4.5$).

Aliquots of the extract (5 mL) were transferred to a 10 mL volumetric flask and made up to 10 mL with corresponding buffer ($\text{pH} = 1$ and $\text{pH} = 4.5$) and allowed to equilibrate for 15 minutes. Three identical samples were prepared for each pH value and anthocyanin content was measured one time for each replicate.

Visible spectra of the obtained solutions were recorded by scanning the absorbance between 400 and 700 nm, in order to determine $\lambda_{\text{VIS max}}$ of the samples, using an UV-VIS Perkin Elmer Lambda 25 double beam spectrophotometer. Quartz cuvettes of 1 cm pathlength were used. Absorbance readings were made against distilled water as a blank.

The absorbances of the samples were measured at 512 nm ($\lambda_{\text{VIS max}}$) and 700 nm.

Pigment content was calculated as equivalents of cyanidin-3-glucoside using $\text{MW} = 449.2 \text{ g/mol}$ and $\epsilon = 26,900 \text{ L/mol/cm}$.

Degradation studies

The extract was divided into 50 mL portions and stored in the dark, well capped to avoid evaporation, at 2°C (in refrigerator), at room temperature (22°C) and in a thermostatic water bath, preheated to 75°C , respectively ($\pm 1^{\circ}\text{C}$). At regular time intervals, samples were removed and analysis were conducted immediately.

ACKNOWLEDGMENTS

The Ministry of Education, Research, Youth and Sports, Romania supported this work (research project no. 147/2011 PN-II-PT-PCCA-2011-3-1-0914).

REFERENCES

- [1]. K.A. Amin, H.A. Hameid II, A.H. Abd Elsttar, *Food and Chemical Toxicology*, **2010**, *48*, 2994.
- [2]. Z.T. Erikson, E.A. Falkenberg, G.A.S. Metz, *PLoS One*, **2014**, *9*(6), e92132.
- [3]. T. Tsuda, F. Horio, K. Uchida, H. Aoki, T. Osawa, *Journal of Nutrition*, **2003**, *133*, 2125.
- [4]. M.A.L. Smith, K.A. Marley, D. Seigler, K.W. Singletary, B. Meline, *Journal of Food Science*, **2000**, *65*, 352.
- [5]. M. Crisan, L. David, B. Moldovan, A. Vulcu, S. Dreve, M. Perde-Schrepler, C. Tatomir, A.G. Filip, P. Bolfa, M. Achim, I. Chiorean, I. Kacso, C. Berghian Grosan, L. Olenic, *Journal of Materials Chemistry B*, **2013**, *1*, 3152.
- [6]. B. Moldovan, L. David, C. Chisbora, C. Cimpoi, *Molecules*, **2012**, *17*, 11655
- [7]. B. Moldovan, L. David, *Molecules*, **2014**, *19*, 8177.
- [8]. M.S. Stankovic, M.D. Topuzovic, *Acta Botanica Gallica: Botany Letters*, **2012**, *159*, 79.
- [9]. A. Castaneda-Ovando, M. Pacecho-Hernandez, M. Paez-Hernandez, J. Rodriguez, C. Galan-Vidal, *Food Chemistry*, **2009**, *113*, 859.
- [10]. W.D. Wang, S.Y. Xu, *Journal of Food Engineering*, **2007**, *82*, 271.
- [11]. R.E. Wrolstad, R.W. Durst, J. Lee, *Trends in Food Science and Technology*, **2005**, *16*, 423.
- [12]. M.M. Giusti, R.E. Wrolstad, *Current Protocols in Food Analytical Chemistry*, Wiley, New York, 2001, F.1.2.1-F1.2.13.
- [13]. B. Moldovan, L. David, R. Donca, C. Chișbora, *Studia Universitatis "Babes-Bolyai", Chemia*, **2011**, *56*, 189-194.
- [14]. J. Hellstrom, P. Matila, R. Karjalainen, *Journal of Food Composition and Analysis*, **2013**, *31*, 12.
- [15]. S.Q. Cao, L. Liu, S.Y. Pan, *Agricultural Sciences in China*, **2011**, *10*, 1992.
- [16]. C.P. Kechinschi, P.V. Guimaraes, C.P. Norena, I.C. Tessaro, L.D. Marczak, *Journal of Food Science*, **2010**, *75*, C173.
- [17]. J. Ahmed, J.U.S. Shivhare, G.S.V. Raghavan, *European Food Research and Technology*, **2004**, *218*, 525.
- [18]. D.K. Mishra, K.D. Dolan, L. Yang, *Journal of Food Science*, **2008**, *73*, E9.

FREEZE-DRYING KINETICS FOR DIFFERENT TYPES OF FOOD PRODUCTS

ADINA MICLĂUȘ^a

ABSTRACT. This study presents the experimental data and the analysis of freeze-drying kinetics of three types of frozen food products: leaves of spinach and watercress, yeast suspension and pre-boiled wet rice. The effective diffusion coefficients for each product during dehydration are determined by applying the mass transfer model described by the Fick's second law. The drying rates are obtained as a function of moisture content, and show specific curves of falling rate period.

Keywords: *freeze-drying, moisture ration, Fick's diffusion model, effective diffusion coefficient, drying rate.*

INTRODUCTION

Freeze-drying or lyophilisation is a unit operation which has been used in a number of applications for many years, most commonly in the food and pharmaceutical industries, in the production of products sensitive to heat: vaccines, pharmaceuticals, biotech products, foods and beverages. The freeze-drying technique, characterized by as high drying rate, low drying temperature and oxygen deficient drying environment, ensures the structural integrity and the preservation of most of the initial raw material properties, such as shape, taste, aroma, colour, flavour, texture, biological activity, nutritive values, vitamins and minerals etc. Up to now, it is the most important technique to dry coffee, enzymes, food ingredients and other high-value foods.

Freeze-drying is a dehydration process during which the moisture/water transformed in ice is removed by warming in the drying chamber under vacuum (the tray with the sample is placed between the heating plates), so that the ice sublimates from frozen materials.

^a *Universitatea Babeș-Bolyai, Facultatea de Chimie și Inginerie Chimică, Str. Kogălniceanu, Nr. 1, RO-400084 Cluj-Napoca, Romania, ghirisan@chem.ubbcluj.ro*

Freeze-drying has three steps: freezing, primary drying and second drying. First the material is frozen completely to convert the moisture into ice, by keeping the conditions of water below those of triple point (4.58 mm Hg, 0 °C) [1]. Then in the drying chamber, when the pressure is well below the vapour pressure of ice, the ice is transferred from the product to the condenser by *sublimation*, elimination of the frozen water, and the inside bounded unfrozen water is eliminated by *desorption* [2].

During sublimation: a) the heat is transferred from the shelf to the frozen material through the tray and the vial, and conducted to the sublimation front, b) the ice sublimates and the water vapour formed passes through the dried portion of the product to the surface of the sample, c) the water vapour is transferred from the surface of the product through the chamber to the condenser, and d) the water vapour condenses on the condenser.

As ice sublimates, the sublimation interface, which starts on the surface of the material, recedes and a porous shell of dried material remains. Considering the mass transfer mechanism, the vaporized water is transported through the porous layer of the dried material. At the end of sublimation step a porous plug is formed. Its pores correspond to the spaces that were occupied by ice crystals [3].

In the secondary drying step, unfrozen water is removed by desorption from the dried layer of the product. This stage is performed by increasing the temperature and by reducing the vapour pressure in the dryer.

In the contrast with mass transfer, which always flows through the dried layer, the heat transfer can take place by conduction through the dried layer or through the frozen layer [4, 5].

The major disadvantage of freeze-drying is the high cost of operation. Compared to air drying processes, which remove water in a single stage, freeze-drying is an expensive process since it takes large operation times and consumes large amounts of energy to freeze the product, to sublimate the ice, to condense the water vapour, and to maintain the vacuum pressure in the system [6, 7].

In the present work, the experimental data obtained during the freeze-drying process of different food products were analysed considering the mass transfer model. Experiments were carried out for: spinach and watercress leaves, which are rich in antioxidants and during the freeze drying can preserve the content of antioxidants as in fresh samples; yeast suspension, which is sensitive to temperature as other microbial species; and wet rice which has a high quantity of vitamins and minerals and can be rehydrated more easily after a freeze drying process.

The drying parameters: effective diffusion coefficient and mass transfer rate were determined using Fick's diffusion model, which described the mass transfer mechanism [8, 9].

RESULTS AND DISCUSSION

There are two type of models used to analyze the freeze-drying kinetics: diffusion models based on mass transfer mechanism and models which describe simultaneous heat and mass transfer processes for the solids.

Mass transfer model

The diffusion or mass transfer model is widely used in describing the mass transfer mechanism. The evolution of drying was characterised by the drying curve considering the variation of the moisture content (kg water/kg dried material) with the time (min) for spinach and watercress leaves, yeast suspension and wet rise grains (Figure 1).

The sample moisture content M was calculated on a dry basis according to equation (1):

$$M = \frac{m_t - m_f}{m_f} \quad (1)$$

M is moisture content dry basis (kg water/kg dried matter), m_t - sample weight at a specific time (kg), and m_f - finale sample dried weight (kg).

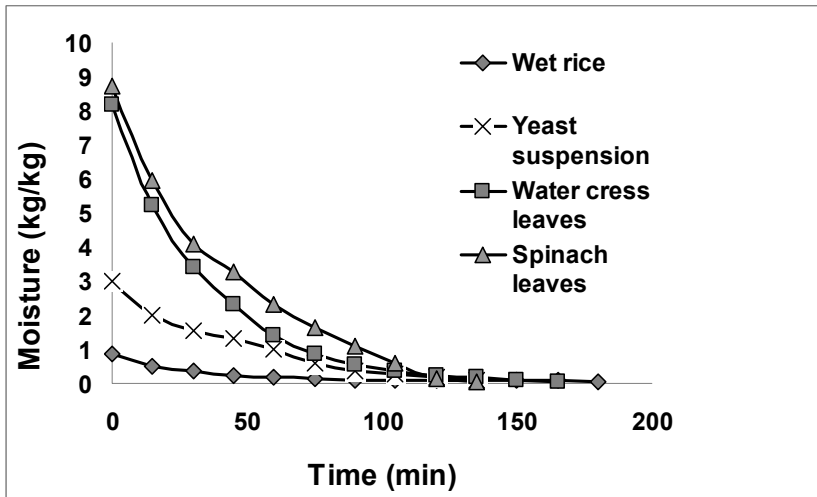


Figure 1. Drying curves.

As the drying curves show, the water loss is higher in the case of leaves than in the case of yeast suspension and than in the case of wet rice, considering the same period of time.

To determine the values of the water loss during the freeze-drying, the moisture ratio (M_R) on wet basis can be expressed in the exponential form of equation (2) [8, 9]:

$$M_R = \frac{M - M_e}{M_0 - M_e} = e^{-kt} \quad (2)$$

k is the drying constant, M , M_0 and M_e – moisture content at each measured time, at the begin and at the end of drying period (kg moisture/kg dried matter).

When the equilibrium moisture content M_e has negligible effect, the equation (2) becomes:

$$M_R = \frac{M}{M_0} = e^{-kt} \quad (3)$$

The moisture reduction was rapid during the initial stage of the drying up to the first hour, and then the moisture reduction is almost constant.

During a drying period of 180 min water cress and spinach lost more than 98 % of the initial moisture, while yeast suspension 96 % and wet rice only 75 %.

From these results, it could be stated that internal resistance to water transfer was greater in wet rice than in yeast suspension and than in leaves of watercress and spinach.

The Fick's second law of unsteady state diffusion was used in order to characterize the freeze-drying of our samples and to calculate the effective moisture diffusivity coefficient D_{eff} , considering constant moisture diffusivity, thin layers and a uniform initial moisture distribution:

$$M_R = \frac{M}{M_0} = Ae^{-\frac{D_{eff}t}{L^2}} \quad (4)$$

L is the thickness of sample.

The dimensionless moisture content (M_R) change during freeze drying is presented in Figure 2.

In order to determine the effective diffusion coefficients (D_{eff}) the experimental drying data in term of $\ln(M_R)$ are plotted versus time (Figure 3, a-c). Each straight line obtained has the slope given as equation (5) shows:

$$\text{Slope} = k = \frac{D_{eff}}{L^2} \quad (5)$$

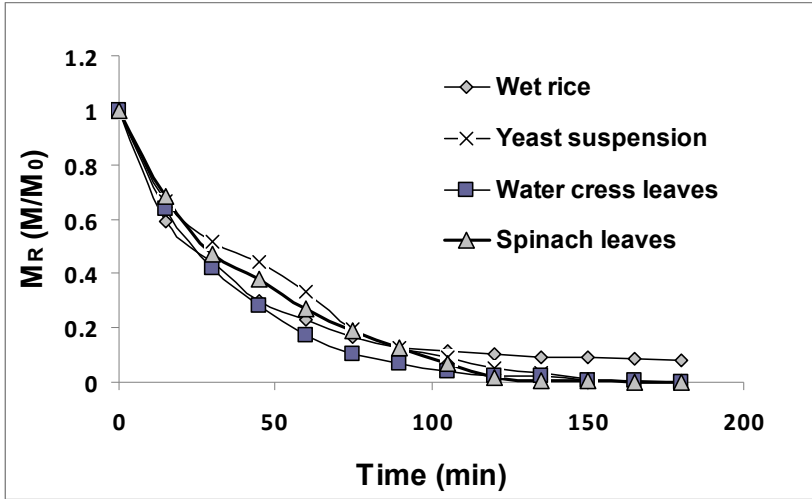


Figure 2. Moisture ratio (M_R) versus freeze drying time.

Diffusion coefficient is a drying constant important in understanding the drying behaviour of the product [10]. The Figure 3 shows for each material two distinct drying stages, with two diffusion coefficients, that can be attributed to the change of drying mechanism or to the change of porosity during freeze drying process.

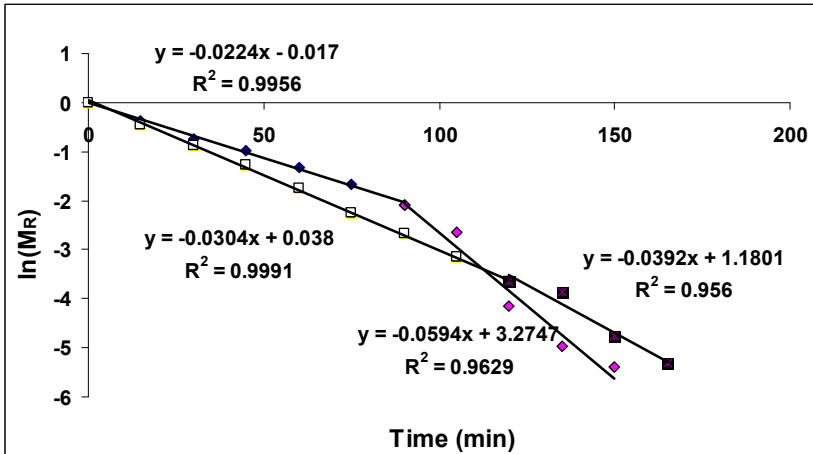


Figure 3. a) Moisture diffusion for freeze drying of spinach (rhomb) and water cress during the time drying (square).

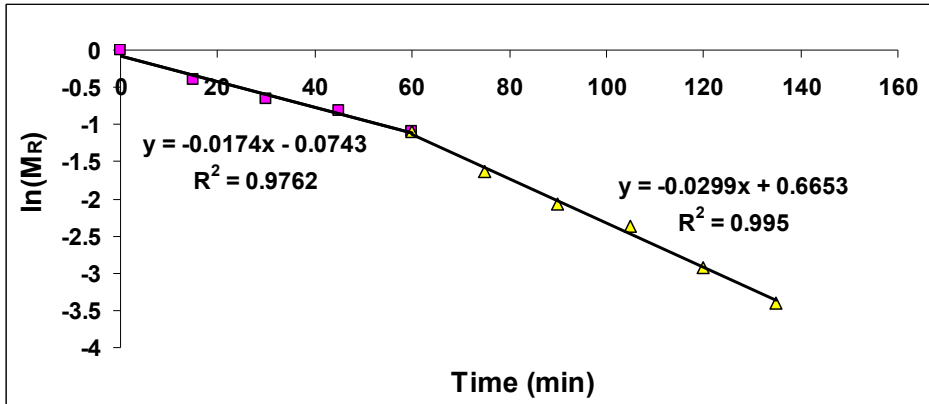


Figure 3. b) Moisture diffusion for freeze drying of yeast suspension during the time drying.

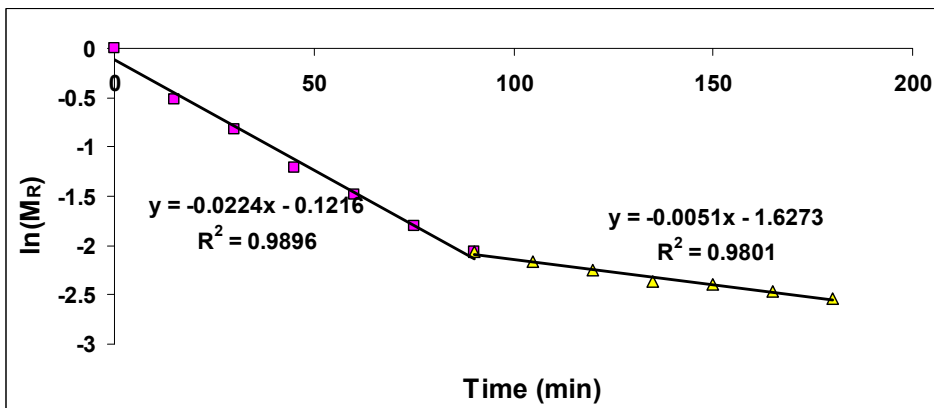


Figure 3. c) Moisture diffusion for freeze drying of wet grains rice in time.

The values of effective diffusivity for spinach are found to vary from $4.973 \cdot 10^{-8} \text{ m}^2/\text{s}$ on the first step to $1.336 \cdot 10^{-7} \text{ m}^2/\text{s}$ on the second step (with an average value of $9.1665 \cdot 10^{-8} \text{ m}^2/\text{s}$) and for the watercress the obtained values vary from $6.84 \cdot 10^{-8} \text{ m}^2/\text{s}$ on the first step to $8.82 \cdot 10^{-8} \text{ m}^2/\text{s}$ on the second step (with an average value of $7.83 \cdot 10^{-8} \text{ m}^2/\text{s}$). In the case of yeast suspension, the obtained diffusion coefficient values are $6.96 \cdot 10^{-8} \text{ m}^2/\text{s}$ in the first step and $1.2 \cdot 10^{-7} \text{ m}^2/\text{s}$ in the second step, (with an average value of $9.48 \cdot 10^{-8} \text{ m}^2/\text{s}$), while in the case of wet rice the values are $8.96 \cdot 10^{-8} \text{ m}^2/\text{s}$ in the first step and $2.04 \cdot 10^{-8} \text{ m}^2/\text{s}$ in the second step (with an average value of $5.5 \cdot 10^{-8} \text{ m}^2/\text{s}$).

The obtained values of diffusion coefficient in the case of leaves and yeast suspension have shown that during freeze-drying the resistance to the mass transfer is higher at initial stage (D_{eff} is lower in first stage) and gradual formation of porous structure improves mass transfer (D_{eff} is higher in the second stage).

In the case of wet rice the value of D_{eff} is higher in the first stage and lower in the second stage, the rice surface being affected by shrinkage, and so the resistance to the mass transfer increases during the experiment.

The drying rates, calculated by equation (6) versus moisture ration are shown in Figure 4.

$$D_R = \frac{\Delta M}{A \cdot \Delta t} \quad (6)$$

where A is the surface area of the tray where each sample is placed.

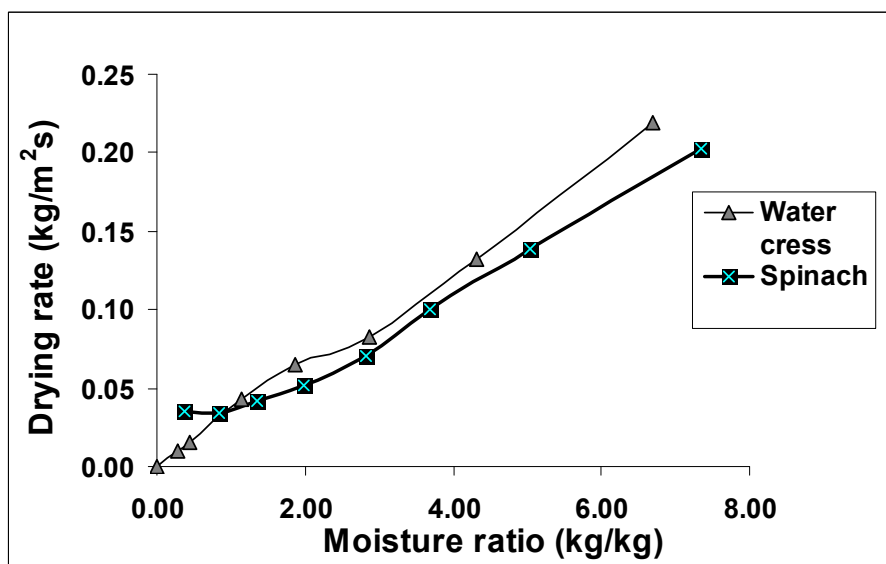


Figure 4. a. Drying rate versus moisture ratio in the case of leaves.

As can be seen in Figure 4, drying rate decreases continuously with the moisture content, which is specific for the falling rate period. This was mainly due to the higher moisture migration from the surface as drying proceeded.

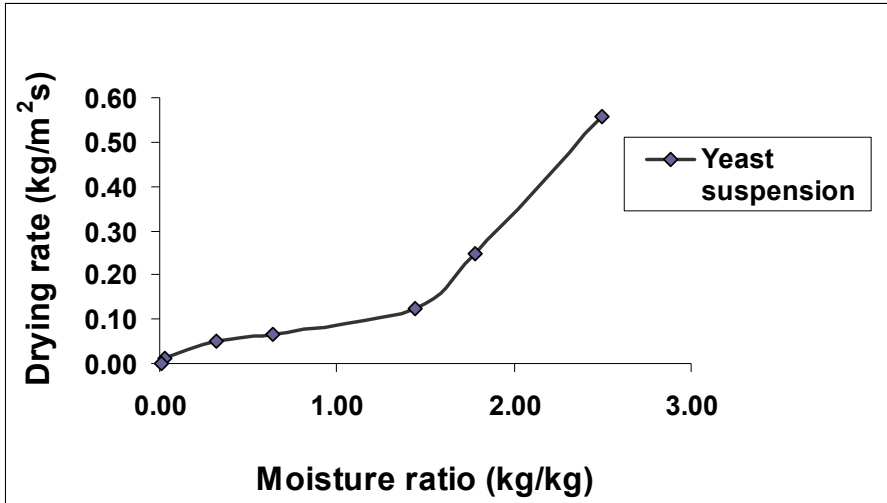


Figure 4. b. Drying rate versus moisture ratio in the case of yeast suspension.

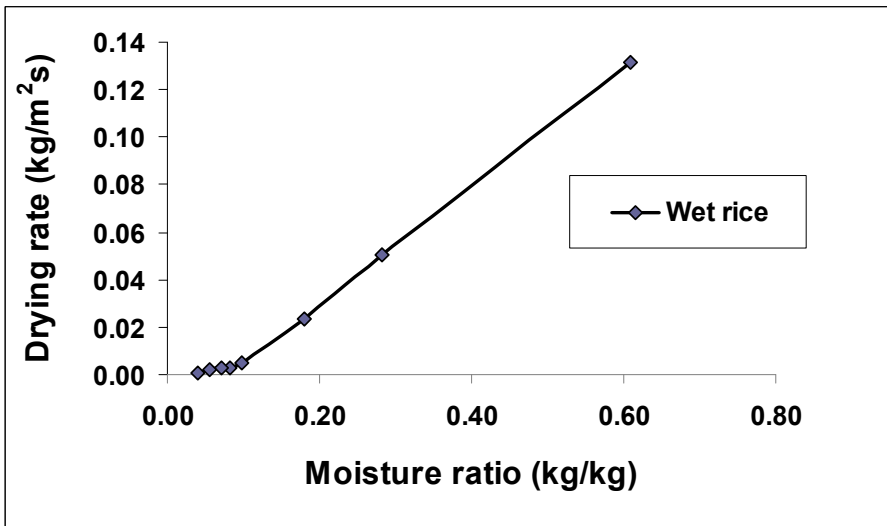


Figure 4. c. Drying rate versus moisture ratio in the case of wet rice.

Higher diffusion rate during freeze drying obtained for the sample containing yeast suspension and leaves of watercress and spinach comparative to wet rice grains can be explained by the better mass transfer in first structures/textures.

In the same time, only in the case of pre-boiled wet rice the diffusion coefficient decreases from the first stage to the second one, which could mean that for this product the second stage of drying involves the decrease of the porosity due to the shrinkage.

CONCLUSIONS

The results obtained by the freeze-drying of spinach, watercress leaves, yeast suspension and pre-boiled wet rice have shown the change of the drying mechanism during the process for each product.

The effective diffusion coefficients were determined by applying the Fick's second law. The values of effective diffusivity were found to vary from $4.973 \cdot 10^{-8} \text{ m}^2/\text{s}$ on the first step to $1.336 \cdot 10^{-7} \text{ m}^2/\text{s}$ on the second step (with an average value of $9.1665 \cdot 10^{-8} \text{ m}^2/\text{s}$) for spinach, from $6.84 \cdot 10^{-8} \text{ m}^2/\text{s}$ on the first step to $8.82 \cdot 10^{-8} \text{ m}^2/\text{s}$ on the second step (with an average value of $7.83 \cdot 10^{-8} \text{ m}^2/\text{s}$) for the watercress, from $6.96 \cdot 10^{-8} \text{ m}^2/\text{s}$ in the first step and $1.2 \cdot 10^{-7} \text{ m}^2/\text{s}$ in the second step (with an average value of $9.48 \cdot 10^{-8} \text{ m}^2/\text{s}$) for yeast suspension, and from $8.96 \cdot 10^{-8} \text{ m}^2/\text{s}$ in the first step and $2.04 \cdot 10^{-8} \text{ m}^2/\text{s}$ in the second step (with an average value of $5.5 \cdot 10^{-8} \text{ m}^2/\text{s}$) for pre-boiled wet rice.

The drying rate has shown for each material continuously decreases with the decrease of moisture content, which is specific for the falling rate period.

EXPERIMENTAL

Each sample with the measured thickness (1.5 mm in the case of leaves, and 2 mm for yeast suspension and wet rice), placed in the tray, was first allowed to freeze for 24 hours at $-40 \text{ }^\circ\text{C}$ in the freezer and than the frozen sample, was placed inside the freeze dryer (ALPHA 1-2 LD_{Plus}, MARTIN CHRIST Gefriertrocknungsanlagen GmbH Germany) for a period of 3 hours at 0.1 – 0.15 mbar. Before placing the sample inside of the vacuum drying chamber, the temperature of the heating plate was reduced to $-40 \text{ }^\circ\text{C}$, the same value as the temperature of the frozen sample. The condenser temperature was kept from $-45 \text{ }^\circ\text{C}$ to $-50 \text{ }^\circ\text{C}$.

By connection to the vacuum pump, the material is warmed and so the ice sublimates without melting. The mass variation of the samples has been measured at each 15 minutes during 3 hours. The samples which were taking out from the freeze dryer were transferred to the desiccators for attaining equilibrium. Three replications were done for each case in order to obtain a reasonable average.

REFERENCES

- [1]. F. Jafar, M. Farid, *Drying Technology*, **2003**, 21(2), 249.
- [2]. S. Khalloufi, J.-L. Robert, C. Ratti, *J. Food Proc. Eng.*, **2005**, 28, 107.
- [3]. N.A. Williams, G.P. Polli, *J. Parenter. Sci. Technol.*, **1984**, 38, 48.
- [4]. M. Karel, "Freeze Drying and Advanced Food Technology", Academic Press, New York, **1975**, 177.
- [5]. J. Welte-Chanes, D. Bermúdez, A. Valdez-Fragoso, H. Mújica-Paz, S.M. Alzamora, "Handbook of Frozen Foods", Marcel Dekker Inc., New York, **2004**, chapter 2.
- [6]. J.P. George, A.K. Datta, *J. Food Eng.*, **2002**, 52, 89.
- [7]. A.I. Liapis, R. Bruttini, In "Freeze Drying. Handbook of Industrial Drying", Ed. A. Mujundar, CRC Press, **2007**, chapter 11.
- [8]. B.K. Bala, "Drying and Storage of Cereal Grains", Enfield N.H: Science Pub. **1997**, chapter 3.
- [9]. V. Kırmacı, H. Usta, T. Menlik, *Drying Technology*, **2008**, 26, 1570.
- [10]. A. Muthukumaran, "Foam-mat Freeze Drying of Egg White and Mathematical Modeling", PhD Thesis, **2007**.

MODEL PREDICTIVE CONTROL OF THE TEMPERATURE IN DRYING FOOD PRODUCTS

VASILE MIRCEA CRISTEA^a

ABSTRACT. The present work addresses the improvement of the drying process of food products by controlling their temperature, using the model predictive control strategy. Forced convection drying with hot air is considered for the slab shaped food product, described in a 2D geometry. Control is based on the model describing the space and time change of the temperature and concentration of water vapours and liquid water in the porous solid together with pressure, drying air velocity, moisture concentration and temperature change in the drying air. Model predictive control of the temperature inside the food slab is simulated using a typical ramp-constant temperature setpoint and results show the incentives of the proposed control strategy, aimed to conform to the drying program of the temperature for preserving the drying product specific quality.

Keywords: *Model predictive control, forced convection drying, food slab*

INTRODUCTION

The market driven forces of the food industry pose important challenges for the food producers, as the demanded quality and quantity of the products are facing severe competition between companies and continuously growing customers' expectations. Originally, the drying process of food products emerged from the traditional and natural way of preserving food for its consumption at a subsequent occasion with respect to their harvest or production time. Later, the reduction of the transportation and storage costs, associated to the relative large period for preserving their quality and the marked demands, have placed the dried food in a contest with the frozen or canned food products. Nevertheless, conserving the organoleptic properties of the dried food is not a trivial task and usually an optimal moisture content is

^a *Babeş-Bolyai University, Faculty of Chemistry and Chemical Engineering, 11 Arany Janos str., RO-400028, Cluj-Napoca, Romania, mcristea@chem.ubbcluj.ro*

desired to accomplish this requirement. When the water content is too large the food may be affected by bio-transformations by the growth of bacteria, yeasts or mould, and decomposes. The overdried food product may change or lose its aroma and other appreciated nutritive properties (e.g. each fruit and vegetable has a critical temperature above which a scorched taste develops).

An overview of the drying technology reveals that there are tens of thousands of products that need to be dried in over a 100 variants of dryers [1]. Mujumdar, Kowalski and Murugesan presented comprehensive and specific studies on the air convective drying of porous materials [2-4]. Representative drying investigations of the food has been carried out by Barbosa-Canovas, Kaya and Ruiz-Lopez [5-7].

Both traditional and new technological solutions require appropriate control systems for ensuring their economic efficiency and quality standards. Model Predictive Control (MPC) is the most promising and appreciated advanced process control methodology used in chemical engineering applications, in standalone or coupled with PID control structures and implemented in either decentralized, supervisory or in multivariable control configurations.

Based on these assumptions, the investigations and results presented in the paper show the way MPC may be used to control the food drying process by imposing a prescribed ramp-constant temperature setpoint for the drying food temperature. The case study of convective drying of carrot food slabs is investigated based on the experimental drying data reported by De Bonis et al. [8] and the preliminary traditional control simulation approach using the PI controller, presented in [9].

RESULTS AND DISCUSSION

The first step in developing the MPC drying application was the selection and software implementation of the mathematical model, which was further used as intrinsic component for the control strategy. The model used in this work consists in the drying model presented by De Bonis [8], with appropriate changes to make it suitable for implementation for control investigations in the COMSOL Multiphysics CFD software [9].

The model is a conjugate one, considering both the transient mass and heat transfer of water in the porous solid body and the surrounding air, together with the momentum transfer describing the flow and pressure of the fluid phase. An important particularity of the model is the irreversible first order kinetics accounted for the vapour and liquid water production or depletion and transport. This approach allows the computation of the moisture, temperature and flow fields and avoids the limitations of the boundary layer assumptions

with its associated need for empirical heat and mass transfer coefficients evaluation [8]. The heat transfer from the drying air to the solid surface is ruled by forced convection, while the heat transfer from the exterior to the interior of the solid is governed by the conduction mechanism. Vaporisation of the liquid water takes place both on the surface of the solid and in its inner volume. Water is basically transported in three ways: by diffusion, due to the liquid water concentration difference between the solid interior and its surface, by capillarity and by diffusion of water vapours from the inner part of the porous solid to its surface, due to vapours pressure differences [8, 9]. The main assumptions inherent to the model are: laminar flow of the drying air; density, specific heat and thermal conductivity of the solid and diffusivity of liquid water and vapours in the solid considered to be moisture dependent [8]; lack of any body force; inclusion of the capillary transport in the diffusion coefficient and assumption of the same diffusivity of the liquid water and vapours in the porous solid. The two considered domains are the solid body and its surroundings, as presented in figure 1.

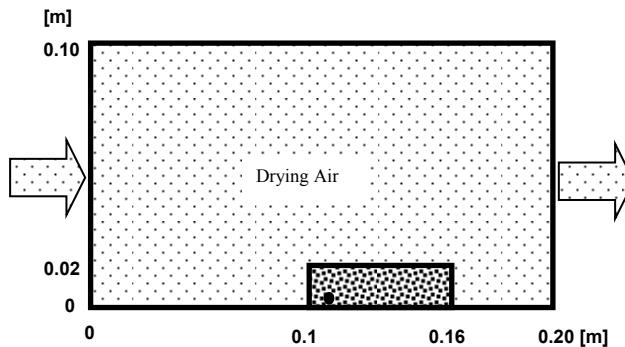


Figure 1. Geometry of the food slab and its associated surroundings.

Appropriate equations describe the two main domains of the food slab and its air surroundings. They are [8]:

$$\frac{\partial c_l}{\partial t} + \nabla \cdot (-D_{ls} \nabla c_l) = -K c_l, \quad (1)$$

$$\frac{\partial c_v}{\partial t} + \nabla \cdot (-D_{vs} \nabla c_v) = -K c_v, \quad (2)$$

$$\rho_s c_{ps} \frac{\partial T}{\partial t} + \nabla \cdot (-k_s \nabla T) = \dot{e}, \quad (3)$$

$$\frac{\partial c_v}{\partial t} + \nabla \cdot (-D_{va} \nabla c_v) = \mathbf{u} \cdot \nabla c_v, \quad (4)$$

$$\rho_a \left(\frac{\partial \mathbf{u}}{\partial t} + \mathbf{u} \cdot \nabla \mathbf{u} \right) = -\nabla p + \mu \cdot \nabla^2 \mathbf{u}, \quad (5)$$

$$\rho_a c_{pa} \frac{\partial T}{\partial t} + \nabla \cdot (-k_a \nabla T) = -\rho_a c_{pa} \mathbf{u} \cdot \nabla T. \quad (6)$$

The following notations have been used: c_l and c_v are the concentrations of liquid water and vapours; D_{ls} , D_{vs} , D_{va} , are the diffusivities of the liquid water, vapours in the porous solid and, respectively, the vapours diffusivity in the air; \mathbf{u} is the air velocity vector; p is the pressure; k_s and k_a are the thermal conductivities in the porous solid and air; \dot{e} is the cooling rate due to evaporation ($\dot{e} = \Delta h_{vap} M / K c_l$, with Δh_{vap} the latent heat of vaporisation and M_l the water molecular weight), ρ_s and ρ_a are the solid and air densities, c_{ps} and c_{pa} are the specific heats for the solid and air phases; μ is the dynamic viscosity; $K = K_0 e^{-E_a/RT} K_1^\alpha$ is the adopted Arrhenius type evaporation relationship [10, 11]. In the last relationship K_0 is a constant determined using experimental data, E_a is the activation energy [11], K_1 is a ratio of the process temperature to the reference temperature and α is a dimensionless temperature factor. The boundary conditions for the equations (2), (3), (4) and (6) account for full continuity for the vapours mass and temperature on the solid surface, excepting the bottom surface.

Model predictive control is the most industrial applied advanced control strategy in process engineering applications, very appreciated for its optimal character, predictive feature, preview ability and straightforward capability of incorporating constraints in the control law [12].

The present paper investigates the MPC control of the temperature in the drying product by manipulating the inlet drying air temperature. The location of the point where the solid temperature is controlled was chosen on the basis of its sensitivity to the temperature changes in time and is described by the coordinates of (0.11, 0.0025) [m], as indicated in figure 1. According to the practice oriented considerations the desired change of the solid temperature has the form of a ramp-constant time change. This temperature setpoint profile is providing a smooth removal of the water from the drying solid, avoiding steep changes that may affect the shape, structure or organoleptic characteristics of the final product.

The MPC temperature control is presented in figure 2. The controller uses an adaptive linearized model of the process obtained by identification based on simulation data from the nonlinear CDF model with time changing inlet drying air temperature.

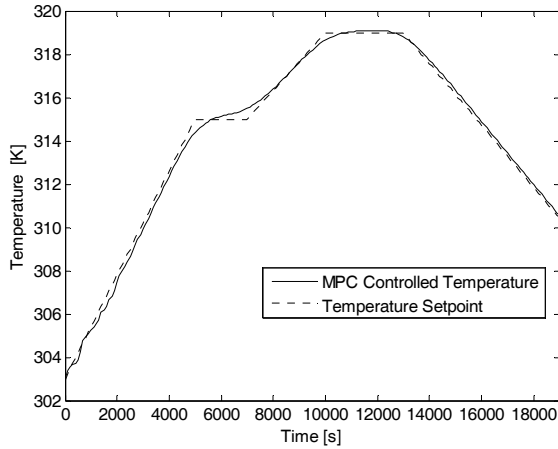


Figure 2. MPC controlled temperature in the drying solid.

The results show the capability of the MPC controller to bring the temperature close to its desired setpoint. It may be also noticed the preview potential of the controller that produces the predictive change of the temperature according to the future desired changes of the temperature setpoint. The liquid water concentration in the aforementioned porous solid point is presented in figure 3.

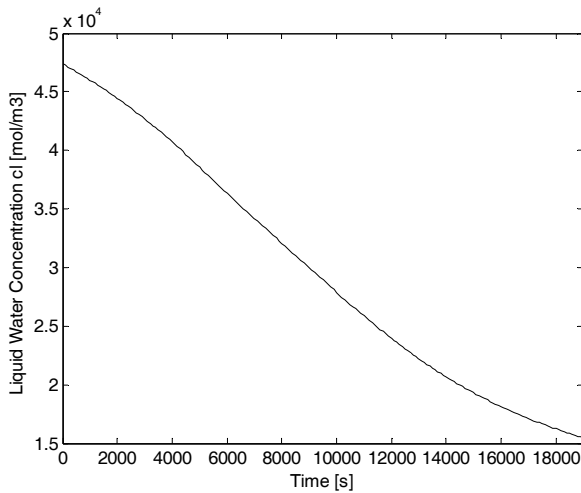


Figure 3. Change of the liquid water concentration in the drying solid.

The MPC controller was tuned such as to provide good control performance all over the range of the temperature setpoint program.

CONCLUSIONS

The distributed parameter mathematical model and the associated dynamic simulator development for the forced convection of the food slab drying process revealed the complex time and space behavior of the liquid and the vapor water content together with the change of the temperature in the porous solid and its surrounding drying air region. Drying process control based on the MPC algorithm has been investigated by controlling the temperature in the drying solid according to a ramp-constant temperature setpoint program. The control results show the efficiency of the proposed temperature control strategy both with respect to the offset and the setpoint tracking, while taking advantage of the prediction and preview capability of MPC. The simulator can be further used for the development of multivariable MPC control of the drying process in order to obtain improvement of the product quality, reduction of the energy consumption and shorter operation time. Based on new experimental data and suitable adjustments the simulator can be used for investigating the improvements of the convective drying in other food products of particular geometries.

EXPERIMENTAL SECTION

The mathematical model and simulator have been validated with experimental data from [7] and [8]. Detailed simulation results have been presented in previous work [9], for the temporal and spatial fields of main variables, showing values in agreement with the results reported in [8]. Initial air inlet temperature of $T_0=353\text{ K}$, moisture of $c_v=7\text{ mol/m}^3$ and velocity of $u=3\text{ m/s}$ have been considered in the simulations. The following numerical constants have been used: $K_0=7000\text{ s}^{-1}$, $E_a=48.7\text{ kJ/mol}$, $\alpha=0$, $c_{i0}=47\text{ kmol/m}^3$ (in the solid substrate), $T_{0s}=303\text{ K}$ and $D_{va}=2.55\cdot 10^{-5}\text{ m}^2/\text{s}$, together with moisture dependent expressions: $c_{ps}=1750+2345(X/(1+X))\text{ J/(kg K)}$, $k_s=0.49+0.443\exp(-0.206X)\text{ W/(m K)}$, $D_{vs}=D_{is}=2.8527\times 10^{10}\exp(0.2283369X)\text{ m}^2/\text{s}$, $\rho_s=440.001+90X\text{ kg/m}^3$, where X is the solid mass moisture content (on dry basis). The model equations for the drying simulator have been implemented in COMSOL Multiphysics CFD software. The drying control study has been performed in Matlab-Simulink using a special developed application for running the CFD nonlinear dryer model. MPC controller used the following tuning parameters: sampling time $T_s=100\text{ s}$, prediction horizon $p=20T_s$, control horizon $m=8T_s$, weight of the manipulated variable rate $uwt=0.5$ and the controlled variable weight $ywt=1$.

REFERENCES

- [1]. A.S. Mujumdar, "An Overview of Innovation in Industrial Drying: Current Status and R&D Needs, in Drying of Porous Materials", Editor Stefan Jan Kowalski, Springer Dordrecht, The Netherlands, **2007**, chapter 1.
- [2]. A.S. Mujumdar (Ed.), "Handbook of Industrial Drying", Taylor and Francis Group, New York, **2007**.
- [3]. S.J. Kowalski, "Drying of Porous Materials", Springer, Dordrecht, The Netherlands, **2007**.
- [4]. K. Murugesan, H.N. Suresh, K.N. Seetharamu, P.A. Aswatha Narayana, T. Sundararajan, *International Journal of Heat and Mass Transfer*, **2001**, 44, 4075.
- [5]. G.V. Barbosa-Canovas, H. Vega-Mercado, "Dehydration of Foods", Chapman &Hall, New York, **1996**.
- [6]. A. Kaya, O. Aydin, I. Dincer, *Journal of Food Engineering*, **2006**, 49, 3094.
- [7]. I.I. Ruiz-Lopez, A.V. Cordova, G.C Rodriguez-Jimenes, M.A. Garcia-Alvaro, *Journal of Food Engineering*, **2004**, 63, 117.
- [8]. M.V. De Bonis, G. Ruocco, *Journal of Food Engineering*, **2008**, 89, 232.
- [9]. V.M. Cristea, A. Irimita, G.S. Ostace, S.P. Agachi, *Computer Aided Chemical Engineering*, **2012**, 30, 932.
- [10]. S. Azzouz, A. Guizani, W. Jomaa, A. Belgith, *Journal of Food Engineering*, **2002**, 55, 323.
- [11]. J.S. Roberts, C.H. Tong, *International Journal of Food Properties*, **2003**, 6, 355.
- [12]. M. Kano, M. Ogawa, *Advanced Control of Chemical Processes*, 7th IFAC International Symposium on Advanced Control of Chemical Processes, **2009**, 7, 10.

QSAR STUDY ON (1-METHYLPYPERIDIN-4-YL) PROPANOATE DERIVATIVES BY SIMILARITY CLUSTER PREDICTION

TEODORA E. HARSA^a, ALEXANDRA M. HARSA^a, AND
MIRCEA V. DIUDEA^{a*}

ABSTRACT. Derivatives of (1-methylpiperidin-4-yl) propanoate, with similar biological characteristics, have been reported for patients with Alzheimer disease [1,2]. QSAR study was performed on a set of 40 (1-methylpiperidin-4-yl) propanoate derivatives, downloaded from the PubChem database and aligned over a hypermolecule that mimics the investigated correlational space. The best models describing log P of these (1-methylpiperidin-4-yl) propanoate derivatives were validated by leave-one-out procedure [3] and best predicted within similarity clusters.

Keywords: (1-methylpiperidin-4-yl) propanoate, log P, QSAR, Hypermolecule, similarity cluster

1. INTRODUCTION

1-[11C]methylpiperidin-4-yl propanoate (i.e. [11C]PMP) and N [11C]methyl piperidin-4-yl acetate ([11C]MP4A) are used as radioligands in positron emission tomography (PET) [4,5]. Synthesis of [11C]PMP can be achieved by direct N-methylation of 4-piperidinyl propanoate with [11C]methyl trifluoromethanesulfonate at room temperature in dimethyl-formamide [6].

Topological indices are numerical representations of the chemical structures, computed on the basis of molecular graph [7]. Topological indices can be easily calculated with TOPOCLUJ software and they have shown good correlation with log P [8,9].

QSAR/QSPR methodologies (Quantitative Structure Activity Relationships/ Quantitative Structure Property Relationships) attempt to correlate molecular structures with their properties or biological activities. QSAR is widely used in pharmacology, environmental search, and agricultural chemistry, etc. [10].

^a Babeş-Bolyai University, Faculty of Chemistry and Chemical Engineering, 11 Arany Janos str., RO-400028, Cluj-Napoca, Romania. * Corresponding author: diudea@gmail.com

Multiple linear regressions (MLR) relate e.g. log P (measuring the lipophilic character or drug-likeness of a given molecule) and topological indices, as shown in refs. [11-13].

2. DATA SET

A set of 40 molecular structures, derivatives of (1-methylpiperidin-4-yl) propanoate, have been downloaded from the Pubchem database [14] (Table 1), together with their log P. The set was split into the training set and test set (25 and 15 molecules, respectively, randomly chosen). The structures have been optimized at Hartree-Fock HF (6-31g(d,p)) level of theory. The calculations were performed in gas phase by Gaussian 09 [15].

Table 1. (1-methylpiperidin-4-yl) propanoate molecular structures (in SMILES code) and their log P (taken from PubChem).

Mol.	Canonical SMILES	Log P	CID
1	<chem>CCC(=O)OC1CCN(CC1)[11CH3]</chem>	1.2	6540307
2	<chem>CC(C)(C)C(=O)OC1CCN(CC1)C(C)(C)C</chem>	3.1	57613500
3	<chem>CC(C)N1CCC(CC1)OC(=O)C(C)(C)C</chem>	2.9	58873543
4	<chem>CC(CC(C)(C)N1CCCC1)OC(=O)C(C)(C)C</chem>	3.8	40500608
5	<chem>CCC(=O)OC1CCN(CC1)CC</chem>	1.5	24843023
6	<chem>CCC(=O)OC1CCN(CC1)C</chem>	1.2	133349
7	<chem>CCOC1CCN(CC1)CCC(=O)OCC</chem>	1.2	61220923
8	<chem>CCN1CCC(CC1)OC(=O)C</chem>	1.1	11480704
9	<chem>CCOC1CCN(CC1)CCC(=O)OC</chem>	0.9	61218612
10	<chem>CCCC(C)OC(=O)CCN1CCCC1</chem>	2.6	71028323
11	<chem>CCC(C)(C)C(=O)OC(C)CN1CCCC1</chem>	3.2	58545331
12	<chem>CCC(C)(C)C(=O)NCCN1CCCC1</chem>	2.2	58795427
13	<chem>CC(C)(C)C(C(=O)N1CCCC1)NC</chem>	1.9	58700497
14	<chem>CC(C)(C)C(CC1=CC=CC=C1)N(C)C</chem>	4	58172339
15	<chem>CC(C)(C)C(=O)C(CC1=CC=CC=C1)N(C)C</chem>	3.4	3637447
16	<chem>CCNC(=O)N1CCC(CC1)C(=O)NC(C)C</chem>	0.5	53548901
17	<chem>CC(C)(C)C1=CC=C(C=C1)C(=O)NC(C)(C)C</chem>	4.6	349124
18	<chem>CC(=O)NC1=CC=C(C=C1)C(=O)NC(C)(C)C</chem>	2	151118
19	<chem>CC1=CC=C(C=C1)C(=O)NC(C)(C)C</chem>	2.9	925429
20	<chem>CC(C)(C)OC(=O)N1CCCC(C1)C=O</chem>	1.1	42325667
21	<chem>CC1CCN(CC1C=O)C(=O)OC(C)(C)C</chem>	1.5	58010030
22	<chem>CC(C)(C)NC(=O)N1CCC(CC1)C(=O)N</chem>	-0.1	894347
23	<chem>CCC(C)(C)NC(=O)C1CCN(CC1)C(=O)N(C)C</chem>	1	47205727
24	<chem>CC(C)(C)NC(=O)C1CCN(CC1)C(=O)N(C)C</chem>	0.5	60779224
25	<chem>CCCC(=O)NCC1CCN(CC1)C(=O)NC(C)(C)C</chem>	1.4	49687908
26	<chem>CC(=O)C1CCN(CC1)C(=O)NC(C)(C)C</chem>	0.7	58171886
27	<chem>CC(C)CC(=O)NCC1CCN(CC1)C(=O)NC(C)(C)C</chem>	1.9	49687914
28	<chem>CC(C)C(=O)NCC1CCN(CC1)C(=O)NC(C)(C)C</chem>	1.6	49687909
29	<chem>CCC(=O)NCC1CCN(CC1)C(=O)NC(C)(C)C</chem>	1.1	49687905
30	<chem>CC(C)(C)CC(C)(C)NC(=O)N1CCC(CC1)C(=O)N</chem>	1.6	24159137
31	<chem>CCC(=O)OC1CC[N]CC1</chem>	0.7	57426704
32	<chem>COC1CCN(CC1)CCC(=O)OC</chem>	0.5	43216573

33	<chem>CC(C)(C)CC(=O)NCC1CCN(CC1)C(=O)NC(C)(C)C</chem>	2.3	49687921
34	<chem>CC(C)CC(C(C)(C)C)NC(=O)C1CCN(CC1)C(=O)N(C)C</chem>	3	56793859
35	<chem>CC(C)C(=O)N1CCC(CC1)C(=O)NC(C)(C)C</chem>	1.5	60726650
36	<chem>CCCC(=O)N1CCC(CC1)C(=O)NC(C)(C)C</chem>	1.3	45596615
37	<chem>CCC(C)(C)NC(=O)C1CCN(CC1)C(=O)C</chem>	1	39959127
38	<chem>CC(=O)N1CCC(CC1)C(=O)NC(C)(C)C</chem>	0.5	17148671
39	<chem>CC(C)(C)C(=O)NCC1CCN(CC1)C(=O)NC(C)(C)C</chem>	2	49687916
40	<chem>CC(=O)CCN1CCC(CC1)OC(=O)C</chem>	0.4	58811219

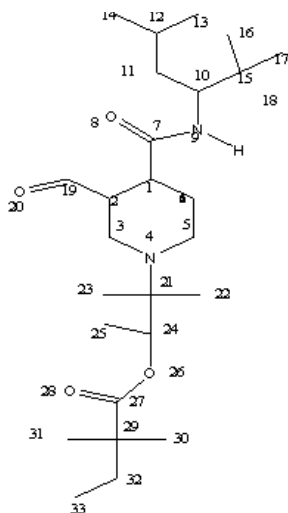


Figure1: Hypermolecule

A hypermolecule (Figure 1) was built up as the reunion of the structural features in all 40 molecules under study [16,17].

3.COMPUTATIONAL DETAILS

Topological indices have been computed by TOPOCLUJ software [8]; some of them (Total adjacency = Adj, Conectivity=C, Detour = De, Distance = Di, D3D), $SD_{k,k=1,2}$, HOMO (in au) and log P are listed in Table 2.

4. RESULTS AND DISCUSSION

4.1. Mass fragments description (case 1)

4.1.1.Data reduction (for log P)

In the step of data reduction, all the descriptors with the variance $Var < 20\%$ and those with intercorrelation larger than 0.80 have been discarded.

Correlation weighting was performed on all the positions in the hypermolecule: the correlating coefficients of the statistically significant positions of the hypermolecule were used to multiply the local descriptors. Next, the correlating weighed local descriptors are summed to give a global descriptor, $SD_i = \sum_j CD_{ij}$ [18-20]. This new descriptor is a linear combination of the local weighed correlating descriptors for the significant positions in the Hypermolecule: H4, H8, H9, H10, H13, H14, H15, H18, H21, H23, H25, H27, H29, H32, H33,

$$\text{Eq: } \log P = 2.849 + 1.0001 \times SD_1, R^2=0.907, \text{ St. Error}=0.327, F=0.327$$

Table 2. log P, correlating descriptors SD, HOMO energy (au) and topological indices for the set of (1-methylpiperidin-4-yl) propanoates in Table 1

Mol.	log P	SD1	SD2	HOMO	Adj	Di	C	CjDi
1	1.2	-1.421	-1.839	-9.207	15	402	16	512
2	3.1	-0.146	-0.567	-9.146	17	562	18	704
3	2.9	0.031	-1.034	-9.175	16	480	17	601
4	3.8	1.026	0.423	-9.025	19	750	20	856.5
5	1.5	-1.410	-2.431	-9.263	13	276	14	352
6	1.2	-1.233	-2.294	-9.322	12	216	13	275
7	1.2	-1.632	-2.248	-9.261	16	537	17	659
8	1.1	-1.429	-2.541	-9.250	12	217	13	281
9	0.9	-1.647	-2.251	-9.272	15	440	16	548
10	2.6	-0.441	-1.187	-9.161	16	531	17	615.5
11	3.2	0.148	-0.884	-9.032	17	574	18	666.5
12	2.2	-0.258	-0.965	-9.244	16	510	17	594.5
13	1.9	-1.088	-2.500	-9.269	15	358	16	433.5
14	4	1.004	0.600	-8.847	15	368	15	444.5
15	3.4	0.971	-0.354	-9.153	17	518	18	610.5
16	0.5	-1.891	-2.983	-9.533	17	588	19	734
17	4.6	1.866	0.247	-9.680	17	556	18	697
18	2	-0.588	-1.523	-9.699	17	582	19	725
19	2.9	-0.588	-0.638	-9.648	15	366	16	458
20	1.1	-1.284	-2.417	-9.801	15	382	17	489.5

21	1.5	-1.284	-2.136	-9.769	16	452	18	578.5
22	-0.1	-2.919	-3.136	-9.694	16	475	18	595
23	1	-1.676	-2.716	-9.501	19	778	21	960
24	0.5	-1.676	-2.653	-9.524	18	667	20	831
25	1.4	-1.447	-2.106	-9.653	20	981	22	1190
26	0.7	-2.227	-3.415	-9.644	16	475	18	595
27	1.9	-0.595	-1.734	-9.665	21	1130	23	1361
28	1.6	-1.094	-2.044	-9.631	20	964	22	1173
29	1.1	-2.164	-2.636	-9.656	19	834	21	1021
30	1.6	-1.330	-2.554	-9.682	20	888	22	1064
31	2.4	-1.233	-1.162	-9.484	11	168	12	212.5
32	2	-1.147	-2.363	-9.282	14	355	15	443
33	2.3	-0.595	-1.387	-9.628	22	1281	24	1534
34	3	-0.160	-0.669	-9.501	23	1308	25	1562
35	1.5	-1.676	-2.243	-9.571	18	667	20	831
36	1.3	-1.871	-2.518	-9.562	18	682	20	846
37	1	-2.082	-2.814	-9.598	17	564	19	698
38	0.5	-2.082	-2.746	-9.599	16	475	18	595
39	2	-0.962	-1.615	-9.562	22	1096	23	1327
40	2	-1.219	-2.170	-9.137	15	434	17	546

4.1.2. QSAR models (for log P)

The models were performed on the training set (the 25 structures in Table 1) and the best results (in decreasing order of R²) are listed below and in Table 3.

(i) Monovariate regression

$$\log P = 2.741 + 1.014 \times SD_1$$

(ii) Bivariate regression

$$\log P = 2.764 + 1.013 \times SD_1 - 0.00004 \times D3D$$

(iii) Three-variate regression

$$\log P = 1.901 + 0.948 \times SD_1 + 0.008 \times De - 0.008 \times CjDi$$

(iv) Four-variate regression

$$\log P = -7.216 + 0.0828 \times SD_1 - 1.011 \times HOMO + 0.969 \times Adj. - 0.879 \times C$$

Table 3. Best models in describing log P in the training set of (1-methylpiperidin-4-yl) propanoate in Table 1

	Descriptors	R ²	Adjust. R ²	St. Error	F
1	SD ₁	0.930	0.927	0.311	304.509
2	HOMO	0.140	0.103	1.088	3.742
3	CjDi	0.009	-0.034	1.168	0.219
4	Di	0.004	-0.039	1.171	0.102
5	De	0.003	0.040	1.172	0.074
6	SD ₁ , D3D	0.930	0.923	0.318	145.776
7	SD ₁ , Di	0.930	0.923	0.318	145.658
8	SD ₁ , De	0.930	0.923	0.318	145.638
9	SD ₁ , CjDi	0.930	0.923	0.318	145.723
10	SD ₁ , Adj.	0.930	0.923	0.318	145.732
11	SD ₁ , De, CjDi	0.944	0.936	0.292	117.235
12	SD ₁ , Adj., C	0.939	0.931	0.302	108.542
13	SD ₁ , De, D3D	0.936	0.927	0.311	102.306
14	SD ₁ , CjDi, CjDe	0.936	0.926	0.312	101.724
15	SD ₁ , Di, D3D	0.932	0.922	0.320	95.885
16	SD ₁ , D3D, HOMO	0.930	0.920	0.325	92.813
17	SD ₁ , HOMO, C	0.930	0.920	0.325	92.783
18	SD ₁ , HOMO, Adj., C	0.952	0.943	0.275	99.593
19	SD ₁ , De, Di, D3D	0.938	0.926	0.313	75.728
20	SD ₁ , HOMO, Di, D3D	0.932	0.931	0.328	68.492

4.1.3. Model Validation (for log P)

(a) Leave-one-out

The best models from Table 3 describing log P of these (1-methylpiperidin-4-yl) propanoate derivatives were validated by leave-one-out LOO procedure, as listed in Table 4.

Table 4. LOO for some models in Table 3

	Descriptors	Q ²	R ² -Q ²	St. Error _{loo}	F _{loo}
1	SD ₁	0.919	0.011	0.334	260.613
5	SD ₁ , D3D	0.913	0.017	0.347	240.626
11	SD ₁ , De, CjDi	0.916	0.028	0.34	250.326
19	SD ₁ , HOMO, Adj., C	0.922	0.03	0.328	272.132

(b) External Validation

The values $\log P$ for the test set of (1-methylpiperidin-4-yl) propanoates were calculated by using equation cf. entry 11, Table 3. Data are listed in Table 5 and the monovariate correlation: $R^2=0.869$, St. Error=0.331, $F=86.123$ is plotted in Figure 2.

Table 5. Calculated values of $\log P$ for the molecules in the test set (Table 1)

Mol.	$\log P$	$\log P_{calc.}$
2	3.1	2.43
3	2.9	2.61
4	3.8	4.14
5	1.5	1.16
30	1.6	1.56
31	2.4	1.30
32	2	1.47
33	2.3	2.12
34	3	2.64
35	1.5	0.98
36	1.3	0.81
37	1	0.66
38	0.5	0.61
39	2	1.72
40	2	1.37

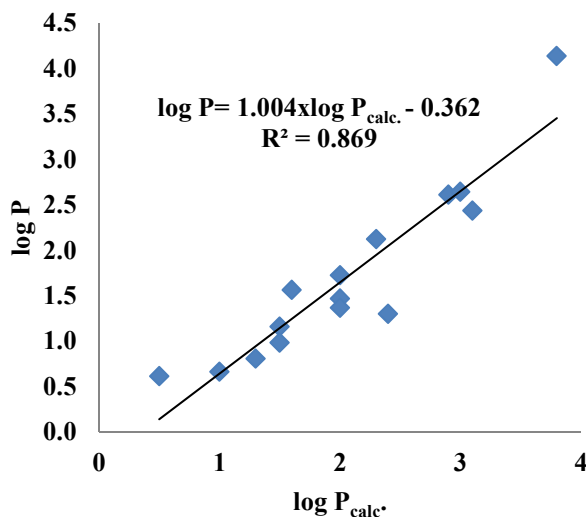


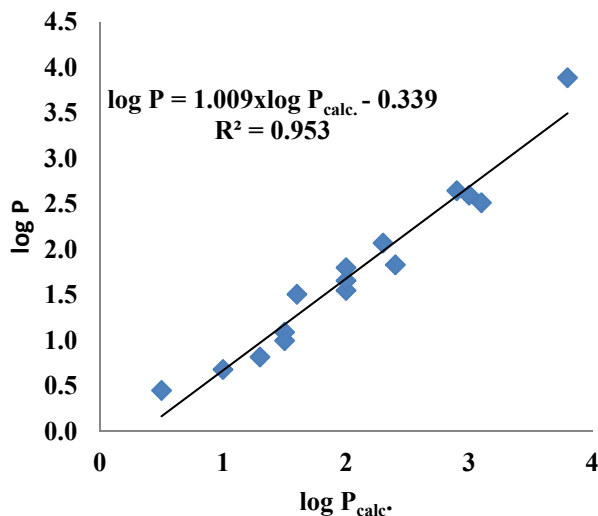
Figure 2. The plot $\log P$ vs. $\log P_{calc.}$ for the test set (external validation)

(c) Similarity Cluster Validation

Validation can also be performed by calculating $\log P$ for the molecules in the test set by using clusters of similarity: each of the 15 molecules is the leader of its own cluster, selected by 2D similarity among the 25 structures of the initial learning set. The values $\log P_{calc.}$ were computed by 15 new equations (the leader being left out) with the same descriptors as in eq. 11, Table 3. Data are listed in Table 6 and the monovariate correlation: $\log P = 1.009 \times \log P_{calc.} - 0.339$ $R^2=0.953$, St. Error=0.197, $F=265.759$ is plotted in Figure 3.

Table 6. Calculated values of log P for the molecules in the test set (Table 1)

Mol.	log P	log P _{calc.}
2	3.1	2.51
3	2.9	2.65
4	3.8	3.89
5	1.5	1.09
30	1.6	1.51
31	2.4	1.83
32	2	1.55
33	2.3	2.07
34	3	2.60
35	1.5	1.00
36	1.3	0.82
37	1	0.68
38	0.5	0.45
39	2	1.66
40	2	1.80

**Figure 3.** The plot log P vs. log P calc. for the test set (similarity cluster validation)

4.2. Partial charges description (case 2)

4.2.1. Data reduction (for log P)

This new descriptor is a linear combination of the local correlating descriptors for the significant positions in the hypermolecule (i.e. H1, H4, H7, H8, H11, H12, H13, H14, H15, H16, H17, H22, H24, H32, H33)

Eq., $\log P = 3.667 + 1.001 \times SD_2$ $R^2 = 0.892$, St. Error = 0.352, F = 313.391

4.2.2. QSAR models (for log P)

The models were performed on the training set (the 25 structures in Table 1) and the best results (in decreasing order of R^2) are listed below and in Table 7.

(i) Monivariate regression

$$\log P = 3.704 + 1.071 \times SD_2$$

(ii) Bivariate regression

$$\log P = 3.182 + 1.078 \times SD_2 - 0.057 \times HOMO$$

(iii) Three-variate regression

$$\log P = 2.847 + 1.088 \times SD_2 - 0.110 \times HOMO - 0.0002 \times De$$

(iv) Four-variate regression

$$\log P = -0.844 + 1.003 \times SD_2 - 0.478 \times HOMO + 0.386 \times Adj. - 0.360 \times C$$

Table 7. Best models in describing log P in the training set of (1-methylpiperidin-4-yl) propanoate in Table1.

	Descriptors	R ²	Adjust. R ²	St. Error	F
1	SD ₂	0.917	0.914	0.36	256.093
2	HOMO	0.192	0.157	1.127	5.470
3	De	0.007	0.036	1.250	0.157
4	Di	0.005	0.039	1.251	0.110
5	SD ₂ , De	0.918	0.911	0.366	123.875
6	SD ₂ , HOMO	0.918	0.910	0.368	122.668
7	SD ₂ , Di	0.918	0.911	0.366	123.881
8	SD ₂ , CjDi	0.918	0.911	0.366	123.843
9	SD ₂ , D3D	0.918	0.911	0.366	123.969
10	SD ₂ , HOMO, De	0.920	0.904	0.381	57.284
11	SD ₂ , CjDi, HOMO	0.919	0.907	0.374	79.230
12	SD ₂ , D3D, De	0.919	0.907	0.375	78.909
13	SD ₂ , Di, D3D	0.919	0.907	0.375	78.921
14	SD ₂ , De, CjDi	0.918	0.907	0.375	78.835
15	SD ₂ , Adj, C	0.918	0.907	0.375	78.634
16	SD ₂ , HOMO, C, Adj,	0.921	0.905	0.378	58.100
17	SD ₂ , C, De, Adj	0.920	0.904	0.381	57.263
18	SD ₂ , HOMO, De, Di	0.919	0.903	0.383	56.755

4.2.3. Model Validation (for log P)

(a) Leave-one-out

The best models in Table 7 describing log P of these (1-methylpiperidin-4-yl) propanoate derivatives were validated by leave-one-out procedure, as listed in Table 8.

Table 8. LOO for some models in Table 7

	Descriptors	Q ²	R ² -Q ²	St. Error _{loo}	F _{loo}
1	SD ₁	0.9	0.017	0.396	206.94
5	SD ₁ , HOMO	0.884	0.034	0.426	175.824
11	SD ₁ , HOMO, De	0.881	0.038	0.432	170.297
19	SD ₁ , HOMO, Adj., C	0.868	0.052	0.455	171.485

(b) External Validation

The values $\log P$ for the test set of (1-methylpiperidin-4-yl) propanoate were calculated by using equation cf. entry 10, Table 7. Data are listed in Table 9 and the monivariate correlation: $\log P = 1.010 \times \log P_{\text{calc.}} - 0.291$ $R^2=0.833$, St. Error=0.286, $F=64.662$ is plotted in Figure 4.

Table 9. Calculated values of $\log P$ for the molecules in the test set (Table 1)

Mol.	$\log P$	$\log P_{\text{calc.}}$
26	0.7	0.07
27	1.9	1.76
28	1.6	1.45
29	1.1	0.84
30	1.6	0.92
31	2.4	2.57
32	2	1.20
33	2.3	2.10
34	3	2.86
35	1.5	1.29
36	1.3	0.99
37	1	0.70
38	0.5	0.79
39	2	1.88
40	2	1.38

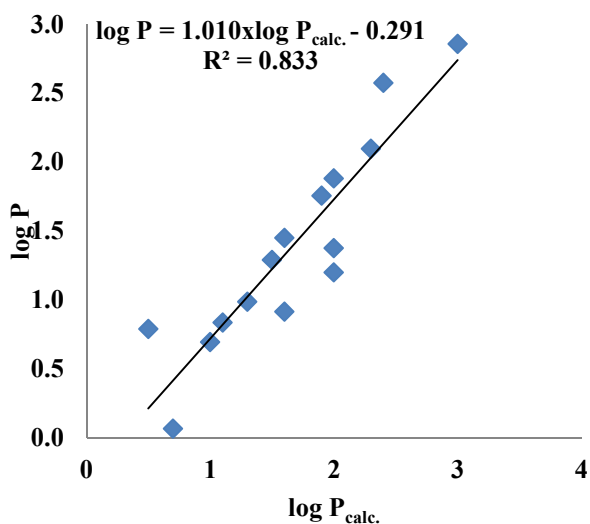


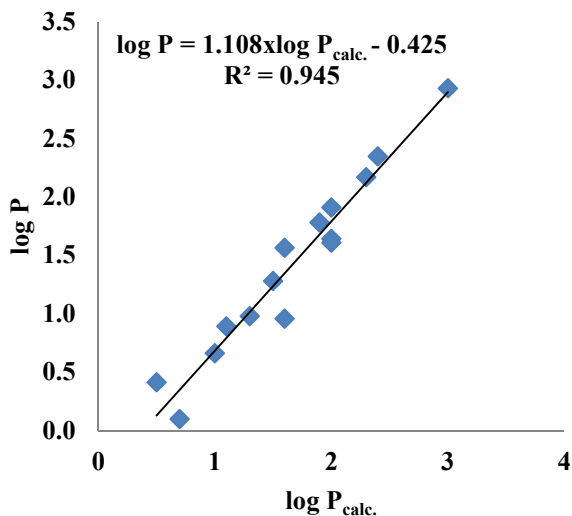
Figure 4. The plot $\log P$ vs. $\log P_{\text{calc.}}$ for the test set (external validation)

(c) Similarity Cluster Validation

Validation was performed by calculating $\log P$ for the molecules in the test set, similar to that in the Section 4.1.3. The values $\log P_{\text{calc.}}$ were computed with the same descriptors as in eq. 10, Table 7. Data are listed in Table 10 and the monivariate correlation: $\log P = 1.108 \times \log P_{\text{calc.}} - 0.425$ $R^2=0.945$, St. Error=0.164, $F=222.647$ is plotted in Figure 5.

Table 10. Calculated values of log P by similarity clusters, for the molecules in the test set.

Mol.	log P	log P _{calc.}
26	0.7	0.10
27	1.9	1.78
28	1.6	1.56
29	1.1	0.89
30	1.6	0.95
31	2.4	2.35
32	2	1.64
33	2.3	2.17
34	3	2.93
35	1.5	1.28
36	1.3	0.98
37	1	0.66
38	0.5	0.41
39	2	1.91
40	2	1.61

**Figure 5.** The plot log P vs. log P calc. for the test set (similarity cluster validation)

CONCLUSIONS

A set of 40 derivatives of (1-methylpiperidin-4-yl) propanoates, downloaded from the PubChem database, has been submitted to a QSAR study, involving the hypermolecule concept.

The set was split into a learning set and a test set, the last one being used for the validation of the models, in the so-called external set validation. Also, the validation was made by a new version of prediction by using similarity clusters.

ACKNOWLEDGMENTS

This paper is a result of a doctoral research made possible by the financial support of the Sectorial Operational Program for Human Resources Development 2007-2013, co-financed by the European Social Fund, under the project POSDRU/159/1.5/S/137750 - "Doctoral and postdoctoral programs - support for increasing research competitiveness in the field of exact Sciences".

REFERENCES

- [1]. F. Liu, Y. Liang, C. Cao, N. Zhou, *Analytica Chimica Acta*, **2007**, 594, 279.
- [2]. C.S. Lee, S.J. Chung, J.S. Kim, *Journal of Clinical Neurology*, **2006**, 2, 83.
- [3]. L. Jäntschi, LOO Analysis (LOO: leave one out), AcademicDirect Library of software, **2005**, Available at:
http://l.academicdirect.org/Chemistry/SARs/MDF_SARs/loo/
- [4]. H. Shinotoh, K. Fukushi, S. Nagatsuka, T. Irie, *Curr Pharm Des.* **2004**, 10, 13, 1505.
- [5]. D.M. Jewett, T.B. Nguyen, D.E. Kuhl, M.R. Kilbourn, *Nuclear Medicine and Biology*, **1998**, 25, 751.
- [6]. S.E. Snyder, L. Tluczek, D.M. Jewett, T.B. Nguyen, D.E. Kuhl, M.R. Kilbourn, *Nucl Med Biol.* **1998**, 25, 8, 751.
- [7]. Q. Shu, J. Wang, B. Peng, D. Wang, G. Wang, *Fuel*, **2008**, 87, 3586.
- [8]. O Ursu, M.V. Diudea, TopoCluj software program. Babes-Bolyai University Cluj, **2005**.
- [9]. I.A. Aguayo-Villarreal, V. Hernández-Montoya, N.A. Rangel-Vázquez, M.A. Montes-Morán, *Journal of Molecular Liquids*, **2014**, 196, 326.
- [10]. F. Liu, Y. Liang, C. Caob, N. Zhoua, *Talanta*, **2007**, 72, 1307.
- [11]. C.A. Nunes, M. P. Freitas, *Journal of Microbiological Methods*, **2013**, 94, 217.
- [12]. T. Cheng, Y. Zhao, X. Li, F. Lin, Y. Xu, X. Zhang, Y.Li, R. Wang, L. Lai, *Journal of Chemical Information and Modelin*, **2007**, 47 (6), 2140.
- [13]. C.D. Moldovan, A. Costescu, G. Katona, M.V. Diudea, *MATCH Commun. Math. Comput. Chem.*, **2008**, 60, 977.
- [14]. Pub. Chem. database, accessed 1.09. **2014**.
- [15]. M.J. Frisch, G.W. Trucks, et. all, *Gaussian Inc Wallingford CT*, **2009**.
- [16]. N.J.Richmond, C.A. Abrams, P.R. Wolohan, E. Abrahamian, P. Willett, R.D. Clark, *J Comput Aided Mol Des*, **20**, **2006**,, 567.
- [17]. A.T. Balaban, A. Chiriac, I. Motoc, Z. Simon, Springer, Berlin, **15**, **1980**.
- [18]. T.E. Harsa, A.M. Harsa, B. Szepler, *Cent. Eur. J. Chem.*, **2014**, 12, 365.
- [19]. A.M. Harsa, T.E. Harsa, S.D. Bolboacă, M.V. Diudea, *Current Computer-Aided Drug Design*, BEntham Science, **2014**, 2, 10, 115.
- [20]. T.E. Harşa,, *Studia UBB Chemia*, LIX, 1, **2014**, 99.

RHEOLOGICAL BEHAVIOR AND MICROBIOLOGICAL STUDIES OF CARBOPOL® HYDROGELS

EMESE SIPOS^a, ZOLTÁN – ISTVÁN SZABÓ^{a*},
LILLA LŐRINCZI^b, ADRIANA CIURBA^c

ABSTRACT. Rheological and microbiological studies were performed for hydrogels prepared with different types of crosslinked polyacrylate polymers (Carbopol® 940, 980 and Ultrez® 10). All hydrogels exhibited typical viscoelastic properties, with no Newtonian flow regimen. Linearizing viscosity profiles, excellent correlations were obtained between logarithmic values of viscosity and shear rate. The study also revealed that Carbopol® 980 and Ultrez® 10 based hydrogels showed higher viscosity than the Carbopol® 940 based. Microbiological studies were performed in order to find a suitable preservative for the prepared hydrogels. Both the diffusion based method and challenge test indicated that phenylmercuric borate was the most effective preservative, regardless of the microorganism tested and can be suitable for preventing antimicrobial growth in the prepared hydrogels.

Keywords: Carbopol®, hydrogel, pseudoplastic, challenge test

INTRODUCTION

Hydrogels are three-dimensional, hydrophilic networks of cross-linked water soluble polymers. They are viscoelastic, solid-like materials, owing their three-dimensional properties to the cross-linking process of the polymer strands of molecules as a result of physical or chemical forces^{1,2}.

^a University of Medicine and Pharmacy Tîrgu Mureş, Faculty of Pharmacy, Department of Drugs Industry and Pharmaceutical Management, Gh. Marinescu 38, RO-540139, Tîrgu Mureş, Romania

^b University of Medicine and Pharmacy Tîrgu Mureş, Faculty of Medicine, Department of Microbiology, Gh. Marinescu 38, RO-540139, Tîrgu Mureş, Romania

^c University of Medicine and Pharmacy Tîrgu Mureş, Faculty of Pharmacy, Department of Pharmaceutical Technology, Gh. Marinescu 38, RO-540139, Tîrgu Mureş, Romania

* Corresponding author szabo.zoltan@umftgm.ro

In recent years, hydrogels have attracted a wide interest due to their responsiveness to environmental stimulants (pH, ionic strength, solvent properties, electrical field etc), hydrophilic nature and biocompatibility. There are several biomedical fields, where hydrogels were successfully applied, such as wound dressing³⁻⁵, tissue engineering⁶, contact lens development^{7,8} etc. A particular interest for hydrogels represents their use as drug delivery systems for various active pharmaceutical ingredients, being beneficial in altering pharmacokinetic properties of incorporated drugs^{1,2}.

Carbopols are a family of synthetic microgels formed by crosslinking linear polyacrylates with various other chemical compounds. They are soluble in polar solvents and due to the hydration of the individual polymer molecules; they partially uncoil and begin to swell. Upon titration with a basic solution (ex. sodium hydroxide), the carboxylic groups in its structure ionize and uncompensated sodium cations lead to an increase in the osmotic pressure, which causes individual polymer strands to swell drastically. The formed system, maintains its gel-like characteristics until local deformations exceed a certain level, upon which the gel network breaks apart and material flow occurs^{9,10}.

Due to their rheological properties, low thixotropy and optical transparency, until recently, Carbopol® gels have been considered *model yield stress fluids*. However, recently, it has been shown that at certain experimental conditions, thixotropic effects and irreversible deformations can occur¹⁰⁻¹².

As it can be observed proper knowledge of the flow behaviour of Carbopol® gels is necessary for their further use in pharmaceutical formulations. Our aim was to investigate the rheological properties of gels of three types of Carbopol® (Carbopol® 940, 980 and Ultrez® 10) in order to find a suitable candidate for a mucoadhesive pharmaceutical form.

Another important aspect of the formed hydrogels is their microbial purity. During formulation studies, it is essential to prove that the future pharmaceutical formulation will provide the needed protection against damages caused by bacterial multiplication or by microbiologic contamination during the period of validity. If a pharmaceutical formulation – especially those obtained with water – does not possess antimicrobial effect, it requires the use of preservatives, for microorganism multiplication prevention or for microorganism contamination restriction. These types of damages – characteristic for multidose forms – can appear both at usual storage conditions and during usage. The use of microbiological preservatives prevents the danger of a possible infection and that of microbial disintegration.

Although the Carbopol® types selected do not constitute an ideal medium for microorganism or fungi, they do not prevent their growth and some microorganisms may develop without causing polymer disintegration.

Therefore, apart from the rheological studies, four different preservatives (combination of methylparaben and propylparaben, phenylmercuric borate, benzoic acid and sodium benzoate) were employed and tested for their efficacy in preventing microbial growth in the prepared hydrogels.

RESULTS AND DISCUSSION

Rheological studies

Flow and viscosity curves were recorded for each of the prepared gels (Fig. 1 and 2).

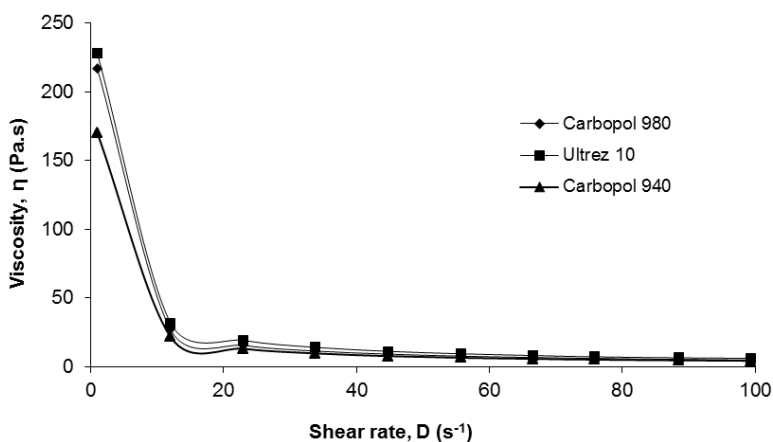


Figure 1. Viscosity curves of the studied hydrogels

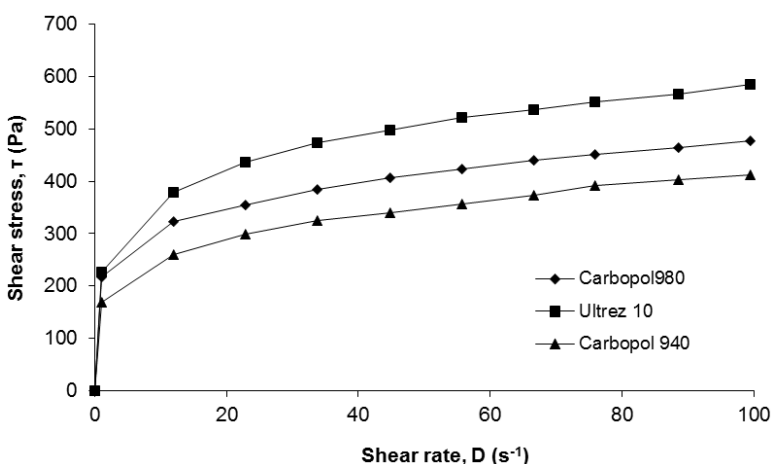


Figure 2. Flow curves of the studied hydrogels

No Newtonian flow regimen has been observed in the selected shear rate region. Viscosity values obtained at low shear rate were around 200 Pa.s for all hydrogels, which decreased significantly, when higher shear rates were applied. When a shear rate of 12 s⁻¹ has been used, viscosity values decreased almost to one tenth of that obtained at a shear rate of about 0.1 s⁻¹. The hydrogel obtained with Ultrez® 10 had the highest viscosity values, followed by Carbopol® 980. The lowest viscosity values were obtained with the hydrogel obtained from Carbopol® 940.

Each viscosity profile exhibited a power law relationship between viscosity and shear rate. Using a simple logarithmic transformation, we can obtain a linear relationship between shear viscosity and shear rate:

$$\log \eta = \log \eta^+ - m \log D$$

where, η - shear viscosity (Pa.s)

D - the shear rate (s⁻¹)

η^+ - the extrapolate viscosity

m - the tangent of the line

Results obtained after linearizing the viscosity curve are shown in Table 1.

Table 1. Results of the linearization of viscosity curves

Carbopol type	Regression equation and coefficient of determination
Carbopol® 980	$y = 2.3286 - 0,8293x; r^2=0,9998$
Ultrez® 10	$y = 2.3591 - 0,7964x; r^2=0,9999$
Carbopol® 940	$y = 2.2185 - 0,8066x; r^2=0,9996$

In all cases, excellent linear correlations were found between logarithmic values of shear viscosity and shear rate. The negative m value confirms the pseudoplastic behaviour of gels *i.e* a decrease in viscosity with increase of shear rate. It indirectly characterizes the binding energy and the number of the bonds from the structure of the formed hydrogels. The bigger the m value, the decrease in viscosity is also bigger, meaning that the breakage of bonds in the coherent structure appears more easily.

Microbiological studies

The total microbial load is an important parameter in evaluating excipients' or drug carriers' suitability in pharmaceutical formulations. Hydrogels prepared from Carbopol® lack intrinsic antimicrobial activity, thus, in order to achieve

acceptable microbiological purity of the drug carrier, four different preservatives were tested for their capacity to prevent microbial growth in the hydrogels prepared (combination of methylparaben and propylparaben, phenylmercuric borate, benzoic acid and sodium benzoate).

Two separate methods were involved in the evaluation, a diffusion-based method and a challenge test for the following microorganisms: *Staphylococcus aureus*, *Pseudomonas aeruginosa*, *Escherichia coli* and *Candida albicans*.

Results of the diffusion-based methods are presented in Table 2, based on the exerted inhibition zones on the selected microorganisms.

Table 2. Results of the microbiological studies obtained with the diffusion-based method

Polymer used	Preservative	Inhibition zones for tested microorganism			
		<i>Staphylococcus aureus</i>	<i>Candida albicans</i>	<i>Escherichia coli</i>	<i>Pseudomonas aeruginosa</i>
Carbopol® 940	1	14.8 ± 0.8	-	9.4 ± 0.5	-
	2	39.2 ± 2.8	24.4 ± 1.5	42.2 ± 0.8	9.6 ± 0.9
	3	22.2 ± 3.0	-	26.6 ± 1.1	-
	4	15.6 ± 1.0	-	20.8 ± 1.9	-
Carbopol® 980	1	20.2 ± 0.8	-	30.0 ± 1.6	-
	2	39.6 ± 1.1	31.2 ± 3.1	41.6 ± 2.7	13.4 ± 1.1
	3	13.2 ± 1.5	-	25.4 ± 1.1	-
	4	14.0 ± 1.6	-	7.0 ± 2.1	-
Ultrez® 10	1	17.2 ± 1.9	-	14.8 ± 1.5	-
	2	39.8 ± 1.5	31.8 ± 2.3	42.2 ± 1.5	10.8 ± 2.2
	3	21.2 ± 3.1	-	25.8 ± 1.3	-
	4	14.0 ± 1.6	-	11.0 ± 1.6	-

Values represent mean inhibition zones ± standard deviations in millimeters

1 – Methylparaben/propylparaben; 2 – Phenylmercuric borate; 3 – Benzoic acid; 4 – Sodium benzoate

Comparing the inhibition zones for the hydrogels prepared, we can observe similar results. The biggest inhibition is observed in the case of phenylmercuric borate solution 0,007 %, both for Gram-positive bacteria (*Staphylococcus aureus*), Gram-negative bacteria (*Escherichia coli*, *Pseudomonas aeruginosa*) and fungi (*Candida albicans*). Moreover, only this preservative was effective in the case of *Candida albicans* and *Pseudomonas aeruginosa*, the other preservatives failing to present any inhibition zone for the mentioned microorganisms. Phenylmercuric borate showed similar inhibition zones, regardless of the Carbopol® type used for the preparation of hydrogels.

Microbial challenge testing was also performed for the prepared hydrogels in order to determine the ability of the preservatives to inhibit the growth of pathogens. The same microorganisms were used for contamination as in the previous study. The duration of the challenge test was 7 days, with periodic sample removals at the start of the test, 6 hours, 24 hours, 48 hours, 168 hours (7 days) and at the end of the challenge test. As expected from the diffusion based test results, out of the four antimicrobial preservatives studied phenylmercuric borate proved to be the most efficient for the microorganisms tested. Formulations containing this preservative, showed no contamination at the 6 hour sampling. Apart from phenylmercuric borate, the combination of methylparaben and propylparaben was also efficiently on *Staphylococcus aureus*, *Pseudomonas aeruginosa* and *Candida albicans* and eliminated completely *Escherichia coli* after 6 hours from Carbopol® 940 and after 24 hours from Carbopol® 980 based hydrogels.

Results indicate that maximum 48 hours after inoculation benzoic acid ensures sterility regardless of the inoculated microorganisms in all hydrogels studied. The highest efficacies were found for the Gram positive microorganism, *Staphylococcus aureus*, which were completely destroyed 6 hours after the inoculation (Table 3).

Sodium benzoate reduces colony count by more than 100 units after two days, regardless of the microorganisms used (Table 4). Furthermore, microorganism count did not increase after this point, thus, meeting regulatory criteria¹³.

CONCLUSIONS

Results of the rheological studies indicate that all hydrogels examined, exhibit a pseudoplastic flow, characteristic of macromolecular dispersions of linear molecules as in the case of carboxyvinyl polymers. Rheological characterization of the obtain hydrogel revealed greater viscosity values for Carbopol® 980 and Ultrez® 10, while the smallest values were obtained for Carbopol® 940.

Microbiological study concludes that all preservatives were able to confer adequate microbiological quality to the prepared hydrogels, as amended by the European Pharmacopoeia. Comparing the different preservatives employed, phenylmercuric borate proved to be the most efficient, regardless of the testing method.

Table 3. Efficacy of benzoic acid as a preservative during the challenge test

Time	Carbopol® 980				Ultrez® 10				Carbopol® 940			
	1	2	3	4	1	2	3	4	1	2	3	4
At inoculation	5.00	5.00	5.00	5.00	5.00	5.00	5.00	5.00	5.00	5.00	5.00	5.00
6 h	-	-	1.69	1.90	1.47	-	1.47	1.30	1.3	-	1.69	1.90
24 h	-	-	1.47	1.69	1.39	-	-	-	-	-	1.30	1.69
48 h	-	-	-	-	-	-	-	-	-	-	-	-

Values indicate logarithmic microorganism colony count

* 1 – *Escherichia coli*; 2 – *Staphylococcus aureus*; 3 – *Pseudomonas aeruginosa*; 4 – *Candida albicans*

Table 4. Efficacy of sodium benzoate as a preservative during the challenge test
Values indicate logarithmic microorganism colony count

Time	Carbopol® 980				Ultrez® 10				Carbopol® 940			
	1	2	3	4	1	2	3	4	1	2	3	4
At inoculation	5.00	5.00	5.00	5.00	5.00	5.00	5.00	5.00	5.00	5.00	5.00	5.00
6 h	2.17	-	2.00	2.17	2.17	1.60	2.17	2.00	2.30	1.77	1.69	2.00
24 h	1.90	-	1.90	1.90	2.00	-	1.90	1.30	2.00	1.69	1.60	-
48 h	1.30	-	-	-	1.90	-	0.84	-	1.69	-	-	-
168 h	1.17	-	-	-	1.84	-	-	-	1.60	-	-	-
336 h	-	-	-	-	-	-	-	-	-	-	-	-

* 1 – *Escherichia coli*; 2 – *Staphylococcus aureus*; 3 – *Pseudomonas aeruginosa*; 4 – *Candida albicans*

EXPERIMENTAL SECTION

Materials

Carbopol® 980, Carbopol® 940, Ultrez™ 10 were from Lubrizol. Sodium hydroxide, methylparaben, propylparaben, phenylhydrargiri boras were purchased from Merck, while sodium benzoate was obtained from Reactiv Bucharest. Agar and Sabouraud medium were obtained from Cantacuzino Institute, Romania. The bacterial strains used in the microbiological studies were the following: *Staphylococcus aureus* (ATCC 6538), *Pseudomonas aeruginosa* (ATCC 9027), *Candida albicans* (ATCC 10231), *Escherichia coli* (ATCC 8739).

Gel preparation

Composition of the prepared hydrogels, used in the microbiological studies is described in Table 5. The gels for the rheological studies were prepared with deionized water, instead of preservative solution.

Carbopol polymers were added to the preservative solution and were allowed it to hydrate. After hydration (in case of Carbopol® 940 and Carpopol® 980 polymer - 30 minutes and in case of Ultrez® 10 polymer - 2 minutes) the dispersion was mixed at a low agitation rate of 500 rpm. The obtained samples were neutralized with sodium hydroxide solution until pH 7 was reached. Thereafter, the remaining aqueous preservative solution was added. The mixture was agitated thoroughly to obtain a clear, viscous gel.

Table 5. Quantitative composition of the prepared hydrogels

Polymer type	Carbopol® 980	Ultrez® 10	Carbopol® 940
Polymer quantity (g)	1.00	1.00	1.00
Sodium hydroxide solution 10.0%(g)	q.s.	q.s.	q.s.
Preservative, aqueous solution* (g)	ad. 100.00	ad. 100.00	ad. 100.00

* The following preservative solutions were used:

Methylparaben/propylparaben 0.18 %/0.02 % (w/w)

Phenylmercuric borate 0.007 % (w/w)

Benzoic acid 0.2 % (w/w)

Sodium benzoate 0.01 % (w/w)

Methods

For rheological studies, a Rheometer MC1 (Paar Physica) was used. Obtained data was analysed with Rheocalc software 1.01. Viscosity determinations had been recorded for ten sequentially increasing and decreasing values of shear rate in the range of 0.995- 99.4 sec⁻¹, at a constant temperature of 25 ± 0.1 °C.

For the microbiological studies, two separate methods were used: one diffusion-based method and a separate, challenge-test.

In the case of the diffusion-based method, a few cavities have been made with small diameter cylinders into the medium, and in each cavity one gram gel had been introduced. Mediums were inoculated on the surface with microbe containing suspensions (3.10⁸ microorganisms in one mL⁻¹). The strains were incubated for 24 hours at 30-35 °C, and then the inhibition zone diameter had been measured.

The challenge test was effectuated according to the Romanian Pharmacopoeia ed. X¹⁴. The hydrogels have been inoculated with microbe containing suspensions (0.1 mL suspension for every 20 grams of hydrogel so as to obtain a concentration of 10⁻⁵ microorganism/gram). The artificially infected hydrogels had been stored at 20-25 °C, and at periodic intervals (at inoculation, 6 h, 24 h, 48 h, 7 days – 168 h and 14 days – 336 h) microorganism number had been determined and logarithmic transformations were made.

ACKNOWLEDGMENTS

This paper was published under the frame of European Social Found, Human Resources Development Operational Programme 2007-2013, project no. POSDRU/159/1.5/S/136893. The first author would like to thank Collegium Talentum for their financial support.

REFERENCES

- [1]. T.R. Hoare and D.S. Kohane, *Polymer (Guildf.)*, **2008**, *49*, 1993–2007.
- [2]. W.A. Laftah, S. Hashim, and A.N. Ibrahim, *Polym. Plast. Technol. Eng.*, **2011**, *50*, 1475.
- [3]. S.P. Tan, P. McLoughlin, L. O’Sullivan, M.L. Prieto, G.E. Gardiner, P.G. Lawlor, and H. Hughes, *Int. J. Pharm.*, **2013**, *456*, 10.
- [4]. P.T.S. Kumar, V.-K. Lakshmanan, T.V Anilkumar, C. Ramya, P. Reshmi, A.G. Unnikrishnan, S.V Nair, and R. Jayakumar, *ACS Appl. Mater. Interfaces*, **2012**, *4*, 2618.
- [5]. R. Jayakumar, M. Prabakaran, P.T. Sudheesh Kumar, S.V Nair, and H. Tamura, *Biotechnol. Adv.*, **2011**, *29*, 322.
- [6]. S. Van Vlierberghe, P. Dubruel, and E. Schacht, *Biomacromolecules*, **2011**, *12*, 1387.
- [7]. X. Gu, J.D. Jennings, J. Snarr, V. Chaudhary, J.E. Pollard, and P.B. Savage, *Invest. Ophthalmol. Vis. Sci.*, **2013**, *54*, 6217.
- [8]. J. Diec, V.E. Evans, D. Tilia, T. Naduvilath, B.A. Holden, and P.L. de la Jara, *Eye Contact Lens*, **2012**, *38*, 2.
- [9]. A. Poumaere, M. Moyers-González, C. Castelain, and T. Burghilea, J. Nonnewton. *Fluid Mech.*, **2014**, *205*, 28.
- [10]. E. Weber, M. Moyers-González, and T.I. Burghilea, J. Nonnewton. *Fluid Mech.*, **2012**, *183-184*, 14–24.
- [11]. A.M.V. Putz and T.I. Burghilea, *Rheol. Acta*, **2009**, *48*, 673.
- [12]. T. Divoux, D. Tamarii, C. Barentin, and S. Manneville, *Phys. Rev. Lett.*, **2010**, *104*, 208.
- [13]. European Pharmacopoeia, 8th edition, Council of Europe, Strasbourg, **2014**.
- [14]. Farmacopeea Română, Ediția a X-a, Editura Medicală Bucuresti, **1993**.

MEASUREMENT METHOD FOR DETERMINING THE RESIDUAL FLUX DEPOSITS IN A HEAT EXCHANGER FROM A CONTROLLED ATMOSPHERE BRAZING LINE

GRIGORE COCIAN^{a,*}, CĂTĂLIN POPA^b

ABSTRACT. The brazing technology of aluminum alloys having the highest efficiency, used at manufacturing heat exchangers, is the controlled atmosphere brazing with the NOCOLOK flux. The major inconvenience of the process is the residual flux retained on the internal surfaces of the heat exchanger, which in certain quantities may react with the cooling agents leading to gels that may compromise the functionality of the heat exchangers. The present paper presents a method of measuring the residual flux quantity based on the repeated experimentation and measurements taken on the horizontal, and vertical brazing manufacturing lines.

Keywords: *brazing technology, heat exchanger, residual flux, Nocolok, experimental, method.*

INTRODUCTION

The new applications for the internal combustion engines with their high performances require being equipped with heat exchangers that function at high thermal and structural load. The most efficient way to conform the heat exchangers to these new specifications is brazing then using the controlled atmosphere process using Nocolok fluxes.

Using the controlled atmosphere brazing process present at RAAL company [1] the following steps have to be followed: firstly the surfaces of the constructing parts have to be plated with the filler material and free of

^a RAAL S.A., Industriei 4A, 420063 Bistrița, Romania.

* Corresponding author: productie@raal.ro

^b Technical University, Science and Material Engineering, Memorandumului street 28 Cluj-Napoca, Romania

impurities in order to achieve the wettability condition; the parts have to be assembled such that the contact between them has to be fixed and discontinuous making capillary spaces at the junctions, the flux has to be present at least on one of the plated surfaces, as showed in Figure 1[2][3], and lastly but not the least the brazing atmosphere has to be composed from an inert gas such as N_2 with O_2 content lower than 100 ppm.[4]

After the preparing step of removing any traces of humidity the assembled structure is heated in ovens with inert atmosphere following a preset profile of temperature: at 565 °C the melted flux deoxidize the surfaces and protect them against the reoxidation, starting with 577 °C the filler material will melt and under the capillarity effect will flow in the spaces between joints, after keeping the structure at the brazing temperature for 2-3 minutes the fast cooling phase begins with the solidification of the filler material and followed by the solidification of the flux melt resulting in residual flux.

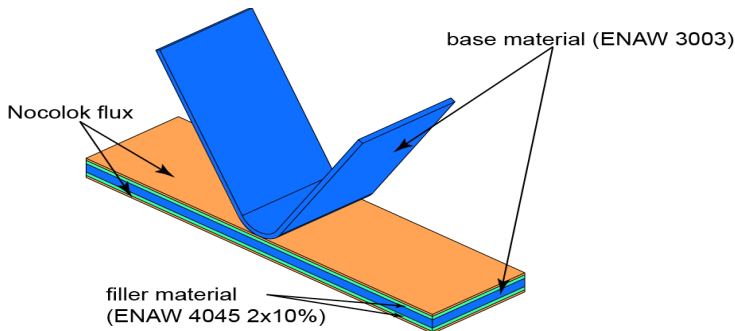


Figure 1. Brazing components

The residual flux can react with the warm cooling agent present in the heat exchanger during exploitation, leading to creation of gels which may compromise the heat exchanger operation. This residual flux imposes the introduction of a new step in heat exchanger manufacturing process, namely the internal cleaning of the heat exchanger. Measuring the residual flux with the filter paper is a long process that increases the manufacturing time and the price of the heat exchanger, and is not very accurate because a part of the residual flux is dissolved in the cleaning fluid.

In this paper we will present an alternative method of determining the residual flux by measuring the conductivity of the cleaning fluid – dematerialized water -and through the K^+ concentration we can determine the amount of residual flux present in the fluid this method presents the advantage that it can be made during the washing process and reduce the time for this process.

RESULTS AND DISCUSSION

Multiple probes where sampled from the same heat exchanger as seen in Figure 2 having different K^+ concentration, measured according to [5][6] for which the conductivity was measured according to [7] with an uncertainty of 2.8% @ 95% confidence level in range of 100÷1200 [$\mu\text{S}/\text{cm}$].

Knowing that the stoichiometric coefficient of the residual's flux, KAlF_4 , K_3AlF_6 , components, has value of 3.42 we can determine the residual flux quantity dissolved in the solution in [mg/l]. The Figure 3 plots the experimental data obtained.

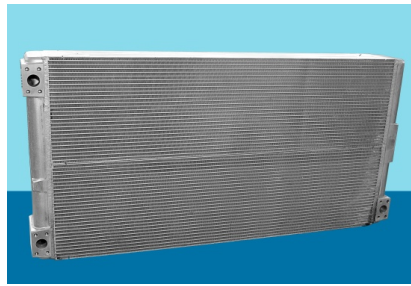


Figure 2. Heat exchanger used in the study

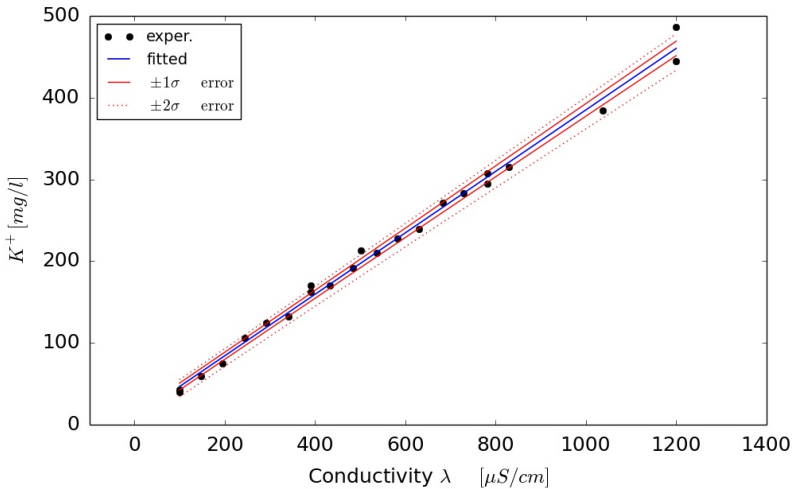


Figure 3. K^+ dependence of conductivity

The experimental data where fitted using a linear function:

$$K^+(\lambda) = a \cdot \lambda + b \quad (1)$$

resulting in the coefficients a and b having the values and the uncertainties[8] presented in Table1:

Table 1. Coefficient values

coefficient	value	1·σ	2·σ
a	0.376	0.007	0.014
b	9.4	4.1	8.2

With the final function being:

$$K^+(\lambda) = (0.276 \pm 0.014) \cdot \lambda + (9.4 \pm 8.2) @ 2 \cdot \sigma \quad (2)$$

The fit has a reduced χ^2 of 0.0033 which tells us that the linear model chosen is a good approximation of the K^+ dependence on conductivity. The fit with the uncertainty at 1·σ and 2·σ is also presented in Figure 3.

Because of the large domain for which the fit was created care should be taken in using it below a conductivity of 200 [$\mu\text{S}/\text{cm}$] where the relative uncertainty of the function rise exponentially, as seen in the Figure 4.

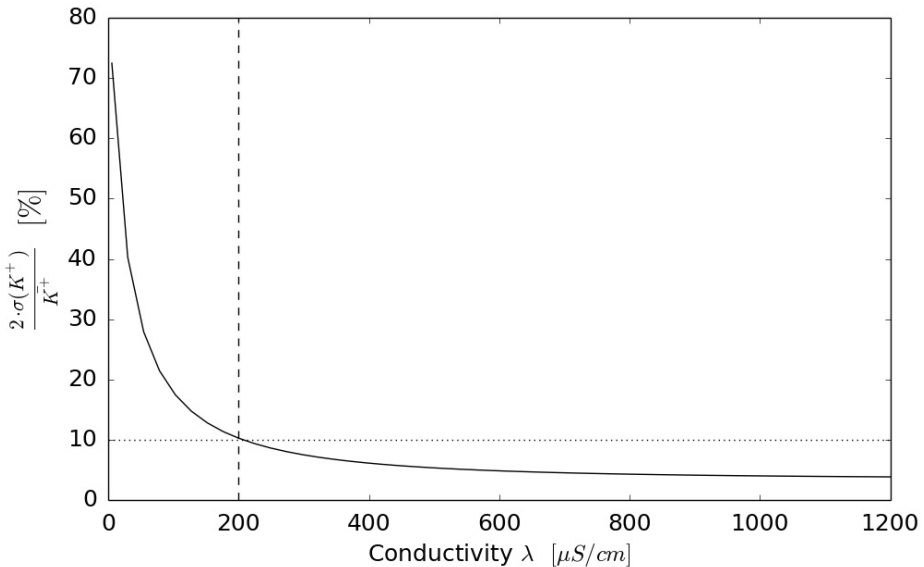


Figure 4. Relative error of the fitted function

The 10 [%] uncertainty at 200 [$\mu\text{S}/\text{cm}$] is reasonable for the residual flux weight estimation, and as can be seen from the Figure 4 the uncertainty drops till a 3.85 [%] at 1200 [$\mu\text{S}/\text{cm}$].

CONCLUSIONS

In real life applications, the residual flux present in heat exchangers after the brazing process, give a conductivity in the range of 250 to 1500 [$\mu\text{S}/\text{cm}$], and knowing that the uncertainty of the K^+ concentration is below 10% in the required range we can conclude that the procedure using the conductivity as a basis for measure the residual flux quantity present in the heat exchangers is a good one.

A second advantage of this method is that it can be easily implemented on the assembly line of the heat exchangers without the need to invest in expensive equipment

With this method implemented the next step will be implementing the complete removal of the residual flux without affecting the support material.

EXPERIMENTAL SECTION

The heat exchanger's constructive parts are mechanically assembled and prior to loading it in the brazing oven the flux is applied by means of immersion in an immersion bath having the composition of 15.5% Nocolok flux, 0.2% Antarox, and 84.3% demineralized water achieving the 5 g/m^2 flux loading.

After the brazing process has finished the heat exchanger's internal volume was washed with demineralized water at 95°C and a constant recirculation speed using a quantity of 240 l of water. The conductivity of the washing solution is monitored and measurements were taken at a constant time interval of 5 minutes until the temperature became constant as in Figure 5.

After a period of approximately 80 min the conductivity of the water begins to have a constant value, which signifies that all the residual flux is contained in the washing fluid.

We proceed further at doing the leaching test that consists in filling a heat exchanger sample with distilled water and inserting it in the thermostatic chamber which is kept at 95 °C for 24 hours.

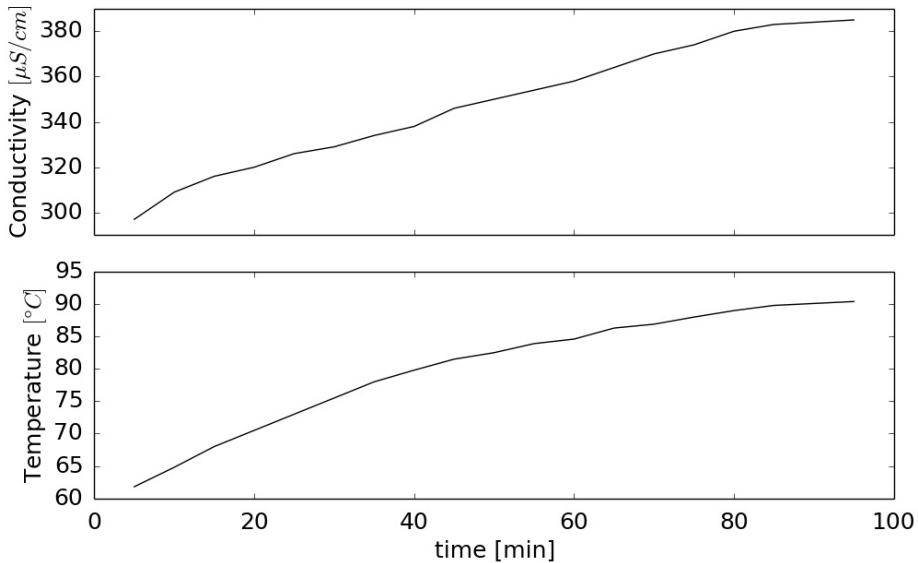


Figure 5. Temperature versus time

After this period the sample is drained of the water content which on which the conductivity and the concentration of the Potassium cations are measured. The initial and final data for this test are showed in the table below:

Table 2. Leaching test data

Quantity	Value	Unit
demineralized water vlume	20	[liter]
time	24	[hours]
mean temperature/test	90	[$^{\circ}\text{C}$]
conductivity at start	5	[$\mu\text{S}/\text{cm}$]
conductivity at end	460	[$\mu\text{S}/\text{cm}$]

This process is repeated for all the measured heat exchangers and for which the data is showed in this study.

ACKNOWLEDGMENTS

We would like to express our gratitude to the heat exchanger manufacturer, the company RAAL, for all the help given during all the phases of this study, and also to the Technical University of Cluj-Napoca for its invaluable knowledge shared with us.

REFERENCES

- [1]. RAAL (2014,December,15), Product Catalog [Online]. Available: <http://www.raal.ro/products.htm>
- [2]. Cocian Grigore, Popa Cătălin, Experimental Studies Regarding Binder's influence on aluminium alloys controlled atmosphere brazing, International Conference on Production Research, Cluj-Napoca, **2014**.
- [3]. C. Kammer, „Aluminium Handbook”, Aluminium-Verlag, **1999**. Vol 1 Fundamentals and materials
- [4]. L. Orman și H. Swidersky, Selective pre-fluxing with adhesives, SOLVAY Congress, Aluminum Brazing, Dusseldorf, **2012**.
- [5]. Water quality - Digestion for the determination of selected elements in water -- Part 2: Nitric acid digestion, ISO 15587-2, **2003**.
- [6]. Water quality - Determination of selected elements by inductively coupled plasma optical emission spectrometry (ICP-OES), ISO 11885, **2007**.
- [7]. Water quality –Determination of electrical conductivity, SR EN 27888, **1997**.
- [8]. M.A. Mueller, G.R. Schade, S.A. Hooks, R.L. Beck, G.F. Clyde, T.W. Dekleva, D. Inthout „Standard Engineering Analysis of Experimental data,” ASHARE, **2004**.

THEORETICAL EVALUATION OF THE AROMATIC CHARACTER OF AZA-PHOSPHA-CORONENES

RALUCA POP^a, MIRCEA DIUDEA^{b*}, MIHAI MEDELEANU^c,
MIHAIELA ANDONI^a

ABSTRACT. Three aza-phospha-compounds, derivatives of coronenes with N and P atoms in ortho, meta and para positions, were proposed. Their possible aromatic character was evaluated by means of local and global aromaticity indices like HOMA, NICS, PDI and HOMO-LUMO gap. The influence of the heteroatom has been discussed, all the results being compared to the ones obtained for coronene. Graphical representations of the Laplacian of electron density outline the influence of the heteroatoms on the aromaticity of the investigated compounds.

Keywords: aromaticity, heterocyclic compounds, NICS index, *ab initio*.

INTRODUCTION

During the last years, the design of new nanomaterials has known an increased interest. The demand for materials with new or improved properties resulted also in the studies regarding their precursors [1-3]. Most of them are compounds within the class of polycyclic aromatic compounds, most prominent examples being corannulene, coronene and sumanene. There are various studies that reported new nanomaterials based on the above-mentioned compounds [4,5].

Another area of interest within this domain is represented by the researches regarding the properties of hetero-aromatic compounds, most of them dealing with properties like aromaticity, conductivity or stability of the new compounds. There are known heterofullerenes with N and O atoms; recently, have published results regarding the design of new nanomaterials with O and S [6,7].

^a University of Medicine and Pharmacy "Victor Babeş" Timișoara, Faculty of Pharmacy, 2 Eftimie Murgu Square, 300041, Timișoara, România

^b Faculty of Chemistry and Chemical Engineering, Babes-Bolyai University, 400028 Cluj, Romania

^c University Politehnica of Timișoara, Faculty of Industrial Chemistry and Environmental Engineering, 300006, Timișoara, România

* Corresponding author: diudea@gmail.com

In this regard, based on our previous studies of aromaticity of various flowers of type $[n:(p_1,p_2)]$ [8], we propose the evaluation of the aromatic character of some substituted coronene derivatives with N and P atoms. The structures are presented in Figure 1 below:

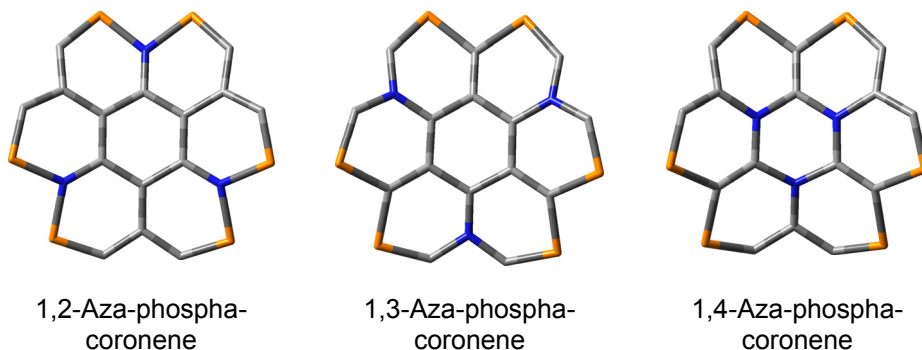


Figure 1. Structures 1-3 investigated during the present study

The differences among the three substitution types will be discussed. Due to the fact that there is no universal definition of aromaticity [9-11], the geometric, magnetic and energetic properties of heterocompounds will be evaluated. In this regard, NICS(0) index [12] will be computed at the center of each 6-membered ring. Large negative values are the proof of a strong aromatic character. Also, HOMO-LUMO gap is a good measure of a stability of the compounds [14]. Highest differences between the energies of frontier HOMO and LUMO orbitals suggest an increased stability (and, thus, aromatic character). Bond length equalization [13], another characteristic of the aromatic compounds, will be evaluated. Electron density maps are presented for each of the investigated compounds.

RESULTS AND DISCUSSIONS

In order to evaluate the aromatic character of the aza-phospha-coronenes, various indices –NICS(0), HOMO-LUMO gap– have been computed. The results were compared to the ones obtained for coronene, which is considered a super-aromatic compound.

Bond length equalization deviation was calculated for each outer ring of the investigated compounds; results are presented in Table 1:

Table 1. Bond length equalization deviation (computed at HF/6-311+G)

Compounds	Bond length equalization deviation	
	Outer rings	
1,2	55.5%	
1,3	58.8%	
1,4	58.3%	
Coronene	0.71%	

The computations show that the presence of the N and P atoms lead to large differences between coronene and heterosubstituted derivatives. Among the three substitution types, the values are very close, so it is difficult to predict a hierarchy of local aromaticity of the outer cycles. NICS (Nucleus-Independent Chemical Shift) index, that quantifies the absolute magnetic shielding at the center of a cyclic compound, has become one of the widely used descriptors of aromaticity. NICS values have been obtained using the GIAO approach [15] implemented in Gaussian 09 package [16] and are depicted in Table below:

Table 2. Values of NICS(0) index (computed at HF/6-311+G)

Compounds	NICS(0) index	
	Inner ring	Outer rings
1,2	0.611	-1.110
1,3	2.565	-4.054
1,4	9.714	-1.440
Coronene	-0.009	-10.406

According to these results, all the central rings of the coronene and its heteroderivatives are non-aromatic; the outer rings of the 1,3-aza-phospha-coronene can be considered aromatic (but much weaker than the ones corresponding to coronene). It appears that the 1,3-substitution type leads to compounds with more pronounced aromatic character than 1,2- and 1,4-substitutions, respectively.

Another local index of aromaticity is the Para-Delocalization Index (PDI). PDI [17] is an electronic index of aromaticity computed within the "atoms-in-molecules" theory, which is employed for the evaluation of the aromatic character of 6-membered rings. It is computed as the average of the atoms situated in para positions within a benzenoid ring. Larger PDI values means a more pronounced aromatic character.

Table 3. Results of PDI index (computed at HF/6-311+G)

Compounds	PDI index	
	Inner ring	Outer rings
1,2	0.027	0.047
1,3	0.025	0.052
1,4	0.014	0.045
Coronene	0.024	0.056

The results presented in Table 3 outline the more pronounced aromaticity of the “petals” of heterocoronenes (also, as predicted by NICS values, the 1,3-substitution type is favored). The low value obtained for the inner cycle of the 1,4-aza-phospha-coronene can be attributed to the presence of the three N atoms.

In order to evaluate the stability of the structures **1-3**, HOMO-LUMO gaps have been computed. The results are closed to the ones obtained for coronene, showing that all the proposed heteroderivatives are stable (especially the compound where the N and P atoms are in ortho positions). Although there are no large differences among the HL values, it must be outlined that these results predict a different hierarchy of aromaticity (compared to the situations where local indices of aromaticity –NICS, HOMA, PDI– have been employed).

Table 4. HL gap (computed at HF/6-311+G)

Compounds	HOMO-LUMO gap (eV)	Symmetry
1,2	8.20	C ₁
1,3	7.63	C ₁
1,4	7.37	C ₁
Coronene	8.95	D _{6h}

Another important parameter that characterizes the aromaticity is the electron density. We propose to estimate what is the influence of the N and P atoms on the electronic density of the vicinal C atoms. The results were compared to the ones obtained for coronene. The numbering of the C atoms is depicted in Figure 2:

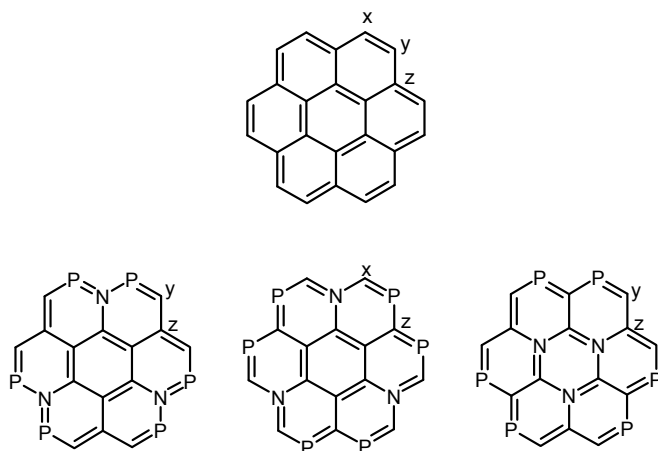


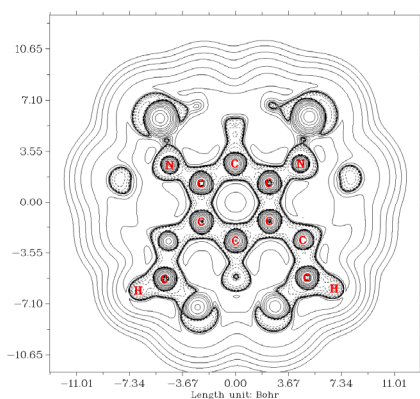
Figure 2. Carbon atoms numbering for the computations of electronic density in a specific point of the cyclic compounds

Table 5. Electron density computed for the outer C atoms (HF/6-311+G)

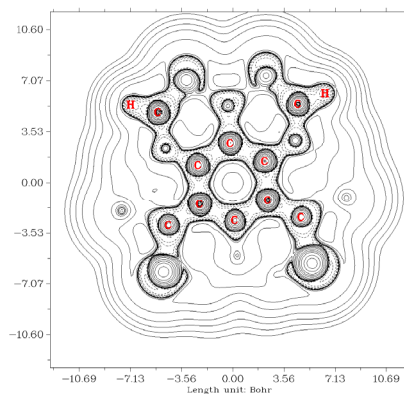
Electron density (a.u.)	x	y	z
1,2	-	$0.1196 \cdot 10^3$	$0.1196 \cdot 10^3$
1,3	$0.1197 \cdot 10^3$	-	$0.1197 \cdot 10^3$
1,4	-	$0.1196 \cdot 10^3$	$0.1196 \cdot 10^3$
Coronene	$0.1195 \cdot 10^3$	$0.1195 \cdot 10^3$	$0.1195 \cdot 10^3$

The results outline that there is no significant difference on the electron density of the C atoms due to the presence of N and P. Also, the results cannot predict a differentiation among the three substitution types.

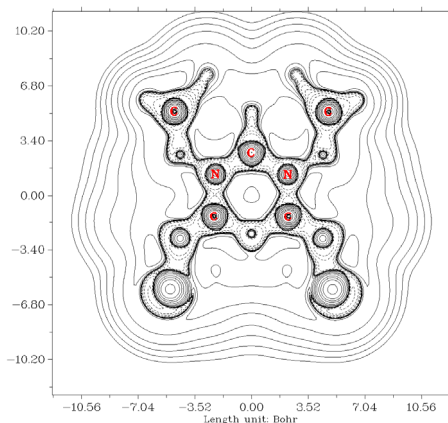
Another possibility for evaluating the aromatic character of compounds **1-3** is the analysis of the Laplacian of electron density [18]. The maps for each compound (and coronene) are depicted in Figure 3 and clearly show the influence of the heteroatoms. It can be observed that the presence of the N and P atoms disrupt the electron delocalization within the coronene derivatives.



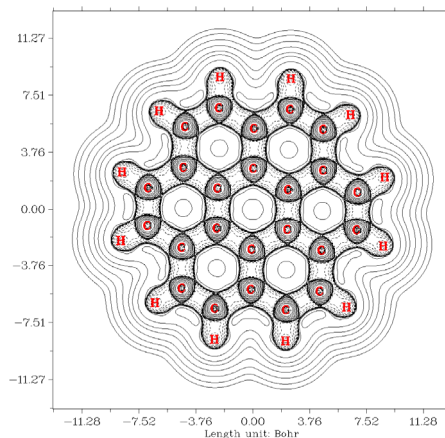
1,2-Aza-phospha-coronene



1,3-Aza-phospha-coronene



1,4-Aza-phospha-coronene



Coronene

Figure 3. Graphical representation of Laplacian of electron density, $\nabla^2 \rho(r)$, for the aza-phospha-coronenes and coronene, respectively.

CONCLUSIONS

Three aza-phospha-coronenes (with heteroatoms in ortho, meta and para positions, respectively) have been proposed. Their aromatic character was evaluated by means of magnetic, energetic and geometric criteria, using both local and global descriptors of aromaticity. All the structures are believed to be stable, taking into the account the values of HOMO-LUMO gap, close to the one corresponding for coronene. In this regard, and also

when taking into account the values of electronic descriptors like PDI, it can be said that the heteroatoms don't have a significant contribution. Instead, values of local indices like NICS and bond length equalization deviation clearly show a decrease of the aromatic character together with the presence of heteroatoms. Among the studied compounds, the 1,3-substitution type appears to be favored (according to NICS and PDI values). Graphical representation of the Laplacian of electron density outlines the influence of the heteroatoms on the aromatic behavior of the compounds.

COMPUTATIONAL DETAILS

All the computations have been performed at HF/6-311+G level of theory. All the structures have been optimized, no imaginary frequencies being obtained. The geometries of all the aza-phospha-coronenes are non-planar. All the computations have been performed with the Gaussian 09W program; exceptions are the electron density calculations and the graphical representation of the Laplacian of electron density, which have been obtained by means of Multiwfn 3.3.4 software [19].

ACKNOWLEDGMENTS

This work was supported by a grant of the Romanian Ministry of Education, CNCS – UEFISCDI, project number PN-II-RU-PD-2012-3-0102.

REFERENCES

- [1]. J.Z. Wen, H. Richter, W.H. Green, J.B. Howard, M. Treska, P.M. Jardin, J.B. Vander Sande, *J. Mater. Chem.* **2008**, *18*, 1561.
- [2]. H. Takehara, M. Fujiwara, M. Arikawa, M.D. Diener, J.M. Alford, *Carbon* **2005**, *43*, 311.
- [3]. B. Saha, S. Irle, K. Mokoruma, *J. Chem. Phys.* **2010**, *132*, 224303.
- [4]. Q. Zhang, H. Peng, G. Zhang, Q. Lu, J. Chang, Y. Dong, X. Shi, J. Wei, *J. Am. Chem. Soc.* **2014**, *136*(13), 5057-5064.
- [5]. S. Sanyai, A.K. Manna, S.K. Pati, *Chem. Phys. Chem.* **2014**, *15*(5), 885-893.
- [6]. G.V. Baryshnikov, R.R. Valiev, N.N. Karaush, B.F. Minaev, *Phys. Chem. Chem. Phys.* **2014**, *16*, 15367.

- [7]. G.V. Baryshnikov, B.F. Minaev, N.N. Karaush, V.A. Minaeva, RSC Adv. **2014**, 4, 25843.
- [8]. M.V. Diudea, A.E. Vizitiu, T. Beu, A. Bende, C.L. Nagy, D. Janezic, J. Mol. Struct.: THEOCHEM **2009**, 904, 28.
- [9]. Krygowski, T.M.; Cyrański, M.K. Chem. Rev. **2001**, 101, 1385-1419.
- [10]. Katritzky, A.R.; Jug, K.; Oniciu, D.C. Chem. Rev. **2001**, 101, 1421-1449.
- [11]. A. Acocella, R.W.A. Havenith, E. Steiner, P.W. Fowler, L.W. Jenneskens, Chem. Phys. Lett. **2002**, 363, 64.
- [12]. Schleyer, P.v.R.; Maerker, C.; Dransfeld, A.; Jiao, H.; Hommes, N.J. J. Am. Chem. Soc. **1996**, 118, 6317.
- [13]. J. Aihara, Bull. Chem. Soc. Japan **2004**, 77(12), 2179-2183.
- [14]. Y. Ruiz-Morales, J. Phys. Chem. A **2002**, 106(46), 11283-11308.
- [15]. Chesnut, D.B.; Moore, K.D., J. Comput. Chem. **1985**, 10, 648.
- [16]. Gaussian 09, Revision B.01, M.J. Frisch, G.W. Trucks, H.B. Schlegel, G.E. Scuseria, M.A. Robb, J.R. Cheeseman, G. Scalmani, V. Barone, B. Mennucci, G.A. Petersson, H. Nakatsuji, M. Caricato, X. Li, H.P. Hratchian, A.F. Izmaylov, J. Bloino, G. Zheng, J.L. Sonnenberg, M. Hada, M. Ehara, K. Toyota, R. Fukuda, J. Hasegawa, M. Ishida, T. Nakajima, Y. Honda, O. Kitao, H. Nakai, T. Vreven, J.A. Montgomery, Jr., J.E. Peralta, F. Ogliaro, M. Bearpark, J.J. Heyd, E. Brothers, K.N. Kudin, V.N. Staroverov, T. Keith, R. Kobayashi, J. Normand, K. Raghavachari, A. Rendell, J.C. Burant, S.S. Iyengar, J. Tomasi, M. Cossi, N. Rega, J.M. Millam, M. Klene, J.E. Knox, J.B. Cross, V. Bakken, C. Adamo, J. Jaramillo, R. Gomperts, R.E. Stratmann, O. Yazyev, A.J. Austin, R. Cammi, C. Pomelli, J.W. Ochterski, R.L. Martin, K. Morokuma, V.G. Zakrzewski, G.A. Voth, P. Salvador, J.J. Dannenberg, S. Dapprich, A.D. Daniels, O. Farkas, J.B. Foresman, J.V. Ortiz, J. Cioslowski, and D.J. Fox, Gaussian, Inc., Wallingford CT, **2010**.
- [17]. J. Poater, X. Fradera, M. Duran, M. Sola, Chem. Eur. J. **2003**, 2, 400.
- [18]. C. Foroutan-Nejad, S. Shahbazian, P. Rashidi-Ranjbar, Phys. Chem. Chem. Phys. **2010**, 12, 12630-12637.
- [19]. Lu, T.; Chen, F.J. Comp. Chem. **2012**, 33, 580.

DETERMINATION OF Cd(II) USING SQUARE WAVE ANODIC STRIPPING VOLTAMMETRY AT A CARBON PASTE ELECTRODE CONTAINING BI-DOPED CARBON XEROGEL

AGLAIA RALUCA DEAC^a, LIVIU COSMIN COTEȚ^b,
GRAZIELLA LIANA TURDEAN^a, LIANA MARIA MURESAN^{a*}

ABSTRACT. A novel carbon paste electrode (CPE) modified with Bi-doped carbon xerogel (BiCXe) is presented as a promising alternative to electrode materials used to replace mercury electrode in detection of heavy metals ions from aqueous solutions. The *ex situ* preparation of BiCXe was realized by sol-gel technique involving a reaction between a mixture of organic compounds (resorcinol, formaldehyde, glycerol formal) and a bismuth salt ($\text{Bi}(\text{NO}_3)_3 \cdot 5 \text{H}_2\text{O}$) in the presence of a catalyst (NH_4OH), followed by gel washing, drying and pyrolysis at $550^\circ\text{C}/2\text{h}$ in inert atmosphere (Ar). Electrochemical investigation of BiCXe-CPE was performed by cyclic voltammetry (CV) and square wave voltammetry (SWV), and the detection of Cd (II) ions by square wave anodic stripping voltammetry (SWASV) in acetate buffer 0.1 M (pH = 4.5). The electroanalytical parameters of the new sensor were determined. The favourable performance of the novel electrode coupled with the mercury-free surface make this sensor very attractive for environmental monitoring of toxic Cd(II) ions.

Keywords: carbon paste electrode; Bi-doped carbon xerogel; Cd(II) detection; square wave voltammetry; anodic stripping;

INTRODUCTION

Detection of heavy metal ions is of big importance, due to their toxicity, their negative impact on ecological quality and their increased presence in the environment. Among the electrodes used for electrochemical detection of heavy metals ions, mercury electrode is the transducer most used, showing the best sensitivity, selectivity and reproducibility due to its regenerative active area [1].

^a Department of Chemical Engineering, "Babes-Bolyai" University, 11 Arany Janos, RO-40 0028 Cluj-Napoca, Romania

^b Laboratory of Electrochemical Research and Nonconventional Materials, "Babes-Bolyai" University, 11 Arany Janos, RO-40 0028 Cluj-Napoca, Romania

* Corresponding author: limur@chem.ubbcluj.ro

However, due to its high toxicity, volatility, the difficulty of handling and miniaturization, the increased purchase price and maintenance, considerable efforts have been made in the last years to replace it with other electrode materials which overcome all these shortcomings, without significant decrease in their electrochemical and sensory properties.

Carbon xerogels (CXe) are microporous carbon materials that have received considerable attention in the literature over the past decade [2–5]. These materials can be produced in different forms (as powders, thin-films, cylinders, spheres, discs, or can be custom shaped) [5]. The most important properties of these materials are their high porosity, controllable surface area and controlled pore size distribution, low electrical resistivity and good thermal and mechanical properties. These properties make them promising materials for several potential applications as electrode material for double layer capacitors or supercapacitors [6], adsorption materials for gas separation [7], catalyst supports [8], column packing materials for chromatography [9], biotechnology [10] and sensing devices [11].

Recently, carbon xerogels containing Bi (BiCXe) have been shown to offer comparable performances to Hg electrodes in detection of heavy metal ions from aqueous solutions [2]. There were reported several methods to develop Bi containing electrodes. They are using: (i) bismuth nano-powders [4]; (ii) bismuth-modified boron doped diamond [12]; (iii) *in situ* bismuth-modified multi-walled carbon nanotubes doped carbon paste [13]; (iv) bismuth-films deposited on different substrates [14-17]; (v) screen-printed electrodes modified with Bi-nanoparticles [3, 18] or Bi films [19].

In this context, the present research aims to investigate a novel electrode material based on Bi-doped carbon xerogel incorporated in carbon paste as a promising alternative to mercury electrode in detection of Cd(II) ions from aqueous solutions. The proposed electrode material was tested for determination of Cd(II) at trace level by using square wave anodic stripping voltammetry (SWASV).

RESULTS AND DISCUSSION

Electrochemical behavior of BiCXe-CPE

The favourable electrochemical characteristics of the new electrode are revealed in figure 1, which shows a comparison between CV and SWV obtained at the BiCXe-CPE and CXe-CPE. SWV is more frequently used, because is a sensitive method that can feel any noise, impurities, surface contamination, etc. which may affect the sensitivity and reproducibility of Bi electrode. To determine the optimum parameters of measurements for the proposed material, some preliminary experiments, using CV and SWV, in buffer solutions were carried out.

Acetate buffer (pH 4.5) was selected as working electrolyte for all experiments due to the fact that it is commonly used by many researchers [20-24], especially in the environmental analysis, as buffer solution for electrochemical measurements that include materials containing Bi, because the response of bismuth is more clearly defined and the oxidation occurs more easily than in other solutions.

In figure 1A are presented the cyclic voltammograms recorded for CXe-CPE and BiCXe-CPE electrodes. The redox process corresponding to Bi oxidation/reduction can be observed on the solid line voltammogram, proving its presence in the carbon paste, respectively in the BiCXe sample. The redox behavior of the BiCXe-CPE is a quasi-reversible process placed at -0.05 V vs. Ag/AgCl, KCl_{sat} (oxidation) and respectively at -0.58 V vs. Ag/AgCl, KCl_{sat} (reduction), with a peak separation (ΔE , defined as difference between anodic and cathodic peak potentials) of 0.53 V.

A similar redox behaviour of BiCXe-CPE is observed in SWV, where the anodic oxidation can be much better observed, and the Bi oxidation peak is placed at -0.12 V vs. Ag/AgCl, KCl_{sat} , (figure 1B).

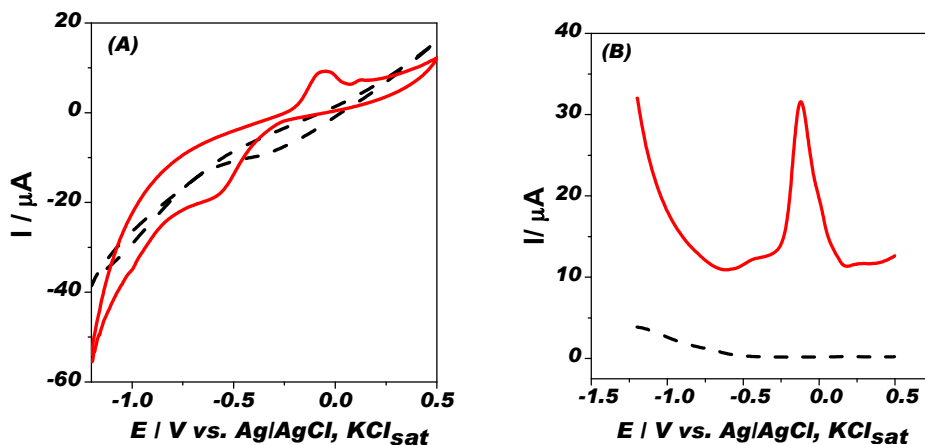


Figure 1. Cyclic (A) and square wave (B) voltammograms for CXe-CPE (dash line) and BiCXe-CPE (solid line). Experimental conditions: electrolyte, 0.1 M acetate buffer (pH 4.5); frequency, 25 Hz; amplitude, 0.05 V; step potential, 0.004 V; starting potential, -1.2 V; equilibration, 10 s without stirring.

In the case of SWV, several frequencies and signal amplitudes were tried in order to get a well-defined answer of the modified carbon paste electrode. It was found out that the optimal frequencies domain is relatively limited. The best response of electrode was recorded between 25-50 Hz (Figure 2), so all further experiments were carried out by using a frequency of 25 Hz.

When the optimal experimental parameters were used, the recorded stripping voltammogram at BiCXe-CPE (solid-line, Figure 1B), shows a clean and undistorted stripping signal.

These results prove clearly that the investigated material contains bismuth. In the same time, it was established that the peak height is proportional to the Bi content in the carbon paste and, respectively, in the xerogel (results not shown).

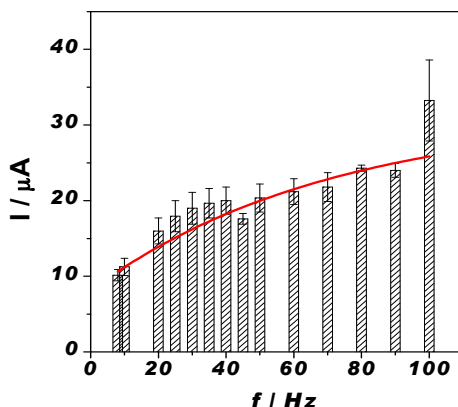


Figure 2. Influence of input signal frequency on the electrochemical response of BiCXe-CPE. Experimental conditions: electrolyte solution, 0.1 M acetate buffer (pH 4.5); frequencies, 8 - 100 Hz; amplitude, 0.05 V; scan rate, 0.004 V; starting potential, -1.2 V; equilibration time, 10 s.

To determine the stability of BiCXe-CPE, the electrode was exposed to a set of four-five successive measurements, in pure 0.1 M acetate buffer (pH 4.5) and SWV were recorded for each experiment (results not shown). There were no significant differences between the responses of the electrode, which indicates good short-time stability.

Detection of Cd(II) at BiCXe-CPE electrodes

The BiCXe-CPE electrode was further examined by recording SWASVs in the presence of Cd(II) ions (figure 3). The voltammogram exhibited a well-defined, sharp and undistorted stripping signal for Cd(II) and Bi(III) with peak potentials placed at -0.750 V and -0.12 V vs. Ag/AgCl, KCl_{sat}, respectively, values in agreement with those reported in the literature [25]. With the increasing of Cd(II) concentration to 20 μM, the potential of Cd(II) and Bi(III) is shifted to much positive values, *i.e.* at -0.665 V ($\Delta E = 0.085$ V) and -0.063 V vs. Ag/AgCl, KCl_{sat} ($\Delta E = 0.039$ V), respectively.

Optimisation of anodic stripping voltammetry conditions for Cd(II) detection was studied. Thus, the influence of the deposition time on the 2 μM Cd(II) ion detection was investigated in the range of 30-360 s. In the inset of

figure 3 a linear dependence was observed with a slope of $1.6 \cdot 10^{-2} \pm 0.02 \cdot 10^{-2} \mu\text{A/s}$ ($R = 0.9994$, $n = 7$). Consequently, a deposition time of 120 s was chosen for further measurements as a compromise between sensibility and experiment duration.

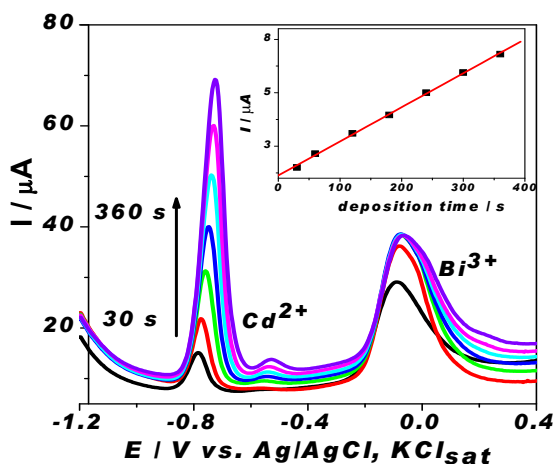


Figure 3. SWASVs of 2 μM Cd (II) at BiCXe-CPE electrode for different deposition time. Inset Cd(II) peak current vs. deposition time dependence. Experimental conditions: electrolyte, 0.1 M acetate buffer (pH 4.5); frequency, 25 Hz; amplitude, 0.05 V; step potential, 0.004 V; starting potential, -1.2 V; deposition potential -1.2 V; deposition time, 30 s to 360s under continuous stirring at 500 rpm; equilibration, 10 s without stirring; electrode conditioning, +0.3 V; duration, 30 s under continuous stirring at 500 rpm.

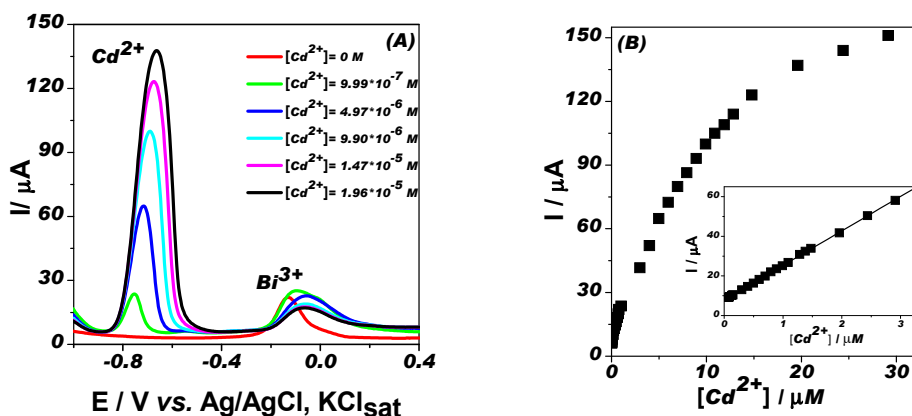


Figure 4. SWASVs recorded on BiXe-CPE for Cd(II) ion detection (A) and corresponding calibration curve (B). Experimental conditions: see Figure 3.

The detection of Cd(II) ions by recording SWASVs in the range of 0-30 μM Cd(II) lead to the obtaining of a corresponding calibration curve (figure 4B). The linear domain is in the range of 0 - 3 μM Cd(II) (figure 4B inset) with a slope of $17.39 \pm 0.07 \text{ A/M}$ ($R = 0.99983$, $n = 21$ points). The detection limit (LOD) was $0.045 \mu\text{M/L}$ (or $5 \mu\text{g/L}$) (signal/noise = 3) The LOD value is in concordance with the maximum contaminant level goals for Cd concentration in drinking water requested by the EU and USA legislations [26-27].

One of the most important performance characteristic of the sensor is its reproducibility, expressed as relative standard deviation (RSD) of the peak current or of the peak potential (results not shown). In the case of three successive measurements of $2 \mu\text{M}$ Cd(II) at BiCXe-CPE in 0.1 M acetate buffer pH 4.5, the mean peak intensity is $2.66 \cdot 10^{-5} \pm 8.38 \cdot 10^{-8} \text{ A}$, with a RSD of 0.31% and the mean peak potential is $-0.753 \pm 0.006 \text{ V vs. Ag/AgCl, KCl}_{\text{sat}}$, with a RSD of 0.8%, respectively. The obtained RSD values indicate a good reproducibility of the obtained sensor, recommending the BiCXe-CPE as a good sensor for Cd(II) detection.

Interference of Pb(II) to Cd(II) detection at BiCXe-CPE electrodes

In order to investigate the possible interference with other heavy metals, SWASVs were recorded in solution containing a mixture of Cd(II) and Pb(II) of same concentrations. In figure 5 it is observed that well-defined peaks attributed to the oxidation of Cd(II), Pb(II) and Bi(III), are placed at -0.766 V , -0.52 V and $-0.03 \text{ V vs. Ag/AgCl, KCl}_{\text{sat}}$, respectively. Even if a shift of oxidation potential is observed when the ions concentration is increasing, the peak separation is enough large to avoid interferences in both Cd(II) or Pb(II) detection in a mixture sample.

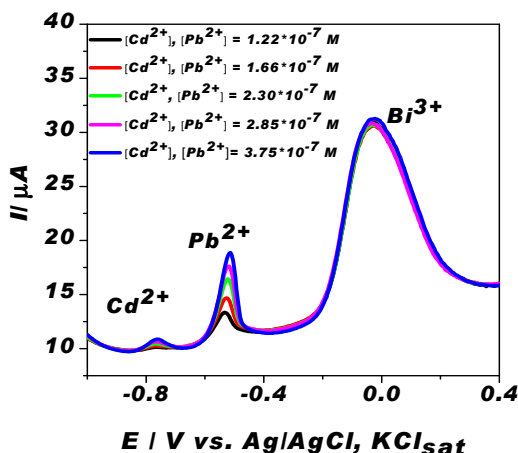


Figure 5. SWASVs responses for increasing concentrations of Cd(II) and Pb(II) at BiCXe-CPE electrode. Experimental conditions: starting potential, $-1.3 \text{ V vs. Ag/AgCl, KCl}_{\text{sat}}$; other conditions see figure 3.

CONCLUSIONS

The BiCXe-CPE electrode successfully exploits the favourable mechanical and electrochemical properties of carbon paste electrodes and combines them with the unique electroanalytical characteristics of Bi-based xerogels.

The modification of carbon paste electrodes with carbon xerogels containing Bi could be used for the sensitive detection of Cd(II) ions, without interfering with Pb detection.

The low cost of graphite, simplicity of fabrication of the BiCXe-CPE electrodes and the obtained detection limit recommend this electrode for replacing mercury electrode in the detection of Cd(II) ions from aqueous solutions.

EXPERIMENTAL

Materials

Chemicals for *ex situ* preparation of Bi-doped carbon xerogel (BiCXe) involve $\text{Bi}(\text{NO}_3)_3 \cdot 5 \text{H}_2\text{O}$ (Alfa Aesar- UK), glycerol formal (Sigma Aldrich), resorcinol - $\text{C}_6\text{H}_6\text{O}_2$, formaldehyde, catalyst NH_4OH , glacial acetic acid (the last three from MERCK, Germany) and $\text{Cd}(\text{NO}_3)_2$, $\text{Pb}(\text{CH}_3\text{COO})_2$ (Reactivul Bucuresti). For carbon paste electrode preparation, graphite powder and paraffin oil from Fluka Sigma-Aldrich, Germany were used. Acetate buffer (0.1 M, pH 4.5) used in SWV experiments was prepared by mixing 0.2 M NaAc (Reactivul Bucuresti, Romania) solution with 0.2 M HAc solution. Cd (II) and Pb(II) 10^{-6}M stock solutions were prepared by dissolving appropriate amounts of $\text{Cd}(\text{NO}_3)_2 \cdot 4 \text{H}_2\text{O}$ and $\text{Pb}(\text{CH}_3\text{COO})_2 \cdot 3 \text{H}_2\text{O}$ into the buffer solution (pH 4.5). All solutions were prepared with double distilled water.

Apparatus and methods

Cyclic and square wave voltammetry (SWV, SWASV) were performed with an AUTOLAB PGSTAT 12/100, Booster 20A, $\mu\text{Autolab}$ type III/ FRA2, electrochemical station. A pH-meter, MV 870 DIGITAL-pH-MESSAGERÄT-PRACITRONIC, was used to measure the pH of solutions. A conventional three-electrode system consisting of a BiCXe-CPE with inner diameter of 2 mm, a counter electrode made of platinum, and an $\text{Ag}/\text{AgCl}/\text{KCl}_{\text{sat}}$ reference electrode were used for electrochemical measurements.

Procedures

Synthesis of BiCXe

The obtaining of the carbon xerogels through sol-gel synthesis consisted in several steps [2]:

- ✓ **sol preparation:** based on the poly-condensation reaction of resorcinol (R) with formaldehyde (F) in basic catalysis of NH_4OH in the presence of glycerol formal / acetic acid containing Bi salt;
- ✓ **gel aging or gelation** in aging-oven;
- ✓ **gel washing:** in acetic acid;
- ✓ **drying** in ambient conditions;
- ✓ **thermal treatment:** pyrolysis (550°C / 2h/ Ar)

The BET analysis revealed that the xerogels have a specific surface area of $80 \text{ m}^2\text{g}^{-1}$ and a specific pore volume of $0.04 \text{ cm}^3\text{g}^{-1}$, suggesting that their structure presents mesopores. In the same time, it was found that Bi did not affect the porosity of the carbon xerogel.

Preparation of the carbon paste electrode containing Bi doped carbon xerogel (BiCXe-CPE)

CXe-CPE (blank) and CXe doped with bismuth-CPE (BiCXe-CPE) electrodes were prepared as follows: graphite powder (0.02 g), CXe or BiCXe (0.04 g) and paraffin oil (30 μL) were carefully mixed in a mortar and then homogenized by continuous hand-mixing for 30 min. (Figure 6, step a). The paste was then introduced in a cylindrical holder (Figure 6, step b) and the electrode surface was smoothed by polishing on a normal clean white paper. The electrode was ready to use, without any further chemical or electrochemical pretreatment. This step was repeated by replacing the used paste with a fresh one before each experiment.

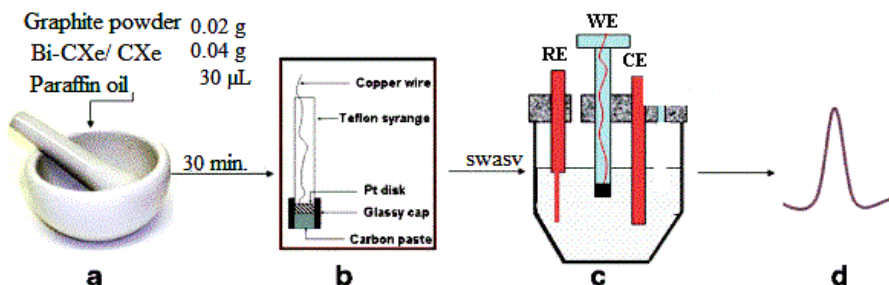


Figure 6. Preparation and characterization of the carbon paste electrode containing xerogels

Electrochemical characterization of the carbon paste electrode containing BiCXe

The working electrode was installed in a conventional electrochemical cell filled with 10 mL acetate buffer 0.1 M, pH = 4.5 (Figure 6, step c) and connected to a potentiostat. Before each experiment, the surface of electrode was renewed and polished on a white paper sheet.

The electrochemical measurements were performed by applying the desired potential to the electrodes and measuring the generated current during the potential scan. The SWV voltammograms were recorded after applying 10 s equilibration period, stage followed by application of a positive- going square wave voltammetric potential scan from -1.2 to 0.5 V vs. Ag/AgCl, KCl_{sat}, with a frequency of 25 Hz, pulse amplitude of 0.05 mV, and step increment of 4 mV. These parameters were fixed after a systematic investigation of the electrochemical process. All the experiments were carried out at room temperature.

ACKNOWLEDGEMENTS

This work was possible due to the financial support of the Sectorial Operational Program for Human Resources Development 2007-2013, co-financed by the European Social Fund, under the project number POSDRU/159/1.5/S/132400 with the title „Young successful researchers – professional development in an international and interdisciplinary environment”.

REFERENCES

- [1]. J. Wang, *Electroanalysis*, **2005**, *17*, 1341.
- [2]. M. Gich, C. Fernandez-Sanchez, L.C. Cotet, P. Niu, A. Roig, *Journal of Materials Chemistry. A*, **2013**, *1*, 11410.
- [3]. I. Svancara, C. Prior, S.B. Hocevar, J. Wang, *Electroanalysis*, **2010**, *22(13)*, 1405.
- [4]. G. Aragay, *Electrochimica Acta*, **2012**, *84*, 49.
- [5]. J.A. Rodrigues, C.M. Rodrigues, P.J. Almeida, I.M. Goncalves, R.G. Comptonb, A.A. Barros, *Analytica Chimica Acta*, **2011**, *701*, 152.
- [6]. J. Lee, S. Yoon, T. Hyeon, S.M. Oh, K.B. Kim, *Chemical Comunication*, **1999**, 2177.
- [7]. A.K. Meena, G.K. Mishra, P.K. Rai, C. Rajagopal, P.N. Nagar, *Journal of Hazardous Materials B*, **2005**, *122*, 161.
- [8]. T.W. Kim, P.W. Chung, I.I. Slowing, M. Tsunoda, E.S. Yeung, V.S.Y. Lin, *Nano Letters* **8**, **2008**, *11*, 3724.
- [9]. M. Steinhart, C. Liang, G.W. Lynn, U. Gösele, S. Dai, *Chemestry of Materials*, **2007**, *19 (10)*, 2383.
- [10]. C. Liang, S. Dai, G.A. Guiochon, *Analytical Chemistry*, **2003**, *75*, 4904.
- [11]. C.-S. Chu, Y.-L. Lo, *Sensors and Actuators B*, **2008**, *129*, 120.
- [12]. Toghil K. E., G.G. Wildgose, A. Moshar, C. Mulcahy, R.G. Compton, *Electroanalysis*, **2008**, *20*, 1731.
- [13]. J. Hua Luo, X. Xia Jiao, N. Bing Li, H. Qun Luo, *Journal of Electroanalytical Chemistry*, **2013**, *689*, 130.

- [14]. D. Martín-Yerga, M. Begoña González-García, A. Costa-García-Nanobioanalysis Group, *Talanta*, **2013**, *116*, 1091.
- [15]. A. Charalambous, A. Economou, *Analytica Chimica Acta*, **2005**, *547*, 53.
- [16]. H. Xu, L. Zeng, D. Huang, Y. Xian, L. Jin, *Food Chemistry*, **2008**, *109*, 834.
- [17]. Y. Wu, N. Bing, H.Q. Luo, *Sensors and Actuators B: Chemical*, **2008**, *133*, 677.
- [18]. J.C. Quintana, F. Arduini, A. Amine, F. Punzo, G. Li Destri, C. Bianchini, D. Zane, A. Curuli, G. Palleschi, D. Moscone, *Analytica Chimica Acta*, **2011**, *707*, 171-177.
- [19]. C. Kokkinos, A. Economou, I. Raptis, C. E. Efstathiou, *Electrochimica Acta*, **2008**, *53*, 5294-5299.
- [20]. V. Rehacek, I. Hotovy, M. Vojs, T. Kups, L. Spiess, *Electrochimica Acta*, **2012**, 192-196.
- [21]. G.D. Pierini, A.M. Granero, M.S. Di Nezio, M.E. Centurión, M.A. Zon, H. Fernández, *Microchemical Journal*, **2013**, 102–106.
- [22]. Y. Tian, Lianzhe Hu, S. Han, Y. Yuan, J. Wang, G. Xu, *Analytica Chimica Acta*, **2012**, 41–44.
- [23]. J. Saturno, D. Valera, H. Carrero, L. Fernandez, *Sensors and Actuators B: Chemical*, **2011**, 92–96.
- [24]. H. Sopha, S.B. Hocevar, B. Pihlar, B. Ogorevc, *Electrochimica Acta*, **2012**, 274–277.
- [25]. S.B. Hocevar, I. Svancara, K. Vytras, B. Ogorevc, *Electrochimica Acta* **2005**, *51*, 706-710.
- [26]. ***Council Directive 98/83/EC of 3 November 1998 on the quality of water intended for human consumption; published in *Official Journal* L 330, 05/12/1998 P. 0032 – 0054;
<http://eur-lex.europa.eu/legalcontent/EN/TXT/?uri=CELEX:31998L0083> visited the 29th of September 2014.
- [27]. *** US Environmental Protection Agency,
<http://water.epa.gov/drink/contaminants/basicinformation/cadmium.cfm> visited the 29th of September 2014.

COMPARATIVE STUDY ON COBALT AND NICKEL NPs FOR MWCNT GROWTH BY TCVD SYSTEM

SEPIDEH SADAT MADANI^a, KARIM ZARE^{a, b,*}, MAHMOOD
GHORANNEVISS^c AND MAJID MONAJJEMI^a

ABSTRACT. In this paper, cobalt and nickel NPs (nanoparticles) effect on carbon nanotubes growth by Thermal chemical vapor deposition (TCVD) is studied. The DC - sputtering system was used to prepare cobalt and nickel thin films on Si substrates. The produced layers were used as metal catalysts for growing carbon nanotubes (CNTs) from acetylene (C₂H₂) gas in the temperature range of 850°C to 1000°C with an interval of 50°C by Thermal Chemical Vapor Deposition (TCVD) technique. Energy Dispersive X-ray (EDX) measurements were used to investigate the elemental composition of the cobalt and nickel NPs deposited on the Si substrates. Also, Atomic Force Microscopy (AFM) was used to characterize the surface morphology of the Co and Ni nanoparticles on the Si substrates. The grown CNTs on the Co and Ni catalyst at different temperatures have been characterized by Raman spectroscopy, Field Emission Scanning Electron Microscopy (FESEM) and High Resolution Transmission Electron Microscopy (HRTEM). The results showed that the diameter of CNTs can be controlled by adjusting the growth temperature, and increasing the temperature leads to increasing the diameter of CNTs. It was found that there is a strong relation between diameter and yield of CNTs at different growth temperature with different catalysts (Co and Ni). Also, the grown CNTs at the temperature of the 850°C using Co catalyst among all of the samples (Co and Ni catalysts) have a minimum diameter and maximum yield.

Keywords: Carbon nanotubes, DC – sputtering, TCVD; Metal catalysts, FESEM, HRTEM

^a Department of Chemistry, Science and Research Branch, Islamic Azad University, Tehran, Iran

^b Department of Chemistry, Shahid Beheshti University, Tehran, Iran

^c Department of Physics, Science and Research Branch, Islamic Azad University, Tehran, Iran

* Corresponding author: prof.zare@gmail.com

INTRODUCTION

In the last decades, low dimensional carbon-based materials such as carbon nanotubes, polymer nanofibers, carbon nanotips, and graphene have attracted great attention due to their novel structures and extensive applications in the areas of nanoelectronic and nanophotonic devices, biology and medicine [1-7]. Three major methods have been developed to grow CNTs: arc discharge [8], laser ablation [9] and chemical vapor deposition (CVD) [10-12]. Among these methods CVD has attracted much attention owing to its advantages including lower cost, high yield, high purity and selective growth of CNTs. There are three main CVD techniques: 1- Thermal CVD (TCVD), 2- Plasma enhanced CVD (PECVD), and 3- Hot filament CVD (HFCVD) [11-13]. The growth of CNTs by CVD contains two steps: preparation of catalyst nanostructure layers and growth of CNTs on the layers. The chemical vapor deposition (CVD) provides a reliable approach to grow nanotubes on different substrates and is suitable for scaled growth of high purity multi-walled and single-walled carbon nanotubes. In addition, CVD operates at substantially lower temperature in comparison to laser ablation and arc discharge processes [14]. In this method, the characteristics of CNTs such as diameter distribution, surface density, morphology and crystallization are significantly affected by the synthesis parameters ranging from growth temperature, pressure, hydrocarbon source and type of substrate to the catalyst characteristics including its morphology, composition and the technique of catalyst preparation [15-21]. It is well known that the catalyst is indispensable for the growth of CNTs in CVD process. A variety of metal catalysts such as Au, Ag, Pt, Pd, Mn, Mo, Mg and Al have been developed for the growth of CNTs [22-26]. However, most of the widely used CNT production methods are based on the use of transition metal catalysts, including Fe, Co, Ni and their alloys [27].

There are several efforts related in the literature about growth time and/or temperature effect on the radius of the CNTs. The results achieved with acetylene (C_2H_2) and CVD technique shows that the diameters of the CNTs increase as the temperature increases [28-30]. It was generally thought that the increase in diameter is due to the extra concentric cylinders in multiwall CNTs. However, a recent study shows that the increase in the diameter is due to nanocrystalline carbon or glassy carbon sheath which expands exponentially with the time [30]. According to the literature, in nearly all CVD-based processes, the precursor gas is a mixture of hydrocarbon source and a diluting or carrier gas such as hydrogen, argon and ammonia.

Here we report a systematic study of the metal catalysts (Co and Ni) effect on the growth of CNTs using thermal CVD method. We have successfully achieved the tuning of the diameter distribution and yield of CNTs by varying the growth temperature using both (Co and Ni) catalysts.

RESULTS AND DISCUSSION

All the growth conditions except the temperature of the system were kept constant in order to investigate the effect of Co and Ni catalysts and temperature variation. Prior to carbon nanotube growth, Energy Dispersive X-ray (EDX) measurements were done to investigate the elemental composition of the cobalt (Figure 1a) and nickel (Figure 1b) catalysts deposited on Si substrates. Atomic Force Microscopy (AFM) in contact mode was used for analyzing the surface morphology of Co and Ni films deposited on Si substrates (Figure 2 (a-d)). AFM images have been obtained in a scanning area of $3\mu\text{m} \times 3\mu\text{m}$. As it is clear, the formation of catalyst particles with a relatively smooth surface can be observed. For the analysis of the uniformity of catalyst distribution along the substrate surface, it is helpful to calculate the roughness value. The average roughness values are 1.91 nm and 2.15 nm for Co and Ni samples, respectively. Root-Mean-Square (RMS) roughness of both samples was measured over the whole area and it was 2.44 nm and 3.27 nm for Co and Ni, respectively. The RMS roughness of a surface is similar to the roughness average, with the only difference being the mean squared absolute values of surface roughness profile.

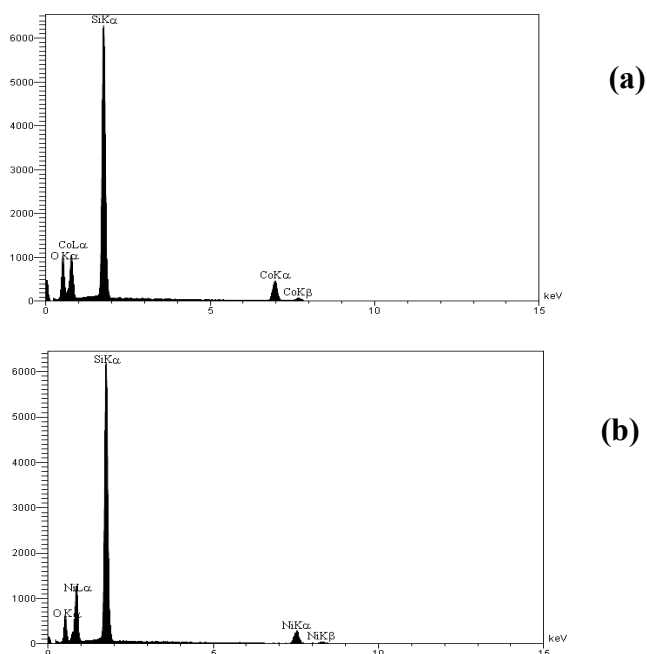


Figure 1. Energy Dispersive X-ray (EDX) measurements show the elemental composition of the (a) cobalt and (b) nickel nanoparticles deposited on Si substrates.

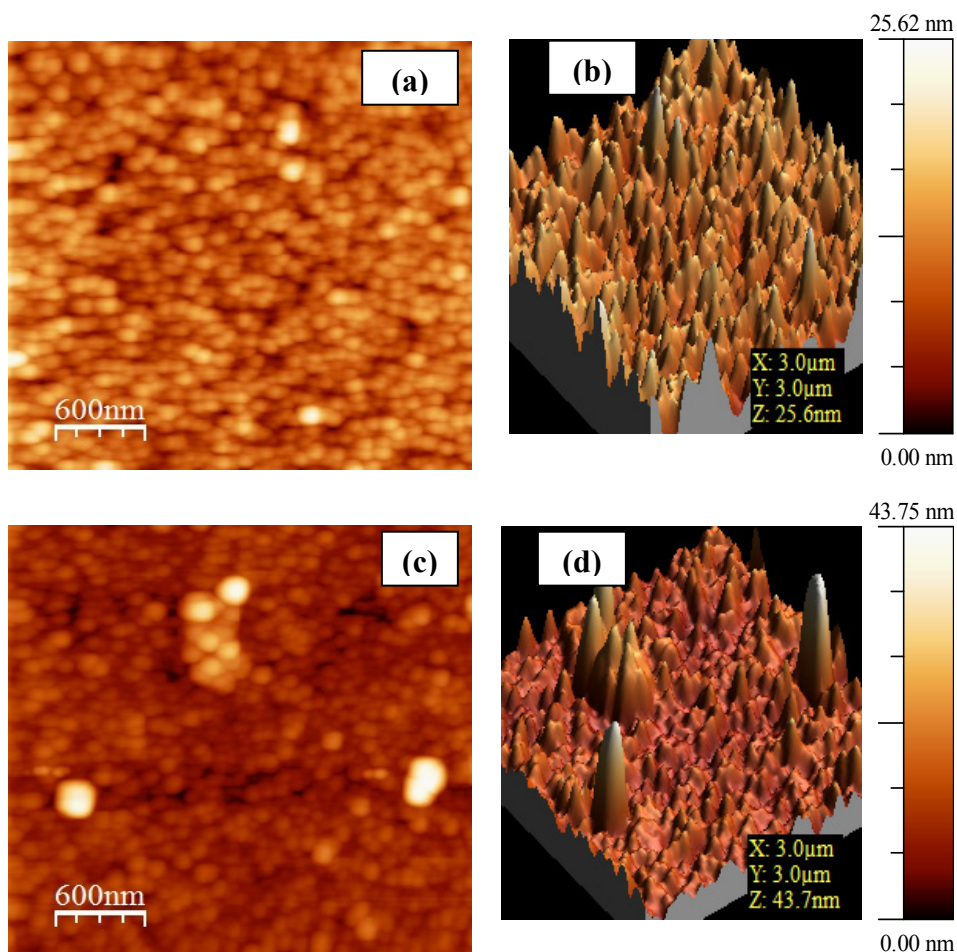


Figure 2. (a) 2D and (b) 3D AFM Images of Co film; (c) 2D and (d) 3D AFM Images of Ni film deposited on Si substrates.

Figure 3 (a-d) shows the FESEM images of CNTs grown on the cobalt nanocatalyst at different growth temperatures 850°C, 900°C, 950°C and 1000°C. In the presence of cobalt catalyst, as the growth temperature to 1000°C was increased, it was found that the diameter distribution of CNTs is raised, which implies that the diameter of grown CNTs increased and yield decreased. Figure 4 (a-d) shows the FESEM images of CNTs grown on the nickel nanocatalyst at different growth temperatures 850°C, 900°C, 950°C and 1000°C. A very small amount of CNTs was produced at 850°C on the Ni catalyst (Figure 4a). As the temperature increased to 900°C, the production of

CNTs has increased dramatically (Figure 4b). At 950°C compared to 900°C, a lower rate of CNTs was observed (Figure 4c). As can be seen in Fig. 4d, at 1000°C, nucleation was performed, but the growth has not taken place. Also, the grown CNTs at 850°C using Co catalyst among all of the samples (Co and Ni catalysts) have a minimum diameter and maximum yield.

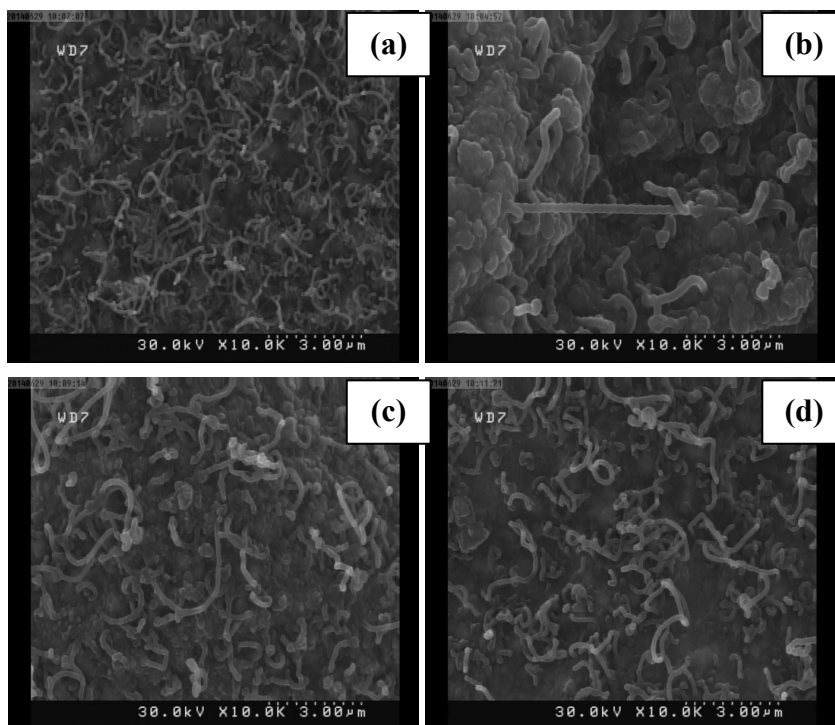


Figure 3. FESEM images of grown CNTs at different growth temperatures on the Co catalyst (a) 850°C, (b) 900°C, (c) 950°C, (d) 1000°C.

Since the quality and the structure of CNTs highly depends on the properties and the type of catalyst material being used, it is essential to study the catalysts. A key factor for controlling the diameter and the number of shells in a CNT is to gain control of the catalyst particle diameter, since they are the basis of the grown CNTs. Optimal growth requires a metal catalyst that exhibit sufficient carbon solubility, rapid carbon diffusion and limited carbide formation. It is important to mention that decomposition with common hydrocarbons, except CH_4 , is highly exothermic and can therefore dramatically increase the catalyst local temperature even if synthesis temperatures are low.

In general, the ability of transition metals to bond with carbon atoms increases with the number of unfilled d-orbitals. Metals with few d-vacancies such as Ni, Fe and Co exhibit finite carbon solubility. For transition metals, the affinity for carbon therefore increases from the right to the left of the periodic table [31-33]. Graphitic carbon will be allowed to form if the carbon concentration overcomes the solubility of carbon in the catalyst particle. For elements that do not form stable carbides (e.g. Cu, Ni, Co, Pb, Sn, Au, Ag, Zn, Cd, Pd, Pt) [34], the critical concentration for the segregation of graphitic carbon is therefore the solubility limit of carbon in the metal.

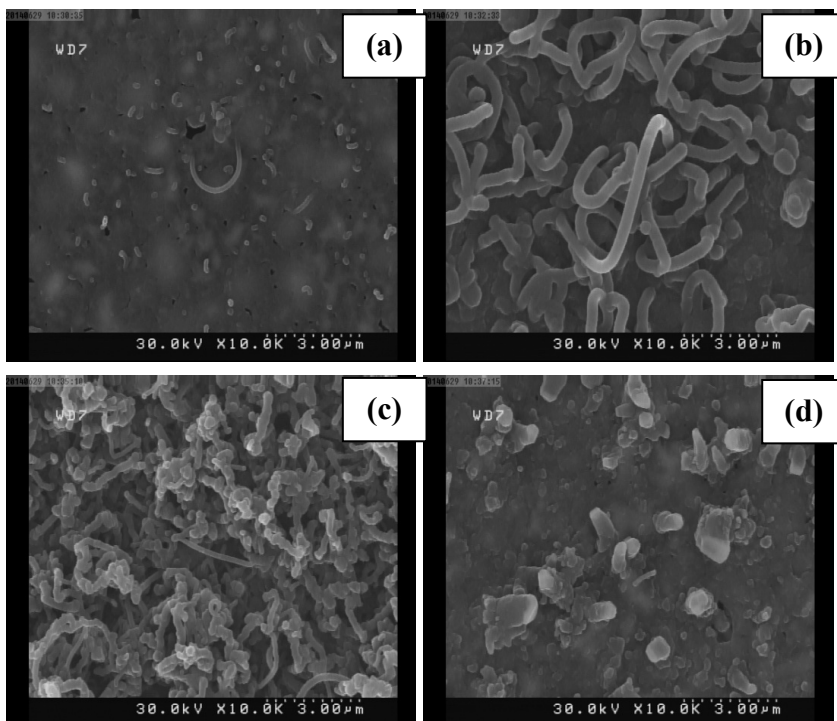


Figure 4. FESEM images of grown CNTs at different growth temperatures on the Ni catalyst (a) 850°C, (b) 900°C, (c) 950°C, (d) 1000°C.

The role of a catalyst is to accelerate a thermodynamically allowed chemical process (e.g. the decomposition of carbon containing molecules) by creating a transition state of lower energy [35]. The corresponding decrease of activation energy depends on the strength of the adsorbate–substrate bond which experimentally is reflected in the heat of adsorption. There is a general trend for the heats of adsorption to decrease from the left to the right of the

periodic table. This trend can be explained by the chemisorption model developed by Nørskov [36] stipulating that molecules adsorbing on transition metals preferentially interact with the d-states near the Fermi level that give rise to bonding and anti-bonding levels. The d-electron contribution to the bonding is therefore proportional to $(1 - f_d)$ where f_d is the degree of filling of the d-band.

When a molecule is adsorbed on a metal surface, the activation barrier for its dissociation is lowered. For instance, the activation barrier for the dissociation of acetylene was measured to be 1.4 eV on Ni (111) instead of 5.58 eV for self-decomposition [37]. If the surface bonds are too strong, the reaction intermediates will remain on the surface and block the adsorption of new reactant molecules. Forming adsorbate–substrate bonds of intermediate strength is an important property for a good catalyst.

It has long been recognized that the size and the surface structure of the catalyst can influence the catalytic activity. A catalytic reaction is defined as structure-sensitive if its conversion rate changes markedly as the size of the catalyst particles are changed. The reactivity of a metal surface is generally associated to both its geometric features and its electronic structure. Classically, the structure sensitivity of a catalytic reaction is associated with a modification of the population of reactive sites (terrace, steps, kinks, surface defects) with decreasing particle size [38].

According to Charles law of kinetic theory of gases [39], when temperature increases, then simultaneously volume of gas, kinetic energy of gas molecules and hence diffusion rate of gas molecules increase in the growth chamber. So when the growth temperature of CNTs increases, the decomposition rate of hydrocarbon in CVD chamber also increases and hence more carbon atoms make contact with catalyst particle and this is the main reason behind increasing the diameter of CNTs with increment in temperature. Also, as temperature increases the equilibrium between the decomposition of hydrocarbon and diffusion of carbon atoms in catalyst particle is also disturbed. So some carbon atoms are deposited on catalyst particle in the form of amorphous and these particles left from growth and hence yield of CNTs decreased.

A mechanism for the formation of carbon fibers on a catalyst particle was proposed by Baker and co-workers [40-42]. In their model, dissociation of carbon precursors on the catalyst surface was followed by diffusion of carbon into the metal catalyst particle. Once the catalyst was saturated with carbon, the carbon precipitated in the form of a fiber that continued to grow as more carbon dissociated and precipitated from the catalyst particle. The growth of carbon nanotubes is usually proposed to follow a similar mechanism. As with carbon spheres, the growing carbon fibers and tubes can also be covered with disordered graphitic flakes that are generated by gas phase carbon species that do not interact with the catalyst particle.

Histograms of diameter distribution of grown CNTs using Co and Ni catalysts, each fitted with a Gaussian curve, are demonstrated in Figure 5. According to these diagrams, the average diameter of the grown CNTs using Co and Ni catalysts is 114 nm and 295 nm, respectively. The average diameter of grown CNTs is greater than the average size of Co and Ni nanoparticles. In view of a direct relation between the nanocatalysts sizes with the diameters of grown CNTs, it can be suggested that the catalyst particles are agglomerated and resulted in greater particles during the process of CNT growth. It seems that such agglomeration is dramatically increased using Ni catalyst; consequently, the average diameter of grown CNTs using nickel catalyst is much larger than CNTs synthesized using cobalt catalyst.

Figure 6 shows the HRTEM image of the grown CNTs at a growth temperature of 850 °C using Co catalyst, which confirms that the morphologies seen in the FESEM images have tubular structure, i.e. they are multi-walled carbon nanotubes (MWCNTs).

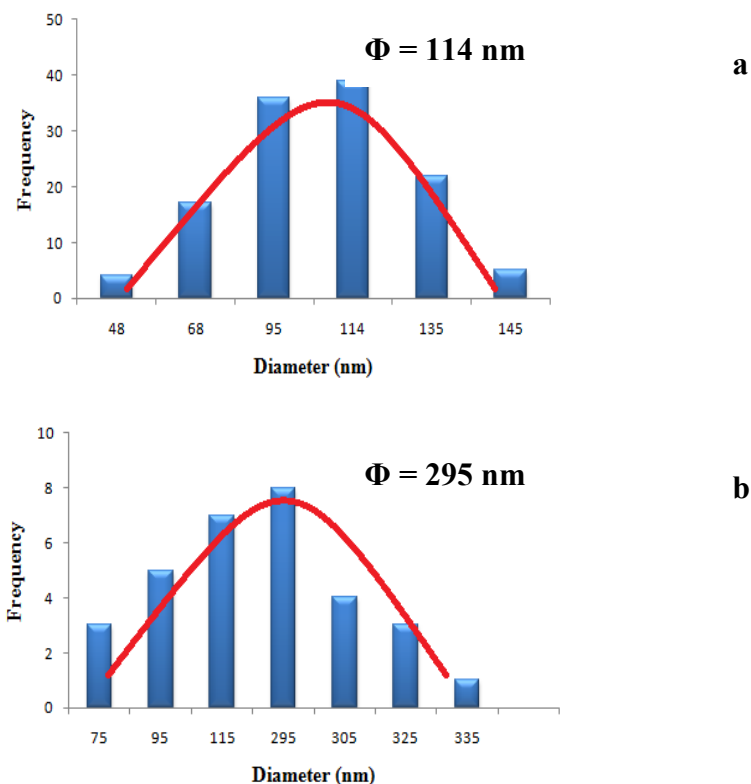


Figure 5. Histograms of diameter distribution of grown CNTs using (a) Co and (b) Ni catalysts. The diameter distributions are fitted with Gaussian curves.

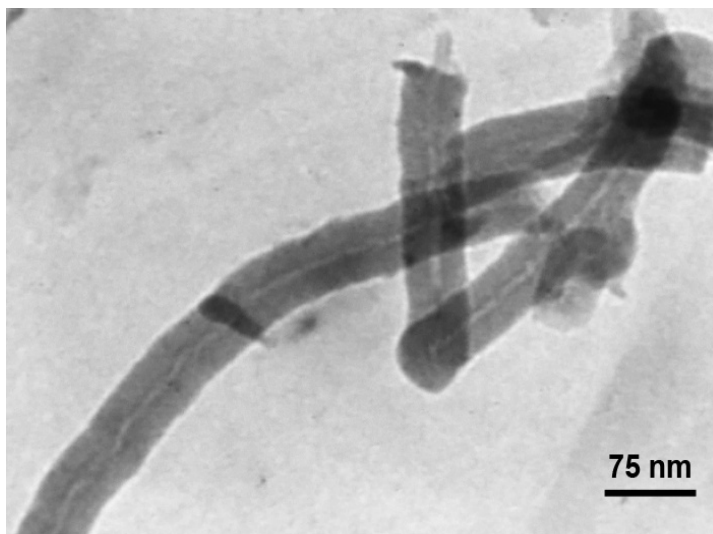


Figure 6. HRTEM image of the grown CNTs at growth temperature of 850°C using Co catalyst.

Raman spectroscopy is one of the most powerful tools for characterization of CNTs. The Raman spectrum of the produced CNTs on the cobalt catalyst at different growth temperatures is shown in Figure 7. The Raman band appearing in the 1500–1605 cm^{-1} region of the wave numbers is attributed to the G band (graphite band) and the one appearing in the 1250–1450 cm^{-1} spectral region is known as D band (disorder induced band). The G band is assigned to C–C vibration frequency of the carbon material with a sp^2 orbital structure and the D band is contributed to the disorder induced vibration of the C–C band [43]. In this work, there are two main peaks in the spectrum. The clear G band indicates the formation of graphitized MWCNTs and the D band indicates the existence of the disorder carbon, such as amorphous carbonaceous particles or defective graphite layers. Also, there is a peak in the region of the radial breathing mode (RBM), i.e. below 300 cm^{-1} of the spectrum. The RBM Raman features correspond to the atomic vibration of the C atoms in the radial direction. Raman spectra of CNTs grown on Co catalyst at the temperatures of 850°C and 950°C show RBM peak that it seems the presence of SWCNT in the cavity of MWCNT is responsible for the appearance of RBM in MWCNT as B. P. Singh et al. reported [44]. The peak intensity ratio I_G/I_D is recognized as a rough measure of sample quality because it is the relative response of graphite carbon to defective carbon.

The G'-band frequency is close to twice that of the D band and is found from 2500 to 2900 cm^{-1} . This is a second-order process from two zone boundary longitudinal optical (LO) phonons. The G' band is an intrinsic property of the nanotubes and graphite, and present even in defect-free nanotubes for which the D band is completely absent. The Raman spectrum of the produced CNTs on the nickel catalyst at different growth temperatures is shown in Figure 8. The ratios of the intensities of G and D peaks, I_G/I_D for produced CNTs by Co and Ni catalysts at different growth temperatures are presented in Table 1.

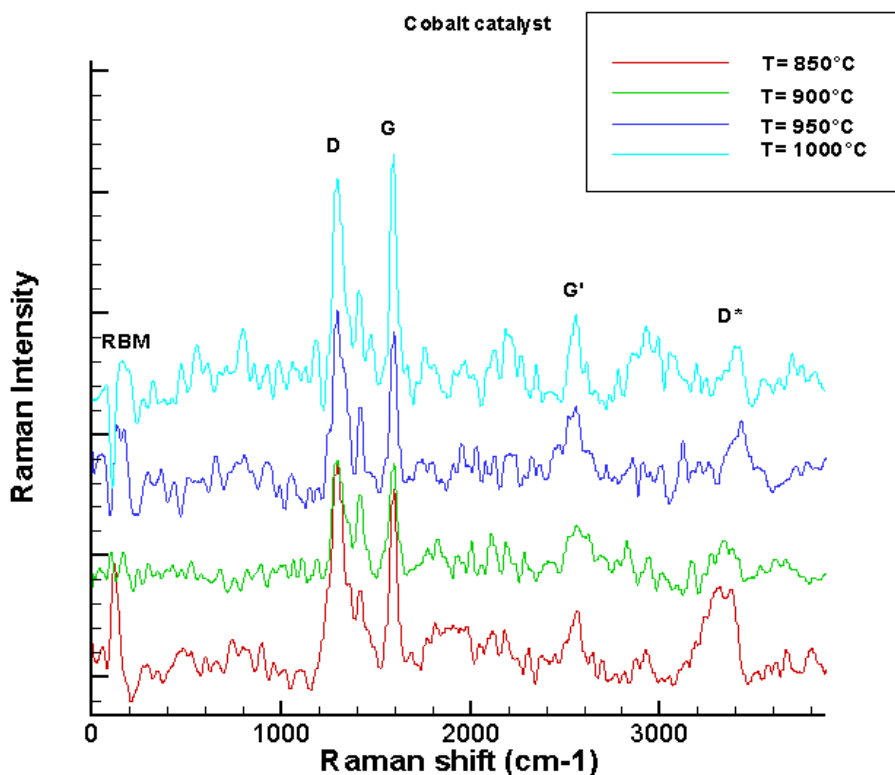


Figure 7. The Raman spectrum of the produced CNTs on the cobalt catalyst at different growth temperatures.

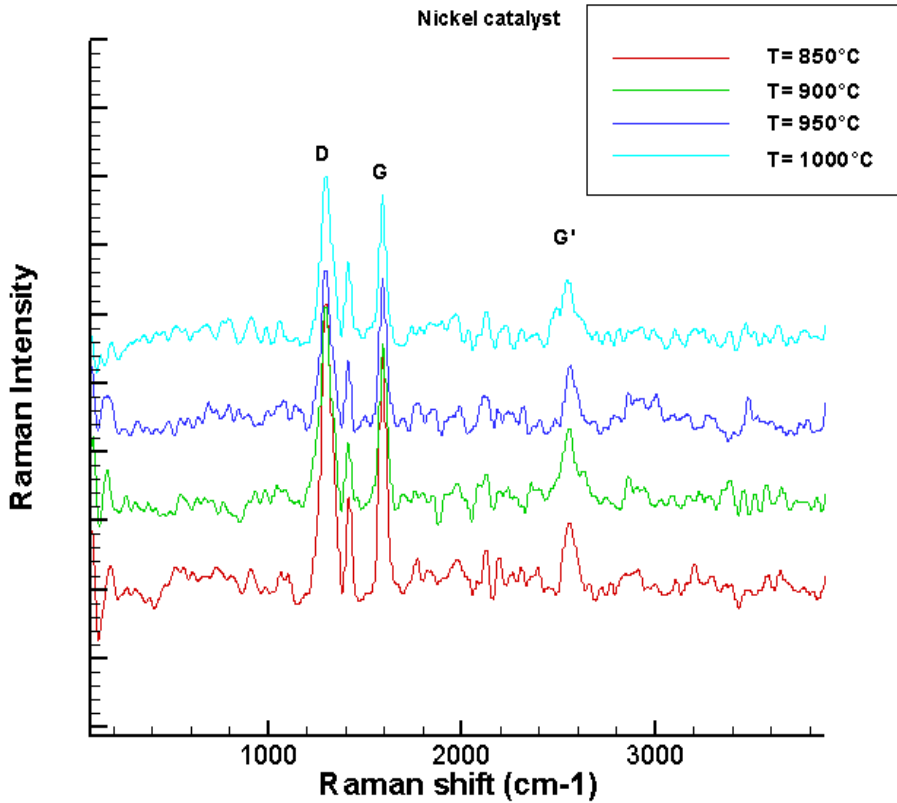


Figure 8. The Raman spectrum of the produced CNTs on the nickel catalyst at different growth temperatures.

Table 1. The ratios of the intensities of G and D peaks, I_G/I_D for produced CNTs by Co and Ni catalysts at different growth temperatures.

Catalyst	Growth temperature	G band (cm ⁻¹)	D band (cm ⁻¹)	I_G/I_D
Co	850 °C	1594.56	1300.73	0.8982
Co	900 °C	1595.69	1294.29	0.9563
Co	950 °C	1594.56	1293.00	0.9155
Co	1000 °C	1586.82	1293.00	1.0444
Ni	850 °C	1591.77	1289.21	0.8049
Ni	900 °C	1594.56	1300.73	0.8460
Ni	950 °C	1586.82	1293.00	0.9411
Ni	1000 °C	1584.40	1293.15	0.8737

Here, the ratio of I_G/I_D is greater than one for the grown CNTs by Co catalyst at a growth temperature of 1000°C indicates that the grown CNTs have good crystalline graphite structure while from FESEM results, it was found that at this temperature the diameter of CNTs is raised and their yield decreased.

CONCLUSIONS

In this paper, the growth of carbon nanotubes over Co and Ni nanoparticles in a temperature range of 850°C - 1000°C was studied. Cobalt and nickel nanoparticles were deposited onto the p-type Si (400) wafers by planar DC-sputtering system. The results showed that the diameter of CNTs can be controlled by adjusting the growth temperature, and increasing the temperature leads to increasing the diameter of CNTs. Also, the ratio of I_G/I_D is greater than one for the grown CNTs using Co catalyst at a growth temperature of 1000°C indicates that the grown CNTs have good crystalline graphite structure. FESEM results showed that the grown CNTs at the temperature of the 850°C using Co catalyst among all of the samples (Co and Ni nanoparticles) have a minimum diameter and maximum yield while a very small amount of CNTs produced at the same temperature using Ni catalyst. For transition metals, the affinity for carbon increases from the right to the left of the periodic table. So, the affinity of cobalt for carbon is greater than the affinity of nickel.

On the role of CNT catalysts, it is worth mentioning that transition metals are proven to be efficient catalysts, not only in CVD but also in arc-discharge and laser-vaporization methods. Therefore, it is likely that these apparently different methods might inherit a common growth mechanism of the CNT, which is not yet clear. Hence this is an open field of research to correlate different CNT techniques in terms of the catalyst's role in entirely different temperature and pressure range.

EXPERIMENTAL SECTION

In the present investigation, p-type Si (400) wafers with size of $1\text{cm} \times 1\text{cm}$ were used as substrates. The wafers were cleaned by ultrasonic method in acetone and ethanol solutions to remove potential residual contaminants prior to deposition. The samples were introduced into the planar DC-sputtering system and then pumped down to a base pressure of 4×10^{-1} Pa. A cobalt plate was used as a cathode and was placed in parallel with the oven which was grounded. The distance between the cathode and anode was about 1 cm.

Argon was introduced into the chamber with a flow of 200 Standard Centimeter Cubic per Minutes (sccm). The cobalt NPs were sputtered on Si substrates when the substrate temperature gradually increased up to 100°C. Deposition time for cobalt sputtering was 30 minutes. This procedure with same conditions was repeated for nickel samples.

The Thermal Chemical Vapor Deposition (TCVD) system in the experiment (Figure 9) was an electric furnace composed of a horizontal quartz glass tube with an internal diameter of 7.5 cm and a length of 80 cm which was operated at atmospheric pressure.

Argon gas with a flow rate of 200 sccm was supplied into the CVD reactor to prevent the oxidation of catalytic metal while raising the temperature to 750°C. The samples were placed in the chamber and the temperature increased to 850°C. After that, Ar flow was switched off. For CNT growth, we used C_2H_2 / NH_3 at 35 / 60 sccm for 15 minutes. The growth was terminated by turning off C_2H_2 / NH_3 flow and the samples were allowed to cool down to room temperature under Ar gas flow. Same experiments were repeated with growth temperature as 850°C, 900°C, 950°C and 1000°C while keeping other growth parameters constant.

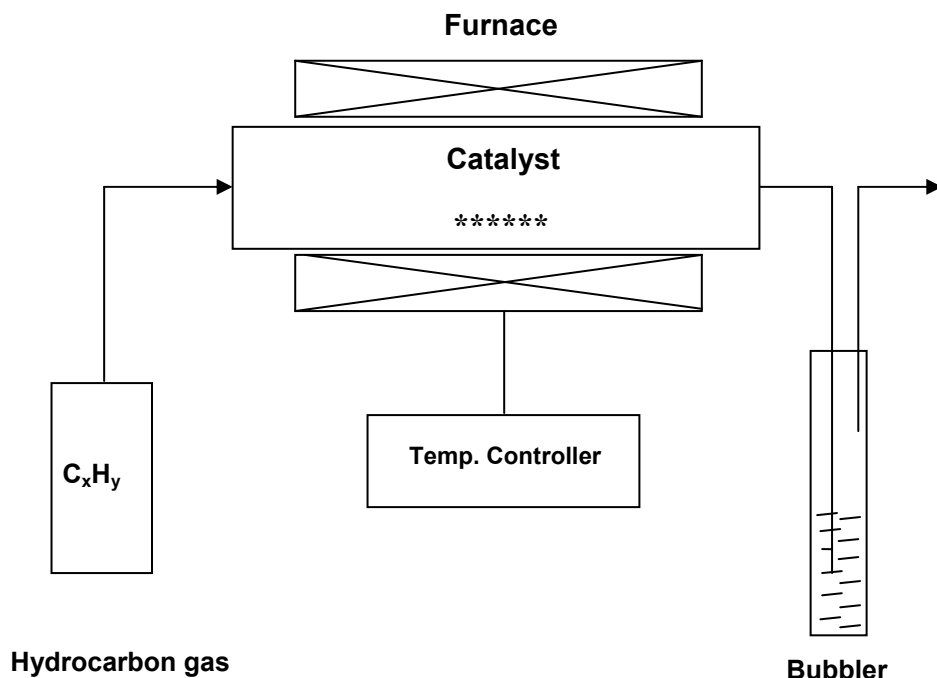


Figure 9. Schematic diagram of TCVD system of nanotube synthesis.

ACKNOWLEDGMENTS

The authors would like to express their thanks to Shahram Solaymani (PhD candidate, Young researchers and Elite club, Islamic Azad University, Kermanshah Branch, Iran) and Dr. Zahra Khalaj (Physics department, Shahre-Qods branch, Islamic Azad University, Tehran, Iran) for their help and cooperation.

REFERENCES

- [1]. Z.L. Tsakadze, K. Ostrikov, C.H. Sow, S.G. Mhaisalkar, Y.C. Boey, *Journal of Nanoscience and Nanotechnology*, 2010, 10, 6575.
- [2]. B. Liu, W. Ren, L. Gao, S. Li, S. Pei, C. Liu, C. Jiang, H.-M. Cheng, *Journal of the American Chemical Society*, 2009, 131, 2082.
- [3]. H. Yu, D. Liao, M.B. Johnston, B. Li, *ACS Nano*, 2011, 5, 2020.
- [4]. B.B. Wang, Q.J. Cheng, X.X. Zhong, Y.Q. Wang, Y.A. Chen, K. Ostrikov, *Journal of Applied Physics*, 2012, 111, 044317.
- [5]. D.H. Seo, S. Kumar, K. Ostrikov, *Carbon*, 2011, 49, 4331.
- [6]. A. Bianco, K. Kostarelos, M. Prato, *Current Opinion in Chemical Biology*, 2005, 9, 674.
- [7]. C.D. Modi, S.J. Patel, A.B. Desai, R.S.R. Murthy, *Journal of Applied Pharmaceutical Science*, 2011, 1, 103.
- [8]. C. Journet, W.K. Maser, P. Bernier, P.A. Loiseau, M.L. de la Chapelle, S. Lefrant, P. Deniard, R. Lee, J.E. Fischer, *Nature*, 1997, 388, 756.
- [9]. A. Thess, R. Lee, P. Nikolaev, H. Dai, P. Petit, J. Robert, C. Xu, Y.H. Lee, S.G. Kim, A.G. Rinzler, D.T. Colbert, G.E. Scuseria, D. Toma'nek, J.E. Fischer, R.E. Smalley, *Science*, 1996, 273, 483.
- [10]. H. Dai, *Surf. Sci.*, 2002, 500, 218.
- [11]. M. Meyyappan, L. Delzeit, A. Cassell, D. Hash, *Plasma Sources Sci. Technol.*, 2003, 12, 205.
- [12]. J.M. Bonard, *Thin Solid Films*, 2006, 501, 8.
- [13]. S. Porro, S. Musso, M. Giorcelli, A. Chiodoni, A. Tagliaferro, *Physica E*, 2007, 37, 16.
- [14]. A.M. Cassell, J.A. Raymakers, J. Kong, H. Dai, *J. Phys. Chem. B.*, 1999, 103, 6484.
- [15]. Y. Chen, D. Ciuparu, S. Lim, Y. Yang, G.L. Haller, L. Pfefferle, *J. Catal.*, 2004, 225, 453.
- [16]. L. Zheng, X. Liao, Y. T. Zhu, *Mater. Lett.*, 2006, 60, 1968.
- [17]. C. Dang, T. Wang, *Appl. Surf. Sci.*, 2006, 253, 904.
- [18]. K. Hernadi, A. Fonseca, J.B. Nagy, A. Siska, I. Kiricsi, *Appl. Catal. A: Gen.*, 2000, 199, 245.

- [19]. O.A. Nerushev, R.E. Morjan, D.I. Ostrovskii, M., Jonsson, M. Sveningsson, F. Rohmund, E. E. B. Campbell, *Physica B*, 2002, 323, 51.
- [20]. P. Sampedro-Tejedor, A. Maroto-Valiente, D. M. Nevskaja, V. Muñoz, I. Rodri'guez-Ramos, A. Guerrero-Rui'z, *Diamond Relat. Mater.*, 2007, 16, 542.
- [21]. A.C. Dupuis, *Prog. Mater. Sci.*, 2005, 50, 929.
- [22]. W. Zhou, Z. Han, J. Wang, Y. Zhang, Z. Jin, X. Sun, Y. Zhang, C. Yan, Y. Li, *Nano Lett.*, 2006, 6, 2987.
- [23]. S. Bhaviripudi, E. Mile, S.A. Steiner III, A.T. Zare, M.S. Dresselhaus, A.M. Belcher, J. Kong, *J. Am. Chem. Soc.*, 2007, 129, 1516.
- [24]. D. Takagi, Y. Homma, H. Hibino, S. Suzuki, Y. Kobayashi, *Nano Lett.*, 2006, 6, 2642.
- [25]. D. Yuan, L. Ding, H. Chu, Y. Feng, T.P. McNicholas, J. Liu, *Nano Lett.*, 2008, 8, 2576.
- [26]. B. Liu, W. Ren, L. Gao, S. Li, Q. Liu, C. Jiang, H.-M. Cheng, *J. Phys. Chem. C*, 2008, 112, 19231.
- [27]. G. Hong, Y. Chen, P. Li, J. Zhang, *Carbon*, 2012, 50, 2067.
- [28]. C.J. Lee, J. Park, Y. Huh, J. Yong Lee, *Chem. Phys. Lett.*, 2001, 343, 33.
- [29]. S. Bandow, S. Asaka, Y. Saito, A.M. Rao, L. Grigorian, E. Richter, P.C. Eklund, *Phys. Rev. Lett.*, 1998, 80, 3779.
- [30]. F.H. Kaatz, M.P. Siegal, D.L. Overmyer, P.P. Provencio, D.R. Tallant, *Appl. Phys. Lett.*, 2006, 89, 241915.
- [31]. M. Hoch, "Phase stability of carbon in FCC and BCC metals", *Calphad*, 1988, 83.
- [32]. O.V. Yazyev, A. Pasquarello, *Phys. Rev. Lett.*, 2008, 100, 156102.
- [33]. R. Yang, P. Goethel, J. Schwartz, C. Lund, *J. Catal.*, 1990, 122, 206.
- [34]. G. Samsonov, *Powder Metall. Met. Ceram.*, 1965, 4, 75.
- [35]. G.A. Somorjai, "Introduction to surface chemistry and catalysis", Wiley, New York, 1994.
- [36]. J. Nørskov, *Phys. Rev. B*, 1982, 26, 2875.
- [37]. S. Hofmann, G. Csanyi, A.C. Ferrari, M.C. Payne, J. Robertson, *Phys. Rev. Lett.*, 2005, 95, 36101.
- [38]. V. Jourdain, C. Bichara, *Carbon*, 2013, 58, 2.
- [39]. N. Tripathi, P. Mishra, Harsh, S.S. Islam, "Effect of Growth Temperature on the Diameter Distribution and Yield of Carbon Nanotubes", *Physics of Semiconductor Devices, Environmental Science and Engineering*, Springer, 2014, 645.
- [40]. B. RTK, P.S. Harris, "Formation of filamentous carbon in chemistry and physics of carbon", *Chemistry and Physics of Carbon*, Marcel Dekker, New York, 1978, 83.
- [41]. B. RTK, *Carbon*, 1989, 27, 315.
- [42]. A. Oberlin, M. Endo, T. Koyama, *J. Cryst. Growth*, 1976, 32, 335.
- [43]. M.S. Dresselhaus, G. Dresselhaus, A. Jorio, A.G. Souza Filho, R. Saito, *Carbon*, 2002, 40, 2043.
- [44]. R. Gupta, B.P. Singh, V.N. Singh, T.K. Gupta, R.B. Mathur, *Carbon*, 2014, 66, 724.

STABLE HYDRATE OF A β -LACTAMCARBALDEHYDE

MONICA IOANA TOȘA^a, BALÁZS KOMJÁTI^b,
JÁNOS MADARÁSZ^c, PÁL KOLONITS^b,
LÁSZLÓ POPPE^b, JÓZSEF NAGY^{b*}

ABSTRACT. Structural features of a stable aldehyde hydrate without a proximal electron withdrawing group are described. The title β -lactamcarbaldehyde has been prepared by hydrolysis of the corresponding imine and characterized by 2D NMR spectroscopy, thermogravimetry and chemical reactions.

Keywords: aldehyde hydrates, β -lactams, geminal diols, 2D NMR, thermogravimetry

*In memoriam Dr. József Nyitrai,
late professor of the Department of Organic Chemistry
and Technology, deceased August 2011.*

INTRODUCTION

Compounds with a β -lactam skeleton are known to possess antibacterial and/or β -lactamase inhibitory activity. In the course of our program of the synthesis of new compounds with condensed β -lactam skeleton, 2,3-cis-4-oxo-1-(4-methoxyphenyl)-3-phthalimidoazetidín-2-carb-aldehyde (**1**) was needed.

According to the literature this aldehyde is available by oxidative methods only i.e. oxidation of i) 3,4-cis-1-(4-methoxyphenyl)-3-phthalimido-4-propenylazetidín-2-one¹, or of 3,4-cis-1-(4-methoxyphenyl)-4-(2-phenylethenyl)-3-phthalimidoazetidín-2-one with ozone²; ii) oxidation of 3,4-cis-4-(1,2-dihydroxyethyl)-1-(4-methoxyphenyl)-3-phthalimidoazetidín-2-one with sodium

^a Babeș-Bolyai University of Cluj-Napoca, Faculty of Chemistry and Chemical Engineering, Department of Chemistry, Arany János 11, 400028-Cluj-Napoca, Romania

^b Budapest University of Technology and Economics, Department of Organic Chemistry and Technology, Műegyetem rkp. 3., H-1111 Budapest, Hungary

^c Budapest University of Technology and Economics, Department of Inorganic and Analytical Chemistry, Műegyetem rkp. 3., H-1111 Budapest, Hungary

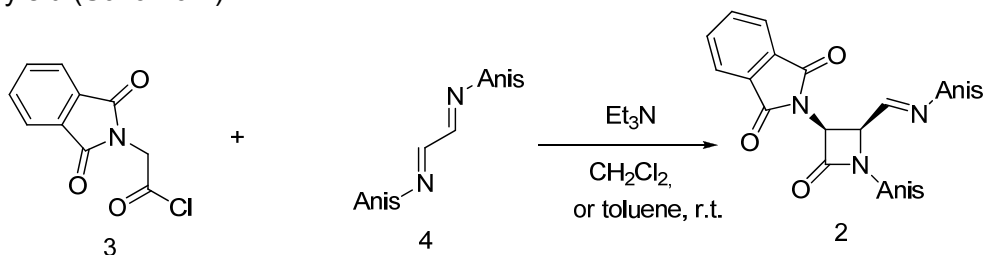
* Corresponding author: jnagy@mail.bme.hu

periodate³, and oxidation of 3,4-*cis*-4-(hydroxymethyl)-1-(4-methoxyphenyl)-3-phthalimidoazetidín-2-one⁴, followed by *in situ* acidic hydrolysis of 3,4-*cis*-1-(4-methoxyphenyl)-4-[(4-methoxyphenyl)-imino-methyl]-3-phthalimidoazetidín-2-one (**2**) in a two phase system^{3,5}. In our hands, however, acidic hydrolysis of 3,4-*cis*-1-(4-methoxyphenyl)-4-[(4-methoxyphenyl)-iminomethyl]-3-phthalimidoazetidín-2-one (**2**) in homogenous water–DMF phase resulted in the formation of a novel compound lacking an aldehyde function. In this communication the structural features of this compound are described.

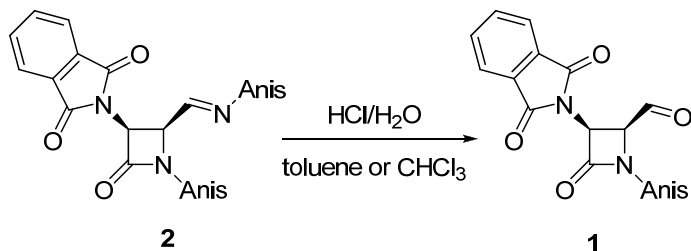
RESULTS AND DISCUSSION

The starting material, 3,4-*cis*-1-(4-methoxyphenyl)-4-[(4-methoxyphenyl)imino-methyl]-3-phthalimidoazetidín-2-one (**2**) was obtained by Staudinger reaction of *N,N'*-(ethane-1,2-diylidene)bis(4-methoxyaniline) (**3**) and phthalimidoacetyl chloride (**4**) (Scheme 1; Note that all β -lactams described in this paper are racemic and only one enantiomer is shown).

Previously Grigg *et al.*³, and Alcaide *et al.*⁵ conducted the same Staudinger reaction but in toluene, followed, without isolation of the imine **2**, by hydrolysis in a two phase system to give 2,3-*cis*-4-oxo-1-(4-methoxyphenyl)-3-phthalimidoazetidín-2-carbaldehyde (**1**) from the organic phase in moderate yield (Scheme 2).

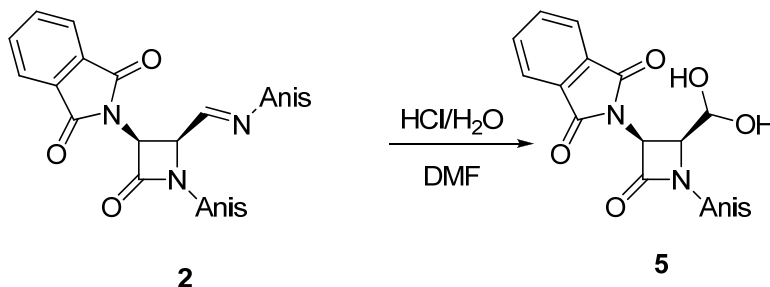


Scheme 1. Staudinger reaction yielding β -lactam imine **2** from bisimine **4** and acid chloride **3**



Scheme 2. Deprotection of β -lactam imine **2** to β -lactam carbaldehyde **3**

We were surprised to find that, when the hydrolysis of the imine **2** was performed in a homogenous HCl/water/DMF system, the reaction resulted in the formation of a new compound (**5**) (Scheme 3).



Scheme 3. Deprotection of β -lactam imine **2** to β -lactam carbaldehyde hydrate **5**

In the IR spectrum of **5** no carbonyl absorption for a formyl group was observed, while broad absorption bands were present in the OH stretching region. Moreover, characteristic signals for an aldehyde group were absent both in the ^1H - and ^{13}C -NMR spectra. Next, besides the normally expected AA'XX' systems of the 4-methoxyphenyl (PMPH) and phthalimido (Phth) units, five additional signals were observed for five hydrogen atoms in the region 4.3–6.6 ppm. Since two of them could be easily assigned to the β -lactam skeleton, the other three had to be attributed to the newly formed functionality. In the ^{13}C -NMR spectra of **5** the sole new signal not related to the 4-methoxyphenyl (PMPH), phthalimido (Phth) or β -lactam units, found at 90.0 ppm, was indicative of the presence of a methine unit bearing two hydroxyl groups.

Finally elemental analysis of **5** was consistent with the molecular formula $\text{C}_{19}\text{H}_{16}\text{N}_2\text{O}_6$ with 0.5 mol water of crystallization. ^1H NMR signal for the latter was overlapped by the signal of the water content of the solvent.

These results suggested that one of the 4-methoxyphenylimino group indeed hydrolyzed, but subsequent reaction of the resulting aldehyde with water provided a stable hydrate **5** (Scheme 3). This unexpected result prompted a more detailed investigation.

Thermal analysis showed in the DTA curve (Figure 1) three endothermic peaks. TG results indicated that the first and the second endothermic transformation, at 71 °C and 135 °C respectively involved weight loss, of, while the third at 219 °C belongs to the melting of the sample where after decomposition started. The first weight loss, with a maximum at 68 °C, (see the DTG curve) – terminated at 90.8 °C (see TG curve) – belongs to the

loss of 0.5 mol/mol of crystallization water. The second weight loss – with a maximum at 132 °C, (see DTG curve) – finished at 153 °C (see TG curve), belongs to the exact loss of one mol/mol of water from the geminal diol moiety of **5**. So the β -lactamcarbaldehyde **1** was formed prior to melting, and it was this carbaldehyde which melted between 217–220 °C. (Lit. value³ of m.p. for compound **1**: 214–216 °C).

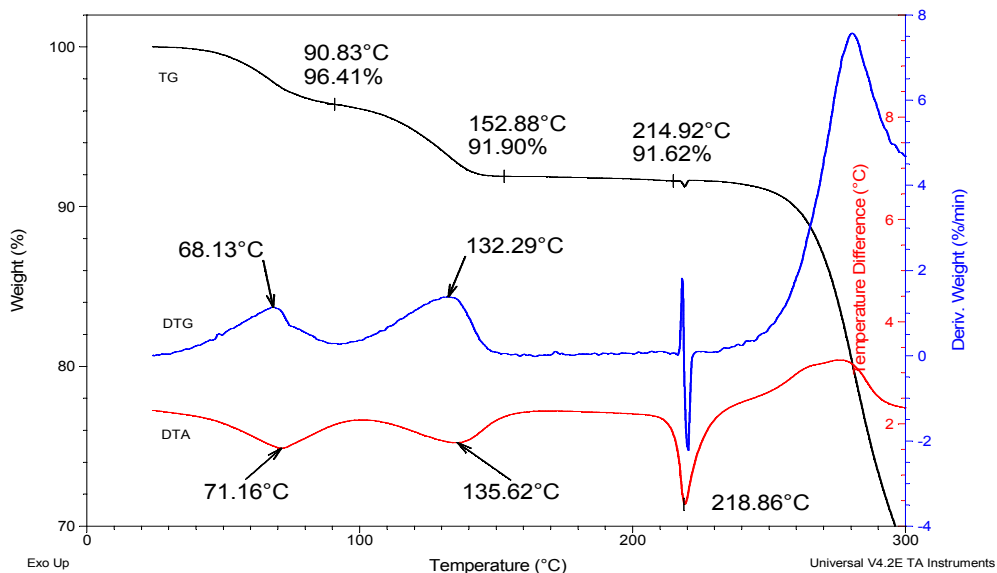


Figure 1. Thermoanalytical investigation of compound **5**:
TG: top black line, DTG: middle blue line, DTA: bottom red line

The structure of compound **5** was further confirmed by NMR investigations. As a basis for comparison the spectra of compound **2** was examined including APT, HMQC, HMBC, COSY and NOESY experiments.

Thus in the NOESY spectrum of **2** correlation between the C₃-H and C₄-H of the β -lactam skeleton indicated their *cis* arrangement (Figure 2).

The *E* configuration of the imine moiety was supported by the correlation between the hydrogen atom of CH=N and the *ortho*-H's of the CH=N-PMPH group (PMPH = 4-methoxyphenyl). The correlation between the C₄-H and the *ortho*-H's of the N₁-PMPH group verified the *trans* arrangement of N₁-PMPH group and C₃-Phth groups.

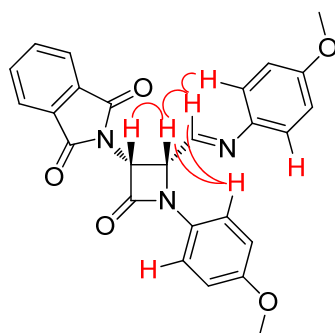


Figure 2. NOESY investigation of compound **2**:
Correlations are marked with red arcs

Relevant ^1H – ^{13}C (hetero) correlations of the signals in the spectra of **5** were supported by APT, HMQC, HMBC, COSY and NOESY methods as well (Figure 3).

The sequence C_3H – C_4H – $\text{CH}(\text{OH})_2$ was unambiguously proved by the $^3J_{\text{HH}}$ scalar couplings observed as follows: i) between β -lactam protons (stereospecific as 6.0 Hz), ii) between C_4H and the methine-H of the geminal diol moiety (7.7 Hz), and iii) between the methine-H and the diastereotopic OH's of the geminal diol moiety (6.5 Hz in $\text{DMSO-}d_6$ as hydrogen bond acceptor).

In the NOESY spectrum correlation was found between protons C_3H and C_4H of the β -lactam skeleton, supporting their *cis* arrangement (Figure 3). Correlation between the C_4H and *ortho*-H's of the N_1 -PMPH group verified the *trans* arrangement of N_1 -PMPH and C_3 -Phth groups.

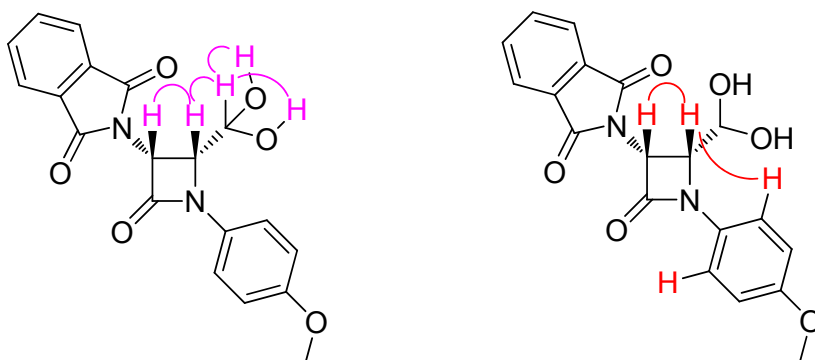
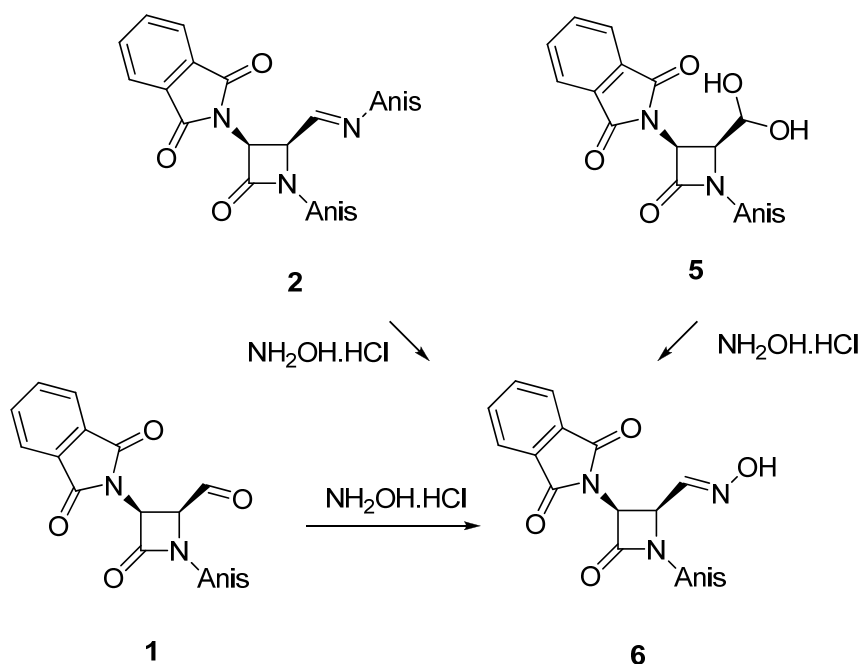


Figure 3. $^3J_{\text{H,H}}$ scalar coupling pattern (pink arcs) and NOESY dipolar correlations (red arcs) of compound **5**

When the solution of **5** in DMSO- d_6 was stored at room temperature for a week a 3:1 mixture of diol **5** and aldehyde **1** could be detected in the NMR spectra. This result proved that slow dehydration of the diol **5** also occurred in a polar but aprotic medium. Note, that the hydrate **5** remained intact during drying its crystals in vacuum at 65 °C.

The structure of compound **5** was verified also by transforming it to the known aldoxime **6**, previously prepared from the aldehyde **1**⁴. We could prepare this aldoxime **6** not only from the imine **2**, but also from our hydrate **5** (Scheme 4).

Aldehyde hydrates (geminal diols) are generally known to be stable only when an electron withdrawing group, such as trichloromethyl in chloral, formyl in glyoxal, or carboxyl in glyoxylic acid, is adjacent to the carbonyl group and but very few examples of aldehyde hydrates stabilized without electron withdrawing effects have been reported. Most of them possess an acylamino group at α - or β -position relative to the geminal diol moiety, e.g. 2-(phenylacetyl-amino)-acetaldehyde hydrate⁶, a benzoyl cytidine derivative⁷, an α -aminoacid derivative⁸, penicillanal hydrate⁹, some aminoacid derivatives¹⁰, a triazine derivative¹¹, and a dimethylglycinal derivative¹².



Scheme 4. Chemical correlation by formation of aldoxime **6**

It has to be noted that in our stable hydrate **5** α -acylamino and β -acylamino units are present adjacent to the geminal diol function. In view of the above examples it can be assumed that hydrates in which no electron withdrawing groups are attached to the parent aldehyde group may be stabilized by hydrogen bonds. We are making efforts to prove this hypothesis.

CONCLUSIONS

Preparation and structural investigations of a stable hydrate **5** of the β -lactamcarbaldehyde **1** are presented. As an extension of existing methods for the preparation of aldehyde **1** we have found, that under aqueous conditions the stable hydrate **5** could be prepared. The dehydrated aldehyde **1** was formed in an organic medium, while the hydrated form **5** arose in a homogenous system containing water. Hydrate **5** was stable in a crystalline form however it was slowly dehydrated on standing in DMSO.

EXPERIMENTAL SECTION

NMR spectra were recorded in CDCl_3 or in DMSO-d_6 on a Bruker DRX-500 or on a Bruker DRX-300 spectrometer and are reported in ppm on the δ scale. Infrared spectra were recorded on a Bruker ALPHA FT-IR spectrometer. TLC was carried out on Kieselgel 60F₂₅₄ (Merck) sheets. Spots were visualized under UV light (Vilber Lourmat VL-6.LC, 254 nm and 365 nm) or by treatment with 5% ethanolic phosphomolybdic acid solution and heating of the dried plates. For thermoanalysis a simultaneous thermogravimetric and differential thermal analysis (TG/DTA) apparatus (STD 2960 Simultaneous DTA-TGA, TA Instruments Inc., USA), a heating rate of $10\text{ }^\circ\text{C min}^{-1}$, an N_2 flow of $130\text{ cm}^3/\text{min}$, sample sizes of ca. 5 mg and open Pt crucibles was used.

3,4-cis-1-(4-Methoxyphenyl)-4-[(E)-(4-methoxyphenyl)iminomethyl]-3-phthalimido-azetidin-2-one (2)

To the solution of *N,N'*-(ethane-1,2-diylidene)bis(4-methoxy-aniline) (10.89 g, 40.59 mmol) and triethyl amine (6 mL, 42.86 mmol) in of dichloromethane (100 mL) was added at $0\text{ }^\circ\text{C}$ a solution of phthalimidoacetyl chloride (8.89 g, 39.75 mmol) in of dichloromethane (50 mL) within 10 min. The reaction mixture was stirred for 2 hours at room temperature, and then it was washed with of water (50 mL). The organic layer was dried over MgSO_4 . After evaporation of the solvent the product was crystallized from methanol (50 mL) at $0\text{ }^\circ\text{C}$ to give 13.46 g (29.56 mmol, 73%) of title compound. $\text{C}_{26}\text{H}_{21}\text{N}_3\text{O}_5$ (455.47)

M.p.: 149-150 °C; *IR* (KBr, cm^{-1}): ν 2954, 1787 (Phth), 1749 (β -lactam), 1719 (Phth), 1602, 1514, 1465, 1445, 1387, 1297, 1246, 1208, 1187, 1127, 1031, 83, 727; $^1\text{H-NMR}$ (500 MHz, CDCl_3 , δ ppm): 3.74 (s, 3H, CH_3O), 3.80 (s, 3H, CH_3O), 5.16 (dd, 1H, $J = 5.8$ Hz, 4-H), 5.86 (d, 1H, $J = 5.8$ Hz, 3-H), 6.77 (d, 2H, $J = 8.9$ Hz, =*N*-PMPH), 6.91 (d, 2H, $J = 8.9$ Hz, 1-PMPH), 6.95 (d, 2H, $J = 8.9$ Hz, *N*-PMPH), 7.46 (d, 2H, $J = 8.9$ Hz, 1-PMPH), 7.73 (m, 2H, Phth), 7.84 (m, 2H, Phth), 8.09 (d, 1H, $J = 5.8$ Hz, $\text{CH}=\text{N}$); $^{13}\text{C-NMR}$ (125 MHz, CDCl_3 , δ ppm): 55.30 (CH_3O), 55.39 (CH_3O), 56.49 (C_3), 60.92 (C_4); 114.17, 114.52, 118.14, 122.06 (PMPH-CH's); 123.71 (Phth-CH), 130.85 (PMPH- C_1), 131.33 (Phth-C), 134.53 (Phth-CH), 142.70 (PMPH- C_1), 156.61 (PMPH- C_4), 156.98 ($\text{C}=\text{N}$), 158.83 (PMPH- C_4), 160.54 (C_2), 166.95 (Phth-CO).

3,4-*cis*-4-(Dihydroxymethyl)-1-(4-methoxyphenyl)-3-phthalimido-azetidín-2-one (5)

3,4-*cis*-1-(4-Methoxyphenyl)-4-[(4-methoxyphenyl)iminomethyl]-3-phthalimidoazetidín-2-one (2) (455 mg, 1.00 mmol) was dissolved in DMF (12 mL) then 1M hydrochloric acid (2 mL) was added in one portion. The reaction mixture was stirred at room temperature for 1.5 hours, and then water (36 mL) was added with stirring, while a precipitate was formed. The precipitate was filtered off, washed with water, methanol and diethyl ether. The white powder was dried in vacuum at 65 °C to give 305 mg (0.808 mmol, 81%) 5 as crystals containing 0.5 mol of crystal water. *Anal.*: $\text{C}_{19}\text{H}_{16}\text{N}_2\text{O}_6 \cdot 0.5 \text{H}_2\text{O}$ (377.36) Calc.: C 60.48, H 4.54, N 7.42 %, found: C 60.52, H 4.52, N 7.13 %;

M.p.: 217-220 °C. *IR* (KBr, ν cm^{-1}): 3537, 3387 (br), 1775 (Phth), 1743 (β -lactam), 1704 (Phth), 1516, 1435, 1401, 1301, 1250, 1208, 1181, 1126, 1109, 1074, 1054, 1032, 1020, 731, 712; $^1\text{H-NMR}$ (500 MHz, DMSO-d_6 , δ ppm): 3.74 (s, 3H, CH_3O), 4.33 (dd, 1H, $J = 6.0$ Hz, $J = 7.7$ Hz, 4-H), 4.95 (td, 1H, $J = 6.5$ Hz, $J = 7.7$ Hz, $\text{CH}(\text{OH})_2$), 5.58 (d, 1H, $J = 6.0$ Hz, 3-H), 6.10 (d, 1H, $J = 6.5$ Hz, OH), 6.49 (d, 1H, $J = 6.5$ Hz, OH), 6.94 (d, 2H, $J = 8.9$ Hz, 1-PMPH), 7.62 (d, 2H, $J = 8.9$ Hz, 1-PMPH), 7.90 (m, 2H, Phth), 7.93 (m, 2H, Phth); $^{13}\text{C-NMR}$ (125 MHz, DMSO-d_6 , δ ppm): 54.34 (C_3), 55.46 (CH_3O), 62.16 (C_4), 89.99 ($\text{CH}(\text{OH})_2$), 113.93, 119.61 (PMPH-CH's); 123.66 (Phth-CH), 131.41 (Phth-C), 131.75 (PMPH- C_1), 135.09 (Phth-CH), 155.86 (PMF- C_4), 162.61 (C_2), 167.28 (Phth-CO).

After standing for a week in DMSO-d_6 at room temperature there were two sets of signals in the NMR spectra. Major component: 3,4-*cis*-4-(dihydroxymethyl)-1-(4-methoxyphenyl)-3-phthalimidoazetidín-2-one (5), minor component: 2,3-*cis*-4-oxo-1-(4-methoxyphenyl)-3-phthalimido-azetidín-2-carbaldehyde (1).

NMR data of **1**: $^1\text{H-NMR}$ (500 MHz, DMSO- d_6 , δ ppm): 3.77 (s, 3H, CH_3O), 5.18 (d, 1H, $J = 6.5$ Hz, 4-H), 5.97 (d, 1H, $J = 6.5$ Hz, 3-H), 7.01 (d, 2H, $J = 9.0$ Hz, PMPH), 7.49 (d, 2H, $J = 9.0$ Hz, PMPH), 7.90 (m, 2H, Phth), 7.93 (m, 2H, Phth), 9.78 (s, 1H, CHO); $^{13}\text{C-NMR}$ (125 MHz, DMSO- d_6 , δ ppm): 55.18 (C_3), 55.55 (CH_3O), 62.34 (C_4), 114.70, 118.31 (PMF-CH's); 124.00 (Phth-CH), 131.02 (Phth-C), 131.06 (PMF- C_1), 135.49 (Phth-CH), 156.32 (PMF- C_4), 161.14 (C_2), 166.90 (Phth-CO), 197.87 (CH=O).

3,4-cis-4-(Hydroxyiminomethyl)-1-(4-methoxyphenyl)-3-phthalimido-azetidin-2-one (6)

Method A: 3,4-cis-4-(dihydroxymethyl)-1-(4-methoxyphenyl)-3-phthalimido-azetidin-2-one (**5**) (193 mg, 0.511 mmol) was dissolved in DMF (5 mL) and then hydroxylamine hydrochloride (345 mg, 4.96 mmol) was added. The reaction mixture was stirred for 30 min, then water (20 mL) was added with stirring, while a precipitate was formed. The precipitate was filtered off, washed with water, methanol and diethyl ether. The white powder was dried in vacuum at room temperature to give 139 mg (74%) of the title compound. $\text{C}_{19}\text{H}_{15}\text{N}_3\text{O}_5$ (365.35) M.p.: 234 °C (lit.: 228-230 °C [4]).

Method B: 3,4-cis-1-(4-methoxyphenyl)-4-[(4-methoxyphenyl)iminomethyl]-3-phthalimidoazetidin-2-one (**2**) (4.60 g, 10.1 mmol) was dissolved in a mixture of methanol (20 mL) and dichloromethane (20 mL), and then hydroxylamine hydrochloride (4.32 g, 62.1 mmol) in water (5 mL) was added. The reaction mixture was stirred for 60 min, and then water (50 mL) was added, and the product was extracted with dichloromethane (2×50 mL). The combined organic extract was washed with water, and dried over MgSO_4 . After evaporation of the solvent the product was crystallized from diethyl ether (20 mL) to give 2.88 g (78%) of title compound.

IR (KBr, ν cm^{-1}): 3377 (br), 3312 (br), 1782, 1722, 1514, 1469, 1388, 1301, 1251, 1206, 1191, 1180, 1130, 1102, 1026, 826, 713; $^1\text{H-NMR}$ (300 MHz, DMSO- d_6): two sets of the signals corresponding to the *E* and *Z* oximes were detected (major isomer ca. 72%, minor isomer ca. 28%), δ (major, ppm): 3.76 (s, 3H, CH_3O), 5.51 (dd, 1H, $J = 5.7$ Hz, $J = 4.2$ Hz, 4-H), 5.92 (d, 1H, $J = 5.7$ Hz, 3-H), 6.80 (d, 1H, $J = 4.2$ Hz, CH=N), 7.01 (d, 2H, $J = 8.7$ Hz, PMPH), 7.34 (d, 2H, $J = 8.7$ Hz, PMPH), 7.92 (m, 4H, Phth), 11.34 (s, 1H, NOH), δ (minor): 3.76 (s, 3H, CH_3O), 5.17 (dd, 1H, $J = 5.7$ Hz, $J = 7.5$ Hz, 4-H), 5.86 (d, 1H, $J = 5.7$ Hz, 3-H), 7.01 (d, 2H, $J = 8.7$ Hz, PMPH), 7.30 (d, 1H, $J = 7.5$ Hz, CH=N), 7.34 (d, 2H, $J = 8.7$ Hz, PMPH), 7.92 (m, 4H, Phth), 11.47 (s, 1H, NOH); $^{13}\text{C-NMR}$ (75 MHz, DMSO- d_6 , δ ppm), two sets of the signals were detected: 54.34 (C_3), 55.40 (CH_3O), 56.05 (C_4), 114.68 and 114.78, 117.80 and 117.99, 123.74 and 123.85, 130.57 and 130.82, 130.88 and 130.95, 135.22 and 135.33, 145.14 (CH=N), 156.05, 160.86, 166.79 and 167.00.

ACKNOWLEDGEMENTS

This research work was supported by the scientific program of "Development of quality-oriented and harmonized R+D+I strategy and functional model at BME" project (TÁMOP-4.2.1/B-09/1/KMR-2010-0002), supported by the New Hungary Development Plan.

REFERENCES

- [1]. (a) X.-F. Ren, M.I. Konaklieva, E. Turos, *Journal of Organic Chemistry*, **1995**, *60*, 4980–4981. (b) X.-F. Ren, M.I. Konaklieva, H. Shi, S. Dickey, D.V. Lim, J. Gonzalez, E. Turos, *Journal of Organic Chemistry*, **1998**, *63*, 8898–8917.
- [2]. A.K. Bose, J.F. Womelsdorf, L. Krishnan, Z. Ubanczyk-Lipkowska, D.C. Shelly, M. S. Manhas, *Tetrahedron*, **1991**, *47*, 5379–5390.
- [3]. R. Grigg, M. Thornton-Pett, J. Xu, .L.-H. Xu, *Tetrahedron*, **1999**, *55*, 13841–13866.
- [4]. (a) J. Fetter, F. Bertha, T. Czuppon, M. Kajtar-Peredy, M. Konkoly Thege, K. Lempert, *Journal of Chemical Research, Miniprint*, **1995**, 2801–2861; (b) B. Alcaide, Y. Martin-Cantalejo, J. Perez-Castells, J. Rodriguez-Lopez, M.A. Sierra, A. Monge, V. Perez-Garcia, *Journal of Organic Chemistry*, **1992**, *57*, 5921–5931.
- [5]. S. Kumar, A.L. Pearson, R.F. Pratt, *Bioorganic and Medicinal Chemistry*, **2001**, *9*(8), 2035–2044.
- [6]. G.H. Jones, M. Taniguchi, D. Teggy, J.G. Moffat, *Journal of Organic Chemistry*, **1979**, *44*, 1309–1317.
- [7]. A. Butenandt, *Hoppe-Seyler's Z. Physiological Chemistry*, **1951**, *288*, 62–63.
- [8]. W.J. Gottstein, G.E. Bocian, L.B. Crast, K. Dadabo, J.M. Essery, J.C. Godfrey, L.C. Cheney, *Journal of Organic Chemistry*, **1966**, *31*, 1922–1924.
- [9]. R Singh, M. Whittaker, Q. Ding, K. Jadwiga, R.G. Micetich, A.V.N. Reddy, G. Thomas, N. Zhou (Naeja Pharmaceutical Inc), *US Patent* **2003**, 6635621.
- [10]. T. Schaefer, F. Wendeborn, M. Gerster, P. Hayoz, B. Schmidhalter, J.L. Budry (CIBA Specialty Chemicals Holding Inc), *EU Patent* **2004**, 1641768 (A2).
- [11]. J. Keck, S. Puschmann, G. Kruger, K.R. Noll, M. Leitold, H. Pieper (Boehringer Ingelheim GmbH), *US Patent* **1978**, 4073942 A1.

COMPUTATIONAL ANALYSIS OF THE STRUCTURAL PROPERTIES OF ALPHA - AND BETA - GALACTOSIDASES

DIANA-LARISA VLĂDOIU^a, VASILE OSTAFE^a,
ADRIANA ISVORAN^{a*}

ABSTRACT. A computational study to compare the global and local physicochemical and structural properties of *alpha*- and *beta*-galactosidases using the retaining catalytic mechanism was performed. These proteins share quite similar global structural properties despite their low sequence similarity, structures superposition resulting in root mean squared deviation (RMSD) values around 1.25 Å for at least 43 alpha carbon atoms pairs. Almost the same RMSD values are obtained for the superposition of the catalytic domains of investigated galactosidases, but for a higher number of alpha carbon atoms pairs (68) reflecting the higher structural similarity of the catalytic domains. There are local individual properties of the surfaces of considered enzymes, *beta*-galactosidases exposing a more complex surface with a higher number of cavities, 42 for eukaryotic *beta*-galactosidases compared to 18 for eukaryotic *alpha*-galactosidases. Furthermore, *beta*-galactosidases usually depict larger and more hydrophobic cavities than *alpha* – galactosidases, the hydrophobicity scores of the biggest cavities being 24 for eukaryotic *beta*-galactosidases and 7 for eukaryotic *alpha*-galactosidases, respectively.

Keywords: *global and local structural properties, surface cavities; surface roughness.*

INTRODUCTION

Enzymatic hydrolysis is a process widely used to break down proteins, cellulose chains, starch and fat molecules into smaller ones: amino acids, monomeric sugars and fatty acids respectively. The enzymatic hydrolysis of glycosidic bonds involves the presence of glycoside hydrolases (GH), a class of enzymes also called glycosidases. They are involved in both industrial and natural processes, from biomass degradation [1] and food processes [2] to normal cellular functions and pathogenesis [3].

^a West University of Timisoara, Timisoara, Faculty of Chemistry – Biology – Geography, Advanced Research Environmental Laboratories, Oituz str. 4, Timișoara, 300086, Romania

* Corresponding author: adriana.isvoran@e-uvf.ro

GH enzymes may be classified in different ways. One of this ways is to use the Enzyme Commission (EC) number [4] but this classification is based on type of catalyzed reaction and the substrate specificity and does not consider structural properties of enzymes and their evolutionary relationships. For GH enzymes, the Carbohydrate-Active enZYmes (CAZy) database [4] contains a sequence-based classification for 133 families. Each GH family contains proteins that are related by sequence which reflects the same structural fold. Some of these families share structural similarity despite their apparently unrelated sequences, have common ancestry and identical catalytic mechanisms forming clans, denoted from A to N [5, 6]. Every clan contains a group of families with significant similarity of their tertiary structures, catalytic residues and mechanism.

GH enzymes use most frequently two catalytic mechanisms for the hydrolysis of the glycosidic bonds: the retaining or the inverting mechanism [7]. There are also some variations of these two mechanisms and a few others mechanisms may be employed by the GH enzymes [4, 8]. The retaining and inverting mechanisms involve two amino acids of the enzyme: a proton donor and a nucleophile/base [9]. These two residues are located at opposite sides of the active site of enzyme and, depending on their spatial positions, hydrolysis occurs via retention or inversion mechanism [9].

Within this study, two classes of glycoside hydrolases were considered: *alpha*-galactosidases (E.C.3.2.1.22) hydrolysing the terminal *alpha*-galactosyl moieties from glycolipids and glycoproteins [10] and *beta*-galactosidases (E.C.3.2.1.23) hydrolysing the β -glycosidic bonds from *beta*-galactosides and glycoproteins [11]. The difference between the retaining catalytic mechanisms of *alpha*- and *beta*-galactosidases consists in the distinct direction the nucleophile attacks the anomeric center at the first carbon of the substrate: it acts on the first carbon belonging to a substrate that contains an *alpha*-linkage for *alpha*-galactosidases, respective to a first carbon belonging to a substrate containing a *beta*-linkage for *beta*-galactosidases [15]. The great interest in studying galactosidases rises from their presence in almost all types of living organisms, their involvement in some diseases [3,12-14] and also from their biotechnological applications [11,16].

As considered galactosidases employ a common catalytic mechanism, our supposition is that they might share structural similarity, even if they belong to distinct families and clans of glycosidases [3]. Similar structural properties of *alpha*- and *beta*-glycosidases regardless of the low sequence identity have been also obtained for glycoside hydrolases family 4 (GH4) of bacteria [17]. Consequently, the study was focused on characterizing and comparing structural and physicochemical properties of *alpha*- and *beta*-galactosidases using retaining catalytic mechanism in correlation with their biological functions and biotechnological applications.

RESULTS AND DISCUSSION

Multiple sequence alignment of the sequences of every class of investigated *alpha*- and *beta*-galactosidases reveals small alignment scores (Tables 1 and 2). Moreover, the multiple sequence alignment for both *alpha*- and *beta*-galactosidases reveals scores varying between 3.46 and 42.36 and there are not conserved residues or regions in sequences of investigated proteins (data not shown).

Table 1. Alignment scores for different families of *alpha*-galactosidases and their catalytic domains

Taxonomy	Family	Similarity score for the entire sequence	Similarity score for the catalytic domains sequences
Bacteria	GH36	9.24÷96.98	3.87÷98.33
	all	2.26÷96.98	
Eukaryota	GH27	27.25÷46.04	
All investigated <i>alpha</i> -galactosidases		2.26÷96.98	

Table 2. Alignment scores for different families of *beta*-galactosidases and their catalytic domains

Taxonomy	Family	Similarity score for the entire protein	Similarity score for the catalytic domains sequences
Archea	GH1	69.73	3.38÷75.76
Bacteria	GH42	30.32	
	GH2	14.82÷32.32	
	all	2.96÷32.32	
Eukaryota	GH35	20.53÷57.34	
	all	5.31÷57.34	
All investigated <i>beta</i> -galactosidases		2.96÷69.73	

All these data reflect the low sequence similarity of considered *alpha*- and *beta*-galactosidases. It is also true for the catalytic domains sequences of investigated proteins. Even if the sequence similarity of considered *alpha*- and *beta*-galactosidases is low and they have distinctive number of amino acids in their sequences, their global physicochemical properties (isoelectric point, net charge, aliphatic and GRAVY indexes), computed using ProtScale tool [18] are similar. The average values of these properties, computed for the entire enzymes and for their catalytic domains respectively are presented in Table 3.

Table 3. Average values of the global physicochemical properties of *alpha*- and *beta*-galactosidases and of their catalytic domains

Protein class	pI	Net charge	Aliphatic index	GRAVY index
<i>alpha</i> - galactosidases	5.61±0.49	-13±2	75.98±6.50	-0.386±0.14
<i>beta</i> - galactosidases	5.90±0.65	-17±4	77.83±4.39	-0.353±0.17
<i>alpha</i> -galactosidases catalytic domains	5.39±0.19	-11±3	70.35±3.45	-0.418±0.09
<i>beta</i> -galactosidases catalytic domains	6.05±0.09	-8±1	73.71±3.33	-0.409±0.03

Student statistical test reflects that, at 0.05 level, the average value of every pair of investigated physicochemical properties does not differ significantly either for the two classes of enzymes neither for their catalytic domains. Both *alpha*- and *beta*-galactosidases reflect an acidic isoelectric point correlated to their negative net charges and the global hydrophilic character and they also reflect a high content of aliphatic residues. There is a significant difference between the values of the GRAVY indexes obtained for the entire enzyme compared to its catalytic domain. It is true for both classes of considered galactosidases and reflects the higher hydrophilicity of the catalytic domains.

The low sequence similarity between *alpha*-galactosidases and *beta*-galactosidases respectively is not reflected in their structural properties. As expected, the root mean squared deviation (RMSD) values obtained by structural superposition of *alpha*- and *beta*-galactosidases are small for the enzymes belonging to the same GH family (Table 4) reflecting their similar global structural properties.

In the case of *alpha*-galactosidases, the highest structural similarity is observed for enzymes belonging to the GH36 family (Figure 1.a) and the lower structural similarity is observed for *Bacteroides thetaiotaomicron* *alpha*-galactosidase (GH97 family) compared to the other *alpha*-galactosidases. This result is in good correlation with the possibility of this enzyme to employ a distinct catalytic mechanisms (inverting) in comparison to the other *alpha*-galactosidases.

Investigated *beta*-galactosidases belong to many families and this is reflected in their structural properties, enzymes belonging to the GH35 family sharing the best structural convergence. Between *beta*-galactosidases belonging to GH35 family, the *Caulobacter crescentus* (3U7V) and *Homo sapiens* (3THC) *beta*-galactosidases are divergent in structure in comparison to *beta*-galactosidases belonging to the other organisms. Their structures are also divergent when compared to the other families of *beta*-galactosidases. Figure 1B illustrates the superposition of human (3THC) and *Trichoderma reesei* (3OG2) *beta*-galactosidases, RMSD=1.124 Å for only 4 equivalent CA atom pairs.

Table 4. The minimum and maximum RMSD values obtained by the superposition of the three dimensional structures of investigated *alpha*- and *beta*-galactosidases (CA-carbon *alpha*)

Galactosidase class	Galactosidase family	Minimum RMSD / Å ²	Number of equivalent CA atoms pairs	Maximum RMSD / Å ²	Number of equivalent CA atoms pairs
<i>alpha</i> -galactosidases	GH36	0.813 for 3MI6 superposed to 4FNR	673	1.139 for 3MI6 superposed to 1ZY9	119
	GH27	0.634 for 3LRL superposed to 3A5V	356	1.040 for 3A21 superposed to 1SZN	239
	all <i>alpha</i> -galactosidases	0.813 for 3MI6 superposed to 4FNR	673	1.351 for 2XN0 superposed to 3A24	8
<i>beta</i> -galactosidases	GH1	0.573 for 1GOW superposed to 4HA3	469	-	-
	GH2	0.944 for 1YQ2 superposed to 3OBA	601	1.142 for 3FN9 superposed to 3BGA	260
	GH35	0.612 for 1TG7 superposed to 3OG2	898	1.124 for 3THC superposed to 3OG2	4
	GH42	1.134 for 1KWG superposed to 3TTY	430	-	-
	all <i>beta</i> -galactosidases	0.612 for 1TG7 superposed to 3OG2	898	1.124 for 3THC superposed to 3OG2	4
<i>alpha</i> - and <i>beta</i> -galactosidases		1.257 for 2XN0 superposed to 3TTS	43	1.090 for 4FNR superposed to 3VD3	4

**Figure 1.** Superposition of structures of galactosidases: (A) *alpha*-galactosidases belonging to the family GH36. (B) *Caulobacter crescentus* (3U7V-grey) and *Homo sapiens* (3THC – black) *beta*-galactosidases. (C) *Lactobacillus acidophilus* *alpha*-galactosidase (2XN0 - black) and *Bacillus circulans* *beta*-galactosidase (3TTS - grey)

Superposition of *alpha*- and *beta*-galactosidases structures reflects overall small structural identity, revealing changes in relative orientation of the domains of proteins, all investigated proteins containing more than one domain. For the superposition of *alpha*- and *beta*-galactosidases the RMSD values range between 1.257 Å for 43 equivalent CA atoms pairs in the case of the superposition of the *Lactobacillus acidophilus* *alpha*-galactosidase (code entry 2XN0) and *Bacillus circulans* *beta*-galactosidase (code entry 3TTS) (Figure 1C) and 1.090 Å for only 4 equivalent CA atoms pairs in the case of the superposition of the *Geobacillus stearothermophilus* *alpha*-galactosidase (code entry 4FNR) and *Escherichia coli* *beta*-galactosidase (code entry 3VD3).

As all investigated enzymes use the same catalytic mechanism, we also compared the structures of their catalytic domains by structural superposition and the results are presented in the Table 5.

Table 5. The minimum and maximum RMSD values obtained by the superposition of the three dimensional structures of the catalytic domains of the investigated *alpha*- and *beta*-galactosidases (CA-carbon *alpha*)

Galactosidase class	Minimum RMSD / Å ²	Number of equivalent CA atoms pairs	Maximum RMSD / Å ²	Number of equivalent CA atoms pairs
<i>alpha</i> -galactosidases	0.632 for 2XN0 superposed to 4FNR	305	1.179 for 3LRL superposed to 3A24	74
<i>beta</i> -galactosidases	0.573 for 1GOW superposed to 4HA3	469	1.289 for 1GOW superposed to 3U7V	20
<i>Alpha</i> - and <i>beta</i> -galactosidases	1.229 for 2XN0 superposed to 1KWG	68	0.939 for 3LRL superposed to 1GOW	7

Figures 2 illustrate the superposition of the catalytic domains of *alpha*-galactosidases (A) (the structure of the catalytic domain of the *Bacteroides thetaiotaomicron* *alpha*-galactosidase is presented in black and the others in grey), *beta*-galactosidases (B) and of the *Saccharomyces cerevisiae* *alpha*-galactosidase (code entry 3LRL) and *Sulfolobus solfataricus* *beta*-galactosidase (code entry 1GOW) that were identified as being the most divergent (C).

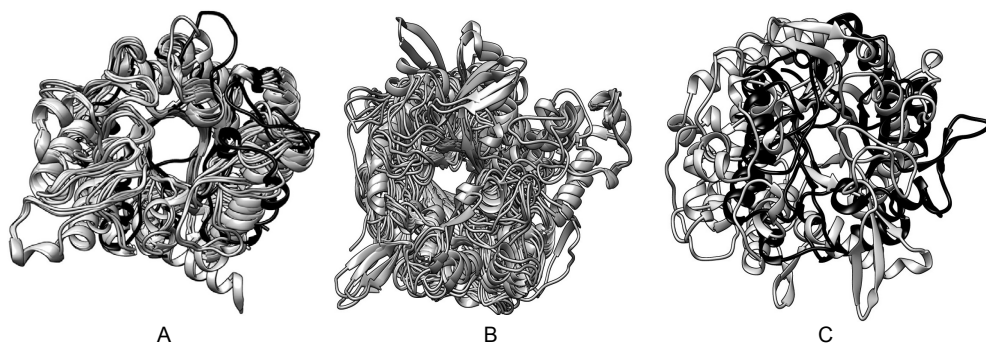


Figure 2. Superposition of structures of the catalytic domains of: (A) alpha-galactosidases (*Bacteroides thetaiotaomicron* alpha-galactosidase is presented in black and the other alpha-galactosidases are shown in grey). (B) beta-galactosidases. (C) *Saccharomyces cerevisiae* alpha-galactosidase (code entry 3LRL – black) and *Sulfolobus solfataricus* beta-galactosidase (code entry 1GOW- grey)

The results presented in Table 5 and illustrated in Figures 2 reveal that the best structural superposition is always obtained for the catalytic domains. All these results highlight that *alpha*- and *beta*-galactosidases using the retaining catalytic mechanism share global structural similarity of their catalytic domains and overall analogous physicochemical properties despite their unrelated sequences.

The average values of the normalized surface areas and the surface fractal dimensions of the monomeric sub-units of *alpha*- and *beta*-galactosidases are presented in Table 6. Student's statistical test has been used to analyze these data and the results reflected that the average values of the normalized surface areas and surface fractal dimensions are not significantly distinct for *alpha*- and *beta*-galactosidases confirming once again their global structural similarity. It is also true for the average values of normalized surface areas and surface fractal dimensions of the catalytic domains of investigated galactosidases: there are not significant differences between the average values corresponding to two classes of enzymes and, furthermore, these average values are not distinct by comparison to those corresponding to the entire enzymes.

Student's statistical test also reveals that, at the 0.05 level, the average values of the surface fractal dimensions are significantly distinct for all monomers compared to multimers reflecting distinct surface roughness of monomers and multimers belonging to the same class of galactosidases and reflecting an increased complexity of the surface shape of the polymers compared to the corresponding monomers. Distinct surface fractal dimensions for monomer and multimer proteins have been previously reported [19]. In addition, the greatest

part of investigated structures comes from polymeric proteins and it is already known that protein-protein interactions often occur through flat regions with a large surfaces area [20] explaining the lower roughness of monomers in comparison to polymers. This observation is also important from biochemical point of view if we take into account that oligomerization has been determined to be a decisive process in influencing the substrate binding for the GH27 enzyme subfamily [21].

Table 6. Average values of normalized surface areas (NSA) and surface fractal dimensions (Ds) of alpha- and beta-galactosidases and their catalytic domains

Protein family	Average value of NSA /Å ²	Average value of D _s
<i>alpha</i> – galactosidase monomers	34.78±1.94	2.30±0.18
<i>alpha</i> – galactosidase multimers	-	2.41±0.16
<i>alpha</i> -galactosidase catalytic domains	37.23±1.74	2.38±0.29
<i>beta</i> - galactosidase monomers	36.13±1.85	2.31±0.05
<i>beta</i> - galactosidase multimers	-	2.36±0.08
<i>beta</i> -galactosidase catalytic domains	40.38±1.56	2.34±0.15

Surface analysis of the considered enzymes shows the hydrophobic character of the identified cavities and that bacterial galactosidases expose the larger cavities (Table 7).

Table 7. Mean values of surface cavities and their geometric properties for alpha- and beta-galactosidases

Protein family	Organism (number of analysed structures)	Average molecular weight / Da	Fpocket analysis			
			Mean number of identified pockets	Mean volume of the most probable pocket / Å ³	Hydrophobicity score	Local hydrophobic density
<i>alpha</i> -galactosidase	Bacteria (10)	75005.86±12134.26	38±7	909±125	24.07±3.04	38.42±4.18
	Eukaryota (5)	48319.74±2474.88	16±3	644±214	7.90±1.96	28.67±5.14
<i>beta</i> -galactosidase	Archea (2)	56106.55±827.38	18±3	520±224	42.72±14.26	34.09±6.23
	Bacteria (10)	93544.64±23680.14	35±6	1091±416	10.64±2.06	39.79±8.06
	Eukaryota (6)	100865.85±17775.18	42±7	848±286	23.16±6.28	34.56±6.06

Considering the necessity of both the shape and chemical complementarity between the protein cavity and ligand, the local hydrophobicity is an important indication of ligand accessibility to the internal pocket. More than it, surface cavities identification and characterization in terms of shape and size are important for structure-based ligand design strategies as cavities of larger size may accommodate non-native ligands.

Surface analysis underline that, contrary to the global structural similarity, there are local surface characteristics that reflects the specificity of every subfamily of *alpha*- and *beta*-galactosidases.

CONCLUSIONS

To our knowledge, this is a first study dealing with comparison of *alpha*- and *beta*-galactosidases structural properties both at global and local levels. It reveals similar global physicochemical and structural properties of the *alpha*- and *beta*-galactosidases despite their unrelated sequences and also specific features concerning local properties of their surfaces. *Beta*- galactosidases expose more complex surfaces than *alpha*-galactosidases with much hydrophobic cavities.

The similarity of the global structural properties, especially concerning the catalytic domains, confirms the identical catalytic mechanism and the common evolutionary ancestry of considered enzymes. The distinct local surface features seem to be correlated to their specificity of interactions. The specific identified features are in good correlation with the fact that some investigated *alpha*- and *beta*-glucosidases contain many catalytic domains, every domain belonging to a different GH family. Understanding of the local surface properties of galactosidases in correlation with their substrate specificity becomes very important as it offers new ways to improve, modify or even inhibit their catalytic activity with direct consequences for the biotechnology industries.

EXPERIMENTAL SECTION

Within this study a few bioinformatics tools were used to analyze and compare sequence and structural properties of *alpha*- and *beta*-galactosidases starting from sequence information retrieved from UniProt data base [22] and structure information retrieved from Protein Data Bank [23] and PISA web server [24].

There are 139 entries concerning *alpha*- and *beta*-galactosidases, respectively putative *alpha*- and *beta*-galactosidases using the retaining catalytic mechanism in the Protein Data Bank (PDB) [23]. As PDB usually contains more than one structural file for a given protein, in our study we considered the crystallographic file with the higher resolution concerning the structure of the native protein (when available) or the structural file of its complex with the substrate, product or inhibitor. The codes entry used in this study are the following: 4FNQ, 4FNR, 2XN0, 3MI6, 1ZY9, 3A21, 2YFN, 4NZJ, 3A24, 3GXT, 3LRL, 3A5V, 1SZN, 1UAS for *alpha*-galactosidases and 1GOW, 4HA3, 3VD3, 3BGA, 1KWG, 3TTY, 1YQ2, 3FN9, 3U7V, 4E8D, 3OG2, 3THC, 3OBA, 4IUG, 1TG7 and 3W5G for *beta*-galactosidases, respectively. In the cases of the structures of complexes made by the enzymes, the ligands have been removed and structural analysis has been performed only on the proteins structures.

The investigated proteins belong to different GH families but all of them use the retaining catalytic mechanism and possess the $(\beta/\alpha)_8$ barrel [25] structural motif, that was identified as their catalytic domain. There is one exception: *alpha*-galactosidase from *Bacteroides thetaiotaomicron* (PDB code entry 3A24). It may act both as an inverting *alpha*-glucoside and a retaining *alpha*-galactosidase [26].

The sequence similarity between the investigated proteins was studied using multiple sequence analysis performed with CLUSTALW2 software [27]. ProtParam tool [18] was used to compute some global physicochemical properties of *alpha*- and *beta*-galactosidases based on their sequences: GRAVY (GRand Average of HYdropathicity) index indicating the hydrophobic or hydrophilic character of the protein, the net charge, theoretical isoelectric point (*pI*) and the aliphatic index.

The evolutionary relationships between proteins that share sequences with low similarity were detected using structural alignment based on the superposition of the atomic coordinate sets of two or more proteins and a minimal root mean square deviation (*RMSD*) between the structures was computed. *RMSD* reflects the degree of dissimilarity of two three-dimensional protein structures and there are different possible subsets of the protein atoms that can be used in producing a structural alignment and calculating the corresponding *RMSD* values, but usually the *alpha* carbon (*CA*) positions were considered [28]. A zero value for the *RMSD* indicates identical structures and it increases for dissimilar structures. Structural similarity of the considered enzymes was compared using the *structure matching* tool in the Chimera software [29]. For the structural alignment and structural analysis only chains A of polymeric proteins were considered, except the computation of the surface fractal dimensions of polymers where all the protein chains present in crystallographic asymmetric unit were analyzed.

The surface properties of investigated proteins both at local and global levels were analyzed. The local properties refer to one region on the protein surface (such as a cavity or pocket) and global properties refer to the overall protein surface. In order to analyze and compare the surface properties of investigated proteins, the normalized surface area, the surface fractal dimension, the number, geometrical and chemical characteristics of surface cavities were also computed. To eliminate the influence of the protein size, the normalized surface area (*NSA*) was obtained by dividing the molecular surface of each protein (computed using Chimera software) to the number of amino acids in corresponding structure.

For multimeric proteins, the *NSA* value for the monomeric sub-unity *A* was computed. *NSA* is used as a measure of the compactness of the protein structure, more compact structures having smaller *NSA* values [30]. Surface fractal dimension (D_s) is a quantitative measure of the global surface complexity. This quantity is defined using the fractal geometry concepts and it was computed using the method proposed by Lewis and Rees [31]. This method considers the scaling law between the surface accessible area (*SA*) and the radius of a rolling probe molecule (*R*) on the surface and the surface fractal dimension, *D_f*, was determined from the slope of the $\log(\text{SA})$ versus $\log(\text{R})$. The surface area of the protein was computed using GETAREA software [32] for probe radii of 1, 1.2, 1.4, 1.6, 1.8 and 2 Å respectively.

The detection of cavities and/or protrusions present at the protein surface and characterization of their local geometric and chemical properties was performed using the Fpocket [33] tool.

Almost all of the identified cavities have hydrophobic character. Considering the necessity of both the shape and chemical complementarity between the protein cavity and ligand, the local hydrophobicity is an important indication of ligand accessibility to the internal pocket, information that is also incorporated into ligand design strategies.

ACKNOWLEDGMENTS

Diana-Larisa VLĂDOIU would like to thank the project POSDRU/159/1.5/S/137750 - "Doctoral and Postdoctoral programs support for increased competitiveness in Exact Sciences research" cofinanced by the European Social Fund within the Sectorial Operational Program Human Resources Development 2007 – 2013 because this work was supported by this strategic grant.

REFERENCES

- [1]. B. Yang, Z. Dai, S.Y. Ding, C.E. Wyman, *Biofuels*, **2011**, 2, 421.
- [2]. J.F. Sorensen, S.K.M. Kragh, O. Sibbesen, J. Delcour, H. Goesaert, B. Svensson, T.A. Tahir, J. Brufau, A.M. Perez-Vendrell, D. Bellincampi, R. d'Ovidio, L. Camardella, A. Giovane, E. Bonnin, N. Juge, *Biochim Biophys Acta*, **2004**, 1696, 275.
- [3]. N. Brás, N. Cerqueira, M.J. Ramos, P.A. Fernandes, "Carbohydrates - Comprehensive Studies on Glycobiology and Glycotechnology", Chuan-Fa Chang Ed., InTech: Rijeka, **2012**; chapter 6.
- [4]. E.C. Webb, "Enzyme nomenclature", Academic Press, San Diego, **1992**, 346.
- [5]. B.L. Cantarel, P.M. Coutinho, C. Rancurel, T. Bernard, V. Lombard, B. Henrissat, *Nucleic Acids Res*, **2009**, 37, D233.
- [6]. B. Henrissat, G. Davies, *Current Opinion in Structural Biology*, **1997**, 7, 637.
- [7]. D. Koshland, *Biological Reviews*, **1953**, 28, 416.
- [8]. V.L. Yip, A. Varrot, G.J. Davies, S.S. Rajan, X. Yang, J. Thompson, W.F. Anderson, S.G. Withers, *J Am Chem Soc*, **2004**, 126, 8354.
- [9]. G. Davies, B. Henrissat, *Structure*, **1995**, 3, 853.
- [10]. P. Manzanares, L.H.D. Graff, J. Visser, *Enzyme Microb. Technol*, **1998**, 22, 383.
- [11]. Q. Hussain, *Critical Reviews in Biotechnology*, **2010**, 30, 41.
- [12]. D.H. Calhoun, D.F. Bishop, H.S. Bernstein, M. Quinn, P. Hantzopoulos, R.J. Desnick, *Proc Natl Acad Sci USA*, **1985**, 82, 7364.
- [13]. J. Lukas, A.K. Giese, A. Markoff, U. Grittner, E. Kolodny, H. Mascher, K.J. Lackner, W. Meyer, P. Wree, V. Saviouk, A. Rolfs, *PLOS Genetics*, **2013**, 9, e1003632.
- [14]. C.F. Yang, J.Y. Wu, F.J. Tsai, *Journal of Biomedical Science*, **2010**, 17, 79.
- [15]. M.V. Shumway, P.P. Sheridan, *Int J Biochem Mol Biol*, **2012**, 3, 209.
- [16]. P. Katrolia, E. Rajashekhara, Q. Yan, Z. Jiang, *Critical Reviews in Biotechnology*, **2013**, 8, 1.
- [17]. D. Craciun, B. Vlad-Oros, N. Filimon, V. Ostafe, A. Isvoran, *Acta Biochimica Polonica*, **2013**, 60, 553.
- [18]. E. Gasteiger, C. Hoogland, A. Gattiker, S. Duvaud, M.R. Wilkins, R.D. Appel, A. Bairoch, "The proteomics protocols handbook", Humana Press, New Jersey, **2005**, 571.
- [19]. D. Craciun, A. Isvoran, R.D. Reisz, N.M. Avram, *Fractals*, **2010**, 18, 207.
- [20]. A.W. White, A.D. Westwell, G. Braheimi, *Expert Reviews in Molecular Medicine*, **2008**, 10, e8.
- [21]. R. Fernandez-Leiro, A. Pereira-Rodríguez, M.E. Cerdan, M. Becerra, J. Sanz-Aparicio, *The Journal of Biological Chemistry*, **2010**, 285, 28020.
- [22]. R. Leinonen, F. Nardone, W. Zhu, R. Apweiler, *Bioinformatics*, **2006**, 22, 1284.

- [23]. H.M. Berman, J. Westbrook, Z. Feng, G. Gilliland, T.N. Bhat, H. Weissig, I.N. Shindyalov, P.E. Bourne, *Nucleic Acids Res*, **2000**, *28*, 235.
- [24]. E. Krissinel, K. Henrick, *J Mol Biol*, **2007**, *372*, 774.
- [25]. C. Branden, J. Tooze, "Introduction to Protein Structure", 2nd ed., Garland Publishing, New York, **1999**, 47.
- [26]. M. Okuyama, M. Kitamura, H. Hondoh, M.S. Kang, H. Mori, A. Kimura, I. Tanaka, M. Yao, *J Mol Biol*, **2009**, *392*, 1232.
- [27]. M.A. Larkin, G. Blackshields, N.P. Brown, R. Chenna, P.A. McGettigan, H. McWilliam, F. Valentin, I.M. Wallace, A. Wilm, R. Lopez, J.D. Thompson, T. J. Gibson, D.G. Higgins, *Bioinformatics*, **2007**, *23*, 2947.
- [28]. P.E. Bourne, I.N. Shindyalov, "Structural Bioinformatics", Wiley-Liss: Hoboken, New Jersey, **2003**, 58.
- [29]. E.F. Pettersen, T.D. Goddard, C.C. Huang, G.S. Couch, D.M. Greenblatt, E.C. Meng, T.E. Ferrin, *J Comput Chem*, **2004**, *25*, 1605.
- [30]. N.I. Dmitry, N.S. Bogatyreva, M.Y. Lobanov, O.V. Galzitskaya, *PLoS ONE*, **2009**, *4*, e6476.
- [31]. M. Lewis, D.C. Rees, *Science*, **1985**, *230*, 1163.
- [32]. R. Franczkiewicz, W. Braun, *J Comput Chem*, **1998**, *19*, 319.
- [33]. V. Le Guilloux, P. Schmidtke, P. Tuffery, *BMC Bioinformatics*, **2009**, *10*, 168.

ALLELOPATHIC EFFECTS AND INSECTICIDAL ACTIVITY OF *Salvia sclarea* L.

JOVANA ŠUĆUR^{a,*}, ALEKSANDRA POPOVIĆ^a, MILOŠ PETROVIĆ^a,
GORAN ANAČKOV^b, DJORDJE MALENCIĆ^a AND DEJAN PRVULOVIĆ^a

ABSTRACT. Extensive use of synthetic pesticides has negative effects on the environment and on human and animal health. Knowledge of allelopathic interactions could provide powerful tools for a better exploitation of natural resources in the management of weeds and insects without using herbicides and insecticides. Therefore effect of two concentrations (0.1% and 0.2%) of *Salvia sclarea* L. aqueous extract on lipid peroxidation process, as well as the activity of the antioxidant enzymes (superoxid dismutase, guaiacol peroxidase, pyrogallol peroxidase and catalase) in leaves and roots of pepper (*Capsicum annum* L.) and black nightshade (*Solanum nigrum* L.) seedlings were examined. Our results showed that lower concentration of *S. sclarea* aqueous extract induced lipid peroxidation in black nightshade roots. The second aim was to evaluate effectiveness of aqueous extract as contact toxicant against whitefly (*Trialeurodes vaporariorum*). It was observed that aqueous extract with concentration of 0.1% showed toxic effect with 56.66% mortality.

Keywords: allelochemicals; antioxidative enzymes; biopesticide; phenolics

INTRODUCTION

Allelopathy is defined as any direct or indirect, useful or harmful effects of one plant on other plants [1]. Although the term allelopathy is most commonly used to describe the chemical interaction between two plants, it has also been used to describe chemical communication between plants and other organisms, including bacteria, insects and mammals [2, 3]. Chemicals that impose allelopathic influences, called allelochemicals, are biomolecules produced in plant secondary metabolism [4, 5]. Phenolic acids were identified as the

^a University of Novi Sad, Faculty of Agriculture, Trg Dositeja Obradovića 8, 21000, Novi Sad, Serbia

^b University of Novi Sad, Faculty of Science, Trg Dositeja Obradovića 3, 21000, Novi Sad, Serbia

* Corresponding author: jovanasucur@yahoo.com

allelopathic agents more often than all other classes of secondary biomolecules [6]. Several studies have shown that plant defense against pathogens, nematodes and insects is based on the release and accumulation of phenolic compounds in soil. Phenolic compounds can offer an alternative to the chemical control of pathogens on agricultural crops [7]. Studies on the mechanisms and modes of action of allelopathic agents have revealed that phenolic compounds affect respiration, nutrient uptake, protein synthesis, photosynthesis, hormone levels, plant water potential and cell division and elongation [8, 9]. One of the main effects of allelochemicals on target plant is induced secondary oxidative stress manifested as uncontrolled production and accumulation of reactive oxygen species (ROS) [10]. Thus, phytotoxins caused disruption of membrane permeability, increased concentration of H_2O_2 , enhanced malondialdehyde (MDA) level and alterations in activities of antioxidant enzymes [10, 11].

The cell can reduce the impact of ROS either by an endogenous and exogenous antioxidant defense [12]. They are classified in enzymatic and non-enzymatic systems [13]. Some of the antioxidant enzymes that are found to provide a protection against potentially deleterious effects of reactive oxygen species are superoxide dismutase, catalase, peroxidase, glutathione peroxidase [14]. These enzymes play important roles in protecting cell [15]. Superoxid dismutase (SOD) is the first enzyme in detoxifying process, which converts superoxide free radical anions ($O_2^{\cdot-}$) to H_2O_2 [16, 17]. Catalase (CAT) and peroxidases metabolize hydrogen peroxide. Peroxidases are a group of oxidoreductases that catalyse H_2O_2 dependent oxidation of a wide variety of substrates [18]. Catalases, in contrast to peroxidases, do not require a reducing substrate for their activity [19].

Salvia sclarea L. (fam. *Lamiaceae*), popularly known as Clary sage, is native to Southern Europe and cultivated worldwide [20, 21]. Clary sage is important source of essential oils and many other compounds derived from different parts of the plant [22, 23]. In aromatherapy, it is a good relaxant for stress, asthma, and digestive problems. *S. sclarea* has shown diverse biological activities manifested by different components that allowed for many medicinal and pharmaceutical applications of the plant materials and extracts [20, 21]. Aqueous extracts of *Salvia* species had inhibitory effect on germination of weed seeds [24].

Knowledge of allelopathic interactions could provide powerful tools for a better exploitation of natural resources in the management of weeds and insects without using synthetic herbicides and insecticides. These compounds are easily biodegradable, environmentally-friendly, and often cheaper than the synthetic ones [25]. Objectives of these experiments were to (i) compare and analyze the allelopathic effect of the aqueous extracts of *Salvia sclarea* L. in two concentrations on pepper and black nightshade antioxidant properties and to explore the properties of this species in the control of weeds and (ii) to evaluate effectiveness of aqueous extract as contact toxicant against greenhouse whitefly.

RESULTS AND DISCUSSION

Chemical composition

Plant phenolics constitute are one of the major groups of compounds which possess a broad spectrum of chemical and biological activities [26]. The total amount of phenols in *S. sclarea* aqueous extract was 22.22 ± 0.64 mg gallic acid (GA) equivalents g^{-1} dry weight (d.w.). Flavonoids as one of the most diverse group of natural compounds are probably the most important natural phenolics [26]. In *S. sclarea* aqueous extract flavonoids were found in amount of 0.35 ± 0.00 mg rutin equivalents g^{-1} d.w. According to Miliauskas et al. [26] the total amount of phenols and flavonoids in *S. sclarea* methanolic extract were 24.00 ± 1.10 mg GA equivalents g^{-1} plant extract and 4.80 ± 0.50 mg rutin equivalents g^{-1} plant extract, respectively.

Table 1. Effect of two concentrations of *Salvia sclarea* aqueous extracts on activities of antioxidant enzymes and on MDA content in leaves of black nightshade seedlings

Time	24h	72h	120h
CAT			
Control	10.34 ± 0.12^a	25.83 ± 1.77^d	15.28 ± 0.15^b
0.1 %	44.79 ± 1.40^f	33.66 ± 0.52^e	26.40 ± 1.00^d
0.2 %	25.61 ± 1.22^d	17.71 ± 0.78^b	20.76 ± 0.94^c
SOD			
Control	16.50 ± 0.04^a	16.28 ± 0.19^a	9.88 ± 0.11^d
0.1 %	21.58 ± 0.19^f	$16.18 \pm 0.05^{a,b}$	15.88 ± 0.06^b
0.2 %	21.12 ± 0.13^e	19.37 ± 0.18^c	16.62 ± 0.06^a
GPX			
Control	$99.26 \pm 6.03^{a,b}$	94.99 ± 7.02^a	87.99 ± 4.50^a
0.1 %	161.55 ± 10.68^c	96.20 ± 8.78^a	$109.40 \pm 5.89^{a,b}$
0.2 %	121.62 ± 6.45^b	196.30 ± 11.87^d	$110.84 \pm 5.30^{a,b}$
PPX			
Control	147.56 ± 4.92^a	148.25 ± 5.16^a	112.65 ± 3.88^c
0.1 %	196.78 ± 3.03^d	155.49 ± 3.56^a	106.92 ± 3.08^c
0.2 %	145.85 ± 7.40^a	242.52 ± 3.72^e	129.29 ± 1.20^b
LP			
Control	1.68 ± 0.04^a	2.15 ± 0.05^c	1.98 ± 0.07^b
0.1 %	2.52 ± 0.07^e	$2.29 \pm 0.07^{c,d}$	2.19 ± 0.02^c
0.2 %	$2.13 \pm 0.04^{b,c}$	2.42 ± 0.06^d	$2.40 \pm 0.06^{d,e}$
The data are mean values \pm standard error. ^{a-f} values without the same superscripts within each column differ significantly ($P < 0.05$)			
CAT, catalase [U mg^{-1} protein]; SOD, superoxide dismutase [U mg^{-1} protein];			
GPX, guaiacol peroxidase [U mg^{-1} protein]; PPX, pyrogallol peroxidase [U mg^{-1} protein];			
LP, lipid peroxidation [nmol MDA mg^{-1} protein]			

Effect of extracts on MDA content and antioxidant enzyme activity in the pepper and black nightshade seedlings

The response of plants to damaging adverse circumstances is closely related to their enzyme activity [27]. For this reason, activities of antioxidant enzymes are frequently used as indicators of oxidative stress in plants [28]. As it is shown in Table 1, the activity of CAT in the leaves of black nightshade plants was significantly increased by the 0.1% *S. sclarea* aqueous extract, 24h after the treatment. The significant increase in the SOD activity was detected after 120 h in plants treated with higher concentration of *S. sclarea* aqueous extract. The highest activities of peroxidases were observed in plants treated with higher concentration 72 h after the treatment. In the roots of black nightshade, the significant increase of CAT activity was detected in plants treated with higher concentration of *S. sclarea* aqueous extract 72 h after the treatment while the lower concentration have the same effect on the activity of SOD after 24 h (Table 2).

Table 2. Effect of two concentrations of *Salvia sclarea* aqueous extracts on activities of antioxidant enzymes and on MDA content in roots of black nightshade seedlings

Time	24h	72h	120h
CAT			
Control	3.61 ± 0.08 ^a	20.06 ± 0.60 ^d	9.36 ± 0.34 ^b
0.1 %	6.11 ± 0.51 ^{ab}	15.24 ± 1.63 ^c	16.84 ± 1.51 ^{c,d}
0.2 %	7.92 ± 0.41 ^b	32.11 ± 2.67 ^e	7.16 ± 0.36 ^{a,b}
SOD			
Control	33.82 ± 0.08 ^a	25.90 ± 1.91 ^c	11.37 ± 0.68 ^f
0.1 %	68.07 ± 0.04 ^d	15.59 ± 1.39 ^e	32.42 ± 0.33 ^a
0.2 %	45.53 ± 0.44 ^b	23.60 ± 1.78 ^c	31.01 ± 0.65 ^a
GPX			
Control	1373.00 ± 99.75 ^{a,d,e}	1405.34 ± 110.34 ^{a,e}	1656.93 ± 196.1 ^d
0.1 %	2488.81 ± 100.99 ^b	1446.97 ± 99.36 ^{a,d,e}	1138.41 ± 46.40 ^e
0.2 %	1982.19 ± 65.68 ^c	1229.42 ± 44.20 ^{a,d,e}	1534.45 ± 29.03 ^{a,d}
PPX			
Control	1304.85 ± 24.37 ^a	1348.32 ± 20.98 ^a	1325.53 ± 56.60 ^a
0.1 %	1792.25 ± 55.88 ^c	1482.55 ± 106.05 ^a	899.80 ± 37.71 ^b
0.2 %	1379.10 ± 36.29 ^a	1474.83 ± 108.25 ^a	1064.56 ± 46.07 ^b
LP			
Control	2.38 ± 0.08 ^a	3.40 ± 0.07 ^d	1.88 ± 0.05 ^c
0.1 %	3.91 ± 0.21 ^e	4.02 ± 0.12 ^e	3.17 ± 0.12 ^d
0.2 %	3.64 ± 0.13 ^{d,e}	4.03 ± 0.14 ^e	2.77 ± 0.07 ^b
The data are mean values ± standard error. ^{a-f} values without the same superscripts within each column differ significantly (<i>P</i> < 0.05)			
CAT, catalase [U mg ⁻¹ protein]; SOD, superoxide dismutase [U mg ⁻¹ protein];			
GPX, guaiacol peroxidase [U mg ⁻¹ protein]; PPX, pyrogallol peroxidase [U mg ⁻¹ protein];			
LP, lipid peroxidation [nmol MDA mg ⁻¹ protein]			

The activities of peroxidases in the roots of black nightshade were significantly affected by the lower concentration of aqueous extracts, 24h after the treatment. After 120h, decrease of peroxidases activities were recorded. The activities of these enzymes showed downward trend with duration of the experiment. These observations are in agreement with earlier studies which reported up/down regulation in antioxidant enzyme activities under allelopathic stress of aqueous extracts from plants [29].

Table 3. Effect of two concentrations of *Salvia sclarea* aqueous extracts on activities of antioxidant enzymes and on MDA content in leaves of pepper seedlings

Time	24h	72h	120h
CAT			
Control	18.32 ± 0.48 ^a	16.84 ± 0.53 ^a	17.88 ± 0.77 ^a
0.1 %	17.35 ± 0.90 ^a	24.11 ± 1.03 ^c	20.52 ± 0.41 ^b
0.2 %	33.40 ± 0.52 ^d	22.28 ± 0.14 ^b	16.54 ± 0.24 ^a
SOD			
Control	11.23 ± 0.06 ^a	7.42 ± 0.04 ^d	5.96 ± 0.28 ^e
0.1 %	12.51 ± 0.03 ^b	7.17 ± 0.01 ^d	6.01 ± 0.01 ^e
0.2 %	10.24 ± 0.11 ^c	7.13 ± 0.02 ^d	4.76 ± 0.03 ^f
GPX			
Control	541.98 ± 11.57 ^a	486.07 ± 18.10 ^b	553.51 ± 22.27 ^a
0.1 %	379.29 ± 15.71 ^c	552.45 ± 11.73 ^a	252.86 ± 4.28 ^e
0.2 %	3339.09 ± 13.45 ^d	259.45 ± 10.47 ^e	317.26 ± 6.97 ^d
PPX			
Control	3551.93 ± 43.84 ^a	3854.00 ± 80.54 ^c	3348.29 ± 62.31 ^b
0.1 %	2198.78 ± 79.73 ^{e,f}	2298.00 ± 51.92 ^e	3026.71 ± 71.26 ^d
0.2 %	2255.68 ± 48.80 ^e	1746.62 ± 58.50 ^g	2051.72 ± 45.81 ^f
LP			
Control	2.52 ± 0.15 ^a	3.02 ± 0.11 ^b	3.29 ± 0.07 ^{b,c}
0.1 %	2.55 ± 0.08 ^a	3.47 ± 0.06 ^c	1.98 ± 0.03 ^d
0.2 %	3.28 ± 0.14 ^{b,c}	3.35 ± 0.14 ^c	1.78 ± 0.03 ^d
The data are mean values ± standard error. ^{a-g} values without the same superscripts within each column differ significantly ($P < 0.05$)			
CAT, catalase[U mg ⁻¹ protein]; SOD, superoxide dismutase [U mg ⁻¹ protein];			
GPX, guaiacol peroxidase [U mg ⁻¹ protein]; PPX, pyrogallol peroxidase [U mg ⁻¹ protein];			
LP, lipid peroxidation [nmol MDA mg ⁻¹ protein]			

An increase in the enzyme's activity in the first 72 h, probably occurs in response to stress [27]. For various plant species under oxidative stress, a significant increase of lipid peroxidation (LP) is observed. Oracz et al. [11] found that symptoms of membrane injuries occurred concomitantly to H₂O₂ accumulation and preceded an increase in the content of MDA, a compound that reveals the occurrence of measurable processes of lipid peroxidation. Thus, lipid peroxidation is a widely used stress indicator of plant membranes [30].

The significant increase in LP intensity was recorded in roots of black nightshade plants treated with lower concentration of *S. sclarea* aqueous extract 120h after the treatment. This could point to the fact that allelopathy provoked stress was strong enough that scavenging effects of SOD, CAT and peroxidases could not prevent oxidative burst and induction of LP. Higher production of MDA in the roots of black nightshade compared with MDA content in leaves showed that roots were more affected by allelochemicals than leaves.

Table 4. Effect of two concentrations of *Salvia sclarea* aqueous extracts on activities of antioxidant enzymes and on MDA content in roots of pepper seedlings

Time	24h	72h	120h
CAT			
Control	22.93±0.67 ^a	20.64 ± 0.58 ^b	10.56 ± 0.22 ^e
0.1 %	18.88 ± 0.48 ^b	13.52 ± 0.86 ^d	5.50 ± 0.44 ^f
0.2 %	20.12 ± 1.22 ^b	15.79 ± 0.45 ^c	6.71±0.32 ^f
SOD			
Control	7.27 ± 0.15 ^a	7.99 ± 0.07 ^b	9.34 ± 0.21 ^e
0.1 %	2.10 ± 0.06 ^h	5.12 ± 0.22 ^c	0.57 ± 0.06 ⁱ
0.2 %	3.33 ± 0.03 ^f	10.04 ± 0.05 ^g	4.55 ± 0.14 ^d
GPX			
Control	2655.56 ± 216.15 ^a	3589.58 ± 147.75 ^c	3315.58 ± 169.82 ^{b,c}
0.1 %	1709.12 ± 163.46 ^d	2530.02 ± 38.35 ^a	981.65 ± 20.54 ^e
0.2 %	3438.82 ± 122.31 ^{b,c}	3138.07 ± 172.15 ^b	1330.66 ± 21.66 ^{d,e}
PPX			
Control	2624.17 ± 25.56 ^a	2543.53 ± 51.18 ^a	1924.63 ± 52.26 ^b
0.1 %	1408.39 ± 51.03 ^d	1705.02 ± 31.87 ^c	587.81 ± 19.84 ^e
0.2 %	1637.99 ± 68.73 ^c	1934.68 ± 75.75 ^b	642.47 ± 15.01 ^e
LP			
Control	2.46 ± 0.07 ^a	2.92 ± 0.09 ^b	2.45 ± 0.08 ^a
0.1 %	2.42 ± 0.12 ^a	3.51 ± 0.30 ^d	1.96 ± 0.10 ^c
0.2 %	2.65 ± 0.11 ^{a,b}	2.50 ± 0.08 ^{a,b}	1.57 ± 0.12 ^c
The data are mean values ± standard error. ^{a-i} values without the same superscripts within each column differ significantly ($P < 0.05$)			
CAT, catalase [U mg ⁻¹ protein]; SOD, superoxide dismutase [U mg ⁻¹ protein];			
GPX, guaiacol peroxidase [U mg ⁻¹ protein]; PPX, pyrogallol peroxidase [U mg ⁻¹ protein];			
LP, lipid peroxidation [nmol MDA mg ⁻¹ protein]			

A significant decrease in activities of peroxidases in the leaves of the pepper plants were detected after treatment with *S. sclarea* aqueous extract, while activity of SOD was not affected by treatment (Table 3). An increase in activity of CAT was detected after 24 h in leaves of plants treated with higher

concentration of *S. sclarea* aqueous extract. In the roots, there was significant decrease in the activity of enzymes particularly of peroxidases and SOD at lower concentration of applied aqueous extracts (Table 4). Our results indicated that allelochemicals had both, inhibitory and stimulatory, effects on enzyme's activity. Similar findings have been reported by other authors [28].

There were no significant increase in LP intensity 24h and 72h after the treatment in leaves and roots of pepper plants treated with higher concentration. Accumulation of MDA was significantly lower in leaves and roots of pepper 120h after the treatment when compared with the control group. It indicated that effects of allelochemicals were low and defensive system of the plant was prevailed.

The phytotoxic effects of extracts were different between two understudy species, which points to the different sensitivity of species when facing allelochemicals [1]. Allelochemicals are selective in their actions and plants are selective in their responses [9]. Gilani et al. [31] found that the plant species have different allelopathic potentials and stimulatory effects of plants were decreased with increasing concentration. The sensitivity of plants dependent on concentration of applied extracts and duration of experiment as well [27, 32].

Toxicity test

Medicinal plants are rich sources of pesticides discovery, especially insecticides [25]. Natural products have low mammalian toxicity, high target specificity and biodegradability, and contain many active ingredients [33]. In the present work aqueous extract of *S. sclarea* was evaluated on greenhouse whitefly. The table 5 shows that mortality rate of greenhouse whiteflies after 96 h was above 50%. More effective formulation, with 56.66% mortality, was concentration of 0.1% *S. sclarea* aqueous extract. Furthermore, *S. sclarea* extracts had an overall excito-repellency against adult house flies [25], and offer effective bioactive compounds for growth inhibition of the fungi [34]. Zavala-Sánchez et al. [35] reported that chloroform extracts from *Salvia microphylla* and *Salvia connivens* had high insecticidal activity, and *Salvia keerlii* and *Salvia ballotiflora* had moderate insecticidal activity against armyworm, *Spodoptera frugiperda*. Tomczyk and Suszko [36] reported that *Salvia officinalis* extracts had toxic effect on larval stages and females of *Tetranychus urticae*. These reports have shown that different species of the genus *Salvia* have toxic effect on insects. Results of other authors indicate a potential use of aqueous plant extracts in pest management of greenhouse whiteflies [37].

Table 5. Mortality of *Trialeurodes vaporariorum* adult fed for 4 days with formulations containing a known concentration (0.1%, 0.2%) of *Salvia sclarea* aqueous extracts

Time	Mortality (%)		
	24h	72h	120h
Control	8.33 ^c	10.00 ^c	16.66 ^{b,c}
0.1 %	6.66 ^{c,d}	40.00 ^a	56.66 ^a
0.2 %	11.66 ^c	41.66 ^a	55.00 ^a

^{a-d} values without the same superscripts within each column differ significantly ($P < 0.001$)

CONCLUSIONS

The effects of *S. sclarea* aqueous extracts were different between pepper and black nightshade seedlings, which points to the different responses of species when facing allelochemicals. Two tested concentrations did not exhibit phytotoxic effect on the pepper or black nightshade seedlings. It was observed that aqueous extract with concentration of 0.1% showed toxic effect on greenhouse whitefly, an important insect pest of many plants including pepper, with 56.66% mortality. Therefore, we concluded that this plant may be explored in the development of bioinsecticides and use of natural substances could be an alternative method of insect control.

EXPERIMENTAL SECTION

Plant material and preparation of the aqueous extract

The aerial parts of the flowering plant *Salvia sclarea* L. were collected in the south of Serbia, in August. Voucher specimens of collected plant was confirmed and deposited at the Herbarium of The Department of Biology and Ecology, Faculty of Science, University of Novi Sad.

The air-dried plant material was ground into powder. The powdery material (10 g) was extracted with 100 ml distilled water (10% w/v). After 24 h, the extract was filtered through filter paper and kept at 4 °C until application.

Determination of total phenolic and flavonoid contents

The total phenolic content of *S. sclarea* aqueous extract was determined according to Folin-Ciocalteu's method [38]. Extract (0.02 ml) was mixed with 3.36 ml of deionized water, 0.4 ml of 20% sodium carbonate and 0.2 ml of 33% Folin–Ciocalteu reagent. After incubation at room temperature for 30 min, the absorbance of the reaction mixture was measured at 720 nm on a spectrophotometer. The data were expressed as mg gallic acid equivalents g⁻¹ dry weight (mg GA equivalents g⁻¹ d.w.).

Total flavonoids were estimated to the method described by Markham [39]. Extract (0.4 ml) was mixed with 1 ml of deionized water and 2.5 ml of aluminium chloride hexahydrate. After incubation at room temperature for 15 min, the reaction mixture absorbance was measured at 430 nm on a spectrophotometer. The data were expressed as mg rutin equivalents g⁻¹ dry weight (mg rutin equivalents g⁻¹ d.w.).

Seedling growth

The pepper (*Capsicum annuum* L.) cv. Anita and black nightshade (*Solanum nigrum* L.) seeds were grown in a controlled climate chamber at 28 °C, 60% relative humidity, a photoperiod of 18 h, and a light intensity of 175 μmol m⁻² s⁻¹, in plastic pots containing sterile sand. After 30 days, the seedlings were transplanted in plastic pots containing 700 ml of Hoagland's solution, and 7 and 14 ml of *S. sclarea* aqueous extract, while pots of control contained the same volume of Hoagland's solution. Seedlings were harvested for further biochemical analyzes 24, 72 and 120 h after the treatments.

Enzyme extraction

Fresh leaves and roots (2 g each) were homogenized in 10 ml of phosphate buffer (0.1 M, pH 7.0). Homogenates were centrifuged for 20 min at 10.000 x g and filtered. The supernatants were used to test enzyme activity and to determine intensity of lipid peroxidation.

Membrane lipid peroxidation and protein content

Lipid peroxidation was measured at 532 nm using the thiobarbituric acid test (TBA) test [40]. The enzyme extract (0.5 ml) was incubated with 2 ml of 20% TCA containing 0.5% thiobarbituric acid for 40 min at 95 °C. The reaction was stopped by cooling on ice for 10 min and the product was centrifuged at 10.000 x g for 15 min. The total amount of TBA-reactive substances is given as nmol malondialdehyde (MDA) equivalents mg⁻¹ protein.

Protein content in homogenates were determined according to the method of Bradford [41], using bovine serum albumin as a protein standard.

Assay of catalase activity

Catalase (CAT) (EC 1.11.1.6) activity was determined according to Sathya and Bjorn [42]. The decomposition of H₂O₂ was followed as a decrease in absorbance at 240 nm. The enzyme extract (0.02 ml extract of leaves and 0.1 ml extract of roots, separately) was added to the assay mixture containing 1 ml for leaves and 1.5 ml for roots 50 mM potassium phosphate buffer (pH 7.0) and 10 mM H₂O₂. The activity of the enzyme was expressed as U per 1 g of protein (U g⁻¹ protein).

Assay of superoxide dismutase activity

Superoxide dismutase (SOD) (EC 1.15.1.1) activity was assayed according to the method of Mandal et al. [40] slightly modified by measuring its ability to inhibit photochemical reduction of nitro blue tetrazolium (NBT) chloride. The reaction mixture contained 50 mM phosphate buffer (pH 7.8), 13 mM L-methionine, 75 μ M NBT, 0.1 mM EDTA, 2 μ M riboflavin and 0.02 ml of the enzyme extract. It was kept under a fluorescent lamp for 30 min, and then the absorbance was read at 560 nm. One unit of the SOD activity was defined as the amount of enzymes required to inhibit reduction of NBT by 50%.

The activity of the enzyme was expressed as U per 1 mg of protein (U mg^{-1} protein).

Assay of peroxidase activity

Peroxidase (EC 1.11.1.7) activity was measured using guaiacol (guaiacol peroxidase; GPX) and pyrogallol (pyrogallol peroxidase; PPX) as substrates according to Morkunas and Gmerek [43]. Peroxidase activity (GPX and PPX) was expressed as U per 1 mg of protein (U mg^{-1} protein).

Pyrogallol peroxidase activity: this method includes the measurement of the content of purpurogallin- a product of pyrogallol oxidation. The enzyme extract (0.02 ml) was added to the assay mixture containing 3 ml of 180 mM pyrogallol and 0.02 ml of 2 mM H_2O_2 . Absorbance was recorded at 430 nm using a spectrophotometer.

Guaiacol peroxidase activity: this method consists of the assay of tetraguaiacol- a colored product of guaiacol oxidation in the investigated sample. The enzyme extract (0.04 ml) was added to the assay mixture containing 3 ml of 20 μ M guaiacol and 0.02 ml of 3 mM H_2O_2 . Absorbance was recorded at 436 nm using a spectrophotometer.

Insects and toxicity test

The experiment on the adult of whitefly, *Trialeurodes vaporariorum* (Westwood, 1856) (Homoptera: Aleyrodidae), collected in the greenhouse, was carried out at the Faculty of Agriculture, University of Novi Sad.

The bioassays were carried out using groups of 20 adult insects *T. vaporariorum*, kept in the transparent laboratory dishes (25 cm x 12 cm), fed on the pepper nursery plants containing a known concentration (0.1%, 0.2%) of aqueous extract. Aqueous extracts were applied together with adjuvant (Trend) for better adhesion to the leaf surface. Pepper plants with water, adjuvant and 20 insects for each were used as controls. The experiment was set in three replicates and control. A no-choice method, in which control and treated plants were placed individually in each dish, was adopted in this experiment. Mortality was checked after 24, 48 and 96 h.

Statistical analysis

Values of the biochemical parameters were expressed as means \pm standard error of determinations made in triplicates and tested by ANOVA followed by comparison of the means by Duncan's multiple range test ($P < 0.05$). Data were analyzed using STATISTICA for Windows version 11.0.

REFERENCES

- [1]. H. Safari, A. Tavili, M. Saberi, *Frontiers of Agriculture in China*, **2010**, 4, 475.
- [2]. M. An, D. L. Liu, I.R. Johnson, J.V. Lovett, *Ecological Modelling*, **2003**, 161, 53.
- [3]. T.L. Weir, S.W. Park, J.M. Vivanco, *Current Opinion in Plant Biology*, **2004**, 7, 472.
- [4]. P.B.S. Bhadoria, *American Journal of Experimental Agriculture*, **2011**, 1, 7.
- [5]. J.A. Blanco, *Ecological Modelling*, **2007**, 209, 65.
- [6]. C.M. Rooth, J.P. Shroyer, G.M. Paulsen, *Agronomy Journal*, **2000**, 92, 855.
- [7]. S.M. Mandal, D. Chakraborty, S. Dey, *Plant Signaling & Behavior*, **2010**, 5, 359.
- [8]. H. Wu, T. Haig, J. Pratley, D. Lemerle, M. An, *Journal of Agricultural and Food Chemistry*, **2000**, 48, 5321.
- [9]. B. Gatti, A.G. Ferreira, M. Arduin, S.C.G.A. Perez, *Acta Botanica Brasilica*, **2010**, 24, 454.
- [10]. R. Bogatek, A. Gniazdowska, *Plant Signaling and Behavior*, **2007**, 2, 317.
- [11]. K. Oracz, C. Bailly, A. Gniazdowska, D. Côme, F. Corbineau, R. Bogatek, *Journal of Chemical Ecology*, **2007**, 33, 251.
- [12]. M. Tosun, S. Ercisli, M. Sengul, H. Ozer, T. Polat, E. Ozturk, *Biological Research*, **2009**, 42, 175.
- [13]. J.K. da Silva, C.B.B. Cazarin, T.C. Colomeu, Â.G. Batista, L.M.M. Meletti, J.A.R. Paschoal, S.B. Júnior, M.F. Furlan, F.G.R. Reyes, F. Augusto, M.R.M. Júnior, R. L. Zollner, *Food Research International*, **2013**,: 53, 882.
- [14]. P. Rani, K. Meena Unni, J. Karthikeyan, *Indian Journal of Clinical Biochemistry*, **2004**, 19, 103.
- [15]. H. Kuthan, H. J. Haussmann, J. Werringloer, *Biochemical Journal*, **1986**, 237, 175.
- [16]. J.M. McCord, I. Fridovich, *Journal of Biological Chemistry*, **1969**, 244, 6049.
- [17]. F. Miller, *Current Opinion in Chemical Biology*, **2004**, 8, 162.
- [18]. M. Hamid, K. Rehman, *Food Chemistry*, **2009**, 115, 1177.
- [19]. D. Inzé, M. Van Montagu, *Current Opinion in Biotechnology*, **1995**, 6, 153.
- [20]. M. Džamić, M. Soković, S. Ristić, J. Grujić-Jovanović, P. Vukojević, D. Marin, *Archives of Biological Science*, **2008**, 60, 233.
- [21]. S. Naseri-moadeli, V. Rowshan, *International Journal of Agriculture and Crop Sciences*, **2013**, 5, 828.

- [22]. M. Hudaib, M.G. Bellardi, C. Rubies-Autonell, J. Fiori, V. Cavrini, *Il Farmaco*, 2001, 56, 219.
- [23]. G. Miliauskas, P.R. Venskutonis, T.A. van Beek, *Food Chemistry*, **2004**, 85, 231.
- [24]. K. Bajalan, E. Oregani, A.A. Moezi, A. Gholami, *Technical Journal of Engineering and Applied Sciences*, **2013**, 3, 485.
- [25]. M.R. Fakoorziba, M.Dj. Moemenbellah-Fard, K. Azizi, H. Shekarpoor, H. Alipoor, *Journal of Health Sciences and Surveillance System*, **2014**, 2, 2.
- [26]. G. Miliauskas, P. R. Venskutonis, T. A. van Beek, *Food Chemistry*, **2004**, 85, 231.
- [27]. T.O. Sunmonu, J. Van Staden, *South African Journal of Botany*, **2014**, 90, 101.
- [28]. P. Cao, C. Liu, D. Li, *African Journal of Biotechnology*, **2011**, 10, 7480.
- [29]. Y. Li, T. Hu, F. Zeng, H. Chen, X. Wu, *Journal of Plant Studies*, **2013**, 2, 158.
- [30]. E. Taulavuori, E.K. Hellström, K. Taulavuori, K. Laine, *Journal of Experimental Botany*, **2001**, 52, 2375.
- [31]. S.A. Gilani, Y. Fujii, Z.K. Shinwari, M. Adnan, A. Kikuchi, K.N. Watanabe, *Pakistan Journal of Botany*, **2010**, 42, 987.
- [32]. M. An, J.E. Pratley, T. Haig, D.L. Liu, *Nonlinearity in Biology, Toxicology, and Medicine*, **2005**, 3, 245.
- [33]. D.M.C. Nguyen, D.J. Seo, H.B. Lee, I.S. Kim, K.Y. Kim, R.D. Park, W.J. Jung, *Microbial Pathogenesis*, **2013**, 56, 8.
- [34]. P.D. Dellavalle, A. Cabrera, D. Alem, P. Larrañaga, F. Ferreira, M.D. Rizza, *Chilean Journal of Agricultural Research*, **2011**, 71, 231.
- [35]. M.A. Zavala-Sánchez, S. Pérez Gutiérrez, D. Romo-Asunción, N.C. Cárdenas-Ortega, M. A. Ramos-López, *Southwestern Entomologist*, **2013**, 38, 67.
- [36]. A. Tomczyk, M. Suszko, *Biological Letters*, **2011**, 48, 193.
- [37]. M. Dehghani, K. Ahmadi, *Bulgarian Journal of Agricultural Science*, 2013, 19, 691.
- [38]. A. Hagerman, I. Harvey-Mueller, H.P.S. Makkar, Quantification of Tannins in Tree Foliage – a Laboratory Manual FAO/IAEA Working Document, Vienna, **2000**, 4.
- [39]. K.R. Marckam, “Methods in Plant Biochemistry”, Academic Press, London, **1989**, 16.
- [40]. S. Mandal, A. Mitra, N. Mallick, *Physiological and Molecular Plant Pathology*, 2008, 72, 56.
- [41]. M.M. Bradford, *Analytical Biochemistry*, **1976**, 72, 248.
- [42]. E. Sathya, M. Bjorn, Plant Stress Tolerance, Humana Press, Oklahoma, **2010**, 273.
- [43]. Morkunas, J. Gmerek, *Journal of Plant Physiology*, **2007**, 164, 185.

MODELLING AND PREDICTION OF LIPOPHILICITY FOR NATURAL COMPOUNDS WITH STRONG BIOLOGICAL ACTIVITY

COSTEL SÂRBU^a, RODICA DOMNICA NAȘCU-BRICIU^{a,*}

ABSTRACT. The goal of this study was to develop high statistical significant models for lipophilicity estimation for a group of 60 compounds with increased toxicity, belonging to alkaloids and mycotoxins. The multiple linear regression modelling was made by means of genetic algorithms as a function of 972 molecular descriptors, computed by ChemOffice and Dragon Plus software and completed by internet available module for Log P computation, ALOGPS 2.1. The compounds classification has been realized using principal component analysis and hierarchical cluster analysis. Data evaluation has been realized by various correlation matrices and relevant graphs. The modelling was made on the basis of 26 compounds with known log P_{exp} values and the results were validated by means of additional models developed for a series of 20 compounds. The other 6 compounds, which were excluded from the modelling process, were used afterwards as test set for prediction and comparison. The most descriptive models were those retaining four descriptors, and in all models were selected at least one computationally expressed log P value (miLogP, KOWWIN and ALOGP most often). All the obtained results are highly suggestive and offer a very pertinent idea regarding the lipophilicity range of natural compounds of increased toxicity. The models were validated considering various statistical parameters and different correlation matrices defined by high statistical significance.

Keywords: *modelling, alkaloids, mycotoxins, toxicity*

INTRODUCTION

The importance of natural products in diseases prevention is known from ancient times and used up to early 1900s, when the “Synthetic Era” began and an increased tendency to replace the natural product drugs with synthetic

^a Babeș-Bolyai University, Faculty of Chemistry and Chemical Engineering, 11 Arany Janos Str., RO-400028, Cluj-Napoca, Romania

* Corresponding author: rodicab2003@yahoo.com

ones has been observed [1]. However, up today they are still intensively used in prevention and treatment of cancer and infectious diseases [2, 3]. On the other side, despite of beneficent effects, some of the most controversial and toxic compounds are also of natural origin. Amongst them there may be mentioned the alkaloids and the mycotoxins. The alkaloids are substances synthesized by plants [4] or even animals [5], which are defined by slightly basic properties, usually associated to the content of nitrogen atoms. These compounds are sophisticatedly combining the beneficent and toxic activities. For examples, the cinchona alkaloids are generally used for malaria treatment, but in overdose it may cause the disease called cinchonism, or the morphine is well known as a strong analgesic drug, but it may cause addiction and also in overdose is leading to asphyxia and death. In the majority of cases the alkaloids are central nervous system stimulants and they are inducing a large variety of biological effects [6]. On the other side the mycotoxins, are natural compounds biosynthesized by moulds, which unlike the alkaloids, do not have any biological beneficent effect. They have strong toxic effects over human and animal health, causing cancer, infertility, liver failure, cirrhosis, etc [7-10].

Most of the biological effects are interconnected to compounds lipophilic character. A typical example is represented by heroin and morphine. These compounds are differing just by the nature of the functional groups (methoxyl or hydroxyl). The heroin, which has a higher lipophilicity induced by the methoxyl groups, may easily crossover the biological membranes and exercises a very strong biological activity after hydrolysis. On the other side, the morphine is crossing the biological membranes more difficult because of the hydroxyl groups and implicitly its activity is lower [11, 12]. The lipophilicity is a property often used in strategies proposed to enhance the passive internalization of drugs into cells [13]. In fact, lipophilicity is an important endpoint used extensively in medicinal chemistry and environmental toxicology in predicting biological and hazardous effects of chemicals [14]. The lipophilicity is experimentally determined as partition coefficient ($\log P$) between two immiscible phases (usually octanol-water), but it may be also computationally expressed [15]. Furthermore, it is a major experimental and theoretical tool in numerous disciplines, including medicinal chemistry, toxicology, pharmacology, and environmental monitoring [16-18]. The lipophilicity of a solute controls its distribution among body fluids, liquid-rich phases, and tissue proteins. For this reason, a quantitative assessment of lipophilicity is of great importance in quantitative structure–activity (or – property) relationship (QSAR/QSPR) studies [19-21]. This methodology is highly advantageous because by means of a generated mathematical model, many effects may be predicted [22-24]. The ideal goal of investigations concerned with the QSPR/QSAR is to predict the behaviour of chemical species from a minimal set of input data [14]. There are many possibilities of modelling,

but one of the most preferred techniques is multiple linear regression (MLR), which is also completed nowadays by partial least square (PLS), principal component regression (PCR), genetic algorithms (GA) and even fuzzy clustering [25-27].

In the view of above considerations, our goal was to construct simple models for predicting the lipophilicity of various alkaloids and mykotoxins of increased toxicity, based on the summation of a contribution value for various physicochemical and structural features. In this work we have attempted to determine the important factors influencing the lipophilicity of toxic compounds and give them quantitative values. The chemometric techniques involved in this study are MLR, PCA, GA, PCR and cluster analysis (CA). The actual study is built on 60 compounds belonging to alkaloids and mycotoxins. Compounds selection for the analysis was based on the known toxic effects and the large diversity concerning their physicochemical characteristics and biological activity. The experimentally determined partition coefficient ($\text{Log } P_{\text{exp}}$) was employed as dependent variable. All the validation procedures strongly support the reliability and quality of results obtained.

RESULTS AND DISCUSSION

The selected compounds, belonging to the mycotoxins and alkaloids, are always presenting complex structures, with nitrogen and/or oxygen heteroatoms involved in the aromatic system. In order to reveal the similarity and differences between the selected compounds some exploratory investigations have been performed, by CA (Figure 1(a)) and PCA (Figure 1(b)). The multivariate exploratory methods were applied on 980 descriptors computed with Chem 3DUltra, Dragon Plus and ALOGPS 2.1. According to Figure 1(a) the investigated compounds are forming two major groups, one formed by narcotics, mycotoxins, and quinine derivatives, while the second is formed by nicotine and caffeine derivatives. Moreover, if investigating Figure 1 (b) there may be observed that the first principal component (PC1) is linearly distributing the investigated compounds and along of this direction the compounds are not separated in groups. Once again the aflatoxins group is considered highly similar with narcotics, quinine derivatives and also ochratoxins. Moreover, the caffeine and nicotine derivatives exhibit high similarities. The literature data are indicating that compounds **18**, **19** and **20** (cytisine and its derivatives) are nicotinic acetylcholine receptor agonist, which means that they interact with the same receptors in the brain, and the cytisine intoxication is similar to nicotine poisoning [11]. The fact that all these compounds are highly related in the PCA chart is an indicative that the entire phenomenon is dictated by their chemical structure and induced lipophilicity.

the obtained values were compared to the observed ones. In the group B were eliminated the values that were covered very well the lipophilicity range, but there was never selected the extremes. In the groups C and D the selected compounds which were left out were different by those selected in group B and finally in the case of group E, the eliminated compounds were those with the maximum (3 compounds) and minimum (3 compounds) lipophilicity level. The obtained models along some statistical parameters (determination coefficient: R^2 , F value, standard deviation: s, cross validated determination coefficient: Q^2 , standard deviation error in calculation: SDEC, standard deviation error of prediction: SDEP, the prediction sum of squares: PRESS or root sum

Table 1. The lipophilicity indices of the investigated compounds

No.	LogP _{exp}	ALOGPs	AC logP	miLogP	KOWWIN	XLOGP2	XLOGP3	ALOGpS	AC logS	Hy	MLOGP	ALOGP
1	2.30	1.97	2.07	2.39	2.17	2.31	2.30	-1.78	-2.55	-0.76	2.41	2.12
2	1.58	2.30	2.25	1.61	1.80	1.69	1.49	-3.14	-3.55	-0.77	2.75	1.80
3	0.76	0.99	1.53	1.10	0.72	0.76	0.76	-1.45	-2.55	0.28	1.93	1.39
4	1.14	1.20	1.72	1.41	1.28	1.08	1.14	-2.72	-2.86	-0.35	2.17	1.64
5		2.00	2.49	2.82	1.97	2.49	2.71	-3.36	-3.40	-0.73	1.51	3.01
6		2.78	2.42	1.74	2.24	1.48	2.06	-2.68	-2.84	-0.82	2.32	1.80
7	1.01	1.06	1.21	0.90	0.88	0.12	0.95	-1.73	-2.47	-0.33	1.38	0.78
8	0.92	1.81	1.70	1.54	1.83	0.71	1.68	-1.89	-2.61	-0.81	2.17	1.78
9	2.95	4.19	3.50	3.52	3.69	3.00	3.94	-4.42	-4.23	-0.79	2.44	3.50
10	-0.07	-1.22	-0.77	0.87	-1.96	-0.60	-1.32	-0.47	-0.21	-0.56	0.29	-0.35
11	-0.78	-0.46	-0.51	-0.95	-0.05	-0.64	-0.78	-1.27	-1.51	0.02	0.40	-0.31
12	-0.02	-0.24	-0.09	0.00	-0.39	-0.48	-0.02	-0.80	-1.48	0.02	-0.00	-0.58
13	-0.73	-0.65	-0.25	-1.09	-1.15	-1.08	-0.73	-1.49	-1.87	1.84	-0.33	-0.72
14	-1.11	-0.85	-0.44	-0.73	-1.19	-0.24	-0.49	-1.43	-1.57	0.94	0.18	-0.78
15	-0.55	-0.55	0.10	-0.27	-0.55	0.07	0.08	-1.02	-1.90	0.94	0.58	-0.10
16	-2.17	-2.00	-3.69	-1.44	-3.61	-2.11	1.63	-1.48	-1.59	2.78	-1.23	-1.76
17		-0.29	0.31	-0.17	-0.28	0.40	0.06	-1.20	-1.87	1.84	0.48	0.28
18		0.56	0.79	0.27	0.60	0.24	0.18	-1.25	-1.30	-0.24	1.40	-0.34
19		1.66	1.64	2.00	2.12	1.22	1.63	-1.05	-1.09	-0.84	2.19	1.42
20		1.39	2.00	1.01	1.03	0.85	0.79	-3.38	-2.31	-0.29	1.11	1.04
21	1.17	0.87	1.24	1.09	1.00	1.13	1.17	-0.24	-0.79	-0.81	1.27	1.24
22	0.36	0.29	0.43	0.27	0.69	0.39	0.36	-0.17	-0.83	0.00	0.12	0.28
23	-0.34	-0.45	-0.11	-0.48	-0.45	-0.34	-0.37	-0.39	-0.91	0.84	-0.29	-0.32
24		0.55	1.00	0.47	0.38	0.68	0.68	-0.30	-1.24	-0.75	0.75	0.46
25		3.10	3.11	2.96	2.95	2.95	3.08	-3.89	-3.19	-0.37	2.04	3.02
26		-0.96	1.23	-1.45	-1.55	1.70	-0.34	-2.71	-2.97	-0.70	-2.61	0.36
27		1.52	1.67	1.47	1.49	1.55	1.54	-0.52	-1.09	-0.82	1.56	1.59
28		2.02	1.49	1.51	3.74	1.15	0.96	-2.48	-2.22	-0.81	1.45	1.39

No.	LogP _{exp}	ALOGPs	AC logP	miLogP	KOWWIN	XLOGP2	XLOGP3	ALOGpS	AC logS	Hy	MLOGP	ALOGP
29		-0.01	-0.06	0.00	-0.06	0.23	0.17	-0.87	-0.52	0.48	0.73	0.05
30		0.89	0.99	0.86	0.72	1.04	0.86	-0.70	-1.39	0.53	1.52	1.04
31	0.87	0.90	1.27	0.45	1.28	1.25	0.97	-1.21	-1.42	-0.24	1.27	1.16
32		1.61	1.70	0.30	1.72	1.38	1.42	-3.39	-1.86	-0.33	1.54	1.30
33	0.07	0.39	0.63	0.41	0.34	0.39	-0.32	-0.18	-0.77	-0.75	0.75	0.30
34		0.41	0.73	0.48	0.34	0.48	0.28	-0.13	-0.80	-0.75	0.75	0.73
35		0.05	-0.53	-0.24	-0.48	-0.56	-0.58	-1.07	-0.41	-0.17	0.17	-0.41
36		0.05	0.18	0.06	-0.80	-0.29	-0.42	-1.54	-0.86	-0.73	0.43	-0.42
37	-1.54	-0.66	0.36	-0.84	-1.80	1.66	-1.31	-1.24	-3.16	-0.70	-1.17	-0.55
38	-1.45	-0.32	-0.20	-0.50	-1.20	0.06	-0.87	-0.61	-0.38	-0.17	-0.06	-0.51
39		-0.64	-0.69	-0.95	-1.32	-0.33	-0.78	-1.11	-0.39	0.53	-0.33	-0.90
40		0.35	0.48	0.56	-0.05	0.30	0.43	-0.64	-0.44	-0.24	0.73	0.34
41		1.61	1.81	1.48	-0.38	0.78	1.62	-2.69	-3.27	-0.73	1.88	1.24
42		1.52	2.16	1.57	-0.17	0.44	1.33	-2.68	-3.04	-0.73	1.96	1.63
43		0.81	1.81	0.91	-1.71	-0.10	0.81	-2.03	-2.86	-0.26	1.60	1.03
44		1.76	0.97	1.52	-1.12	1.00	1.77	-2.53	-2.98	-0.70	1.93	1.25
45		1.81	1.32	1.61	-0.91	0.66	1.47	-2.56	-2.75	-0.70	2.01	1.64
46		0.81	0.97	0.95	-2.44	0.13	0.95	-1.75	-2.57	-0.24	1.67	1.04
47		1.17	1.06	0.90	-1.88	0.09	0.54	-2.18	-2.76	-0.26	1.12	0.63
48		1.06	1.41	1.00	-1.67	-0.51	0.25	-1.97	-2.54	-0.26	1.20	0.75
49		1.69	1.64	1.14	-0.16	1.08	1.22	-2.47	-3.21	-0.28	1.69	1.28
50	3.44	2.82	2.84	3.06	3.29	2.60	2.88	-2.99	-3.10	-0.38	2.19	2.73
51	2.68	3.20	2.94	3.03	3.21	2.69	2.68	-2.89	-3.08	-0.40	2.50	2.75
52		3.36	3.13	3.30	3.43	2.97	3.69	-3.02	-3.16	-0.38	2.28	3.13
53		2.77	3.25	3.22	3.49	2.92	2.99	-4.76	-4.23	-0.38	2.38	2.92
54		2.85	2.92	3.40	4.24	2.89	3.37	-3.48	-3.83	-0.82	2.38	3.13
55		1.36	2.47	4.53	3.60	4.04	3.96	-4.95	-4.50	-0.79	2.71	3.95
56	1.93	1.68	1.48	1.84	1.85	0.57	1.93	-2.29	-3.55	-0.83	2.90	1.15
57	0.98	1.85	1.27	1.46	1.49	0.13	0.98	-3.09	-3.59	-0.79	2.31	1.11
58	4.74	3.18	2.56	1.74	4.41	3.67	4.74	-4.25	-4.22	0.95	3.21	3.35
59		3.72	1.95	1.13	3.77	3.05	4.11	-4.32	-3.48	0.95	2.72	2.68
60		3.49	3.01	3.81	4.70	3.99	5.07	-4.71	-4.34	0.26	3.43	3.60

square: RSS) are enlisted in Table 2. Analysing the obtained models there may be remarked that in each model at least one of the computed log P values was selected (mostly KOWWIN, ALOGPs, miLogP, ALOGP and XLOGP3). These values are computed by fragmental (KOWWIN and miLogP), atomistic (ALOGP-using Ghose and Crippen algorithm), topological (ALOGPs) and also empirical (XLOGP3) algorithm. The selection of these lipophilicity descriptors in the best models is not randomly since during the last years, they have proved to be the most descriptive computed lipophilicity indices [28, 29]. Moreover, according to the selected descriptors, the log P_{exp} values are a consequence of

Table 2. The GA linear multiple regression models for lipophilicity prediction

No	Models	Q ²	R ²	s	F	SDEP	SDEC	PRESS	RSS
Models build on 26 compounds (Group A)									
1	$\text{Log } P_{\text{exp}} = 0.1395 + 0.8255 \text{KOWWIN}$	0.88	0.91	0.52	230	0.56	0.50	8.21	6.41
2	$\text{Log } P_{\text{exp}} = -0.2349 + 0.6514 \text{KOWWIN} + 0.0125 \text{Vs}$	0.91	0.93	0.45	155	0.48	0.42	6.03	4.67
3	$\text{Log } P_{\text{exp}} = 0.1091 + 1.0709 \text{A} \text{LogPs} - 0.9774 \text{Mor20m} + 4.7996 \text{Mor32m}$	0.96	0.97	0.32	213	0.33	0.29	2.77	2.26
4	$\text{Log } P_{\text{exp}} = 1.2519 + 0.3954 \text{miLogP} + 0.5413 \text{KOWWIN} + 3.4885 \text{Mor32m} - 5.7300 \text{HATS1u}$	0.96	0.98	0.26	255	0.32	0.23	2.64	1.37
5	$\text{Log } P_{\text{exp}} = -0.6331 + 1.1622 \text{A} \text{LogPs} + 0.2518 \text{X1v} - 1.6898 \text{MATS3e} - 0.2352 \text{DP09} + 4.5783 \text{Mor32m}$	0.98	0.99	0.22	276	0.23	0.19	1.41	0.97
Models build on 20 compounds (Group B; without compounds 4, 13, 23, 33, 51, 57)									
1	$\text{Log } P_{\text{exp}} = 0.1816 + 0.83271 \text{KOWWIN}$	0.86	0.90	0.58	161	0.64	0.55	8.19	6.06
2	$\text{Log } P_{\text{exp}} = -0.2941 + 0.6324 \text{KOWWIN} + 0.0298 \text{As}$	0.91	0.93	0.50	112	0.53	0.46	5.71	4.23
3	$\text{Log } P_{\text{exp}} = -0.9193 - 1.9805 \text{MATS3e} + 0.0912 \text{RDF055m} + 1.1346 \text{ALOGP}$	0.94	0.96	0.37	140	0.41	0.33	3.40	2.20
4	$\text{Log } P_{\text{exp}} = -0.6413 + 0.8452 \text{A} \text{LogPs} - 1.6617 \text{MATS3m} + 3.5942 \text{Mor32m} + 0.4381 \text{MLOGP}$	0.96	0.98	0.31	157	0.34	0.37	2.25	1.41
5	$\text{Log } P_{\text{exp}} = 3.8334 - 0.9217 \text{A} \text{LogPs} + 0.8379 \text{miLogP} + 0.8175 \text{KOWWIN} - 3.3724 \text{Ovality} + 0.0005 \text{PMIY}$	0.96	0.98	0.26	178	0.35	0.22	2.42	0.93
Models build on 20 compounds (Group C; without compounds 1, 7, 21, 31, 37, 56)									
1	$\text{Log } P_{\text{exp}} = -0.2090 + 1.0901 \text{ALOGP}$	0.87	0.91	0.55	174	0.61	0.52	7.40	5.49
2	$\text{Log } P_{\text{exp}} = -0.4625 + 0.5522 \text{KOWWIN} + 0.0116 \text{D/D}$	0.91	0.94	0.46	129	0.50	0.53	5.02	3.62
3	$\text{Log } P_{\text{exp}} = -3.3935 + 2.4782 \text{GATS3p} + 0.0163 \text{Vs} + 1.0494 \text{ALOGP}$	0.96	0.98	0.28	240	0.32	0.25	2.11	1.27
4	$\text{Log } P_{\text{exp}} = -4.7179 + 3.5208 \text{GATS3e} + 0.7891 \text{Mor10v} + 0.0106 \text{Vs} + 1.2385 \text{ALOGP}$	0.98	0.99	0.18	426	0.22	0.16	0.97	0.51
5	$\text{Log } P_{\text{exp}} = 0.0973 + 0.6455 \text{XLOGP2} - 3.2650 \text{MATS3e} + 0.0660 \text{RDF015u} - 8.0145 \text{G1m} + 0.5829 \text{ALOGP}$	0.99	0.99	0.15	536	0.16	0.12	0.51	0.30
Models build on 20 compounds (Group D; without compounds 2, 9, 22, 38, 50, 58)									
1	$\text{Log } P_{\text{exp}} = -0.1992 + 0.9829 \text{miLogP}$	0.89	0.91	0.39	188	0.41	0.37	3.31	2.68
2	$\text{Log } P_{\text{exp}} = -0.0780 + 0.6053 \text{miLogP} + 0.3286 \text{KOWWIN}$	0.95	0.96	0.27	207	0.28	0.24	1.61	1.21
3	$\text{Log } P_{\text{exp}} = -0.9215 + 0.3604 \text{miLogP} + 2.2192 \text{DISPp} + 0.4643 \text{MLOGP}$	0.95	0.97	0.24	171	0.26	0.22	1.40	0.93
4	$\text{Log } P_{\text{exp}} = -0.01782 + 0.7195 \text{miLogP} + 0.3036 \text{KOWWIN} + 0.7766 \text{MATS4m} - 0.2757 \text{Mor08u}$	0.97	0.98	0.18	234	0.21	0.16	0.92	0.49
5	$\text{Log } P_{\text{exp}} = -0.8269 + 0.7924 \text{miLogP} + 0.3270 \text{KOWWIN} + 0.6819 \text{MATS4e} - 0.3205 \text{Mor08e} + 12.6679 \text{R4u+}$	0.99	0.99	0.13	352	0.14	0.11	0.39	0.24

No	Models	Q ²	R ²	s	F	SDEP	SDEC	PRESS	RSS
Models build on 20 compounds (Group E; without compounds 9, 16, 37, 38, 50, 58)									
1	$\text{Log } P_{\text{exp}} = -0.05856 + 0.8986\text{miLogP}$	0.89	0.91	0.33	177	0.34	0.31	2.30	1.94
2	$\text{Log } P_{\text{exp}} = -0.0541 + 0.5530\text{miLogP} + 0.4046\text{XLOGP3}$	0.94	0.95	0.24	171	0.26	0.22	1.31	1.00
3	$\text{Log } P_{\text{exp}} = 0.5240 + 0.4764\text{miLogP} + 0.3904\text{XLOGP3} - 4.0970\text{HATS3m}$	0.95	0.97	0.21	195	0.24	0.18	1.12	0.58
4	$\text{Log } P_{\text{exp}} = 0.9268 + 0.4889\text{miLogP} + 0.4650\text{XLOGP3} - 2.0570\text{Mor27p} - 14.8156\text{R3m+}$	0.98	0.99	0.15	246	0.16	0.13	0.53	0.32
5	$\text{Log } P_{\text{exp}} = 1.7449 + 0.3402\text{miLogP} + 0.5925\text{XLOGP3} - 0.6149\text{piPC03} - 0.1954\text{Mor05u} - 0.5576\text{Mor30e}$	0.98	0.99	0.14	209	0.16	0.12	0.50	0.28

the molecular conformation/configuration and also of the atoms nature, since the most selected descriptors were from the 2D autocorrection and 3D MoRSE descriptors. These are completed by WHIM descriptors which are also very descriptive in partition coefficient prediction, since they are 3D dimensional descriptors based on the calculation of principal component axes computed from a weighted covariance matrix obtained by the molecule geometrical coordinates. They contain information concerning, size, symmetry, shape and distribution of the molecular atoms [30]. Other descriptors were belonging to the following categories: steric, Randic molecular profiles, RDF descriptors, topological descriptors, connectivity indices, geometrical descriptors and GETAWAY descriptors. The most selected descriptor (in all groups) was miLogP (12 times), followed by KOWWIN (10 times), ALOGP (5 times) and XLOGP3 (4 times). All the results and even the selected class of descriptors are in fair agreement with observations made by our group in previous studies [20, 21] and also by Benfenati [31].

Furthermore, as can be seen from the Table 2 the statistical parameters of quality are increasing while the number of selected variables is bigger. However, this doesn't mean that the predictive capacity is higher, since the coefficients level may be a consequence of over-fitting. Even if the Q² has an increased value, the prediction capacity may be low, especially for compounds not included in the training set. In order to observe, which models are more valuable, a correlation matrix has been made between computed and experimental Log P values and the predicted ones (Table 3).

There may be observed that Log P_{exp} is strongly correlating to ALOGP and to KOWWIN, which is in fact expected since they were often selected in the best models obtained. In addition, it is strongly correlated to the predicted values. Investigating the correlation of the predicted values with experimental ones, there may be observed that the highest correlations were obtained for

Table 3. The correlation matrix between the experimental and computed log P values and the predicted ones (bold values indicate correlation coefficients higher than 0.90, while italic bolded values indicate correlation coefficients between 0.80 and 0.89)

Group	Predicted Log P	ALOGPs	AC logP	miLogP	KOWWIN	XLOGP2	XLOGP3	MLOGP	ALOGP	ALOGps	AC logs	Log P _{exp}
A	LogP 1	0.83	0.78	0.78	1.00	0.84	0.80	0.74	0.84	-0.62	-0.53	0.95
	LogP 2	0.88	0.81	0.82	0.98	0.88	0.87	0.79	0.89	-0.72	-0.64	0.97
	LogP 3	0.94	0.85	0.86	0.87	0.83	0.89	0.86	0.91	-0.72	-0.65	0.98
	LogP 4	0.84	0.80	0.88	0.95	0.86	0.88	0.80	0.91	-0.69	-0.62	0.99
	LogP 5	0.94	0.85	0.85	0.83	0.79	0.87	0.87	0.89	-0.69	-0.66	0.99
B	LogP 1	0.83	0.78	0.78	1.00	0.84	0.80	0.74	0.84	-0.62	-0.53	0.95
	LogP 2	0.91	0.84	0.85	0.95	0.88	0.89	0.82	0.92	-0.76	-0.69	0.96
	LogP 3	0.88	0.87	0.90	0.80	0.88	0.91	0.82	0.97	-0.79	-0.79	0.98
	LogP 4	0.93	0.82	0.85	0.81	0.77	0.88	0.91	0.89	-0.69	-0.65	0.99
	LogP 5	0.75	0.73	0.85	0.92	0.85	0.84	0.74	0.86	-0.67	-0.60	0.99
C	LogP 1	0.91	0.92	0.93	0.84	0.91	0.91	0.82	1.00	-0.77	-0.75	0.95
	LogP 2	0.86	0.79	0.81	0.95	0.89	0.88	0.76	0.89	-0.74	-0.64	0.96
	LogP 3	0.87	0.84	0.88	0.77	0.87	0.92	0.79	0.96	-0.79	-0.78	0.97
	LogP 4	0.84	0.83	0.86	0.67	0.81	0.87	0.78	0.93	-0.76	-0.78	0.98
	LogP 5	0.84	0.85	0.86	0.78	0.93	0.89	0.74	0.95	-0.77	-0.77	0.95
D	LogP 1	0.86	0.85	1.00	0.78	0.79	0.84	0.84	0.93	-0.68	-0.67	0.90
	LogP 2	0.90	0.87	0.96	0.93	0.86	0.87	0.85	0.94	-0.69	-0.65	0.95
	LogP 3	0.89	0.85	0.94	0.80	0.77	0.84	0.92	0.90	-0.64	-0.61	0.92
	LogP 4	0.89	0.85	0.96	0.89	0.83	0.87	0.87	0.93	-0.67	-0.64	0.95
	LogP 5	0.89	0.85	0.96	0.88	0.80	0.85	0.86	0.92	-0.66	-0.63	0.94
E	LogP 1	0.86	0.85	1.00	0.78	0.79	0.84	0.84	0.93	-0.68	-0.67	0.90
	LogP 2	0.90	0.84	0.97	0.82	0.84	0.95	0.85	0.96	-0.76	-0.73	0.93
	LogP 3	0.91	0.85	0.97	0.83	0.84	0.94	0.85	0.96	-0.74	-0.71	0.93
	LogP 4	0.90	0.82	0.94	0.81	0.82	0.94	0.85	0.94	-0.73	-0.70	0.93
	LogP 5	0.86	0.77	0.90	0.87	0.86	0.96	0.79	0.92	-0.73	-0.67	0.93
	Log P _{exp}	0.92	0.87	0.90	0.95	0.84	0.86	0.89	0.95	-0.72	-0.65	1.00

groups A and B, while the lowest is obtained in case of group E. This observation is indicating that for a more accurate prediction a very important step is the selection of the training set. The correlation with log P values obtained for group A was expected because there was no elimination made and each particular value has been contributed to the final model. On the other side, in case of group B, the elimination was made in such a manner that the entire range was described, without eliminating the extreme values, which allowed them to have a significant contribution to the final developed models. However, when the eliminated values were the extreme ones, the correlation was lower because the model was built in a reduced range and then used

for outside values prediction. On the basis of this observation there may be concluded that the selection of training set in case of prediction models generation is crucial and it may affect the reliability of the entire following results. Moreover, it is indicating that the elimination of the values, which would be used further for prediction evaluation (test set), must cover as much as possible the training, but the extreme values must be kept. The viability of the models which led to the best correlation with experimental values (models with 4 descriptors) is illustrated by the representation of the observed vs. predicted values (Figure 2). The statements above are also very well supported by histograms and normal distribution and box and whisker plot presented in Figure 3 and 4.

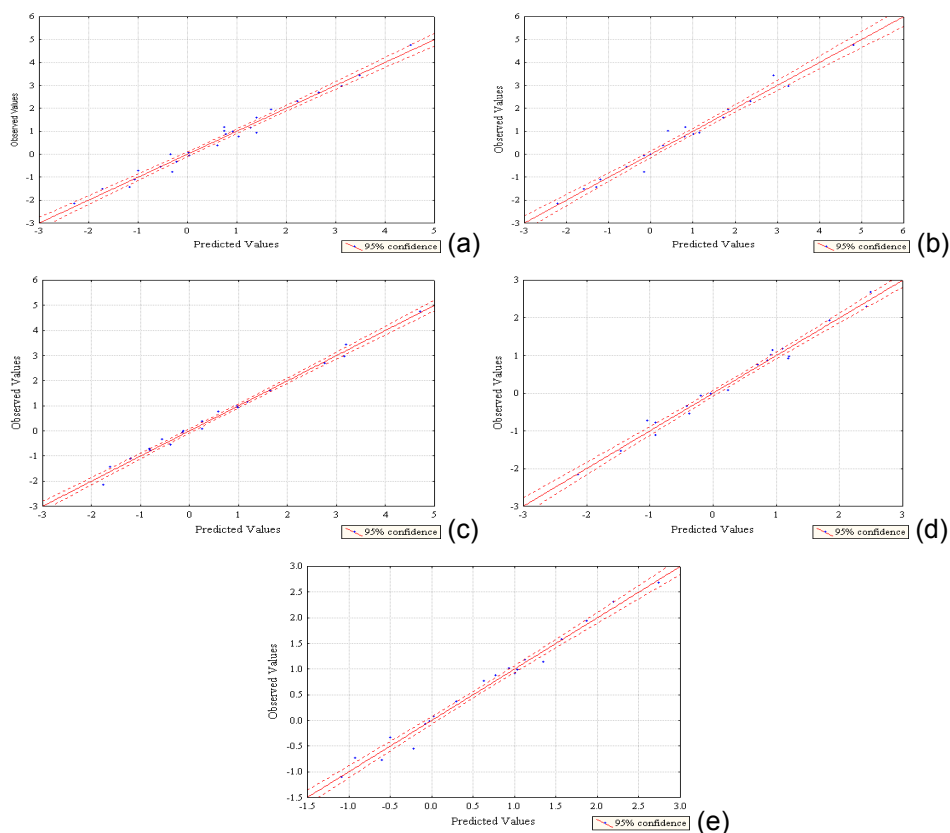


Figure 2. Graphs of predicted vs observed values corresponding to the best models: group A (a), group B (b), group C (c), group D (d), and group E (e).

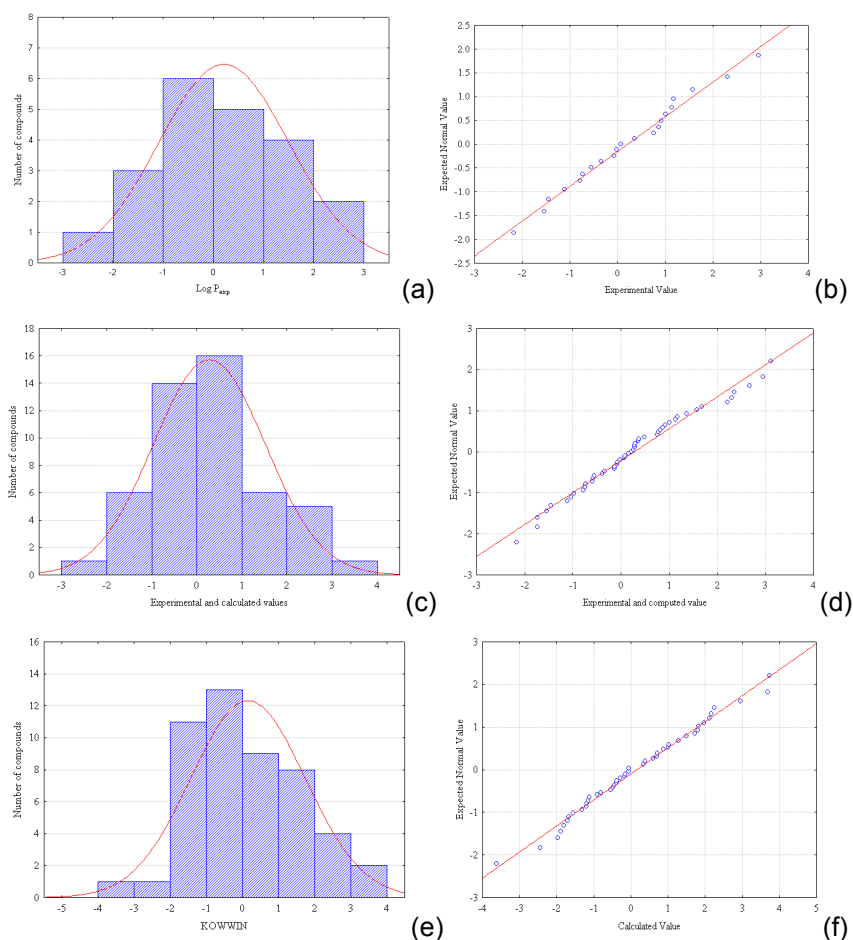


Figure 3. Histograms and normal probability plot of data corresponding to experimental (a,b), experimental including estimated values by model E (5)-(c,d), and KOWWIN values (e,f).

In order to observe the ability of the obtained models to predict the lipophilicity the list of $\text{Log } P_{exp}$ has been completed with the predicted values (were missing) and correlated with the computed ones (Table 4). The maximum value of the correlation coefficient (r) in this case is 0.98, and it is observed that once again the best correlations are obtained with ALOGP and KOWWIN. In all cases the $\text{log } S$ values have led to lower statistical correlations, which mean that the solubility descriptors are not describing very well the lipophilicity.

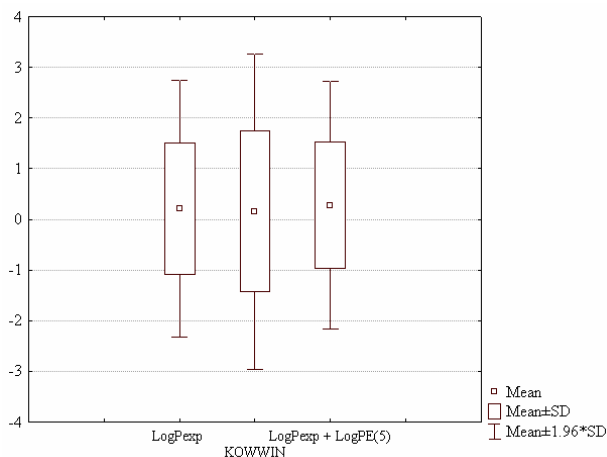


Figure 4. Box and whisker plot of data corresponding to experimental, experimental including estimated values by model E (5), and KOWWIN values.

In many situations the PCR combined with GA for property modelling is leading to more appropriate results. However, in our case the obtained models had lower statistical quality and prediction capacity. The highest Q^2 value that was reached was 0.91. If comparing to the models presented in Table 2, there is no doubt that the classical modelling has led to better results. This may be explained by the fact that the PCA has the ability to concentrate in the first few components the entire information contained in the initial matrix. This is in many cases advantageous, but as can be seen from the models presented in Table 2, only few descriptors are correctly defining the lipophilicity, while the others have no positive contribution. The inefficient prediction models obtained by PCR-GA may be a consequence of the large of useless information retained in the scores of the first principal components involved later in the modelling. The principal components are a consequence of all the descriptors and most of them do not describe correctly the lipophilicity, which is finally leading to the lower quality models.

As can be observed from Table 1, the lipophilicity range is generally between -3 to 3, which means that for a high biological activity is very important to have a certain level of lipophilicity, in order to cross the biological membranes. This range is indicating that for an increased activity the lipophilicity level doesn't have to be too high, when appear the situation of total absorption in the adipose tissue (i.e. skin discoloration in case of carotene overdose), or the opposite situation when the compounds are unable to cross in simple form the biological membranes (i.e. water biological membrane crossing by means of an aquaporine protein). These observations are indicating that the partition phenomena take place at cellular level when the lipophilicity is in an optimal range.

Table 4. The Correlation matrix between the experimental and predicted lipophilicity values vs. the computed lipophilicity indices (bold values indicate correlation coefficients higher than 0.90, while italic bolded values indicate correlation coefficients between 0.80 and 0.89)

Group	Log P*	ALOGPs	AC logP	miLogP	KOWWIN	XLOGP2	XLOGP3	MLOGP	ALOGP	ALOGps	AC logS
A	1	0.81	0.75	0.79	0.98	0.84	0.82	0.73	0.84	-0.62	-0.52
	2	0.86	0.80	0.83	0.96	0.87	0.87	0.78	0.89	-0.69	-0.60
	3	0.93	0.84	0.86	0.86	0.82	0.89	0.86	0.90	-0.71	-0.65
	4	0.84	0.80	0.88	0.94	0.86	0.88	0.80	0.90	-0.69	-0.62
	5	0.93	0.84	0.85	0.82	0.79	0.88	0.87	0.89	-0.69	-0.65
B	1	0.81	0.76	0.79	0.98	0.84	0.82	0.73	0.84	-0.63	-0.52
	2	0.88	0.82	0.86	0.94	0.87	0.90	0.81	0.92	-0.73	-0.65
	3	0.87	0.87	0.90	0.80	0.87	0.91	0.81	0.97	-0.77	-0.76
	4	0.93	0.82	0.85	0.80	0.77	0.88	0.90	0.89	-0.68	-0.65
	5	0.74	0.72	0.85	0.92	0.85	0.84	0.72	0.86	-0.66	-0.59
C	1	0.89	0.89	0.91	0.84	0.88	0.91	0.82	0.97	-0.75	-0.73
	2	0.84	0.78	0.82	0.94	0.87	0.87	0.77	0.88	-0.71	-0.61
	3	0.87	0.85	0.88	0.78	0.85	0.91	0.81	0.95	-0.77	-0.76
	4	0.85	0.84	0.87	0.68	0.79	0.87	0.79	0.93	-0.75	-0.78
	5	0.85	0.85	0.88	0.80	0.89	0.90	0.78	0.95	-0.78	-0.74
D	1	0.87	0.85	0.94	0.82	0.81	0.87	0.86	0.93	-0.69	-0.68
	2	0.88	0.84	0.91	0.92	0.86	0.88	0.84	0.93	-0.69	-0.64
	3	0.89	0.84	0.90	0.82	0.79	0.86	0.89	0.90	-0.66	-0.63
	4	0.89	0.84	0.93	0.89	0.84	0.89	0.87	0.93	-0.69	-0.65
	5	0.89	0.84	0.93	0.89	0.82	0.88	0.87	0.93	-0.68	-0.66
E	1	0.87	0.86	0.94	0.82	0.81	0.87	0.86	0.93	-0.69	-0.68
	2	0.90	0.87	0.93	0.84	0.86	0.91	0.86	0.96	-0.73	-0.70
	3	0.90	0.88	0.93	0.85	0.85	0.90	0.86	0.95	-0.71	-0.68
	4	0.91	0.87	0.91	0.84	0.84	0.90	0.87	0.95	-0.70	-0.67
	5	0.89	0.85	0.90	0.90	0.89	0.91	0.83	0.94	-0.71	-0.65

* Log P_{exp} known + predicted

CONCLUSIONS

The quantitative structure-lipophilicity relationships of 60 structurally diverse bioactive compounds have been investigated in order to develop a sound predictive model for the lipophilicity estimation of natural compounds with strong biological activity. The lipophilicity expressed as Log P was found to be significantly influenced by a series of descriptors coded as 2D autocorrection,

3D MoRSE or WHIM. The modelling process validated through different methodologies of training set selection, has been supported by highly relevant statistical parameters and graphs. The obtained results were highly descriptive and in a very good agreement with the computed lipophilicity indices. The best models were those with four retained descriptors, but the models with three, two or one descriptor produce also relevant results in a very good agreement with computed lipophilicity indices. In addition, the results obtained in this study for a large number of important natural compounds add a real and useful contribution to the data collection concerning their characteristics and might be a starting point for future investigation concerning the optimal lipophilicity range.

EXPERIMENTAL SECTION

The selected compounds for this study belong to alkaloids and mycotoxins group, as follows: cocaine (1), heroine (2) morphine (3), codeine (4), noscapine (5), thebaine (6), oxycodone (7), hydromorphone (8), papaverine (9), caffeine (10), theobromine (11), theophylline (12), xanthine (13), hypoxanthine (14), allopurinol (15), uric acid (16), oxypurinol (17), cytosine (18), sparteine surrogate (19), varenicline (20), nicotine (21), nicotinic acid (22), nicotinamide (23), n-formyl normicotine (24), brevicolline (25), pyridine,3-(1-methyl-1-oxido-2-pyrrolidinyl)-,1-oxide (26), n-ethyl normicotine (27), anabaseine (28), rac-trans 3'-aminomethyl nicotine (29), rac-2-amino nicotine (30), anabasine (31), anatalline (32), cotinine (33), ortho-cotinine (34), rac-trans-cotinine carboxylic acid (35), rac-trans-cotinine carboxylic acid methyl ester (36), cotinine n-oxide (37), 3-hydroxy cotinine (38), rac 3'-hydroxy cotinine 3-carboxylic acid (39), rac3'hydroxy-methyl nicotine (40), aflatoxin B1 (41), aflatoxin B2 (42), aflatoxin B2a (43), alatoxin G1 (44), aflatoxin G2 (45), aflatoxin G2a (46), aflatoxin M1 (47), aflatoxin M2 (48), aflatoxicol (49), quinine (50), cinchonine (51), hydroquinine (52), quinotoxine (53), quinone (54), bromoquinotoxine (55), strychnine (56), brucine (57), ochratoxin A (58), ochratoxin B (59) and ochratoxin C (60). The Log P_{exp} for 26 of the above mentioned compounds has been obtained from different databases (www.chemspider.com; http://esc.syrres.com/esc/est_kowdemo.htm; www.vcclab.org; and <http://www.biobyte.com>). Both experimental and computed lipophilicity indices are enlisted in Table 1. In order to obtain the desired information, the first two web pages had required the CAS registry number of the compounds, while the last two had required the SMILE formula, which was obtained on www.molinspiration.com.

The molecular descriptors for the selected compounds were computed with ALOGPS 2.1 Internet module, Chem Office 8.0 and Dragon Plus 5.4 software. The ALOGPS 2.1 was able to compute six log P values (ALOGPs,

AC logP, miLogP, KOWWIN, XLOGP2 and XLOGP3) and two Log S values (ALOGpS and AC logS) on the basis of compounds SMILE formula. Previous of descriptors computation, the structure of each molecule has been drawn in Chem Draw 8.0 application, and the obtained structures were further energetically optimised by means of molecular mechanics force field procedure included in Hyperchem version 8.0 (www.hyper.com) and the resulting geometries were further refined by means of the semi-empirical method Parametric Method-3 using the Fletcher–Reeves algorithm and a gradient norm limit of 0.009 kcal Å⁻¹. The optimized geometries were loaded by the above presented software in order to calculate the molecular descriptors. The Chem Office 8.0 software through the application Chem 3DUltra allows the computation of 30 descriptors classified as electronic, steric and thermodynamic ones, while Dragon Plus 5.4 allows the computation of 942 descriptors belonging to the following groups: constitutional descriptors, walk and path counts, information indices, edge adjacency indices, Randic molecular profiles, RDF descriptors, WHIM descriptors, functional groups counts, charge descriptors, topological descriptors, connectivity indices, 2D autocorrelation, Burgen eigenvalues, eigenvalue based indices, geometrical descriptors, 3D-MoRSE descriptors, GETAWAY descriptors, atom centred fragments and molecular properties. The correlations, graphs, PCA and CA were realized by Statistica 8.0 software, while GA was made by MobyDigs 1.0 software. The developed models have been designed to retain 1 to 5 descriptors. The modelling has been realized on the basis of the matrix formed by the computed descriptors and also on the basis of the scores obtained by applying PCA on the matrix formed by the computed descriptors.

ACKNOWLEDGMENTS

This work was possible with the financial support offered by Romanian Ministry of Education, Research, Youth and Sport through research grant PN-II-ID-PCE-2011-3-0366 (Project Manager: C. Sârbu).

REFERENCES

1. J. D. McChesney, S. K. Venkataraman, J. T. Henri, *Phytochemistry*, **2007**, *68*, 2015.
2. D. J. Newman, G. M. Cragg, K. M. Snader, *Journal of Natural Products*, **2003**, *66* (7), 1022.
3. G. M. Cragg, D. G. I. Kingston, D. J. Newman, "Anticancer Agents from Natural Products"; CRC Press, Boca Raton, **2005**.
4. K. E. Panter, L. F. James, *Journal of Animal Science*, **1990**, *68*, 892.

5. R. A. Saporito, M. A. Donnelly, T. F. Spande, H. M. Garraffo, *Chemoecology*, **2012**, 22, 159.
6. R. Andraws, P. Chawla, D. L. Brown, *Progress in Cardiovascular Diseases*, **2005**, 47, 217.
7. A. Yiannikourisa, J.-P. Jouany, *Animal Research*, **2002**, 51, 81.
8. N. W. Turner, S. Subrahmanyam, S. A. Piletsky, *Analytica Chimica Acta*, **2009**, 632, 168.
9. C. A. Robbins, L. J. Swenson, M. L. Nealley, R. E. Gots, B. J. Kelman, *Applied Occupational and Environmental Hygiene*, **2000**, 15 (10), 773.
10. M. Z. Zheng, J. L. Richard, J. Binder, *Mycopathologia*, **2006**, 161, 261.
11. S. Berger, D. Sicker, „Classics in Spectroscopy“, Wiley-VCH, Weinheim, **2009**.
12. K. C. Nicolaou, T. Morgan, “Molecules that changed the world”, Wiley-VCH, Weinheim, **2008**.
13. R. Pignatello, S. Guccione, S. Forte, C. Di Giacomo, V. Sorrenti, L. Vicari, G. U. Barretta, F. Balzanoc, G. Puglisi, *Bioorganic & Medicinal Chemistry*, **2004**, 12, 2951.
14. A. A. Toropov, A. P. Toropova, *Journal of Molecular Structure: Theochem*, **2001**, 538, 197.
15. I. V. Tetko, J. Gasteiger, R. Todeschini, A. Mauri, D. Livingstone, P. Ertl, V. A. Palyulin, E. V. Radchenko, N. S. Zefirov, A. S. Makarenko, V. Y. Tanchuk, V. V. Prokopenko, *Journal of Computer-Aided Molecular Design*, **2005**, 19, 453.
16. B. Testa, P. A. Carrupt, P. Gaillard, F. Billois, P. Weber, *Pharmaceutical Research*, **1996**, 13, 335.
17. M. J. Waring, *Expert Opinion on Drug Discovery*, **2010**, 5, 235.
18. Q. Du, G. A. Artec, *Journal of Computer-Aided Molecular Design*, **1996**, 10, 133.
19. M. Kompany-Zareh, *Medicinal Chemistry Research*, **2009**, 18, 143.
20. C. Sârbu, C. Onișor, M. Posa, S. Kevresan, K. Kuhajda, *Talanta*, **2008**, 75, 651.
21. C. Onișor, M. Poša, S. Kevrešan, K. Kuhajda, C. Sârbu, *Journal of Separation Science* **2010**, 33, 3110.
22. S. Trapp, R. W. Horobin, *European Biophysics Journal*, **2005**, 34, 959.
23. M. Jaiswal, P. V. Khadikar, C. T. Supuran, *Bioorganic & Medicinal Chemistry Letters*, **2004**, 14, 5661.
24. G. Caron, G; Ermondi, A. Damiano, L. Novaroli, O. Tsinman, J. A. Ruell, A. Avdeef, *Bioorganic & Medicinal Chemistry*, **2004**, 12, 6107.
25. T. Takagi, M. Sugeno, *IEEE Transactions on Systems, Man, and Cybernetics*, **1998**, 15, 116.
26. C. Sârbu, D. Casoni, A. Kot-Wasik, A. Wasik, J. Namiešnik, *Journal of Separation Science*, **2010**, 33, 2219.
27. D. Casoni, J. Petre, V. David, C. Sârbu, *Journal of Separation Science*, **2011**, 34 (3), 247.
28. R. D. Briciu, A. Kot-Wasik, A. Wasik, J. Namiešnik, C. Sârbu, *Journal of Chromatography A*, **2010**, 1217, 3702.
29. C. Sârbu, R. D. Nașcu-Briciu, D. Casoni, A. Kot-Wasik, A. Wasik, J. Namiešnik, *Journal of Chromatography A*, **2012**, 1266, 53.
30. R. Todeschini, M. Lasagni, E. Marengo, *Journal of Chemometrics*, **1994**, 8, 263.
31. E. Benfenati, “Quantitative Structure Activity Relationships for Pesticide Regulatory Purposes”, Elsevier, Amsterdam, **2007**, chapter 8.